UNIVERSIDADE DE LISBOA
INSTITUTO SUPERIOR TÉCNICO

Fluorescently-labeled DNA Probes Functionalized onto Gold Nanorods for Signal Enhancement of Nucleic Acids' Detection

David José Roxo Botequim

Supervisor: Doctor Pedro Miguel Neves Ribeiro Paulo

Co-Supervisor: Doctor Duarte Miguel de França Teixeira dos Prazeres

Thesis approved in public session to obtain the PhD Degree in Biotechnology and Biosciences

Jury final classification: Pass with Distinction

2020

UNIVERSIDADE DE LISBOA

INSTITUTO SUPERIOR TÉCNICO

Fluorescently-labeled DNA Probes Functionalized onto Gold Nanorods for Signal Enhancement of Nucleic Acids' Detection

David José Roxo Botequim

Supervisor: Doctor Pedro Miguel Neves Ribeiro Paulo

Co-Supervisor: Doctor Duarte Miguel de França Teixeira dos Prazeres

Thesis approved in public session to obtain the PhD Degree in Biotechnology and Biosciences

Jury final classification: Pass with Distinction

Jury

Chairperson: Doctor Isabel Maria de Sá Correia Leite de Almeida, Instituto Superior Técnico da Universidade de Lisboa

Members of the Committee:

Doctor João Pedro Estrela Rodrigues Conde, Instituto Superior Técnico da Universidade de Lisboa

Doctor João Carlos dos Santos Silva e Pereira de Lima, Faculdade de Ciências e Tecnologia da Universidade Nova de Lisboa

Doctor Eulália Fernanda Alves de Carvalho Pereira, Faculdade de Ciências da Universidade do Porto

Doctor Fábio Monteiro Fernandes, Instituto Superior Técnico da Universidade de Lisboa

Doctor Pedro Miguel Neves Ribeiro Paulo, Instituto Superior Técnico da Universidade de Lisboa

Funding Institution

FCT - Fundação para a Ciência e a Tecnologia

2020

À minha família e amigos
(To my family and friends)

Acknowledgements

The achievement of this stage in my graduation and scientific career could only be possible due to the contribution of several persons and institutions to whom I am deeply grateful. Indeed, gratitude flows through me in gigantic waves.

My first salute goes to Dr. Pedro Paulo, not only in the quality of my Supervisor but also for his friendship since the very beginning of our working together. I must highpoint his remarkable support, availability and patience, the impressive sharing of knowledge and wisdom, and the intense contribution to challenging ideas and for fruitful discussions. But most importantly, the passion that he conveys and puts into his work is definitely outstanding and inspiring. Altogether, these were meaningful benefits for the progress of my research, and to overcoming obstacles and reaching milestones. To my Co-supervisor, Prof. Duarte Miguel Prazeres, I am also truly thankful for always being supportive, to follow and discuss achievements and drawbacks of the research, and to give his vital feedback and critical opinion at important and decisive moments.

The research work of this doctoral thesis was developed in two groups of "Instituto Superior Técnico": the former Molecular Photochemistry and Photonic Materials (MPPM) Group (recently integrated in the Photoactive Molecules, Photonics and Functional Materials Group) of "Centro de Química Estrutural" and the Bioengineering Research Group (BERG) of the Institute for Bioengineering and Biosciences. Hence, appreciations should be given to a number of people of these groups. I owe special thanks to Prof. Sílvia Costa for always being interested, helpful and encouraging in the paths of research that I was following. Along with her extraordinary scientific experience and readiness to share and discuss science, these were valuable assets. To all the colleagues of the former MPPM group I address my words of acknowledgment. Especially to Dr. Vanda Serra for being such an enthusiastic co-worker and friend that provided constant support and enriching scientific discussions, and to Dr. Agnieszka Jóskowiak for her friendship, collaboration and important criticism. But also, to the undergraduate and master's students - André Graça, Alexandra Francisco, Nuno Neto, Tiago Policarpo, Sofia Serra, Inês Silva - that I had the opportunity and the pleasure to meet and work with, sometimes introducing them to the laboratory and research environments, and assisting in their guidance. Regarding the BERG, I acknowledge the collaboration of Dr. Sofia Martins and I appreciate the companionship and the positive influence that several co-workers and Ph.D. colleagues had in everyday moments, at the BIOTECnico (Biotechnology and Biosciences) Ph.D. Program workshops and in my work. In particular Rui Silva for his friendship and the amazing times and pleasant conferences that we shared. His interest, engagement and critical view in broader areas of my research led us to great discussions, to work together and to accomplish the publication of articles, contributing definitely to the improvement of my work.

Prof. Eduardo P. Melo from "Centro de Ciências do Mar" from University of Algarve must also be highlighted, remarkably for providing conditions in his laboratories for the cell internalization assays. Regarding my visiting period in the Molecular Biosensing for Medical

Diagnostics Group of the Eindhoven University of Technology, I would like to acknowledge Dr. Peter Ziljstra for welcoming me, for his supervision, and for contributing to my comfort in an all-new working environment and country. Special thanks are also owed to several members of the group for their constructive co-working interactions, namely Yuyang Wang and Matěj Horácek for their friendship, for training me and assisting in the dark-field microscopy equipment.

I also would like to acknowledge the financial funding from "Fundação para a Ciência e a Tecnologia" for my Ph.D. grant (PD/BD/113630/2015). This grant was only possible due to the BIOTECnico Ph.D. Program, and in this regard, I also acknowledge its Director, Prof. Isabel Sá-Correia. The financial budget made available through BIOTECnico also allowed me to disseminate my ongoing work in several international conferences, both in oral and poster communications. Some of these meetings turned out to be essential for the advances of my doctorate studies and enriched me scientifically and personally.

Last but not least, it is a privilege to have friends and family who have been a fundamental anchor throughout my doctorate years. Thanks to them I had the chance to live great moments, to share my research purposes, to talk about the downs and to celebrate the ups encountered in the Ph.D. path. For the presence and good feelings, I acknowledge Guilherme, my friends and colleagues from my master's degree in biomedical engineering, from "Santo-Amaro/Fonte da Pedra" and from the gyms. A special feeling of gratitude to my Mother Maria Fernanda and my sister Brigite for the strong bonds that connect us, my nephew Henrique (Sky is not the limit), Paulo, Juan, my uncle Horácio, my grandmother Maria José, my family members living in the USA and France, and Angela for the love ride. I am forever thankful for their unconditional support, care, affection, enlightenment and love.

Resumo

Os biosensores são ferramentas fundamentais em várias áreas da nossa sociedade contemporânea, incluindo na medicina e nos cuidados de saúde, sendo úteis em diagnóstico e em terapêutica ao providenciarem a deteção de biomarcadores associados a doenças. Em particular, a área da nanomedicina, na qual a nanotecnologia é aplicada à biotecnologia e à medicina, poderá contribuir para o desenvolvimento de biosensores inovadores que num futuro próximo virão a colmatar a necessidade de testes de diagnóstico para análises no ponto de atendimento (ou *POC* do acrónimo em inglês). Esta abordagem representará uma melhoria significativa nos cuidados de saúde prestados à generalidade da população.

Foi neste contexto científico e tecnológico que a presente tese de doutoramento foi desenvolvida. É assim dada uma contribuição para este esforço coletivo na área de nanobiosensores através da investigação de sondas fluorescentes de DNA conjugadas com nanopartículas de ouro. Estes sensores nanohíbridos foram idealizados para melhorar a deteção de ácidos nucleicos propostos na literatura como biomarcadores associados a doenças. A sinalização por fluorescência é baseada em sondas artificiais de DNA em gancho (ou *hairpin*) conhecidas como faróis moleculares (*molecular beacons*). A função da partícula metálica, por sua vez, extravasa a de uma simples plataforma à nano-escala, dado que esta pode atuar como antena ótica e induzir intensificações elevadas na emissão do corante fluorescente. O trabalho de investigação foi dedicado principalmente à avaliação da intensificação da emissão de sondas fluorescentes de DNA pelo efeito antena das nanopartículas de ouro, de modo a alcançar a amplificação do sinal ótico em sensores baseados na fluorescência.

Estudos detalhados do efeito de intensificação foram realizados por microscopia confocal de fluorescência com sensibilidade para molécula individual e em combinação com espectroscopia de partícula única. As experiências revelaram intensificações máximas de duas e três ordens de grandeza para a emissão de corantes fluorescentes na gama do vermelho induzidas, respetivamente, por um nanobastonete de ouro ou, em alternativa, por um dímero de nanoesferas de ouro. Posteriormente, foi otimizada a funcionalização da superfície de nanobastonetes de ouro através da validação de um método para colocar sondas fluorescentes de DNA especificamente nas extremidades de nanobastonetes. Isto assegurou uma intensificação efetiva da emissão dos nanohíbridos em cerca de uma ordem de grandeza, enquanto o revestimento indiscriminado da superfície levou a uma indesejada supressão da emissão, tal como medido num volume macroscópico por técnicas de espectroscopia de fluorescência em estado estacionário.

Para a criação dos sensores nanohíbridos foram explorados e testados vários sistemas modelo baseados em faróis moleculares conjugados com nanobastonetes de ouro. Os faróis moleculares foram desenhados para operar com base numa mudança na eficiência do processo de transferência de energia em ressonância pelo mecanismo de Förster (FRET) desencadeada por alterações na conformação do *hairpin*. O par doador-aceitante selecionado consistiu no corante Atto-647N e nas moléculas supressoras DDQ II ou QSY 21. Os ensaios preliminares foram realizados com alvos de RNA ou DNA sintéticos cujas sequências foram propostas na literatura para o diagnóstico médico de doenças infeciosas, tais como o dengue e a doença do sono, e ainda uma sequência de um microRNA proposto para o diagnóstico do cancro e/ou doenças cardiovasculares. A resposta limitada destes faróis moleculares no reconhecimento dos alvos conduziu ao desenvolvimento de uma nova sonda em gancho que emprega o próprio nanobastonete de ouro como aceitante de energia. A funcionalização seletiva dos nanobastonetes com esta nova sonda foi desenvolvida com sucesso. No entanto, os testes preliminares com os nanohíbridos resultaram até agora numa sinalização do alvo que ficou aquém das expectativas. A conjugação de sondas de DNA em gancho revelou-se por isso um percurso desafiante, mas, acima de tudo, estimulante e promissor, dado que é esperado que possa vir a contribuir para novas oportunidades na aplicação dos sensores nanohíbridos em testes no ponto de atendimento para efeitos de diagnóstico médico.

Palavras-chave: Nanopartículas de ouro, DNA marcado com corantes fluorescentes, Nanoantenas plasmónicas, Funcionalização seletiva de nanopartículas, Sinalização de ácidos nucleicos por sondas fluorescentes.

Abstract

Biosensors are fundamental tools in several areas of our contemporary society, including medicine and healthcare, being useful in diagnostics and therapeutics, as they provide the detection of disease biomarkers. In particular, the field of nanomedicine, in which nanotechnology is applied to biotechnology and medicine, may contribute to the development of innovative biosensors that in a near future will fulfill the demand for diagnostic tests towards point-of-care testing. This will create significant solutions and improvements upon the general public healthcare.

The present doctoral thesis was developed in this scientific and technological context. Thus, a contribution is given toward this collective effort in the field of nanobiosensors with research studies on fluorescently-labeled DNA probes conjugated onto gold nanoparticles. These nanohybrid sensors were envisioned for improved detection of nucleic acids proposed in the literature as disease biomarkers. The fluorescence signalling is based on artificial DNA hairpin probes known as molecular beacons, and the role of the metal particle is more than that of a nano-scaled platform, as it can act as an optical antenna and induce large enhancements in the dye's emission. The research work was mostly dedicated to the evaluation of the emission enhancement of dye-labeled DNA probes by the antenna effect of the gold nanoparticles, in order to achieve amplification of the optical signal in fluorescence-based sensors.

Detailed studies of the enhancement effect were performed by confocal fluorescence microscopy with single-molecule sensitivity and combined with single-particle spectroscopy. The experiments afforded top enhancements of two and three orders of magnitude for the emission of red-emitting dyes, induced, respectively, by one gold nanorod or, alternatively, by one dimer of gold nanospheres. Afterward, the surface functionalization of gold nanorods was optimized through the validation of a method for loading dye-labeled DNAs specifically onto the nanorods' tips. This ensured effective emission enhancement in the nanohybrids of about one order of magnitude, while indiscriminate surface coating led to undesired emission quenching, as measured in a macroscopic volume by steady-state fluorescence spectroscopy.

For the creation of the nanohybrid sensors, various model systems based on molecular beacons were explored and tested in conjugation with gold nanorods. The molecular beacons were designed to function based on a variation on the efficiency of the resonance energy transfer process by the Förster mechanism (FRET) prompted by changes in the hairpin conformation. The selected donor-acceptor pair consisted of the dye Atto-647N and the quencher molecules DDQ II and QSY 21. Preliminary assays were performed with synthetic RNA and DNA targets, whose sequences were proposed in the literature for medical diagnostics of infectious diseases,

such as dengue and sleeping sickness, and also a sequence of a microRNA proposed for diagnostics of cancer and/or cardiovascular diseases. The limited response of these molecular beacons in the targets' recognition led to the development of a novel hairpin probe that employs the gold nanorod itself as an energy acceptor. The tip-functionalization of nanorods with this new probe was successfully performed, but exploratory tests with the nanohybrids resulted until now on a target fluorescence signalling below the expectations. The conjugation of DNA hairpin probes revealed to be a challenging path, but mainly a stimulating and promising one, for it is expected to contribute to new opportunities in the application of the nanohybrid sensors in point-of-care tests for medical diagnostics purposes.

Keywords: Gold nanoparticles, Fluorescently-labeled DNA, Plasmonic nanoantennas, Tip-selective functionalization of nanoparticles, Fluorescence signalling of nucleic acids.

List of acronyms and symbols

2D	Two-dimensional
2PA	Two-photon absorption
3D	Tri-dimensional
ACF	Autocorrelation function
AFM	Atomic Force Microscopy
ATP	Adenosine triphosphate
AUT	11-amine-1-undecanethiol
BEM	Boundary element method
bp	Base pairs
CATT	Card agglutination test for trypanosomiasis
CEA	Cysteamine
CSF	Cerebrospinal fluid
CTAB	Cetyltrimethylammonium bromide
DDA	Discrete dipole approximation
DDQ II	Deep Dark Quencher II
DENV	Dengue virus
dsDNA	Double-stranded deoxyribonucleic acid
EGFP	Enhanced green fluorescence protein
ELISA	Enzyme-linked immunosorbent assay
FCS	Fluorescence Correlation Spectroscopy
FDTD	Finite-difference time-domain
FEM	Finite element method
FLIM	Fluorescence Lifetime Imaging Microscopy
FLCS	Fluorescence Lifetime Correlation Spectroscopy
FOM	Figure of merit
FRET	Förster Resonance Energy Transfer
FWHM	Full-Width at Half Maximum
F-Seq	Atto-647N labeled DNA strand
GFP	Green fluorescent protein
HD	Hairpin probe for dengue viral RNA target
HDTD	HD hybridized with dengue viral RNA target
IC	Internal conversion
IgM	Immunoglobulin M antibody
IgG	Immunoglobulin G antibody
IRF	Instrument Response Function
ISC	Intersystem crossing

LED	Light-emitting diode
LED595nm	Light-emitting diode with maximum wavelength at 595 nm
LNA	Locked nucleic acid
LOD	Limit of detection
LSP	Longitudinal Surface Plasmon
LSPR	Localized Surface Plasmon Resonance
MEF	Metal enhanced fluorescence
miRNA or miR	MicroRNA
MPTMS	(3-mercaptopropyl)-trimethoxysilane
mRNA	Messenger RNA
MT(PEG)$_4$	Methyl-PEG-thiol
NA	Numerical aperture
NanoLED594nm	Light-emitting diode with maximum wavelength at 594 nm
NIR	Near-infrared
NMR	Nuclear Magnetic Resonance spectroscopy
NPA-Bt	Photo-crosslinker with a nitrophenyl azide group
NR	Nanorod
NS	Non-selective functionalization
NS1	Dengue non-structural protein 1
OD	Optical density
PBS	Phosphate-buffered saline buffer
PBST	Phosphate-buffered saline buffer with Tween 20
PCR	Polymerase chain reaction
PEF	Plasmon-enhanced fluorescence
PEG	Polyethylene glycol
PEG0, PEG4	Biotin-linker thiols
PNA	Peptide nucleic acid
POC	Point-of-care
PSF	Point-spread function
PVA	Polyvinyl alcohol
PVP	Polyvinylpyrrolidone
qRT-PCR	quantitative Reverse Transcription - Polymerase Chain Reaction
QSY 21	QSY™ 21 quencher
Q-Seq	DDQ II or QSY 21 labeled DNA strand
RAIRS	Reflection Adsorption Infrared Spectroscopy
RDT	Rapid diagnostic test
RI	Refractive index
RIU	Refractive index unit

RT-LAMP	Reverse transcription loop-mediated isothermal amplification
RT-PCR	Reverse transcription - polymerase chain reaction
SA	Streptavidin
SAM	Self-assembled monolayer
SDS	Sodium dodecyl sulfate
SEF	Surface enhanced fluorescence
SEM	Scanning Electron Microscopy
SERS	Surface-Enhanced Raman Scattering
SPAD	Single-photon avalanche diode
SPR	Surface plasmon resonance
ssDNA	Single-stranded deoxyribonucleic acid
TBE	Tris-borate EDTA buffer
TCSPC	Time-Correlated Single Photon Counting
TD	Dengue viral RNA target sequence
TEM	Transmission Electron Microscopy
TFPA-Bt	Photo-crosslinker with a perfluorinated aryl azide group
TM	MiRNA-145 target sequence
TS	Sleeping sickness DNA target sequence
TTTR	Time-tagged time-resolved
UV	Ultraviolet
WHO	World Health Organization
XPS	X-Ray Photoelectron Spectroscopy
YFP	Yellow fluorescent protein

$\mathbf{A}_e$	Area of emission spectra of dye-particle assemblies
$\mathbf{A}_o$	Area of emission spectra after dye displacement
$\boldsymbol{C}\mathbf{r}^{\perp}$	End-effect term for rotational diffusion
$\boldsymbol{C}\mathbf{t}$	End-effect term for translational diffusion
$\boldsymbol{d}$	Nanorod's diameter
$\boldsymbol{D}_r^{\perp}$	Rotational diffusion coefficient
$\boldsymbol{D}_t$	Translational diffusion coefficient
$\Delta\mathbf{G}^{\circ}$	Change in the Gibbs free energy
$\Delta\mathbf{H}^{\circ}$	Change in enthalpy
$\Delta\boldsymbol{\lambda}$	Longitudinal surface plasmon shift
$\Delta\mathbf{S}^{\circ}$	Change in entropy
$\boldsymbol{E}$	Electric field
$\boldsymbol{E}_0$	Incident electric field

E_{FRET}	FRET efficiency
E_{loc}	Local electric field
$\mathbf{E}_{local.i}$	Internal electric field at the position of the ith dipole
E_{scat}	Scattered electric field
ε	Dielectric function of gold
ε_0	Dielectric constant of vacuum
ε_A	Molar absorptivity of an acceptor molecule
ε_B	Dielectric constant of background medium
f_F	Overall fluorescence enhancement
F/F^0	Overall fluorescence enhancement factor
γ_{em}	Fluorescence emission rate
γ_{exc}	Excitation rate
I	Excitation laser intensity
I_0	Number of photons of the excitation light
I_D	Normalized emission spectrum of a free donor molecule
$\mathbf{I}_{un}$	Area of the long decay component
$I(t)$	Number of photons detected at time *t*
$\langle \mathbf{I} \rangle$	Mean trace intensity
$\langle I_{peak} \rangle$	Average emission intensity
k	Wavenumber of emitted light
k_0	Intrinsic radiative decay rate of a dye
k^2	Orientation factor
K**a**	Apparent affinity constant
$\mathbf{k}_{IC}$	Non-radiative decay rate due to internal conversion
$\mathbf{k}_{ISC}$	Non-radiative decay rate due to intersystem crossing
$\mathbf{k}_{nr}$	Non-radiative decay rate
K_{nr}	Non-radiative decay rate due to a metal nanoparticle
$\mathbf{k}_r$	Radiative emissive decay rate
K_r	Plasmon-enhanced radiative decay rate
L	Nanorod's length
λ	Wavelength
$\lambda_{exc.}$	Excitation wavelength
λ_{LSP} **or** λ_{max}	LSPR peak wavelength
λ_p	Wavelength of the plasma oscillation frequency of a bulk metal
n	Refractive index
N_A	Avogadro constant
<N>	Average number of dye molecules in the detection volume
p	Ratio between the nanorod's length and diameter

$\boldsymbol{p}$	Transition dipole moment
$\boldsymbol{p_0}$	Point-like dipole
$\boldsymbol{P_{ex}}$	Excitation power
ϕ_{ET}	Quenching efficiency
$\boldsymbol{\Phi_F}$	Fluorescence quantum yield
$\boldsymbol{\Phi_m}$	Fluorescence quantum yield of a dye near a metal nanoparticle
$\boldsymbol{\Phi_T}$	Energy transfer efficiency
$\boldsymbol{r}$	Donor-acceptor separation distance
$\mathbf{r_0}$	Position of a dye
$\boldsymbol{R_0}$	Förster critical radius
$\mathbf{S_0}$, $\mathbf{S_1}$, $\mathbf{S_2}$	Singlet electronic states
$\boldsymbol{\sigma}$	Absorption cross section of a dye
$\boldsymbol{t}$	time
$\mathbf{T_1}$, $\mathbf{T_2}$	Triplet electronic states
$\mathbf{T_m}$	Melting temperature
τ	Fluorescence lifetime
τ_1	Fast relaxation time
τ_2	Slow relaxation time
τ_m	Fluorescence lifetime of a dye near a metal nanoparticle
τ_w	Long relaxation time
$\tau_\perp$	Short relaxation time
V_c	Volume of the cubic elements
$\varnothing$	Diameter

Table of contents

Figure index

Table index

CHAPTER 1

INTRODUCTION

1. Introduction

Healthcare and quality of life are fundamental pillars of contemporary societies, to which science, technology and modern medicine contributed tremendously in the last two centuries, by granting advances in the understanding and knowledge about human health and disease. Due to this progress, a variety of diagnostic and therapeutic procedures are performed today in hospitals, clinics and several other healthcare facilities worldwide, even if with different levels of availability to patients. One pivotal approach for medical diagnostics/therapeutics is the development of biosensors for detection of biological molecules, known in this context as biomarkers (short for biological markers). These can provide critical information about normal physiological states, pathological conditions or disease stages and severity.

Biosensors are essential for a broad spectrum of human activity besides medicine and clinical diagnostics, namely environmental monitoring, drug discovery, biomedicine, food safety and inspection, forensic sciences, and biotechnology. One promising route for the creation of biosensors relies on nanoscience and nanotechnology. Ever since Richard Feynman's suggestion in the early 1960s that "there's plenty of room at the bottom", an exponential growth of research occurred in these fields. The 21st century brought into light unique material properties that can only be attained at the nanometric scale. Indeed, nanomaterials have contributed to major breakthroughs in several important areas of our modern society, paving the way for new medical, pharmaceutical, biotechnological, environmental, electronic and energetic applications. In medical research, nanomedicine is now considered one of the emerging and fastest advancing areas.[1]

In recent years, nanomedicine has enabled significant progresses in disease diagnostics and therapeutics, offering novel imaging and sensing technologies, as well as treatment solutions. The contribution of nanotechnology for the development of biosensing devices represents one of the foremost ambitions in life sciences and clinical diagnostics. It has the final purpose of bringing vital health benefits and outstanding opportunities for the world population. Combined with new therapeutics, this is of outmost importance in the globalized world of the 21st century, in which diseases are more prone to arise, such as cancer, cardiovascular diseases, neurological disorders, diabetes, but also pathogenic infectious diseases, caused by bacteria, parasites, fungi, or viruses. A contemporary example is that of the current coronavirus disease COVID-19 pandemic initiated by the appearance of the virus SARS-CoV-2. Altogether, these diseases cause huge impacts in the individual human life, significant morbidity and mortality, and changes in human behavior and in how society functions, thus, impacting the burden in the global health and economy.

Improvements foreseen from the implementation of biosensors will support medical professionals with rapid, accurate and reproducible tests. This capacity will provide early disease diagnosis and allow proper monitoring and prognosis of patients, if possible at a personalized medical level. The combination of nanotechnology with microfabrication, and improvements in the knowledge about biomarkers, is actively providing new biosensing platforms, though mainly in academic research, with only few examples of companies entering the market.

Optical detection is now considered one of the main strategies in biosensor design. In fact, optical biosensors are one of the most represented type of biosensor in all areas, and in the medical field this is not an exception. It is believed by the scientific community, that this strategy can surpass in the upcoming years some of the challenges that conventional diagnosis techniques currently face. They can also contribute to turn medical care accessible to the public by providing clinical analysis outside research laboratories in the scope of point-of-care (POC) testing.[2] The demand for diagnostic tests towards much-needed POC tools is important to bring healthcare closer to the patient, not only for countries with technological and financial conditions, but mostly for countries with fragile public health facilities, and for remote or unstable/insecure regions. Due to some of its potential advantages, such as high sensitivity, wide dynamic range, multiplexing capabilities, and possibility for miniaturization, certainly optical biosensing may allow soon the realization of those devices.

The performance of optical biosensors is pivotal for the detection of biomarkers at preliminary stages of diseases when their concentrations in cells or tissues and in the blood, urine, serum, plasma or other body fluids is ultra-low.[3,4] Specific biomarkers for the early diagnosis of several diseases that are of particular interest in the scope of this doctoral thesis are nucleic acids. These are fascinating biopolymers and the simple fact that each organism possesses its own DNA is enough to stimulate a scientist's curiosity. Besides that, qualitative and quantitative analysis of DNA and RNA is of great importance in other fields, such as gene expression studies and drug discovery. Today, the most common methods for studying DNA and RNA respectively, are Polymerase Chain Reaction (PCR) and Reverse Transcription - Polymerase Chain Reaction (RT-PCR). These techniques involve synthetic DNA oligonucleotides for detection and quantification of low quantities of nucleic acids, after a large number of amplification cycles, with high sensitivity.[5]

While this manuscript was being prepared, RT-PCR was being used worldwide for testing the population in response to the unprecedented pandemic outbreak of the COVID-19 disease. The spread of COVID-19 revealed that most countries were unprepared to sustain the transmission of the virus and placed governments and healthcare systems under pressure to provide the best adequate solutions for prevention of contagion and deaths. RT-PCR tests have been allowing controlled isolation and tracing of people, and although it may be the 'gold-standard' for the detection of SARS-CoV-2 viral RNA, and for nucleic acid detection in general, there is still a risk for false-negative and false-positive results.[6,7] Moreover, RT-PCR is usually time-consuming (several hours), complex, requires expensive equipment, highly trained personnel and quantification may be affected by variations in amplification efficiency and background amplification. Other techniques are available, also involving nucleic acid amplification tests or different approaches, but each presents their own limitations. Therefore, now it is even more vital that the scientific community makes a clear contribution for the conception of alternative methods that can push forward nucleic acid detection/quantification

for disease diagnostics. Ideally by providing increased sensitivity and reliability, and delivering a much simpler and faster (in a question of minutes) test.

The integration of metal nanoparticles, with their unique and remarkable optical properties, into optical biosensors is a promising approach in view of the above-mentioned requirements. Metal nanoparticles can provide a variety of transduction signals for highly sensitive biomolecular detection in optical sensing, such as refractive index, light absorption, or luminescence, just to mention a few.[8,9] In principle, these particles could make a relevant contribution when integrated with microfabrication techniques, to meet the ASSURED criteria for biosensors (Affordable, Sensitive, Specific, User-friendly, Rapid and robust, Equipment-free and Deliverable to end-users).[10,11]

In the last years, the use of metal nanoparticles as optical nanoantennas to modify the emission properties of fluorescent molecules or other emitters has been intense.[12–14] These have already provided some progresses towards the collective effort of developing and improving optical biosensors, in particular, by providing means to amplify response signals from fluorescence-based biosensors.[15–17] Nanoparticle-based signal amplification, induced by their plasmonic antenna effect, holds indeed great potential in achieving high sensitivity and selectivity for detection of biomarkers, including nucleic acids. Therefore, in the scope of this doctoral thesis, a contribution toward this strategy was pursued by investigating plasmonic gold nanoparticles functionalized with fluorescently-labeled DNA probes, as promising platforms for fluorescence-based biosensors.

A particular type of nucleic acid probe, generally known as molecular beacon, was designed and conjugated onto plasmonic gold nanorods to develop a nanohybrid biosensor for enhanced optical detection of selected nucleic acid biomarkers. For proof-of-concept and illustration of the approach versatility, three synthetic sequences were used as target biomarkers: i) RNA from dengue virus; ii) DNA from sleeping sickness parasites, and; iii) microRNA-145, a circulatory microRNA (miRNA or miR) associated with cancer and cardiovascular diseases. A more comprehensive framework that guided the choice of these target biomarkers for the above-mentioned diseases is given in Chapter 2.

In this introductory chapter, the theoretical principles of fluorescence relevant for fluorescence-based sensors are initially overviewed. Next, the effects of metal nanoparticles on fluorescence are presented. The chapter ends by summarizing the use of biosensors for biomarkers' detection: a synopsis is given on fluorescent DNA probes, with particular focus on molecular beacons, and on biosensing applications of the probes while functionalized onto metal nanoparticles, highlighting reported works on beacons conjugated onto gold nanorods.

1.1. Principles of fluorescence

The phenomenon of fluorescence has fascinated individuals over centuries. It is incredible to look to all the applications possible nowadays using fluorescent molecules, so-called fluorophores

or dyes. Their use is widespread and has exploded in the past two decades, mostly being employed in academia and industry, in areas such as medicine (including diagnostics), life and biological sciences, biotechnology, environment, forensic sciences, agriculture, electronics or security, to mention a few. Since the first report on the observation of fluorescence made in 1565 by N. Monardes, and the introduction of the term fluorescence by G. G. Stokes later in 1853,[18] a lot of efforts have been made to elucidate the phenomenon. Fluorescence has advanced from an analytical tool to a more intricate detection technique. Work on fluorescence has been recognized with two Nobel Prizes in Chemistry, which were awarded for the discovery and development of the green fluorescent protein (GFP), in 2008, and, more recently, for the development of super-resolution microscopy in 2014.

Fluorescence is currently a dominant methodology in flow cytometry, DNA sequencing, genetic analysis, cell biology, staining of gels followed by electrophoresis, microscopy imaging (e.g. *in vivo* tri-dimensional (3D) imaging of cells, small animals or internal structures of humans) or fluorescence immunoassays.[19–21] Fluorescence makes it possible to study individual proteins, visualize cell proteins without invasive techniques, map the genome of an organism, or image early cancer detection. Thus, it is a powerful tool for biotechnological, biomedical and medical research by increasing the understanding of healthy conditions and diseases. It is not misplaced to state that fluorescence will continue to contribute with rapid innovations, advances and synergies in biology, biotechnology, medicine and nanotechnology.

1.1.1. Molecular fluorescence

Fluorescence is a particular form of luminescence. The later can be defined as spontaneous emission of radiation from an electronically or vibrationally excited species not in thermal equilibrium with its environment.[22] When the excitation is induced by photon absorption, luminescence is called photoluminescence. Briefly, the excited species results from an atom or a molecule that is excited by absorption of the photon energy, which promotes an electron from a lower energy level of the ground state configuration of the atom/molecule to reach an unoccupied level of higher energy. Then, the excited species, which is unstable due to the higher energy of the excited state relatively to the ground state, releases its excess energy when the quantum system relaxes to its ground state. This energy can be released radiatively in the form of emitted photons and can occur in the ultraviolet (UV), visible or near-infrared (NIR) regions of the electromagnetic radiation spectrum. Photoluminescence can be further classified into two main types - fluorescence and phosphorescence - according to the excited state's nature.

Fluorescence is a spontaneous photon emission process from an excited molecular entity with retention of spin multiplicity, in contrast to phosphorescence.[22,23] An energy diagram known as the Perrin-Jablonski diagram is typically used to describe the de-excitation pathways subsequent to light absorption by a molecule (Figure 1.1). This diagram illustrates the electronic states of a molecule and the radiative and non-radiative transitions between them. The electronic states are vertically denoted by energy level and horizontally by spin multiplicity. They are represented

together with arrows indicating the possible transitions between them, exemplifying in a simple way the possible processes: photon absorption, fluorescence, phosphorescence, internal conversion (IC), intersystem crossing (ISC), delayed fluorescence (not represented in the diagram), and triplet-triplet transitions (also not represented). The singlet electronic states are denoted by S_0 (ground state), S_1, S_2, etc. and the triplet states by T_1, T_2, etc. At each of these electronic states are represented the number of vibrational energy levels, normally classified as 0, 1, 2, etc.

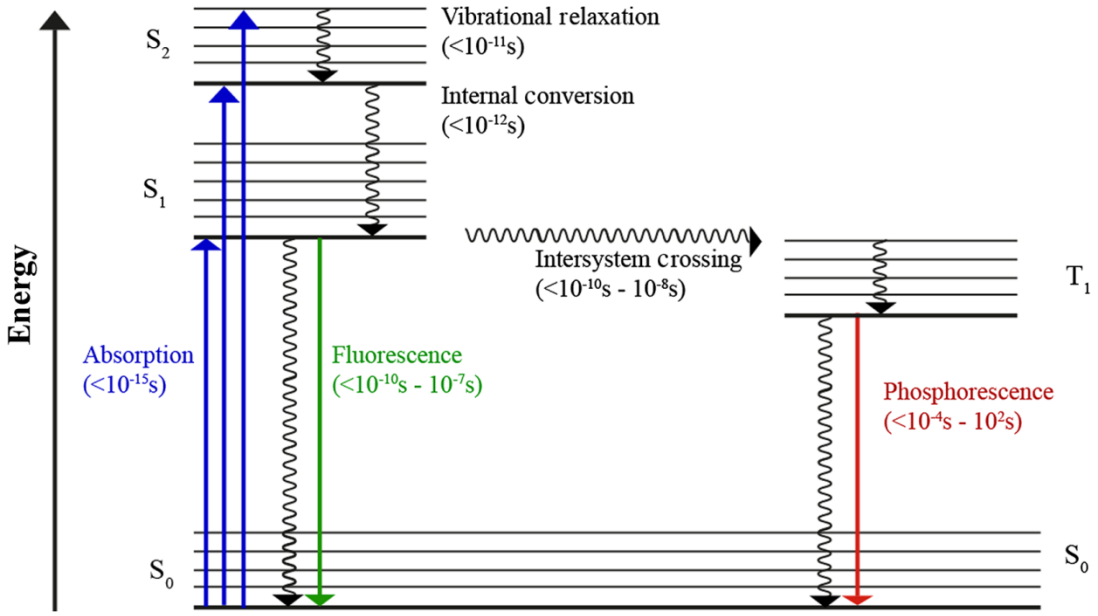

Figure 1.1 - Perrin-Jablonski diagram representing the relative positions of the electronic energy levels of a molecule. The transitions between states are depicted as vertical lines to illustrate the instantaneous nature of light absorption. Radiative and non-radiative (internal conversion and intersystem crossing) processes are represented. S_0 is the ground state, S_1 and S_2 are two different excited states with singlet electronic configuration, and T_1 is a triplet electronic state. Adapted from Ref. 24.

As depicted in Figure 1.1, photon absorption occurs from the lowest vibrational energy level, S_0, and it can bring a molecule to one of the vibrational levels of S_1, S_2. The subsequent possible de-excitation processes include: i) IC, which is a non-radiative transition between two electronic states of the same spin multiplicity; ii) ISC, another non-radiative transition, this one between two isoenergetic vibrational levels belonging to electronic states of different multiplicities ($S_1 \rightarrow T_1$); iii) phosphorescence, which is a radiative process emitted from another excited state and occurs after ISC from a singlet, S_1, to a triplet state, T_1, in which the electron in the higher energy orbital has the same spin orientation as the electron in the lower energy orbital; iv) delayed fluorescence that results from reverse ISC from $T_1 \rightarrow S_1$; v) triplet-triplet transitions; and vi) fluorescence.[22,23]

A fluorophore is usually excited to some higher vibrational level of either S_1 or S_2, due to variations in the equilibrium molecular configuration between different electronic states. However, intramolecular vibrational relaxation and IC promptly occur, and fluorescence emission generally results from a thermally equilibrated vibrational state of the electronically excited state,

in this case the lowest energy vibrational state of S_1. Fluorescence can then occur, typically in the nanosecond timescale, by a singlet-singlet radiative process corresponding to the emission of photons accompanying the $S_1 \rightarrow S_0$ relaxation. Due to energy losses by vibrational relaxation, emission from an excited molecule is generally shifted to longer wavelengths relatively to its absorption light wavelength. The difference between the maximum peak wavelength in the absorption and emission spectra of a fluorophore is called Stokes shift.[22,23] In addition to vibrational relaxation, fluorophores can display further "apparent" Stokes shifts due to excited-state reactions, complex formation, and/or energy transfer. Typically, larger Stokes shifts make the detection of a fluorophore easier, due to less overlap between excitation and detection (emission) wavelengths.[25] However in most cases, the absorption spectrum partly overlaps the fluorescence emission spectrum, i.e. a fraction of light is emitted at shorter wavelengths than the absorbed light. In general, the differences between the vibrational states are similar in the ground and excited states, so the emission spectrum often resembles the first absorption band ($S_0 \rightarrow S_1$ transition), in what is known as mirror image rule. The characteristics mentioned make fluorescence a very powerful technique because by filtering the excitation light one can recover only the emitted light of a fluorophore with minimal background signals.[22,23]

Fluorescence can be measured in a spectrofluorometer, an equipment commercially developed in the 1950s. The spectral data obtained is generally presented as excitation and emission spectra, that vary widely and are dependent upon the chemical structure of the fluorophore and the solvent in which it is dissolved. When describing fluorescence emission, molar absorptivity, fluorescence quantum yield (Φ_F) and fluorescence lifetime (τ) are perhaps the most important characteristics of a fluorophore or a given system.[22,23] Molar absorptivity measures how strongly a given molecule can absorb light at a given wavelength, being operationally related with the number of molecules in the excited state after excitation. The fluorescence quantum yield is defined as the number of emitted photons relative to the number of absorbed photons. The fluorescence lifetime refers to the average time the molecule spends in the excited state prior to its return to the ground state, i.e. before emitting a photon; it determines the time available for the fluorophore to interact with its environment or diffuse through it, defining the time window for observation of dynamic phenomena.

In the quantum yield determination, one must focus on the processes responsible for the dye returning to the ground state. In particular, the radiative decay rate (k_r) and the non-radiative decay rate (k_{nr}), which can encompass several processes (e.g. see Figure 1.1). The fraction of dyes that decay through emission, and hence the quantum yield, is given by the ratio:[22,23]

$$\Phi_F = \frac{k_r}{k_r + k_{nr}} \quad (1)$$

Concerning the lifetime of an excited state, it can be expressed by the equation:

$$\tau = \frac{1}{k_r + k_{nr}} \quad (2)$$

As exemplified in Figure 1.1, the lifetime of the singlet state ranges from tens of picoseconds to hundreds of nanoseconds, typically being around 1-10 ns, whereas the triplet state lifetime is much longer (microseconds to seconds). The lifetime can be related to the quantum yield by:

$$\Phi_F = k_r \times \tau \quad (3)$$

As for photon emission from a sample of dyes excited by an ultrashort light pulse, it can be described as a first order kinetic process (Equation 4) with an excited state lifetime, τ, where $I(t)$ is the number of photons detected at time t and I_0 is the number of photons when the excitation energy pulse is delivered.[23]

$$I(t) = I_0 e^{-\frac{t}{\tau}} \quad (4)$$

The overall fluorescence emission rate may be obtained from the product of both the excitation rate, γ_{exc}, and the quantum yield.

$$\gamma_{em} = \gamma_{exc} \Phi_F \quad (5)$$

Fluorescence intensity of a dye can be decreased by a wide variety of processes. For convenience, all possible non-radiative decay processes are grouped with the single non-radiative decay rate constant, but typically, it includes the IC and the ISC processes (k_{IC} + k_{ISC}). Any mechanism that leads to the depopulation of the excited state through non-radiative processes will reduce the quantum yield. In the case that the quantum yield is close to unity, the radiationless decay rate is much smaller than the rate of radiative decay, that is $k_{nr} << k_r$.

Some physical and chemical parameters of the molecule's environment that may affect the intrinsic fluorescence characteristics (quantum yield, lifetime and also emission spectra) are: temperature, solvent polarity and viscosity, rate of solvent relaxation, pressure, pH, hydrogen bonds, ions, and electric potential.[22] Other factors may include conformational changes of the dyes, internal charge transfer, excited state reactions, dye-dye interactions and quenchers (atoms or molecules that suppress fluorescence).[22]

1.1.2. Resonant energy transfer

Suppression of the fluorescence intensity of a fluorophore due to intra- or intermolecular interactions is called quenching. Different photophysical or photochemical processes are involved in multiple mechanisms of quenching, such as excimer or exciplex formation, electron

or proton transfer, and energy transfer.[22] However, in the scope of this thesis, only resonant energy transfer will be discussed, in particular concerning the operation of molecular beacons.

Electronic energy transfer between molecules occurs *via* radiative or non-radiative processes. It can be described by assuming that a decaying excited molecule (donor) behaves as an oscillating dipole that can transfer its excitation energy to another oscillating dipole of a nearby molecule (acceptor), during the lifetime of the donor excited state. Radiative transfer occurs at a donor-acceptor distance larger than the wavelength of the emitted photon and it implies that the donor effectively emits a photon that is later absorbed by the acceptor. On the other hand, non-radiative transfer happens at distances shorter than the wavelength, through either a Förster or Dexter mechanism, that operationally may be further classified as static or dynamic quenching.[22,23] Normally, both forms of non-radiative quenching may exist in molecular beacon probes,[26–30] but more details about the actuation of the two mechanisms in these probes are given in section 1.4.1. Here and following, an overview about both mechanisms will be presented.

Static (or contact) quenching is referred to two cases: 1) Perrin quenching, that is a phenomenological description of the existence of a quenching sphere-of-action model, where effective quenching occurs inside but not outside the sphere, and it requires close proximity, but not physical association, between molecules; 2) the formation of a ground-state complex between molecules (donor/acceptor).[22,23,27] Basically, in the second case, the electronic structure of the complex and its photophysical properties may differ significantly from its constituents, such that it may become non-fluorescent. The ground-state complex has its own electronic properties that may depend strongly on the interaction between the donor and acceptor transition dipole moments, resulting in a significantly different absorption spectrum from its molecular components. This quenching is also very well known for aggregates of identical dyes that often occur through hydrophobic effects when the dye molecules stack together to minimize contact with water.[31,32] It is more common in planar aromatic dyes that are coupled through electrostatic and hydrophobic forces that can enhance quenching. High temperatures and addition of surfactants tend to disrupt ground-state complex formation.

Dynamic quenching corresponds to two energy transfer mechanisms: collisional quenching and Förster Resonance Energy Transfer (FRET).[22,23] The former occurs when a donor in the excited state is deactivated upon contact with an acceptor in the same solution. When the molecular collision occurs, the donor returns to the ground state without emission of fluorescence. One type of collisional quenching is Dexter mechanism, which is a short-range phenomenon that can arise only when donor and acceptor are close enough to allow intermolecular orbital overlap required for electron exchange. In opposition, FRET occurs through space due to diffusive encounters between donor and acceptor molecules, hence it does not require collisions or any other form of contact between molecules. In the specific case of the designed molecular beacons investigated in this thesis, the expected dominant fluorescence

quenching is FRET, as discussed later in section 1.4.1, so next are given some general considerations about this mechanism.

FRET quenching assumes that a donor exchanges energy with another molecule having resonant energy transitions, hence the use of the term resonance. It occurs through long-range dipole-dipole interactions between the transition dipoles of the molecules, in which a donor in an excited electronic state transfers its excitation energy directly to a nearby acceptor. Consequently, the energy level of the dye returns to the ground state without emission of a photon. Both donor and acceptor, that can be named as a donor-acceptor or a FRET pair, retain their intrinsic properties.[23,26] In fact, in Förster quenching the absorption spectra of the molecules does not change, in contrast to static quenching, but the fluorescence intensity and lifetime of the dye decrease by the same factor, while static quenching does not change the dye's lifetime.[29]

Although, generally, the donor and the acceptor are two fluorescent dyes, FRET does not require that the acceptor is a fluorescent molecule. Today a number of non-fluorescent acceptors (dark quenchers)[33–35] are popular and used as viable alternatives to typical FRET acceptors for biophysical fluorescence studies.

Förster quenching depends on the ability of the donor to transfer energy to the acceptor through various factors, such as: 1) the separation between the donor and acceptor molecules, within a range that allows for non-negligible dipole-dipole interactions; 2) the spectral overlap between the donor emission and acceptor absorption; 3) the quantum yield of the donor; 4) the oscillator strength for acceptor's absorption; and 5) the relative orientation of donor and acceptor transition dipoles.[22,23,26,27,29]

The magnitude of FRET efficiency is dependent primarily on the donor-acceptor separation distance (r) in relation to the Förster critical radius R_0 (Equation 6). At R_0, energy transfer and spontaneous decay are equally probable, thus FRET is 50% efficient, meaning that half of the donor excited-states decay by transferring energy to the acceptor.[22,23]

$$E_{FRET} = \frac{1}{1 + \left(\frac{r}{R_0}\right)^6} \tag{6}$$

The formula shows that the efficiency of energy transfer is inversely proportional to the sixth power of the donor-acceptor distance. Therefore, it rapidly declines to zero at distances larger than the Förster radius. This distance dependence of FRET is useful to measure distances between donors and acceptors by calculating the Förster radius that can be determined from spectroscopic data and assuming Equation 7. In this equation, the orientation factor k^2 is 2/3 (for an isotropic molecular orientation), Φ_D^0 is the quantum yield of the free donor, N_A the Avogadro constant, n is the refractive index, I_D is the normalized emission spectrum of the free donor and ε_A is the molar absorptivity of the acceptor, both in the region of spectral overlap, and λ is the wavelength.[22,23]

$$R_0^6 = \frac{9000(ln\ 10)k^2\Phi_D^0}{128\pi^5 N_A n^4}\int_0^\infty I_D(\lambda)\varepsilon_A(\lambda)\lambda^4 d\lambda \quad (7)$$

Usually, values of Förster radius are in the 1-10 nm range, which are comparable to biological macromolecules (3-6 nm), like nucleic acids and proteins. Clearly, FRET efficiency can be previously predicted from the spectral properties of the donor-acceptor pair, allowing for the design of experiments based on known structural features and sizes of the samples of interest, as it was the case in this thesis. FRET is one of the few tools that allows measuring inter- and intramolecular nanometer distances and their changes in real-time, *in vitro* and *in vivo*, both at the ensemble and the single-molecule level. Hence, it is used as a spectroscopic/molecular ruler in many biological applications, e.g. to estimate distances in supramolecular associations, biomolecules, membranes and even cells, but also as a probe for studying biomolecular structures, dynamics, and conformations, and in more broad applications such as optical imaging and medical diagnostics.[36–39]

1.1.3. Single-molecule fluorescence

Throughout the years technological advances have offered new uses of fluorescence. Novel technologies are rapidly adopted, as illustrated by fluorescence microscopy, a mainstream tool in biological and biomedical sciences. This outstanding evolution was mainly due to the development of confocal microscopes, which provide a significant imaging improvement over conventional microscopes. In the basis of these improvements are two working mechanisms that provide high resolution: point illumination and a confocal pinhole (a micrometric aperture).[22,40,41] The first allows light illumination to be focused onto the focal plane by scanning a sample point-to-point. The single diffraction-limited point decreases the amount of scattering, and allows deep penetration onto samples to create sharp and detailed images of a section (two-dimensional, 2D) or an entire object (3D). The pinhole filters light from above and below the focal point (out-of-focus light), allowing a virtual absence of out-of-focus blur. The association of fluorescence and confocal microscopes, made fluorescence confocal microscopy as the most common high-resolution fluorescence imaging technique, extensively applied in biology for example, for membrane and cell studies, including in individual living cells.[19,42]

The inclusion of time-resolved measurements in fluorescence confocal microscopy fostered the development of fluorescence lifetime imaging techniques, or FLIM.[20,43] This technique explores the excited state lifetime of fluorophores as a contrast mechanism for imaging, with each region of a sample displaying the corresponding lifetime, providing sub-micrometric spatial resolution. FLIM also provides measurements that are independent of the sample's concentration, because although the intensity of a fluorophore depends on its concentration, lifetime does not, but instead it can be influenced by the molecular environment (changes in pH, temperature or FRET pairs), reflecting the utility of the technique. For instance, it is a robust approach to quantify FRET and study biological interactions and dynamics.[44,45]

Fluorescence lifetimes are typically on the order of nanoseconds, and most instruments follow one of two approaches: time domain or frequency domain methods. In the time domain that is of interest here, the time-course of fluorescence intensity decay after pulsed excitation is directly measured. The most widely used approach to this measurement is TCSPC.[20,22,23,43] This technique is a detection mode in which very sensitive detectors and low detection rates are used to operate in single-photon detection. The basic principle relies on the fact that the probability of detecting a single emitted photon at time *t*, after an exciting pulse, is proportional to the fluorescence intensity at that time, over many excitation cycles. It requires a high repetition rate excitation source, such as a pulsed laser light, in order to accumulate enough photon statistics that usually are represented as a photon-arrival histogram. This can be used to reconstruct a fluorescence intensity decay curve, that when fitted allows to calculate the characteristic lifetime of the dye. In such experiments, the excitation power is set so that the probability of detecting more than one photon per cycle is low. Timing resolution of a TCSPC is measured by an overall performance factor called Instrument Response Function (IRF), which comprises all the instrumental sources of delayed response that affects time resolution and that ideally should be infinitely short, resulting in a better time resolution. Remarkably, pulsed laser excitation and single-photon counting makes it possible to measure fluorescence decays with sub-nanosecond time resolution.

It is now possible to visualize the nanoworld *via* fluorescence and "invisible" molecules can be revealed to the eye due to the exceptional high sensitivity provided by fluorescence, that can reach the lowest measurable quantity - single-molecule detection. Indeed, thanks to outstanding progress in instrumentation, it is now feasible to detect a single fluorescent molecule. After the pioneering work of Michel Orrit,[46] that 30 years ago demonstrated for the first time the detection of the fluorescence signal from one molecule, the field of single-molecule optics and related fields have seen an exponential rise. Actually, single-molecule fluorescence detection now offers new opportunities in analytical, material, and biological sciences. As a comparison, in bulk measurements, the properties of individual molecules are hidden in ensemble averages, whereas observation at the single-molecule level provides new insights into physical, chemical, and biological phenomena.

Several methods are available in the field of single-molecule fluorescence detection.[36,47] FLIM and single-molecule spectroscopy techniques, such as Fluorescence Correlation Spectroscopy (FCS) rely on single-molecule detection sensitivity to give unprecedented detailed information of the studied systems. For example, to observe interactions between very low concentrations of biological species in real-time, or for characterization and better comprehension of nanomaterials.[43,48,49]

FLIM is a particularly powerful technique to study nanoparticles deposited onto a surface, such as a coverslip. Since these nanomaterials are smaller than the wavelength of the excitation light (sub-resolution), an image resembling the nanomaterial shape is not obtained. Instead, a construction of the image is made using a point-spread function (PSF) - a 3D diffraction pattern

of light emitted from an infinitely small point source in the sample - that result in an ellipsoidal image pattern. The PSF is usually described by a 3D Gaussian approximation and its Full-Width at Half Maximum (FWHM), usually in a range between 250-450 nm in the perpendicular plane to light propagation. By merging spatial and time resolution with high detection sensitivity, FLIM is able to measure fluorescence lifetimes of individual emitters. However, its ability for single-particle studies in solution is limited, because the probed species may enter or leave the observation volume due to Brownian diffusion. In those studies, FCS technique offers an interesting alternative, since it allows evaluation of stochastic fluorescence emission based on a different operation of the same confocal fluorescence microscope setup, as detailed next.[50,51]

FCS is a versatile technique, useful for observation of freely diffusing molecules (the typical lower limit concentration is ca. 1 pM) in a small volume defined by a focused laser beam and a confocal aperture. It allows continuous observation for longer periods of time while measuring the molecules' time-dependent intensity fluctuations, as a result of some dynamic process that lead to constant entry and exit of dyes in the excitation volume. Basically, in a first moment the confocal volume is empty and no fluorescence is being measured. When a dye diffuses into the focused light beam, there is a burst of emitted photons due to multiple excitation-emission cycles of the dye, and fluorescence is measured until the dye diffuses out of the effective volume. The outcome is a graph showing fluorescent fluctuations over time; thus, FCS is based on the statistical analysis of the temporal fluctuations of fluorescence intensity by computing the second order correlation of the intensity time trace. Since FCS measurements are dependent on the intensity during the diffusion of dyes along the confocal volume, these can be affected by phenomena such as photoblinking (intermittent switching between bright and dark states) and photobleaching (irreversible oxidation or reduction of a dye that causes quenching).[52] FSC can give information about any molecular process that induces a change in fluorescence brightness. This includes for instances, physical and chemical processes such as translational or rotational diffusion, association-dissociation rate constants, molecular aggregation or concentration, conformational dynamics, or hydrodynamic radii.[53] Also, one can determine the diffusion coefficient of a dye or monitor DNA hybridization when there is associated a large change in diffusion coefficient.[54]

The use of single-molecule fluorescence techniques to study fluorescence-based (bio)sensing follows naturally from the above-mentioned advances. Even though single-molecule sensitivity is still far from real-life applications in biosensor devices, such feature has the potential to grant high sensitivity, great versatility, short response times, selectivity, spatial and temporal resolution, and non-invasive, multi-analyte measurements.[55]

1.2. Plasmon-enhanced fluorescence

The use of organic fluorescent molecules is currently the most common option for fluorescence-based biosensors.[55] For this purpose, a dye must fulfill some requirements:

1) display high brightness by combining high absorptivity and quantum yield; 2) have good photostability (almost all dyes are photobleached upon continuous illumination) particularly for microscope optics in which excitation light is highly focused; 3) have defined spectral or chemical properties; and 4) avoid perturbing the biomolecule or process in study, as much as possible. However, most of the dyes commonly used end up by failing in one or several of these criteria. When the issue is low brightness or low photostability, then difficulties in detection at very low concentrations or at single-molecule detection level become evident. One possible strategy to overcome this limitation consists in using metal nanoparticles as optical antennas to tailor the photophysical rates of organic dyes.

A metal nanoparticle can act as an optical antenna through its localized surface plasmon modes, as illustrated in Figure 1.2.[8] Briefly, the oscillations of the free electrons of a metal nanoparticle can be excited resonantly when illuminated with light of an appropriate wavelength. The electric field of light causes the displacement of the electrons relatively to the metal lattice atoms, that become positively charged and, thus, create a restoring force that sustain the collective and coherent oscillations of the charge density, which are confined by the particle's surface. When in resonance, the frequency of the incident photons matches the plasmon mode frequency and gives rise to a well-defined extinction band (in transmission mode) and to an intense light scattering (in reflection mode).

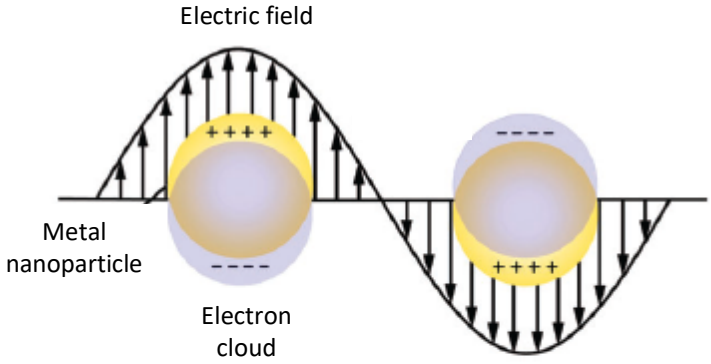

Figure 1.2 - Schematic of a localized surface plasmon showing the displacement and resulting oscillation of the surface conduction electrons of a metal nanoparticle in response to an incident light/external electric field. Adapted from Ref. 56.

Localized surface plasmon resonance (LSPR) is at the core of the modifications that plasmonic antennas induce on dye's emission properties by accelerating its excitation and decay rates (both radiative and non-radiative).[57–60] In fact, the intrinsic photophysical rates of a dye can become accelerated by orders of magnitude. To describe the plasmonic interactions on molecular fluorescence, different designations have been attributed, like surface enhanced fluorescence (SEF),[61,62] metal-enhanced fluorescence (MEF)[16,17,63] or plasmon-enhanced fluorescence (PEF).[15,64–66] Applications that use this approach are still in an embrionary phase with most appearing in the last years in academic research due to the productive synergy between plasmonics and fluorescence spectroscopy to achieve better control over spontaneous emission.

The strong enhancement of fluorescence is one of the most promising features of plasmonic control over spontaneous emission. Firstly, the strongly localized field of a plasmonic particle acts like an antenna where nearby dyes are exposed to an apparent greater light intensity, thus, leading to an accelerated excitation rate. Then, for the desired effect, the nanoparticle should accelerate the radiative over the non-radiative decay rate and as a result, there can be an increase in the quantum yield and a decrease in the lifetime. As it decays from the excited state, the dye can be described as an oscillating dipole, mostly like a radiating antenna, and it can induce oscillations of the free electrons of a nearby particle through its surface plasmon modes.[13,67] Indeed, the decay rate of emitters depends on the local density of excited states. When a dye is placed close to a particle, its plasmon modes provide a higher local density of states, which in turn accelerates the decay rate of the emitter and shortens its excited state lifetime. This process is known as Purcell effect,[12] and is more significant in emissive molecules that have a low quantum yield, commonly known as weak emitters.

These previous effects are better understood by considering a simplified scheme (Figure 1.3), of a Perrin-Jablonski diagram for a two-state system. Here, and besides fluorescence (k_r), other non-radiative decay channels are lumped together in a single decay rate constant (k_{nr}), and the effects of a nearby metal particle are highlighted by the green boxes.[68]

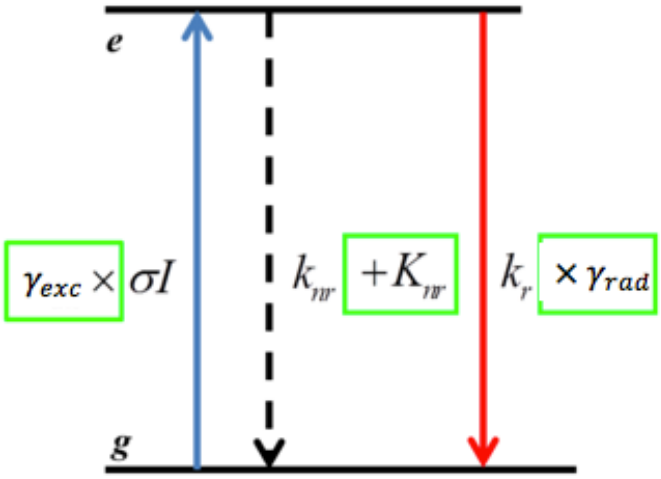

Figure 1.3 - Simplified two-level scheme that describes the excitation and decay rates of a dye in the absence and in the vicinity of a metal nanoparticle (green boxes). Here σ represents the absorption cross section of the dye and *I* the excitation laser intensity. Adapted from Ref. 68.

In the dye-particle conjugate, different interactions can occur depending on separate effects on the dye's excitation and emission.[69] For instance, if the presence of the particle results in an increased rate of excitation, γ_{exc}, this will result in increased brightness without changing the dye's quantum yield or lifetime. This is due to the excitation rate (Equation 8) that normally depends on the absorption cross section of the dye (σ) and the excitation laser intensity (I), which on their turn scales with the transition dipole moment (p) and the electric field (E) squared (below the optical saturation limit).[12] The plasmon-enhanced excitation rate represents a useful

outcome that can decrease the incident light intensities and the background, and also result in selective excitation of dyes near the particle.

$$\gamma_{exc} \propto \sigma I \propto |p \cdot E|^2 \tag{8}$$

Another possible consequence is an increase in the radiative decay rate of the dye due to the particle. In this situation, the quantum yield (Φ_m) and lifetime (τ_m) of the dye are given respectively by:

$$\Phi_m = \frac{\gamma_{rad} \times k_r}{\gamma_{rad} \times k_r + K_{nr} + k_{nr}} \tag{9}$$

and

$$\tau_m = \frac{1}{\gamma_{rad} \times k_r + K_{nr} + k_{nr}} \tag{10}$$

The non-radiative rate of the dye in the presence of the metal comprises both the non-radiative rate of the dye, k_{nr}, and the additional non-radiative rate induced by the particle, K_{nr} (mostly energy transfer to the particle's resonant plasmon modes). From the equations above it can be seen that lifetime decreases in the metal's presence, because typically $\gamma_{rad} \times k_r$ and K_{nr} account for an increase in the denominator of τ_m. As for the quantum yield, it mostly increases if the dye's intrinsic quantum yield is well below one ($k_{nr} \gtrsim k_r$), and the acceleration of k_r overtakes that of K_{nr}, i.e. $\gamma_{rad} \times k_r > K_{nr}$. On the other hand, if the dye's intrinsic quantum yield is already one ($k_{nr} \ll k_r$), then it cannot be enhanced. In general, the plasmon effect on the dye's quantum yield is more intricate to analyze, because it involves a ratio between intrinsic and plasmon-accelerated decay rates.

The overall fluorescence enhancement factor (Equation 11) that contributes to the detected emission signal is obtained from the product of the excitation rate enhancement, γ_{exc}, and the relative quantum yield of the dye modified by the particle (Φ_m refers to the dye-particle conjugate quantum yield and Φ_F refers to that of the dye).[12]

$$\frac{F}{F^0} = \gamma_{exc} \times \frac{\Phi_m}{\Phi_F} \tag{11}$$

The excitation rate enhancement is obtained from $\gamma_{exc} = |E|^2/|E_0|^2$ which is the near-field enhancement at the incident wavelength. The quantum efficiency term, $\frac{\Phi_m}{\Phi_F}$, is determined at the emission wavelength, thus to maximize fluorescence enhancement, the plasmonic resonance of the particle must overlap with the emission spectral range of the dye.[12,15,70]

The overall LSPR effect on the photophysical properties of emitters depends on the details of the plasmon modes and the near-field close to the particle's surface, that on their turn are strongly influenced by the shape, size, and composition of the particle and by the refractive index of the surrounding medium.

Another key aspect is the dye-particle separation, because of the crossed effects on excitation, radiative and non-radiative decay rates in the plasmon near-field, that changes drastically with the distance between both entities, as qualitatively exemplified in Figure 1.4.

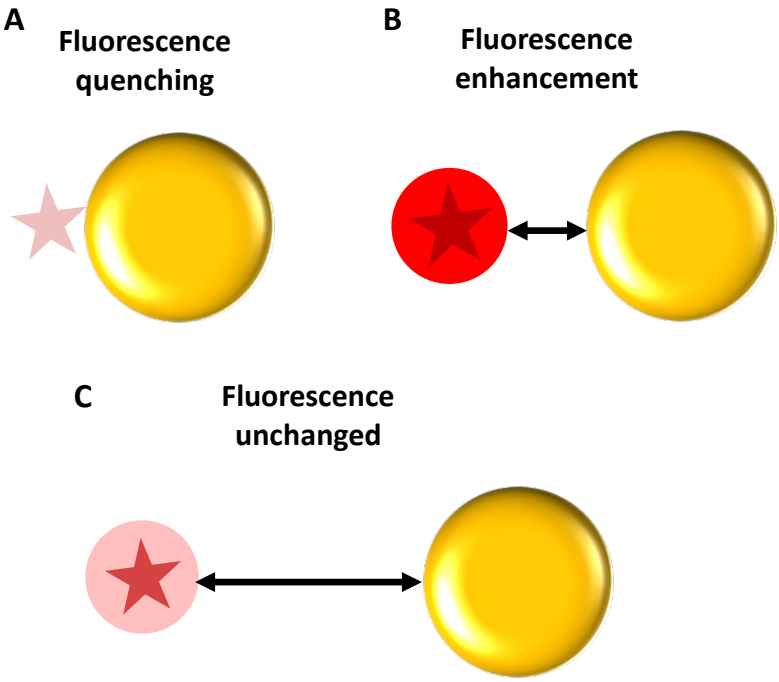

Figure 1.4 - Changes in molecular fluorescence intensity with respect to the dye-metal nanoparticle separation distance. (A) Fluorescence quenching due to a very short separation. (B) Fluorescence enhancement due to an intermediate and optimal separation and (C) undisturbed fluorescence due to a longer separation. Adapted from Ref. 71.

At very close dye-particle distances, quenching by the metal surface mostly overcomes the near-field enhancement effects on the dye's excitation and radiative decay rate.[57,58] This occurs because alternative non-radiative decay pathways, such as electron transfer or energy transfer, dominate for dyes near the particle, being that these processes detrimental for enhanced emission. Energy transfer decay pathway occurs when excitation energy is resonantly transferred from the dye to the particle, being then dissipated as heat. It enables the use of metal nanoparticles as quenchers for biosensing assays, because both dye and particle constitute a donor-acceptor pair. Due to the large absorption cross section of metal nanoparticles, this pair benefit of extended Förster radius when compared to combinations of dyes and organic (dark) quenchers.[72,73]

Typically, there is an optimal location (intermediate distance) for emission enhancement a few nanometers away from the metal surface (Figure 1.4B) provided by the increased rate of radiative decay. In the third case, fluorescence remains unchanged due to a longer distance (Figure 1.4C) where the effects on radiative and non-radiative decay rate acceleration fade away, so the original

quantum yield is again obtained. In some cases, to guarantee a proper distance, it is necessary to cover the particle with a spacer, such as a layer of a dielectric (non-metallic) material (e.g. silica, titania, alumina), organic polymers, polyelectrolytes, or a biomolecule (proteins, DNA, aptamers and others). Silica is actually one of the most used coating material of metal nanoparticles, as well highlighted in a recent review.[74]

Besides the distance dependence on the fluorescence enhancement, also the orientation of the dye must be convenient relative to the nanoparticle.[75] Another key aspect is the spectral dependence of plasmon-coupled emission.[76,77] The largest effects occur when the plasmon resonance of the nanoparticle is close to the dye's excitation wavelength and, correspondingly, the dye's emission is slightly red-shifted relatively to the plasmon peak wavelength.[64,68] This is also important because in the absence of any overlap, there will be no excitation wavelength in common to allow simultaneous excitation of both entities. For a particular dye, the spectral overlap condition can be attained by changing the particle's composition, size, or shape in order to tune its surface plasmon resonance.

1.3. Design of dye-particle assemblies for PEF

The enhancement of very weak emitters is potentially interesting for studying intrinsically fluorescent systems with low quantum yields, e.g. proteins or metal complexes, because their detection by optical techniques may become possible without the need of labeling. Also, the emission enhancement of strongly fluorescent molecules by their conjugation with metal nanoparticles can result in even brighter fluorescent objects of interest for imaging and biosensing applications. However, the role of plasmonic antennas for modifying photophysical or photochemical processes extends far beyond the effects of intensity changes, such as emission enhancement and quenching.[57,59,78–81] Antennas can also tailor the emission spectrum or lifetimes,[82–85] including down to subpicosecond lifetimes,[86] control emission directionality,[87–89] for the manipulation of optical selection rules,[90] enhancement of FRET efficiency,[91] reduction of dye photobleaching,[92] spatial confinement in photopolymerization,[93] or improvement of energy conversion in solar cells.[94]

Much research has been directed towards the synthesis of new nanoparticles and their assembly into nanostructures, particularly for their conjugation with fluorescent dyes (or other emitters) or with dye-labeled biomolecules. This conjugation of emitters onto metal nanoparticles is a promising approach to develop strongly emissive nanoprobes with fluorescence emission intensities much more pronounced than their isolated components. Indeed, in recent years, an increasing number of reports have illustrated the use of metal nanoparticles as antennas to modify the emission properties of dyes or other emitters.[12–14,95] These also have the potential as multifunctional probes that can be addressed by optical techniques in biological systems to perform imaging, sensing, drug delivery, theranostics or other therapeutic functions (e.g. cancer treatment with photodynamic and photothermal therapies).[9–11,67,96–101] In these nanoconjugates,

the role of the particles is frequently more than just that of a nano-sized carrier owing to their extraordinary optical properties, and in particular, to the ability to perform as antennas.

The development of wet-chemistry methods for the synthesis of colloidal metal nanoparticles offers the possibility of preparing a variety of particle types (Figure 1.5) and, therefore, to tune their optical properties,[99,102–104] including the plasmon-enhanced near-field for effective dye's emission. Looking into the literature, it is possible to infer that most particles and structures synthesized for the purpose of fluorescence enhancement studies, are commonly made of gold or silver as metals, with just few examples using copper[105,106] and aluminum.[107–109]

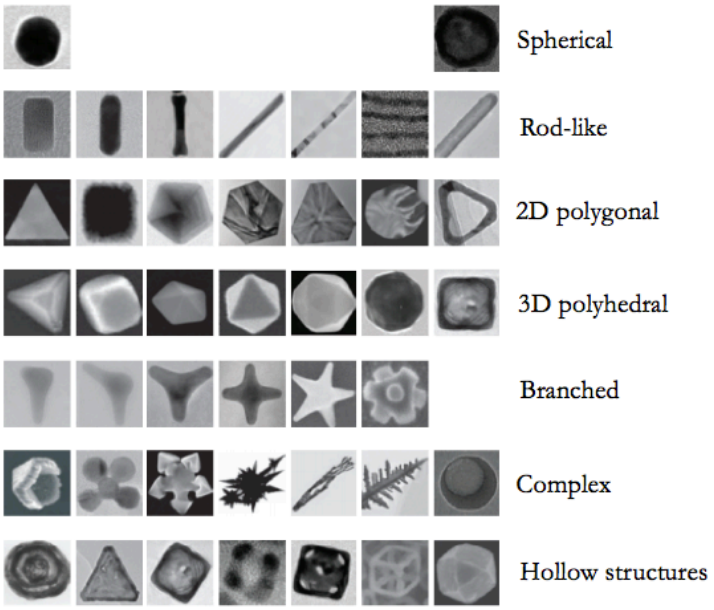

Figure 1.5 - Variety of shapes of plasmonic nanoparticles. Shapes from row one to six: spherical, rod-like, 2D polygonal, 3D polyhedral, branched and various complexities. Row seven encompasses other polygonal and polyhedral particles, but hollow, as the last particle in each of the other rows. Adapted from Ref. 110.

Gold and silver nanoparticles exhibit at specific incident wavelengths, strong light scattering and the appearance of intense LSPR extinction bands. Hence, the main reason for choosing these metal nanoparticles for fluorescence enhancement are their LSPRs, that are within the visible to NIR wavelengths. But also their ease of synthesis with different shapes and sizes to tune the extinction bands wavelengths, their distance-dependent optical properties and their accessible surface functionalization,[103,104] possible with different surface chemistries for coupling of several dyes and biomolecules. The dielectric properties of silver, including higher molar extinction coefficient, higher efficiency of light scattering, and namely its lower dissipation in the visible range, allow for larger plasmon-enhanced fields that yield better antenna effects when compared to gold.[111,112] However, silver nanoparticles are prone to oxidation and, thus, gold is preferred because of its chemical stability.

Different shapes and sizes of metal nanoparticles have been reported in fluorescence enhancement studies. The relative contribution of extinction and scattering of a particle depends

on these morphological characteristics, and normally its extinction shifts to longer wavelengths as the size increases, which can be useful for specific applications. In order to obtain large fluorescence enhancements, it is necessary to employ plasmonic nanostructures that generate intense near-fields. Since anisotropic and elongated particle shapes of gold or silver,[99,102,112] such as rods, bipyramids, cubes, hexagons, triangles, disks, or stars, display surface plasmon resonances that span from red to infrared spectral ranges for which dissipation is weak, this results in plasmon resonances with strong near-field enhancements. These are mostly concentrated at the regions of large surface curvature or at the sharp features of the particles' surface, designated as plasmon hot-spots. In section 1.3.1 the role of gold nanorods as plasmonic antennas is elucidated, because only this elongated particle shape was used to develop the proposed nanohybrid biosensors.

Since new and more innovative nanoparticles and nanostructure assemblies and arrays are created to improve fluorescence enhancements of dyes, it seems obvious that a crucial step is to model the overall outcomes of the nanomaterials. In this way, their fluorescence efficiency can be determined even before they are designed, synthesized or assembled/fabricated, saving time and resources. Mie's theory can be used to calculate optical properties of metal colloids when these are smaller than the incident wavelength.[8] On the other hand for complex particle geometries, there are computational methods for electromagnetics that can theoretically simulate the extinction properties of particles and their outcome on the emitter's decay rate enhancements. For this purpose, discrete dipole approximation (DDA),[113,114] finite-difference time-domain (FDTD),[115,116] finite element method (FEM)[117,118] or the boundary element method (BEM)[119,120] are often methods of choice. In fact, DDA simulations were implemented at the host laboratory and were used for the design and modeling of dye-particle conjugates studied in this thesis.

1.3.1. Gold nanorods as plasmonic antennas

Gold nanorods are one of the most relevant and promising metal nanoparticles for fluorescence enhancement of dyes. These nanorods have been extensively investigated for this purpose due to their many advantages, namely: i) the chemical stability of gold combined with well-established colloidal methods for nanorod synthesis with controlled size and shape dispersion; ii) the ability to tune their optical response across the NIR biological window by changing their aspect ratio and iii) the large plasmon near-field at the nanorod tips (hot-spots), provided by the longitudinal surface plasmon (LSP) mode.[103,121–123]

Early reports on dye nanoconjugates based on gold nanorods were mostly concerned on the fundamental properties of plasmon-coupled emission such as fluorescence enhancement,[124–127] emission directionality,[125,128] spectral reshaping,[129] or assisted energy transfer processes.[130] More recently, there have been numerous reports on dye-nanorod conjugates as dual mode probes for combined imaging and therapeutic functions, such as photothermal or photodynamic therapies,[131–147] or for sensing intracellular components, a topic discussed later in § 1.4.2. In this view, gold nanorods have been conjugated with a diversity of organic dyes, such as

cyanines,[132,135,141] phthalocyanines,[131,143] porphyrins[140,144,148] and chlorins,[134,142] but also, with inorganic emitters, like semiconductor quantum-dots,[137,149] rare-earth doped particles[150] and metal clusters.[151] The strategies of dye-particle conjugation also comprise a diversity of approaches such as chemical attachment of dye molecules using thiol derivatization,[134,135] non-covalent supramolecular assembly,[138,140] entrapment in a polymer or silica shell,[131,133] or even a combination of the previous strategies.[132,137]

The ability of single gold nanorods to perform as optical antennas that afford large fluorescence enhancements has been demonstrated for a diversity of emitters using single-molecule fluorescence detection.[68,152–154] In particular, it was shown that for weak emitters the overall enhancement factors can surpass 1000-fold emission increase for resonant plasmonic enhancement of fluorescence[68] or 3000-fold for a NIR dye using a DNA-based transient binding technique.[154] The fluorescence enhancement of a strong emitter by a gold nanorod dimer fixed on a DNA origami nanobreadboard was also reported, with the smallest gap providing the highest enhancement, 470-fold.[69] Recently, dimers of gold nanorods in end-to-end configuration having strong plasmon hot-spot gaps allowed even larger enhancements of about 10000-fold for a weak emitter.[155] The next section develops on this topic of fluorescence enhancement by nanogap optical antennas.

1.3.2. Gold nanodimers as plasmonic antennas

The nanometric gaps in nanostructure arrays or assemblies of particles also concentrate strong near-fields, and can act as powerful hot-spots.[80,156–163] Therefore, besides the dye-particle separation and orientation, and their spectral overlap, it is also important to selectively attach the dye at plasmon hot-spots to maximize emission antenna effects. For instance, dimers of spherical gold nanoparticles are capable of enhancing fluorescence emission by 2 or more orders of magnitude.[156–161,163] The longitudinal coupling of the individual plasmons in dimer particles gives rise to an hybridized plasmon mode that produces an intense near-field concentrated in the gap region.[164,165] The field enhancement is particularly strong for dimers of gold particles of several tens of nanometers in diameter combined with gap separations of a few nanometers. Such dimer particles afford the largest emission enhancements reported up to now, ranging from 600-[156] to 5000-fold,[160] later up to 15000-fold[161] and even 1 million.[163]

Normally, the gold dimer nanospheres are prepared in colloidal suspension by self-assembly,[156] assembly using double-stranded DNA spacers[158,163] or DNA origami structures,[157,160] or as nanoarrays by top-down fabrication.[159,161] Through top-down procedures a gold bowtie antenna formed by a dimer of nanotriangles provided 1340-fold emission intensification of a relatively inefficient dye, being one of the most highest values reported for this kind of nanostructure.[80] It is important here to be aware that top-down techniques still need a more simple and economic fabrication approach. Currently they are to complex and time-consuming to be cost effective in real-life practical applications, thus the preference for colloidal metal nanoparticles in most of the reported works.

Plasmon hot-spots in nanoparticles are also sensitive to local changes in the medium's refractive index, exhibiting a perceptible surface plasmon resonance wavelength shift in response to variations in the medium. These plasmon shifts constitute another important detection scheme widely developed, reported and extensively reviewed, known as LSPR sensing.[8,166–169]

1.4. Biosensors for detection of biomarkers

According to the IUPAC, a biosensor can be defined as "a compact analytical device incorporating a biological or biologically derived sensing element, either integrated within or intimately associated with a physicochemical transducer".[170] The biological component can be a tissue, microorganism, enzyme, antibody, protein, or nucleic acid that is used as recognition system, or bioreceptor, to sense specific target analytes.[55,171] These devices use physicochemical transducers (optical, electrochemical, thermometric, piezoelectric, magnetic, or mechanical) to convert the recognition event from the bioreceptors into a detectable and measurable signal. Essentially, biosensors consist of three components: (1) the receptor, to identify the stimulus; (2) the transducer, to convert the stimulus to an output; and (3) the output system, that involves amplification and display of the output in an adequate format. The analytical performance of a biosensor takes in consideration its dynamic range, reproducibility, selectivity, sensitivity, figures of merit, and detection limits.[2]

The potential of biosensors for biomarker detection is undeniable. To be ideal, biomarkers should be safe, stable, easy to obtain and to measure by non-invasive procedures, cost efficient, sensitive, specific, quantifiable, robust and predictive. But also, detectable by simple and inexpensive methods, non-overlapped with other diseases, and consistent across gender and ethnic groups. To date, none of the available biomarkers satisfy all of these criteria.[172] Their major limitations are sensitivity, low specificity and false positive results. In addition, the ones currently available in body fluids like serum/plasma are mostly based on proteins.

1.4.1. Fluorescent nucleic acid probes: molecular beacons

DNA shows great practical advantages for biological and medical research due to its specific recognition properties and structural features, like: simplicity of oligonucleotide synthesis, predictable double helical structures, excellent biological function and affinity, molecular recognition capacity, high selectivity, nanoscale controllability and excellent biocompatibility.[173,174] Although nucleic acids have nucleotides with nitrogenous bases that look like aromatic molecules, they are only weakly fluorescent or totally non-fluorescent and thus cannot be directly used in fluorescence-based detection. To overcome this limitation, a wide variety of organic and aromatic dyes have been developed to label nucleic acids and other biomolecules.[175]

In the last decades fluorescent nucleic acid probes and assays containing labeled dyes, mostly by covalent attachment, have been developed for monitoring DNA reactions and for allowing nucleic acid detection. The majority are doubly-labeled for FRET schemes between a donor dye and an acceptor quencher. Molecular beacons are an important example relevant in the context

of this thesis. These were invented by Tyagi and Kramer in 1996 to support real-time and in solution hybridization assays.[176] These single-stranded oligonucleotide fluorogenic probes display a stem-and-loop structure, named hairpin (Figure 1.6). The loop region contains a sequence that is complementary to the target sequence, and that closes due to a self-complementary end forming a stem. The dye and quencher moieties are labeled in opposite ends of the stem. In the closed hairpin the molecules are near, providing a low emission state - signal off - due to quenching of the donor's fluorescence by energy transfer to the acceptor. In the presence of a nucleic acid target, the molecular beacon undergoes a conformational reorganization due to the loop hybridization with the target. Since the hairpin stem is less stable than the binding between the loop and the target, the structure opens. The rigidity of the probe-target helix separates dye and quencher, preventing their energy transfer, which results in restoration of fluorescence of the dye and in a bright emission state - signal on - indicative of nucleic acid detection.

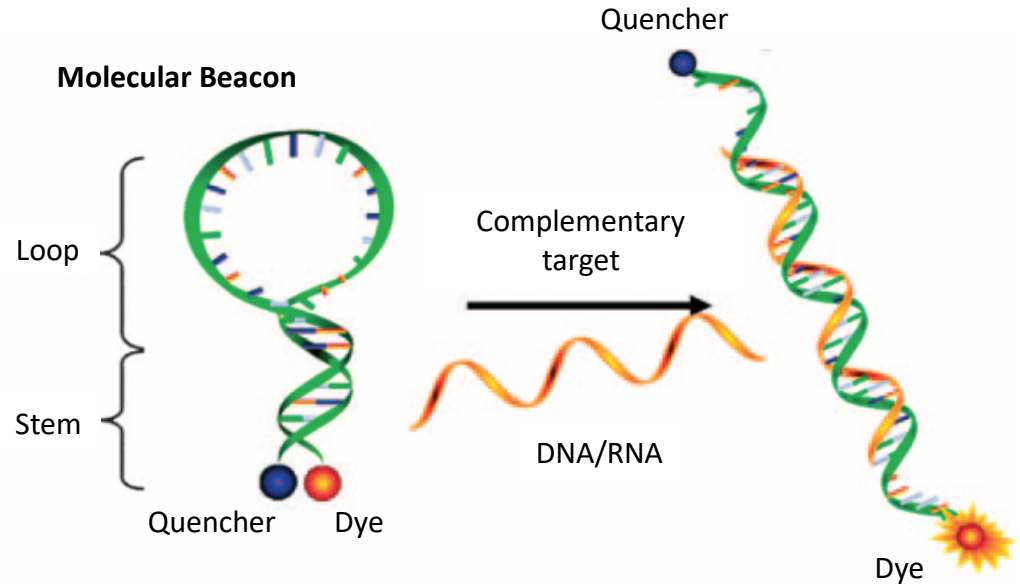

Figure 1.6 - Molecular beacon structure and fluorescence signal off-on sensing working principle. A hairpin sequence is labeled with a dye and a quencher in each end of the stem. The nucleic acid (DNA or RNA) target is complementary with the loop region of the hairpin. The sensing mechanism occurs upon hybridization of the target with the loop region of the hairpin, that induces a change on the hairpin from a closed conformation of low fluorescence emission to an open conformation, which increases the distance between dye and quencher resulting in high emission of fluorescence that signals the detection event. Adapted from Ref. 177.

In dual-labeled nucleic acid probes, FRET quenching is often used but other types of quenching may also occur, independently or associated with FRET.[26–30,178] For instance, a donor-acceptor pair that interacts by photoinduced electron transfer or that forms a non-emissive ground-state complex could be used for beacons with a "close-contact" type of quenching.[179] On the other hand, quenching by FRET allows to study dynamics of the hairpin, that can open and close regularly in an equilibrium process, because it is effective over a wide range of donor-acceptor distances.

Other than the traditional molecular beacon, several stem-loop configurations have then been developed, with probe designs including wavelength-shifting,[180] tripartite,[181] ratiometric bimolecular,[182–184] and bimolecular[185] beacon probes, such as the ones designed in this thesis and that are exemplified in Figure 1.7. The design of this probe consists of a hairpin sequence labeled only with a quencher molecule that assembles through hybridization with a single-stranded DNA (ssDNA) sequence labeled with a dye, thus forming the beacon with the donor-acceptor pair. The mode of action of the fluorescence signalling sensing is then similar to that of traditional beacons. Other bimolecular beacons where the dye labels the ssDNA internally rather than at the end have been previously reported.[186–188]

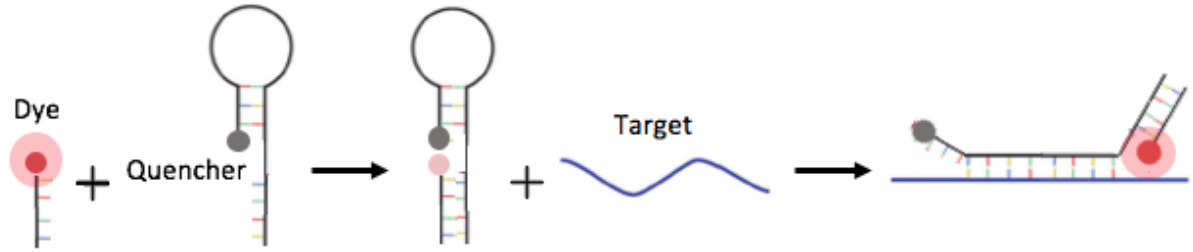

Figure 1.7 - Bimolecular beacon probe for fluorescence signal off-on sensing of nucleic acids. The structure of this probe is formed by hybridization of a ssDNA sequence labeled with a dye and a ssDNA hairpin labeled with a quencher (left side). In the closed hairpin conformation (center), the proximity of dye and quencher provides a low emission state - signal off. Upon hybridization of the target with the loop region of the hairpin, it opens, which increases the dye-quencher distance, thus restoring fluorescence and affording a high emissive state - signal on - indicative of detection (right side).

Molecular beacon probes have many advantages that attracted much interest. These include ease of synthesis, unique functionality, inherent signal transduction mechanism, distinctive thermodynamic, relative low fluorescence background, molecular specificity, structural tolerance to various modifications and reversible binding to the target. But there are some particular disadvantages to beacons, such as high cost and difficulty in purification due to the possible formation of secondary structures. Their unique structural and thermodynamic properties provide a high degree of molecular specificity, with the ability to differentiate between two target sequences that differ only by a single nucleotide. For this reason, hairpin DNA probes appear to be better alternatives to conventional linear probes for mismatch discrimination in assays for single-nucleotide polymorphism and mutations.[178,189–191] They can also be created with a palette of different coloured dyes, from which the fluorescence of all can be suppressed simultaneously by a single broad-spectrum universal quencher. This allowed the creation of multicoloured molecular beacons,[192] useful for multiplexed detection of different nucleic acid targets.

Both FRET and non-FRET probes provide a complete set of approaches for DNA detection, analysis and quantification, genetic studies, and DNA sequencing by allowing the monitoring of DNA and RNA reactions, like hybridization, cleavage, amplification and folding. They also allow the determination of distances in protein-DNA complexes and the detection of topological DNA changes, mutations, and single-nucleotide polymorphisms. For example, PCR and their variants

use FRET probes to monitor DNA amplification.[193,194] In the reaction, these are either cleaved (like TaqMan® probes), combined with amplified DNA (like scorpion primers), or undergo a conformation change in the presence of a complementary DNA target (like molecular beacons). Some examples of probes used in real-life applications include TaqMan®, minor groove binding (TaqMan®, Pleiades and Eclipse), molecular beacons and dumbbell molecular beacons, tentacle and quenched autoligation (QUAL) probes, molecular break lights, molecular torches, and primers (scorpions and duplex scorpions, Amplifuor®, cyclicons).[193–195] Probes with an oligonucleotide sequence only labeled with one molecule or with two sequences labeled each other with donor or acceptor using FRET have been also designed, such as Angler® primers and ResonSense® probes, and adjacent and HybProbes, respectively. These FRET probes are DNA- and RNA-based and in most cases, they signal the reaction/detection occurrence with fluorescence emission by eliminating the quenching effect on the donor. Non-FRET-based designs are also available, such as LUX™ primers, and HyBeacon™ and strand-displacement probes (Yin-Yang probes).[30,193,194]

Besides quantitative PCR, molecular beacons have been widely used in several applications, being highlighted: i) enzyme detection;[196] ii) real-time monitoring of messenger RNA (mRNA)-DNA hybridization;[197] iii) visualization of the distribution and transport,[198] and delivery and detection,[199,200] of endogenous mRNA in live cells (including cancer lines); iv) detection of DNA;[201] v) signal-on strategies to bioimage (detect) gene expression of multiple mRNAs[202] and miRNAs[203] transfected into cancer cells, in the last case also *in vivo*; vi) detection of multiple miRNAs in cancer cell-derived exosomes in high human serum concentration;[204] vii) cancer theragnosis using doxorubicin and miRNA detection;[205] and viii) development of biosensors for nucleic acid detection, and other targets, in solid surfaces[174,190,206] or when merged with nanotechnology, a topic that will be further highlighted in the next section.

1.4.2. Nanoparticle-based biosensors for nucleic acid detection

Nanoparticle-based biosensors display remarkable advantages when compared to bulk materials due to: i) larger surface areas that are excellent as carriers of bioreceptors thus contributing to enhance the optical signal transduction; ii) nanoscale sizes that extend the limitation of structure miniaturization, allowing the design of low-cost and minimized equipment for POC diagnostics; iii) they contact directly with the microenvironment, therefore may accelerate signal transduction, improve rapid analysis' ability and lower detection limits. Due to the creation of metal nanoparticles/nanostructures with unique and remarkable properties, several colorimetric,[207–211] Surface-Enhanced Raman Scattering (SERS),[212–217] LSPR,[8,166–169,218,219] electrochemical,[220–225] chemiluminescent,[226] fluorescent, and dual-mode (integrating two detection schemes)[227-230] biosensors have emerged in the last decade. Some of these provide possible responses for sensitive biomolecular detection and are included in the category of optical biosensors, that commonly use transduction signals from light absorption, Raman scattering, refractive index, and luminescence, including fluorescence.

The focus here is in metal nanoparticle-based fluorescent biosensors, since fluorescence detection offers numerous important advantages over other methods. One of the reasons for the huge increase in fluorescence-based detection is probably the versatility of transduction signals that fluorescent molecules or dye-particle conjugates can offer. This versatility is due to a change in some intrinsic property (fluorescence intensity, excitation or emission spectra, wavelength, anisotropy, quantum yield, or lifetime) that is triggered in response to the specific interaction with the target.[55] With a relatively simple detection process, other advantages include: i) a non-destructive and minimally invasive way of tracking or analyzing biological molecules; and ii) detection of multiple targets using different emission wavelengths - multiplexed detection. Obviously, the sensitivity is limited by the fluorescence signal that is generated. In this view, the emission enhancement provided by plasmonic nanoantennas is a desired strategy to improve significantly the detection sensitivity of these biosensors.

Similarly, to other nanostructured sensors, specificity in molecular interactions can be built-in by easily modifying the nanostructure's surface with dye-labeled bioreceptors, in which are included oligonucleotides. The use of plasmon-enhanced fluorescent biosensors is still limited to academic research, even though their advantages - like, ease of synthesis, biocompatibility, controlled sizes, high surface-to-volume ratios, high emission rates, photostability and color tenability, detection of ultra-low concentrations of biomarkers - are ideal for real-life applications. Besides, this type of probes could also find other applications beyond strictly sensing, such as imaging and therapy.[177,231–235]

The attachment of dye-labeled oligonucleotides to the surface of plasmonic particles commonly uses the covalent gold-thiol chemistry, following several available methods recently described in a review.[236] Since the pioneering works of Mirkin's[237] and Alivisatos's[238] groups on oligonucleotide-gold nanoparticles conjugates in 1996, the number and complexity of designed nanoconjugates increased significantly accounting for a vast literature. Hereafter, some examples of state-of-the-art biosensing platforms are presented with a special focus on the detection of nucleic acids.

One key advancement in the field was the invention in 2007 by the Mirkin's group of the nanoflare for transfection and detection of mRNA in living cells.[239] This platform consists of a spherical gold nanoparticle densely functionalized with a thiol-modified ssDNA monolayer that is hybridized to a flare/reporter strand (a short oligonucleotide strand labeled with a dye). Due to the quenching ability of the particle, detectable fluorescence from the reporter strand is negligible. Upon target binding, the reporter strand is released through competitive hybridization and a fluorescence signal proportional to the amounts of target can be detected in real time. Further improvements in the nanoflare platform were then performed.[240–243]

Sensing probes based on nanoflares have been reported in various biomedical applications.[244] The most important are in the context of cancer, for example in the isolation and detection of live circulating tumor cells.[245] Cancer-related nucleic acid sequences have also been detected,

mostly miRNAs and mRNAs. Some examples of miRNAs include miR-30a with a limit of detection (LOD) of 2.4 pM in living cancer cells,[246] and multiplexed detection of miR-21 and miR-141 in various cancer cell lines, and in a cell free system with LOD's of 0.9 nM (miR-21) and 1.2 nM (miR-141).[247] Other example of RNA, human telomerase RNA, was detected in cancer cells using a variant of the nanoflare known as sticky-flare.[248] DNA (survivin) detection with a limit of 372 pM was also reported using enhanced fluorescence polarization.[249] Besides cancer, a specific RNA sequence of native classical suine fever virus was detected at a low amount of 0.05 pg/μL.[250] Another example of a target nucleic acid that has been also vastly detected is mRNA and as such deserves attention. Cancer-related targets include: BRCA1 using the FLIM technique,[251] c-myc,[252] TK1 with FRET nanoflares,[253] vimentin,[254] survivin in an adjuvant cancer gene/photothermal therapy with gold nanostars[255] and with dual FRET nanoprobes.[256] But also multiplexing of actin and survivin,[257] of keratin 8 and vimentin using dimers of gold spheres,[258] and of c-myc, TK1 and GalNAc-T.[259]

Nanoflares have been also reported for detection of other targets using aptamers - specially designed DNAs/RNAs with nucleotides' sequences that determine their specificity for certain targets (ions, small molecules, enzymes, proteins). These aptamer nanoflares, mostly composed of gold particles, detected adenosine triphosphate (ATP),[260,261] heavy metal ions (Pb^{2+} and Hg^{2+}),[262] potassium ions,[263] telomerase,[264] staphylococcal enterotoxin B (with platinum-coated gold rods and upconversion particles that acted as fluorescence donors),[265] and three analytes (adenosine, potassium ion, and cocaine) simultaneously.[266]

Besides nanoflares, another approach used conjugated dye-labeled DNA probes on gold particles deposited in a porous silicon microcavity to detect DNA with a limit of 10 pM.[267] Strategies with upconversion nanoparticles have been also investigated. For example, multifunctional pyramids composed of gold-Cu_9S_5, upconversion and silver-S particles, allowed dual miRNA detection. In particular, miR-203b with a LOD of 0.09 fmol/10 μg RNA and miR-21 with a LOD of 0.23 fmol/10 μg RNA at the cellular level, while also providing photothermal therapy in a tumor-bearing animal model.[268] Detection of other targets following various approaches were also reported for ATP,[269,270] nucleolin,[271] human platelet-derived growth factor-BB,[272] recombinant hemagglutinin protein of the H5N1 influenza virus,[273] prostate specific antigen,[274,275] and multiplexing of cytochrome c and caspase-3.[276]

Nucleic acid signal amplification techniques enabling the sensitive detection of ultra-low concentrations of specific targets have been developed in the last years. These are mostly based on enzymatic reactions, or on DNAs that perform catalytic reactions, such as catalytic hairpin assembly and DNAzymes, or hybridization chain reaction, that have the ability to recognize specifically a broad range of targets.[277,278] In some examples with gold particles, a split-DNAzyme probe detected miR-21 with a limit of 10 pM in living cells,[279] a nicking endonuclease-powered 3D DNA nanomachine detected 75 fM of DNA from a drug-resistant strain of *Mycobacterium tuberculosis*, even with a LOD of 20 pM in 10-fold-diluted human serum,[280] and an exonuclease

III-powered DNA walker provided also DNA detection (10 fM).[281] The incorporation of DNA nanotechnology, that *per se* can act as a natural biological sensor, into biosensors, has been progressively studied as an attractive and powerful building biomaterial for formation of nanostructures.[172,282,283] Using this approach, a more intricate gold particle nanostructure used a duplex-specific nuclease and 3D DNA tetrahedron-structured probes to detect multiple miRNAs.[284] A linear range covering 5 magnitudes (10^{-12}-10^{-16}) and a low LOD of 12.59 aM, 17.8 aM and 44.7 aM for miR-16, miR-21 and miR-26a, respectively, were achieved.

1.4.3. Molecular beacons conjugated onto metal nanoparticles

The examples of biosensing platforms described in this section are exclusively of molecular beacons conjugated with metal nanoparticles to produce a nanohybrid sensor. But first, in a study combining gold particles of different sizes with DNA hairpins labeled with FRET pairs, single-molecule FRET was used to investigate hairpin dynamics.[285] Single-molecule fluorescence enhancements of 3-5 fold and substantial reduction of FRET efficiency were reported. Furthermore, gold particles did not influence the kinetic and dynamic parameters of the hairpin closing/opening processes, and larger particles produced greater fluorescence enhancements due to larger scattering efficiency.

Nucleic acid biosensing has been shown using gold particles where 16S rRNA of *Escherichia coli* was detected.[286] Another work concerns a complex structure based on silver particles attached to a DNA origami pillar functionalized with a molecular beacon that targeted a DNA sequence (1 nM) while affording fluorescence quenching and enhancement.[179] More favorable results were obtained using contact quenching between dye and quencher in the closed hairpin, which provided 3.6-fold fluorescence enhancement in the open hairpin. Later, this structure detected Zika virus-specific artificial DNA and RNA, both with 1 nM, in buffer and in heat-inactivated human blood serum.[287] For DNA, fluorescence enhancements of 4.9- and 7.3-fold for serum and serum-free samples were reported. As for RNA, only ca. 37% of the hairpins opened, compared to 52% for DNA, because RNA has a tendency to form more secondary/tertiary structures than DNA. In this work, multiplexed detection of the Zika-specific target DNA and of another DNA sequence, using different plasmonic antennas for each target, was also performed.

Despite these reports, limitations of beacons conjugated to metal particles exist, including incomplete dye quenching and insufficient signal recovery. The use of metal particles as quenchers solves these problems. The particles are efficient energy acceptors of dye's emission, allowing the replacement of the organic quenchers in the beacons (Figure 1.8). Because of the strong long-range FRET quenching ability, resulting essentially from non-radiative energy transfer from the dye to the metal, this can provide a large and greatly improved off-on contrast/signal-to-background ratio for beacons.[73,178]

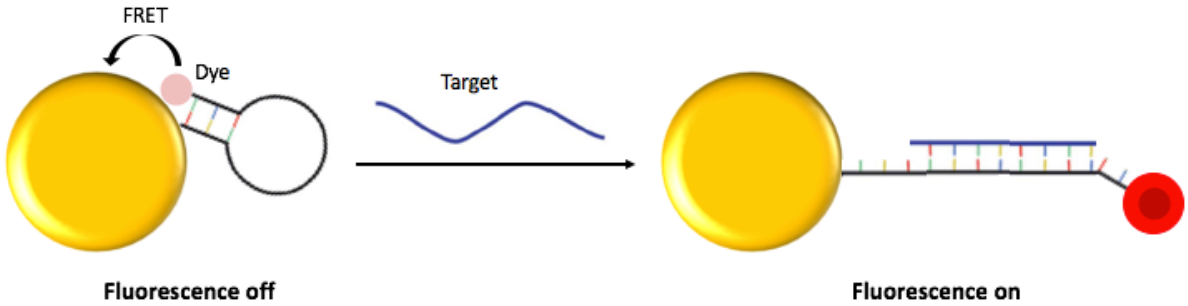

Figure 1.8 - Schematic illustration of a nucleic acid detection strategy based on a gold nanoparticle functionalized with a molecular beacon labeled only with a dye. In the closed form, the hairpin allows proximity of the dye to the particle's surface resulting in quenching of fluorescence by FRET, because the particle acts as an energy acceptor. Upon target hybridization with the loop region of the hairpin, fluorescence is restored due to a larger distance of the dye relatively to the particle and is also enhanced due to the particle's antenna effect.

For DNA detection, the strategy of the figure above with gold particles was earlier used and showed high quenching efficiencies.[288,289] Next, surface-immobilized particles, namely of silver, achieved a LOD of 100 pM[290] and of gold, using a fixed value of 1 μM of DNA, provided 3-fold improvement in fluorescence emission.[291] Larger gold particles of 100 nm were then reported for over 96.8% quenching efficiency and a signal increase of 1.23 due to the hairpin opening, with a LOD below 100 pM.[292] For a biologically related DNA target, ΔF508 cystic fibrosis associated mutation, a LOD of 1 nM and 7-fold increase in fluorescence were reported.[293] MiRNAs have been also detected with hairpin DNA-coated gold particles. MiR-122 detection with a limit of 0.01 pM and a linear range from 0.05 to 50 pM was performed,[294] and a theranostics system formed by a pair of hairpins was designed for miRNA-21 targeted imaging and photothermal treatment in cancer cells.[295] As for mRNAs, detection in live cancer cells include: tyrosinase,[296] glyceraldehyde 3-phosphate dehydrogenase and respiratory syncytial virus,[297] STAT5B,[298,299] and multiplexing of TK1 and GalNAc-T (and matrix metalloproteinases),[300] and of TK1, survivin, c-myc and GalNAc-T.[301]

In some literature, the term gold nanobeacon has been used to refer to the type of probes described in this section. Several examples of gold nanobeacons have been developed for: i) real time *in vitro* synthesis of RNA;[302] ii) intersection of both pathways of interference RNA regulating gene expression (small interfering RNA by directly downregulating a specific gene, EGFP, and silencing endogenous upregulated miR-21) in cancer cells;[303] iii) targeting and silencing a specific mRNA (antisense) in live cancer cells;[304] iv) detection of a mutant Kras gene in a theranostics platform that inhibited cancer cells and metastasis in a murine tumor model;[305] and v) endogenous enhanced green fluorescence protein (EGFP) mRNA detection in embryos of a fli-EGFP transgenic zebrafish line, with simultaneous tracking and localization of the silencing events.[306] To study the photophysics of these probes, time-resolved fluorescence spectroscopy was used, and conformational switching and energy transfer processes were investigated.[307]

Concerning nucleic acid amplification techniques applied in association with the nanohybrids, numerous works exist in the literature with gold particles for miRNA detection. A swing DNA

nanomachine used two hairpin DNA probes for intracellular miR-21 sensing with a LOD of 0.1 nM.[308] A DNA-fueled and catalytic molecule machinery for miR-21 imaging and detection provided a LOD of 67 pM,[309] and hairpin-locked-DNAzyme probes allowed miR-141 detection with a limit of ca. 25 pM,[310] both in living cancer cells. A miR-21-5p target-assisted FRET signal amplification afforded a LOD of 1.5 fM with a linear range from 10 fM to 10 nM.[311] Multiplex detection of miR-21, miR-373 and miR-155, using a toe-hold strand-displacement reaction and hairpin-locked DNAzyme, even reached respectively low LOD's of 179, 58.8 and 24.9 aM, and fluorescence enhancements of about 4.48-, 2.65- and 3.49-fold.[312]

More complex structures have been also created, such as DNA-coated gold particle-quantum dot core-satellite assemblies for detection of intracellular miR-21 with a limit of 0.05 amol/ng RNA (296 copies per cell) and application for *in vivo* tumor imaging.[313] Using other particle shapes, ERBB2 cancer gene DNA was detected with a limit of 2.4 zeptomole by porous gold disks,[314] and for other targets, such as telomerase, *in situ* imaging in live cells was performed with gold bipyramids,[315] and single-molecule detection and *in situ* imaging in cancer cells was achieved with gold triangular plates.[316] But in the later, the hairpin was linked to the tips of the triangles by means of biotin-streptavidin recognition motif. Extra examples of targets besides nucleic acids, but with gold spheres, include multiple endonucleases (namely HaeIII, EcoRI, and EcoRV) in homogeneous solutions,[317] and four organophosphorus pesticides in real samples.[318]

Focusing on gold nanorods as a plasmonic substrate for molecular beacons, a vast literature exists. An approach using nanorods as ordered arrays in a biochip substrate for DNA sensing was implemented.[319] The opening of the beacon led to a doubling of the fluorescence intensity, a linear relationship from 10 pM to 10 nM and a LOD of 10 pM. A DNA sensor for the detection of *Escherichia coli*, mainly the O157: H7 eaeA gene, was also constructed, but using gold-coated silver nanorods, and provided a low LOD of 3 aM and high specificity.[320] Time-resolved fluorescence spectroscopy studies on hairpin probes using gold nanorods were also reported, considering a fixed value of 500 nM for DNA detection.[321] Regarding miRNA detection, reports include miR-21-responsive cell imaging and photothermal therapy in living mice,[322] and amplification approaches. In a work, two hairpin probes were functionalized on the terminal and side surfaces of nanorods, and NIR laser triggered target strand displacement amplification allowed detection of miR-373 in various single living cells and in multicellular tumor spheroids.[323] In RNA detection, a beacon labeled with a quencher instead of a dye, and conjugated into silica-coated gold nanorods covered with ternary (CdSeTe) quantum dots, was used for Novovirus RNA sensing with a linear range from 2 to 18 copies/mL and a LOD of 1.2 copies/mL.[324] For mRNA detection, targets include c-myc,[325] cellular Lrg1 using citrate-capped gold nanorods[326] and a theranostic platform for intracellular survivin imaging guided photothermal therapy using two hairpins and a dye-labeled hybrid DNA.[327]

The strategy of using nanogap plasmonic hot-spots between particles to increase sensitivity in nucleic acid detection was also performed. Two oligonucleotides, one linked to a gold sphere and

another to a gold-coated silver sphere, placed a dye in the nanogap of the particles, that upon plasmon coupling interactions gave 100-fold enhancement when compared to quenched dye-gold particles.[328] The enhanced fluorescence was further explored for detection of a DNA sequence with a limit of 3.1 pM. The regioselective functionalization of gold nanorods with molecular beacons was also recently achieved, by placing the probes in the tips of the particles.[329] Further assembly in a tip-to-tip configuration provided hot-spot nanogaps for enhanced fluorescence in miRNA detection. The approach also benefited from a target-triggered strand displacement amplification reaction, which combined with single counting of dye molecules, provided miR-21 detection with a low limit of 97.2 aM and selectivity.

In general, nanoparticle-based fluorescent biosensors provide nucleic acid detection with limits ranging from a few picomolar to a few attomolar. However, most that reach LOD's in the attomolar range are based on DNA amplification methods that have been implemented in association with nanohybrids for increased sensitivity. These methods require extra addition of an enzyme or a catalytic fuel, making the whole process complicated, comprising excessive reagents and being time-consuming (days), thus hampering the translation of the nanohybrids from academic research to POC and clinical diagnostics applications. Moreover, the reported low fluorescence enhancements are far from the latest progresses in the field of plasmonics that have provided enhancements of several orders of magnitude. Hence, these have not yet been fully explored for fluorescence-based biosensors.

1.4.4. Single-molecule detection of nucleic acid hybridization

The ultimate sensitivity of nucleic acid detection is the single-molecule sensing of hybridization. DNA hybridization at single-molecule detection level has been achieved with several strategies, namely using a micromechanical technique with micrometer-sized beads,[330] with single-gold particles in a NIR plasmon resonance microscopy real-time measurement,[331] using single-gold rods for plasmonic enhancements of whispering gallery modes excited in microsphere cavities,[332,333] and with zero-mode waveguide nanostructures using dye-labeled oligonucleotides.[334]

Single nanoparticle plasmonic sensors are also contributing for single biomolecule sensing by being used in several approaches that are implemented in a variety of experimental techniques to detect a large range of analytes.[104,335–339] But others strategies are also being developed, based on a digital single-particle switch sensor for continuous monitoring of analytes, including DNA.[340] Regarding plasmon-enhanced fluorescence, it already showed the possibility for single-molecule sensing by using a DNA origami pillar with two gold particles forming a dimer, that provided direct visualization of association and dissociation of short DNA sequences.[157] Certainly, as numerous efforts have been made to devise more relevant and practical plasmon-enhanced fluorescent biosensors, a successful implementation of this approach is expected to achieve high sensitivity and selectivity with ideal fluorescence amplification. This approach is considered now one of the most promising paths that may lead to achieve the ultimate single-biomolecule

detection sensitivity and allow its implementation on biosensors for real-life applications. However, despite the recent improvements, some challenges from a biological perspective still need to be addressed for relevant applications in real microenvironments.

One of the fundamental problems is non-specific adsorption, which in turn entails decreased sensitivity and has an influence on colloidal stability. Low fluorescence enhancement in biological fluids may occur due to aggregation of colloidal nanoparticles in the absence of targeted molecules, which yields misleading signals and increased background signals. Better elucidation about the interactions between dyes, nanoparticles and biomolecules, both in homogenous solutions and in more complex biological environments, is also required. Biosensing assays always require strict experimental conditions to preserve the particles' properties for fluorescence enhancement and, in most cases, the proof-of-concept has been reported by providing the results under controlled experimental conditions. As a consequence, validation of these results in real samples must be a priority, and a clarification of the interactions between particles and biomolecules in biological fluids needs to be addressed, alongside with the call for more robust and pragmatic advances.

1.5. References

(1) Pelaz, B.; Alexiou, C.; Alvarez-Puebla, R. A.; Alves, F.; Andrews, A. M.; Ashraf, S.; Balogh, L. P.; Ballerini, L.; Bestetti, A.; Brendel, C.; Bosi, S.; Carril, M.; Chan, W. C. W.; Chen, C.; Chen, X.; Chen, X.; Cheng, Z.; Cui, D.; Du, J.; Dullin, C.; Escudero, A.; Feliu, N.; Gao, M.; George, M.; Gogotsi, Y.; Grünweller, A.; Gu, Z.; Halas, N. J.; Hampp, N.; Hartmann, R. K.; Hersam, M. C.; Hunziker, P.; Jian, J.; Jiang, X.; Jungebluth, P.; Kadhiresan, P.; Kataoka, K.; Khademhosseini, A.; Kopeček, J.; Kotov, N. A.; Krug, H. F.; Lee, D. S.; Lehr, C.-M.; Leong, K. W.; Liang, X.-J.; Ling Lim, M.; Liz-Marzán, L. M.; Ma, X.; Macchiarini, P.; Meng, H.; Möhwald, H.; Mulvaney, P.; Nel, A. E.; Nie, S.; Nordlander, P.; Okano, T.; Oliveira, J.; Park, T. H.
; Penner, R. M.; Prato, M.; Puntes, V.; Rotello, V. M.; Samarakoon, A.; Schaak, R. E.; Shen, Y.; Sjöqvist, S.; Skirtach, A. G.; Soliman, M. G.; Stevens, M. M.; Sung, H.-W.; Tang, B. Z.; Tietze, R.; Udugama, B. N.; VanEpps, J. S.; Weil, T.; Weiss, P. S.; Willner, I.; Wu, Y.; Yang, L.; Yue, Z.; Zhang, Q.; Zhang, Q.; Zhang, X.-E.; Zhao, Y.; Zhou, X.; Parak, W. J. Diverse Applications of Nanomedicine. *ACS Nano* **2017**, *11* (3), 2313–2381. https://doi.org/10.1021/acsnano.6b06040.
(2) Liu, J.; Jalali, M.; Mahshid, S.; Wachsmann-Hogiu, S. Are Plasmonic Optical Biosensors Ready for Use in Point-of-Need Applications? *The Analyst* **2020**, *145* (2), 364–384. https://doi.org/10.1039/C9AN02149C.
(3) Schwarzenbach, H.; Nishida, N.; Calin, G. A.; Pantel, K. Clinical Relevance of Circulating Cell-Free MicroRNAs in Cancer. *Nat. Rev. Clin. Oncol.* **2014**, *11* (3), 145–156. https://doi.org/10.1038/nrclinonc.2014.5.
(4) Filipów, S.; Łaczmański, Ł. Blood Circulating MiRNAs as Cancer Biomarkers for Diagnosis and Surgical Treatment Response. *Front. Genet.* **2019**, *10*. https://doi.org/10.3389/fgene.2019.00169.
(5) Ohan, N. W.; Heikkila, J. J. Reverse Transcription-Polymerase Chain Reaction: An Overview of the Technique and Its Applications. *Biotechnol. Adv.* **1993**, *11* (1), 13–29. https://doi.org/10.1016/0734-9750(93)90408-F.
(6) Tahamtan, A.; Ardebili, A. Real-Time RT-PCR in COVID-19 Detection: Issues Affecting the Results. *Expert Rev. Mol. Diagn.* **2020**, *20* (5), 453–454. https://doi.org/10.1080/14737159.2020.1757437.

(7) Woloshin, S.; Patel, N.; Kesselheim, A. S. False Negative Tests for SARS-CoV-2 Infection - Challenges and Implications. *N. Engl. J. Med.* **2020**, *383* (6), e38. https://doi.org/10.1056/NEJMp2015897.
(8) Mayer, K. M.; Hafner, J. H. Localized Surface Plasmon Resonance Sensors. *Chem. Rev.* **2011**, *111* (6), 3828–3857. https://doi.org/10.1021/cr100313v.
(9) Wu, Y.; Ali, M. R. K.; Chen, K.; Fang, N.; El-Sayed, M. A. Gold Nanoparticles in Biological Optical Imaging. *Nano Today* **2019**, *24*, 120–140. https://doi.org/10.1016/j.nantod.2018.12.006.
(10) Zhou, W.; Gao, X.; Liu, D.; Chen, X. Gold Nanoparticles for In Vitro Diagnostics. *Chem. Rev.* **2015**, *115* (19), 10575–10636. https://doi.org/10.1021/acs.chemrev.5b00100.
(11) Cordeiro, M.; Ferreira Carlos, F.; Pedrosa, P.; Lopez, A.; Baptista, P. Gold Nanoparticles for Diagnostics: Advances towards Points of Care. *Diagnostics* **2016**, *6* (4), 43. https://doi.org/10.3390/diagnostics6040043.
(12) Giannini, V.; Fernández-Domínguez, A. I.; Heck, S. C.; Maier, S. A. Plasmonic Nanoantennas: Fundamentals and Their Use in Controlling the Radiative Properties of Nanoemitters. *Chem. Rev.* **2011**, *111* (6), 3888–3912. https://doi.org/10.1021/cr1002672.
(13) Novotny, L.; van Hulst, N. Antennas for Light. *Nat. Photonics* **2011**, *5* (2), 83–90. https://doi.org/10.1038/nphoton.2010.237.
(14) Biagioni, P.; Huang, J.-S.; Hecht, B. Nanoantennas for Visible and Infrared Radiation. *Rep. Prog. Phys.* **2012**, *75* (2), 024402. https://doi.org/10.1088/0034-4885/75/2/024402.
(15) Bauch, M.; Toma, K.; Toma, M.; Zhang, Q.; Dostalek, J. Plasmon-Enhanced Fluorescence Biosensors: A Review. *Plasmonics* **2014**, *9* (4), 781–799. https://doi.org/10.1007/s11468-013-9660-5.
(16) Jeong, Y.; Kook, Y.-M.; Lee, K.; Koh, W.-G. Metal Enhanced Fluorescence (MEF) for Biosensors: General Approaches and a Review of Recent Developments. *Biosens. Bioelectron.* **2018**, *111*, 102–116. https://doi.org/10.1016/j.bios.2018.04.007.
(17) Fothergill, S. M.; Joyce, C.; Xie, F. Metal Enhanced Fluorescence Biosensing: From Ultra-Violet towards Second Near-Infrared Window. *Nanoscale* **2018**, *10* (45), 20914–20929. https://doi.org/10.1039/C8NR06156D.
(18) Stokes G. G. On the Change of Refrangibility of Light. 101., *Phil. Trans. R. Soc. Lond.* **1852**, 142, 463-562
(19) Drummen, G. Fluorescent Probes and Fluorescence (Microscopy) Techniques — Illuminating Biological and Biomedical Research. *Molecules* **2012**, *17* (12), 14067–14090. https://doi.org/10.3390/molecules171214067.
(20) Marcu, L. Fluorescence Lifetime Techniques in Medical Applications. *Ann. Biomed. Eng.* **2012**, *40* (2), 304–331. https://doi.org/10.1007/s10439-011-0495-y.
(21) Susaki, E. A.; Ueda, H. R. Whole-Body and Whole-Organ Clearing and Imaging Techniques with Single-Cell Resolution: Toward Organism-Level Systems Biology in Mammals. *Cell Chem. Biol.* **2016**, *23* (1), 137–157. https://doi.org/10.1016/j.chembiol.2015.11.009.
(22) Valeur, B.; Berberan-Santos, M. N. Molecular Fluorescence. In *digital Encyclopedia of Applied Physics*; Wiley-VCH Verlag GmbH & Co. KGaA: Weinheim, Germany, 2009; pp 477–531. https://doi.org/10.1002/3527600434.eap684.
(23) Lakowicz, J. R. Principles of Fluorescence Spectroscopy, Third Edition. *J. Biomed. Opt.* **2008**, *13* (2), 029901. https://doi.org/10.1117/1.2904580.
(24) Sauer, L. Review of Clinical Approaches in Fluorescence Lifetime Imaging Ophthalmoscopy. *J. Biomed. Opt.* **2018**, *23* (09), 1. https://doi.org/10.1117/1.JBO.23.9.091415.
(25) Gao, Z.; Hao, Y.; Zheng, M.; Chen, Y. A Fluorescent Dye with Large Stokes Shift and High Stability: Synthesis and Application to Live Cell Imaging. *RSC Adv.* **2017**, *7* (13), 7604–7609. https://doi.org/10.1039/C6RA27547H.
(26) Johansson, M. K.; Fidder, H.; Dick, D.; Cook, R. M. Intramolecular Dimers: A New Strategy to Fluorescence Quenching in Dual-Labeled Oligonucleotide Probes. *J. Am. Chem. Soc.* **2002**, *124* (24), 6950–6956. https://doi.org/10.1021/ja025678o.

(27) Johansson, M. K.; Cook, R. M. Intramolecular Dimers: A New Design Strategy for Fluorescence-Quenched Probes. *Chem. - Eur. J.* **2003**, *9* (15), 3466–3471. https://doi.org/10.1002/chem.200304941.
(28) Marras, S. A. E.; Kramer, F. R.; Tyagi, S. Efficiencies of Fuorescence Resonance Energy Transfer and Contact-Mediated Quenching in Oligonucleotide Probes. *Nucleic Acids Res.* **2002**, *30* (21), 8.
(29) Katherine Johansson, M. Choosing Reporter-Quencher Pairs for Efficient Quenching Through Formation of Intramolecular Dimers. In *Fluorescent Energy Transfer Nucleic Acid Probes*; Humana Press: New Jersey, 2006; Vol. 335, pp 17–30. https://doi.org/10.1385/1-59745-069-3:17.
(30) Marras, S. A. E. Selection of Fluorophore and Quencher Pairs for Fluorescent Nucleic Acid Hybridization Probes. In: Fl*uorescent Energy Transfer Nucleic Acid Probes*; Humana Press: New Jersey, **2006**; Vol. 335, pp 3–16. https://doi.org/10.1385/1-59745-069-3:3.
(31) Arbeloa, I. L. Dimeric and Trimeric States of the Fluorescein Dianion. Part 1.—Molecular Structures. *J Chem Soc Faraday Trans 2* **1981**, *77* (10), 1725–1733. https://doi.org/10.1039/F29817701725.
(32) Khairutdinov, R. F.; Serpone, N. Photophysics of Cyanine Dyes: Subnanosecond Relaxation Dynamics in Monomers, Dimers, and H- and J-Aggregates in Solution. *J. Phys. Chem. B* **1997**, *101* (14), 2602–2610. https://doi.org/10.1021/jp9621134.
(33) Le Reste, L.; Hohlbein, J.; Gryte, K.; Kapanidis, A. N. Characterization of Dark Quencher Chromophores as Nonfluorescent Acceptors for Single-Molecule FRET. *Biophys. J.* **2012**, *102* (11), 2658–2668. https://doi.org/10.1016/j.bpj.2012.04.028.
(34) Holzmeister, P.; Wünsch, B.; Gietl, A.; Tinnefeld, P. Single-Molecule Photophysics of Dark Quenchers as Non-Fluorescent FRET Acceptors. *Photochem Photobiol Sci* **2014**, *13* (6), 853–858. https://doi.org/10.1039/C3PP50274K.
(35) Myochin, T.; Hanaoka, K.; Iwaki, S.; Ueno, T.; Komatsu, T.; Terai, T.; Nagano, T.; Urano, Y. Development of a Series of Near-Infrared Dark Quenchers Based on Si-Rhodamines and Their Application to Fluorescent Probes. *J. Am. Chem. Soc.* **2015**, *137* (14), 4759–4765. https://doi.org/10.1021/jacs.5b00246.
(36) Gust, A.; Zander, A.; Gietl, A.; Holzmeister, P.; Schulz, S.; Lalkens, B.; Tinnefeld, P.; Grohmann, D. A Starting Point for Fluorescence-Based Single-Molecule Measurements in Biomolecular Research. *Molecules* **2014**, *19* (10), 15824–15865. https://doi.org/10.3390/molecules191015824.
(37) Blouin, S.; Craggs, T. D.; Lafontaine, D. A.; Penedo, J. C. Functional Studies of DNA-Protein Interactions Using FRET Techniques. In *DNA-Protein Interactions*; Leblanc, B. P., Rodrigue, S., Eds.; Methods in Molecular Biology; Springer New York: New York, NY, 2015; Vol. 1334, pp 115–141. https://doi.org/10.1007/978-1-4939-2877-4_8.
(38) Hellenkamp, B.; Schmid, S.; Doroshenko, O.; Opanasyuk, O.; Kühnemuth, R.; Rezaei Adariani, S.; Ambrose, B.; Aznauryan, M.; Barth, A.; Birkedal, V.; Bowen, M. E.; Chen, H.; Cordes, T.; Eilert, T.; Fijen, C.; Gebhardt, C.; Götz, M.; Gouridis, G.; Gratton, E.; Ha, T.; Hao, P.; Hanke, C. A.; Hartmann, A.; Hendrix, J.; Hildebrandt, L. L.; Hirschfeld, V.; Hohlbein, J.; Hua, B.; Hübner, C. G.; Kallis, E.; Kapanidis, A. N.; Kim, J.-Y.; Krainer, G.; Lamb, D. C.; Lee, N. K.; Lemke, E. A.; Levesque, B.; Levitus, M.; McCann, J. J.; Naredi-Rainer, N.; Nettels, D.; Ngo, T.; Qiu, R.; Robb, N. C.; Röcker, C.; Sanabria, H.; Schlierf, M.; Schröder, T.; Schuler, B.; Seidel, H.; Streit, L.; Thurn, J.; Tinnefeld, P.; Tyagi, S.; Vandenberk, N.; Vera, A. M.; Weninger, K. R.; Wünsch, B.; Yanez-Orozco, I. S.; Michaelis, J.; Seidel, C. A. M.; Craggs, T. D.; Hugel, T. Precision and Accuracy of Single-Molecule FRET Measurements—a Multi-Laboratory Benchmark Study. *Nat. Methods* **2018**, *15* (9), 669–676. https://doi.org/10.1038/s41592-018-0085-0.
(39) Lerner, E.; Cordes, T.; Ingargiola, A.; Alhadid, Y.; Chung, S.; Michalet, X.; Weiss, S. Toward Dynamic Structural Biology: Two Decades of Single-Molecule Förster Resonance Energy

Transfer. *Science* **2018**, *359* (6373), eaan1133. https://doi.org/10.1126/science.aan1133.
(40) *Cell Biological Applications of Confocal Microscopy*, 2. ed.; Matsumoto, B., Ed.; Methods in cell biology; Acad. Press: Amsterdam, 2002.
(41) Wiley Encyclopedia of Biomedical Engineering, 6-Volume Set by Metin Akay, John Wiley & Sons, Inc., 2006.
(42) Sung, M.-H.; McNally, J. G. Live Cell Imaging and Systems Biology: Live Cell Imaging and Systems Biology. *Wiley Interdiscip. Rev. Syst. Biol. Med.* **2011**, *3* (2), 167–182. https://doi.org/10.1002/wsbm.108.
(43) Breusegem, S. Y.; Levi, M.; Barry, N. P. Fluorescence Correlation Spectroscopy and Fluorescence Lifetime Imaging Microscopy. *Nephron Exp. Nephrol.* **2006**, *103* (2), e41–e49. https://doi.org/10.1159/000090615.
(44) Cremazy, F.; Manders, E.; Bastiaens, P.; Kramer, G.; Hager, G.; Vanmunster, E.; Verschure, P.; Gadellajr, T.; Vandriel, R. Imaging in Situ Protein–DNA Interactions in the Cell Nucleus Using FRET–FLIM. *Exp. Cell Res.* **2005**, *309* (2), 390–396. https://doi.org/10.1016/j.yexcr.2005.06.007.
(45) Morton, P. E.; Parsons, M. Measuring FRET Using Time-Resolved FLIM. In *Cell Migration*; Wells, C. M., Parsons, M., Eds.; Methods in Molecular Biology; Humana Press: Totowa, NJ, 2011; Vol. 769, pp 403–413. https://doi.org/10.1007/978-1-61779-207-6_27.
(46) Orrit, M.; Bernard, J. Single Pentacene Molecules Detected by Fluorescence Excitation in a *p*-Terphenyl Crystal. *Phys. Rev. Lett.* **1990**, *65* (21), 2716–2719. https://doi.org/10.1103/PhysRevLett.65.2716.
(47) Shashkova, S.; Leake, M. C. Single-Molecule Fluorescence Microscopy Review: Shedding New Light on Old Problems. *Biosci. Rep.* **2017**, *37* (4), BSR20170031. https://doi.org/10.1042/BSR20170031.
(48) *Single Molecule Detection in Solution: Methods and Applications*, 1st ed.; Zander, C., Enderlein, J., Keller, R. A., Eds.; Wiley-VCH: Berlin, 2002.
(49) Moerner, W. E.; Shechtman, Y.; Wang, Q. Single-Molecule Spectroscopy and Imaging over the Decades. *Faraday Discuss.* **2015**, *184*, 9–36. https://doi.org/10.1039/C5FD00149H.
(50) Ortega, A.; García de la Torre, J. Hydrodynamic Properties of Rodlike and Disklike Particles in Dilute Solution. *J. Chem. Phys.* **2003**, *119* (18), 9914–9919. https://doi.org/10.1063/1.1615967.
(51) Dominguez-Medina, S.; Chen, S.; Blankenburg, J.; Swanglap, P.; Landes, C. F.; Link, S. Measuring the Hydrodynamic Size of Nanoparticles Using Fluctuation Correlation Spectroscopy. *Annu. Rev. Phys. Chem.* **2016**, *67* (1), 489–514. https://doi.org/10.1146/annurev-physchem-040214-121510.
(52) Schuster, J.; Brabandt, J.; von Borczyskowski, C. Discrimination of Photoblinking and Photobleaching on the Single Molecule Level. *J. Lumin.* **2007**, *127* (1), 224–229. https://doi.org/10.1016/j.jlumin.2007.02.028.
(53) Enderlein, J.; Gregor, I.; Patra, D.; Dertinger, T.; Kaupp, U. B. Performance of Fluorescence Correlation Spectroscopy for Measuring Diffusion and Concentration. *ChemPhysChem* **2005**, *6* (11), 2324–2336. https://doi.org/10.1002/cphc.200500414.
(54) Rigler, R.; Elson, E. S. *Fluorescence Correlation Spectroscopy: Theory and Applications*; Schäfer, F. P., Toennies, J. P., Zinth, W., Series Eds.; Springer Series in Chemical Physics; Springer Berlin Heidelberg: Berlin, Heidelberg, 2001; Vol. 65. https://doi.org/10.1007/978-3-642-59542-4.
(55) *Fluorescence-Based Biosensors: From Concepts to Applications*, 1. ed.; Morris, M. C., Ed.; Progress in molecular biology and translational science; Elsevier, Acad. Press: Amsterdam, 2013.
(56) Wang, C.; Shi, Y.; Yang, D.-R.; Xia, X.-H. Combining Plasmonics and Electrochemistry at the Nanoscale. *Curr. Opin. Electrochem.* **2018**, *7*, 95–102. https://doi.org/10.1016/j.coelec.2017.11.001.
(57) Anger, P.; Bharadwaj, P.; Novotny, L. Enhancement and Quenching of Single-Molecule Fluorescence. *Phys. Rev. Lett.* **2006**, *96* (11). https://doi.org/10.1103/PhysRevLett.96.113002.
(58) Kühn, S.; Håkanson, U.; Rogobete, L.; Sandoghdar, V. Enhancement of Single-Molecule

Fluorescence Using a Gold Nanoparticle as an Optical Nanoantenna. *Phys. Rev. Lett.* **2006**, *97* (1). https://doi.org/10.1103/PhysRevLett.97.017402.
(59) Bharadwaj, P.; Anger, P.; Novotny, L. Nanoplasmonic Enhancement of Single-Molecule Fluorescence. *Nanotechnology* **2007**, *18* (4), 044017. https://doi.org/10.1088/0957-4484/18/4/044017.
(60) Taminiau, T. H.; Stefani, F. D.; van Hulst, N. F. Single Emitters Coupled to Plasmonic Nano-Antennas: Angular Emission and Collection Efficiency. *New J. Phys.* **2008**, *10* (10), 105005. https://doi.org/10.1088/1367-2630/10/10/105005.
(61) Fort, E.; Grésillon, S. Surface Enhanced Fluorescence. *J. Phys. Appl. Phys.* **2008**, *41* (1), 013001. https://doi.org/10.1088/0022-3727/41/1/013001.
(62) Dostálek, J.; Knoll, W. Biosensors Based on Surface Plasmon-Enhanced Fluorescence Spectroscopy (Review). *Biointerphases* **2008**, *3* (3), FD12–FD22. https://doi.org/10.1116/1.2994688.
(63) Geddes, C. D. Metal-Enhanced Fluorescence. John Wiley & Sons, Inc., Hoboken, New Jersey, 2010.
(64) Darvill, D.; Centeno, A.; Xie, F. Plasmonic Fluorescence Enhancement by Metal Nanostructures: Shaping the Future of Bionanotechnology. *Phys. Chem. Chem. Phys.* **2013**, *15* (38), 15709. https://doi.org/10.1039/c3cp50415h.
(65) Dong, J.; Zhang, Z.; Zheng, H.; Sun, M. Recent Progress on Plasmon-Enhanced Fluorescence. *Nanophotonics* **2015**, *4* (1). https://doi.org/10.1515/nanoph-2015-0028.
(66) Li, J.-F.; Li, C.-Y.; Aroca, R. F. Plasmon-Enhanced Fluorescence Spectroscopy. *Chem. Soc. Rev.* **2017**, *46* (13), 3962–3979. https://doi.org/10.1039/C7CS00169J.
(67) Xin, H.; Namgung, B.; Lee, L. P. Nanoplasmonic Optical Antennas for Life Sciences and Medicine. *Nat. Rev. Mater.* **2018**, *3* (8), 228–243. https://doi.org/10.1038/s41578-018-0033-8.
(68) Khatua, S.; Paulo, P. M. R.; Yuan, H.; Gupta, A.; Zijlstra, P.; Orrit, M. Resonant Plasmonic Enhancement of Single-Molecule Fluorescence by Individual Gold Nanorods. *ACS Nano* **2014**, *8* (5), 4440–4449. https://doi.org/10.1021/nn406434y.
(69) Zhang, T.; Gao, N.; Li, S.; Lang, M. J.; Xu, Q.-H. Single-Particle Spectroscopic Study on Fluorescence Enhancement by Plasmon Coupled Gold Nanorod Dimers Assembled on DNA Origami. *J. Phys. Chem. Lett.* **2015**, *6* (11), 2043–2049. https://doi.org/10.1021/acs.jpclett.5b00747.
(70) Giannini, V.; Sánchez-Gil, J. A. Excitation and Emission Enhancement of Single Molecule Fluorescence through Multiple Surface-Plasmon Resonances on Metal Trimer Nanoantennas. *Opt. Lett.* **2008**, *33* (9), 899. https://doi.org/10.1364/OL.33.000899.
(71) Willets, K. A.; Wilson, A. J.; Sundaresan, V.; Joshi, P. B. Super-Resolution Imaging and Plasmonics. *Chem. Rev.* **2017**, *117* (11), 7538–7582. https://doi.org/10.1021/acs.chemrev.6b00547.
(72) Li, M.; Cushing, S. K.; Wu, N. Plasmon-Enhanced Optical Sensors: A Review. *The Analyst* **2015**, *140* (2), 386–406. https://doi.org/10.1039/C4AN01079E.
(73) Chance, R.R., Prock, A. and Silbey, R., 1978. Molecular Fluorescence and Energy Transfer Near Interfaces. In Advances in Chemical Physics (eds I. Prigogine and S.A. Rice, 2007). https://doi.org/10.1002/9780470142561.ch1
(74) Hanske, C.; Sanz-Ortiz, M. N.; Liz-Marzán, L. M. Silica-Coated Plasmonic Metal Nanoparticles in Action. *Adv. Mater.* **2018**, *30* (27), 1707003. https://doi.org/10.1002/adma.201707003.
(75) Tóth, E.; Ungor, D.; Novák, T.; Ferenc, G.; Bánhelyi, B.; Csapó, E.; Erdélyi, M.; Csete, M. Mapping Fluorescence Enhancement of Plasmonic Nanorod Coupled Dye Molecules. *Nanomaterials* **2020**, *10* (6), 1048. https://doi.org/10.3390/nano10061048.
(76) Bharadwaj, P.; Novotny, L. Spectral Dependence of Single Molecule Fluorescence Enhancement. *Opt. Express* **2007**, *15* (21), 14266. https://doi.org/10.1364/OE.15.014266.
(77) Vukovic, S.; Corni, S.; Mennucci, B. Fluorescence Enhancement of Chromophores Close to

Metal Nanoparticles. Optimal Setup Revealed by the Polarizable Continuum Model. *J. Phys. Chem. C* **2009**, *113* (1), 121–133. https://doi.org/10.1021/jp808116y.
(78) Kühn, S.; Håkanson, U.; Rogobete, L.; Sandoghdar, V. Enhancement of Single-Molecule Fluorescence Using a Gold Nanoparticle as an Optical Nanoantenna. *Phys. Rev. Lett.* **2006**, *97* (1). https://doi.org/10.1103/PhysRevLett.97.017402.
(79) Horimoto, N. N.; Imura, K.; Okamoto, H. Dye Fluorescence Enhancement and Quenching by Gold Nanoparticles: Direct Near-Field Microscopic Observation of Shape Dependence. *Chem. Phys. Lett.* **2008**, *467* (1–3), 105–109. https://doi.org/10.1016/j.cplett.2008.10.067.
(80) Kinkhabwala, A.; Yu, Z.; Fan, S.; Avlasevich, Y.; Müllen, K.; Moerner, W. E. Large Single-Molecule Fluorescence Enhancements Produced by a Bowtie Nanoantenna. *Nat. Photonics* **2009**, *3* (11), 654–657. https://doi.org/10.1038/nphoton.2009.187.
(81) Yuan, H.; Khatua, S.; Zijlstra, P.; Yorulmaz, M.; Orrit, M. Thousand-Fold Enhancement of Single-Molecule Fluorescence Near a Single Gold Nanorod. *Angew. Chem. Int. Ed.* **2013**, *52* (4), 1217–1221. https://doi.org/10.1002/anie.201208125.
(82) Muskens, O. L.; Giannini, V.; Sánchez-Gil, J. A.; Gómez Rivas, J. Strong Enhancement of the Radiative Decay Rate of Emitters by Single Plasmonic Nanoantennas. *Nano Lett.* **2007**, *7* (9), 2871–2875. https://doi.org/10.1021/nl0715847.
(83) Ringler, M.; Schwemer, A.; Wunderlich, M.; Nichtl, A.; Kürzinger, K.; Klar, T. A.; Feldmann, J. Shaping Emission Spectra of Fluorescent Molecules with Single Plasmonic Nanoresonators. *Phys. Rev. Lett.* **2008**, *100* (20). https://doi.org/10.1103/PhysRevLett.100.203002.
(84) Busson, M. P.; Rolly, B.; Stout, B.; Bonod, N.; Bidault, S. Accelerated Single Photon Emission from Dye Molecule-Driven Nanoantennas Assembled on DNA. *Nat. Commun.* **2012**, *3* (1). https://doi.org/10.1038/ncomms1964.
(85) Li, J.; Krasavin, A. V.; Webster, L.; Segovia, P.; Zayats, A. V.; Richards, D. Spectral Variation of Fluorescence Lifetime near Single Metal Nanoparticles. *Sci. Rep.* **2016**, *6* (1). https://doi.org/10.1038/srep21349.
(86) Schedlbauer, J.; Wilhelm, P.; Grabenhorst, L.; Federl, M. E.; Lalkens, B.; Hinderer, F.; Scherf, U.; Höger, S.; Tinnefeld, P.; Bange, S.; Vogelsang, J.; Lupton, J. M. Ultrafast Single-Molecule Fluorescence Measured by Femtosecond Double-Pulse Excitation Photon Antibunching. *Nano Lett.* **2020**, *20* (2), 1074–1079. https://doi.org/10.1021/acs.nanolett.9b04354.
(87) Kosako, T.; Kadoya, Y.; Hofmann, H. F. Directional Control of Light by a Nano-Optical Yagi–Uda Antenna. *Nat. Photonics* **2010**, *4* (5), 312–315. https://doi.org/10.1038/nphoton.2010.34.
(88) Giessen, H.; Lippitz, M. Directing Light Emission from Quantum Dots. *Science* **2010**, *329* (5994), 910–911. https://doi.org/10.1126/science.1194352.
(89) Munechika, K.; Chen, Y.; Tillack, A. F.; Kulkarni, A. P.; Plante, I. J.-L.; Munro, A. M.; Ginger, D. S. Spectral Control of Plasmonic Emission Enhancement from Quantum Dots near Single Silver Nanoprisms. *Nano Lett.* **2010**, *10* (7), 2598–2603. https://doi.org/10.1021/nl101281a.
(90) Jain, P. K.; Ghosh, D.; Baer, R.; Rabani, E.; Alivisatos, A. P. Near-Field Manipulation of Spectroscopic Selection Rules on the Nanoscale. *Proc. Natl. Acad. Sci.* **2012**, *109* (21), 8016–8019. https://doi.org/10.1073/pnas.1121319109.
(91) de Torres, J.; Mivelle, M.; Moparthi, S. B.; Rigneault, H.; Van Hulst, N. F.; García-Parajó, M. F.; Margeat, E.; Wenger, J. Plasmonic Nanoantennas Enable Forbidden Förster Dipole–Dipole Energy Transfer and Enhance the FRET Efficiency. *Nano Lett.* **2016**, *16* (10), 6222–6230. https://doi.org/10.1021/acs.nanolett.6b02470.
(92) Pellegrotti, J. V.; Acuna, G. P.; Puchkova, A.; Holzmeister, P.; Gietl, A.; Lalkens, B.; Stefani, F. D.; Tinnefeld, P. Controlled Reduction of Photobleaching in DNA Origami–Gold Nanoparticle Hybrids. *Nano Lett.* **2014**, *14* (5), 2831–2836. https://doi.org/10.1021/nl500841n.
(93) Ueno, K.; Juodkazis, S.; Shibuya, T.; Yokota, Y.; Mizeikis, V.; Sasaki, K.; Misawa, H.

Nanoparticle Plasmon-Assisted Two-Photon Polymerization Induced by Incoherent Excitation Source. *J. Am. Chem. Soc.* **2008**, *130* (22), 6928–6929. https://doi.org/10.1021/ja801262r.
(94) Warren, S. C.; Thimsen, E. Plasmonic Solar Water Splitting. *Energy Env. Sci* **2012**, *5* (1), 5133–5146. https://doi.org/10.1039/C1EE02875H.
(95) Haran, G.; Chuntonov, L. Artificial Plasmonic Molecules and Their Interaction with Real Molecules. *Chem. Rev.* **2018**, *118* (11), 5539–5580. https://doi.org/10.1021/acs.chemrev.7b00647.
(96) Chinen, A. B.; Guan, C. M.; Ferrer, J. R.; Barnaby, S. N.; Merkel, T. J.; Mirkin, C. A. Nanoparticle Probes for the Detection of Cancer Biomarkers, Cells, and Tissues by Fluorescence. *Chem. Rev.* **2015**, *115* (19), 10530–10574. https://doi.org/10.1021/acs.chemrev.5b00321.
(97) Lucky, S. S.; Soo, K. C.; Zhang, Y. Nanoparticles in Photodynamic Therapy. *Chem. Rev.* **2015**, *115* (4), 1990–2042. https://doi.org/10.1021/cr5004198.
(98) Abadeer, N. S.; Murphy, C. J. Recent Progress in Cancer Thermal Therapy Using Gold Nanoparticles. *J. Phys. Chem. C* **2016**, *120* (9), 4691–4716. https://doi.org/10.1021/acs.jpcc.5b11232.
(99) Yang, X.; Yang, M.; Pang, B.; Vara, M.; Xia, Y. Gold Nanomaterials at Work in Biomedicine. *Chem. Rev.* **2015**, *115* (19), 10410–10488. https://doi.org/10.1021/acs.chemrev.5b00193.
(100) Varna, M.; Xuan, H. V.; Fort, E. Gold Nanoparticles in Cardiovascular Imaging: **2017**, 19.
(101) Dykman, L. A.; Khlebtsov, N. G. *Gold Nanoparticles in Biomedical Applications*; CRC Press, Taylor & Francis Group: Boca Raton London New York, 2018.
(102) Li, N.; Zhao, P.; Astruc, D. Anisotropic Gold Nanoparticles: Synthesis, Properties, Applications, and Toxicity. *Angew. Chem. Int. Ed.* **2014**, *53* (7), 1756–1789. https://doi.org/10.1002/anie.201300441.
(103) Locatelli, E.; Monaco, I.; Comes Franchini, M. Surface Modifications of Gold Nanorods for Applications in Nanomedicine. *RSC Adv.* **2015**, *5* (28), 21681–21699. https://doi.org/10.1039/C4RA16473C.
(104) Sriram, M.; Zong, K.; Vivekchand, S.; Gooding, J. Single Nanoparticle Plasmonic Sensors. *Sensors* **2015**, *15* (10), 25774–25792. https://doi.org/10.3390/s151025774.
(105) Sugawa, K.; Tamura, T.; Tahara, H.; Yamaguchi, D.; Akiyama, T.; Otsuki, J.; Kusaka, Y.; Fukuda, N.; Ushijima, H. Metal-Enhanced Fluorescence Platforms Based on Plasmonic Ordered Copper Arrays: Wavelength Dependence of Quenching and Enhancement Effects. *ACS Nano* **2013**, *7* (11), 9997–10010. https://doi.org/10.1021/nn403925d.
(106) N. K., R.; Gorthi, S. S. Enhancement of the Fluorescence Properties of Double Stranded DNA Templated Copper Nanoparticles. *Mater. Sci. Eng. C* **2019**, *98*, 1034–1042. https://doi.org/10.1016/j.msec.2019.01.042.
(107) Chowdhury, M. H.; Ray, K.; Gray, S. K.; Pond, J.; Lakowicz, J. R. Aluminum Nanoparticles as Substrates for Metal-Enhanced Fluorescence in the Ultraviolet for the Label-Free Detection of Biomolecules. *Anal. Chem.* **2009**, *81* (4), 1397–1403. https://doi.org/10.1021/ac802118s.
(108) Dorh, N.; Sarua, A.; Stokes, J.; Hueting, N. A.; Cryan, M. J. Fluorescent Emission Enhancement by Aluminium Nanoantenna Arrays in the near UV. *J. Opt.* **2016**, *18* (7), 075008. https://doi.org/10.1088/2040-8978/18/7/075008.
(109) Barulin, A.; Claude, J.-B.; Patra, S.; Bonod, N.; Wenger, J. Deep Ultraviolet Plasmonic Enhancement of Single Protein Autofluorescence in Zero-Mode Waveguides. *Nano Lett.* **2019**, *19* (10), 7434–7442. https://doi.org/10.1021/acs.nanolett.9b03137.
(110) Tan, S. J.; Campolongo, M. J.; Luo, D.; Cheng, W. Building Plasmonic Nanostructures with DNA. *Nat. Nanotechnol.* **2011**, *6* (5), 268–276. https://doi.org/10.1038/nnano.2011.49.
(111) Zhang, X.-F.; Liu, Z.-G.; Shen, W.; Gurunathan, S. Silver Nanoparticles: Synthesis, Characterization, Properties, Applications, and Therapeutic Approaches. *Int. J. Mol. Sci.* **2016**, *17* (9), 1534. https://doi.org/10.3390/ijms17091534.
(112) Lee, S.; Jun, B.-H. Silver Nanoparticles: Synthesis and Application for Nanomedicine. *Int. J. Mol. Sci.* **2019**, *20* (4), 865. https://doi.org/10.3390/ijms20040865.
(113) Draine, B. T.; Flatau, P. J. Discrete-Dipole Approximation For Scattering Calculations.

J. Opt. Soc. Am. A **1994**, *11* (4), 1491. https://doi.org/10.1364/JOSAA.11.001491.
(114) Yurkin, M. A.; Hoekstra, A. G. The Discrete-Dipole-Approximation Code ADDA: Capabilities and Known Limitations. *J. Quant. Spectrosc. Radiat. Transf.* **2011**, *112* (13), 2234–2247. https://doi.org/10.1016/j.jqsrt.2011.01.031.
(115) Wu, Y.; Nordlander, P. Finite-Difference Time-Domain Modeling of the Optical Properties of Nanoparticles near Dielectric Substrates. *J. Phys. Chem. C* **2010**, *114* (16), 7302–7307. https://doi.org/10.1021/jp908980d.
(116) Gedney D. S. Introduction to the Finite-Difference Time-Domain (FDTD) Method for Electromagnetics, Morgan & Claypool Publishers, 2011.
(117) Musa, S. M. Computational Finite Element Methods in Nanotechnology, Taylor & Francis Group, LLC, 2013.
(118) Grand, J.; Le Ru, E. C. Practical Implementation of Accurate Finite-Element Calculations for Electromagnetic Scattering by Nanoparticles. *Plasmonics* **2020**, *15* (1), 109–121. https://doi.org/10.1007/s11468-019-01014-8.
(119) Liaw, J.-W. Simulation of Surface Plasmon Resonance of Metallic Nanoparticles by the Boundary-Element Method. *J. Opt. Soc. Am. A* **2006**, *23* (1), 108. https://doi.org/10.1364/JOSAA.23.000108.
(120) Mäkitalo, J.; Suuriniemi, S.; Kauranen, M. Boundary Element Method for Surface Nonlinear Optics of Nanoparticles. *Opt. Express* **2011**, *19* (23), 23386. https://doi.org/10.1364/OE.19.023386.
(121) Chen, H.; Shao, L.; Li, Q.; Wang, J. Gold Nanorods and Their Plasmonic Properties. *Chem Soc Rev* **2013**, *42* (7), 2679–2724. https://doi.org/10.1039/C2CS35367A.
(122) Khatua, S.; Orrit, M. Probing, Sensing, and Fluorescence Enhancement with Single Gold Nanorods. *J. Phys. Chem. Lett.* **2014**, *5* (17), 3000–3006. https://doi.org/10.1021/jz501253j.
(123) Vigderman, L.; Khanal, B. P.; Zubarev, E. R. Functional Gold Nanorods: Synthesis, Self-Assembly, and Sensing Applications. *Adv. Mater.* **2012**, *24* (36), 4811–4841. https://doi.org/10.1002/adma.201201690.
(124) Bardhan, R.; Grady, N. K.; Cole, J. R.; Joshi, A.; Halas, N. J. Fluorescence Enhancement by Au Nanostructures: Nanoshells and Nanorods. *ACS Nano* **2009**, *3* (3), 744–752. https://doi.org/10.1021/nn900001q.
(125) Ming, T.; Zhao, L.; Yang, Z.; Chen, H.; Sun, L.; Wang, J.; Yan, C. Strong Polarization Dependence of Plasmon-Enhanced Fluorescence on Single Gold Nanorods. *Nano Lett.* **2009**, *9* (11), 3896–3903. https://doi.org/10.1021/nl902095q.
(126) Su, H.; Zhong, Y.; Ming, T.; Wang, J.; Wong, K. S. Extraordinary Surface Plasmon Coupled Emission Using Core/Shell Gold Nanorods. *J. Phys. Chem. C* **2012**, *116* (16), 9259–9264. https://doi.org/10.1021/jp211713y.
(127) Abadeer, N. S.; Brennan, M. R.; Wilson, W. L.; Murphy, C. J. Distance and Plasmon Wavelength Dependent Fluorescence of Molecules Bound to Silica-Coated Gold Nanorods. *ACS Nano* **2014**, *8* (8), 8392–8406. https://doi.org/10.1021/nn502887j.
(128) Ming, T.; Zhao, L.; Chen, H.; Woo, K. C.; Wang, J.; Lin, H.-Q. Experimental Evidence of Plasmophores: Plasmon-Directed Polarized Emission from Gold Nanorod–Fluorophore Hybrid Nanostructures. *Nano Lett.* **2011**, *11* (6), 2296–2303. https://doi.org/10.1021/nl200535y.
(129) Zhao, L.; Ming, T.; Chen, H.; Liang, Y.; Wang, J. Plasmon-Induced Modulation of the Emission Spectra of the Fluorescent Molecules near Gold Nanorods. *Nanoscale* **2011**, *3* (9), 3849. https://doi.org/10.1039/c1nr10544b.
(130) Zhao, L.; Ming, T.; Shao, L.; Chen, H.; Wang, J. Plasmon-Controlled Förster Resonance Energy Transfer. *J. Phys. Chem. C* **2012**, *116* (14), 8287–8296. https://doi.org/10.1021/jp300916a.
(131) Jang, B.; Park, J.-Y.; Tung, C.-H.; Kim, I.-H.; Choi, Y. Gold Nanorod−Photosensitizer Complex for Near-Infrared Fluorescence Imaging and Photodynamic/Photothermal Therapy *In Vivo*. *ACS Nano* **2011**, *5* (2), 1086–1094. https://doi.org/10.1021/nn102722z.
(132) Zhang, Y.; Qian, J.; Wang, D.; Wang, Y.; He, S. Multifunctional Gold Nanorods with

Ultrahigh Stability and Tunability for In Vivo Fluorescence Imaging, SERS Detection, and Photodynamic Therapy. *Angew. Chem. Int. Ed.* **2013**, *52* (4), 1148–1151. https://doi.org/10.1002/anie.201207909.
(133) Jia, Q.; Ge, J.; Liu, W.; Liu, S.; Niu, G.; Guo, L.; Zhang, H.; Wang, P. Gold Nanorod@silica-Carbon Dots as Multifunctional Phototheranostics for Fluorescence and Photoacoustic Imaging-Guided Synergistic Photodynamic/Photothermal Therapy. *Nanoscale* **2016**, *8* (26), 13067–13077. https://doi.org/10.1039/C6NR03459D.
(134) Zhang, C.; Cheng, X.; Chen, M.; Sheng, J.; Ren, J.; Jiang, Z.; Cai, J.; Hu, Y. Fluorescence Guided Photothermal/Photodynamic Ablation of Tumours Using PH-Responsive Chlorin E6-Conjugated Gold Nanorods. *Colloids Surf. B Biointerfaces* **2017**, *160*, 345–354. https://doi.org/10.1016/j.colsurfb.2017.09.045.
(135) Huang, Y.; Liu, Q.; Wang, Y.; He, N.; Zhao, R.; Choo, J.; Chen, L. Gold Nanorods Functionalized by a Glutathione Response Near-Infrared Fluorescent Probe as a Promising Nanoplatform for Fluorescence Imaging Guided Precision Therapy. *Nanoscale* **2019**, *11* (25), 12220–12229. https://doi.org/10.1039/C9NR02296A.
(136) Wang, Z.; Zong, S.; Yang, J.; Li, J.; Cui, Y. Dual-Mode Probe Based on Mesoporous Silica Coated Gold Nanorods for Targeting Cancer Cells. *Biosens. Bioelectron.* **2011**, *26* (6), 2883–2889. https://doi.org/10.1016/j.bios.2010.11.032.
(137) Wu, Q.; Chen, L.; Huang, L.; Wang, J.; Liu, J.; Hu, C.; Han, H. Quantum Dots Decorated Gold Nanorod as Fluorescent-Plasmonic Dual-Modal Contrasts Agent for Cancer Imaging. *Biosens. Bioelectron.* **2015**, *74*, 16–23. https://doi.org/10.1016/j.bios.2015.06.010.
(138) Jin, H.; Liu, X.; Gui, R.; Wang, Z. Facile Synthesis of Gold Nanorods/Hydrogels Core/Shell Nanospheres for PH and near-Infrared-Light Induced Release of 5-Fluorouracil and Chemo-Photothermal Therapy. *Colloids Surf. B Biointerfaces* **2015**, *128*, 498–505. https://doi.org/10.1016/j.colsurfb.2015.02.049.
(139) Wang, X.-W.; Gao, W.; Fan, H.; Ding, D.; Lai, X.-F.; Zou, Y.-X.; Chen, L.; Chen, Z.; Tan, W. Simultaneous Tracking of Drug Molecules and Carriers Using Aptamer-Functionalized Fluorescent Superstable Gold Nanorod-Carbon Nanocapsules during Thermo-Chemotherapy. *Nanoscale* **2016**, 8, 7942-7948.
(140) Zeng, J.-Y.; Zhang, M.-K.; Peng, M.-Y.; Gong, D.; Zhang, X.-Z. Porphyrinic Metal-Organic Frameworks Coated Gold Nanorods as a Versatile Nanoplatform for Combined Photodynamic/Photothermal/Chemotherapy of Tumor. *Adv. Funct. Mater.* **2018**, *28* (8), 1705451. https://doi.org/10.1002/adfm.201705451.
(141) Gournaris, E.; Park, W.; Cho, S.; Bentrem, D. J.; Larson, A. C.; Kim, D.-H. Near-Infrared Fluorescent Endoscopic Image-Guided Photothermal Ablation Therapy of Colorectal Cancer Using Dual-Modal Gold Nanorods Targeting Tumor-Infiltrating Innate Immune Cells in a Transgenic *TS4 CRE/APC*$^{lox\_1468}$ Mouse Model. *ACS Appl. Mater. Interfaces* **2019**, *11* (24), 21353–21359. https://doi.org/10.1021/acsami.9b04186.
(142) Huang, X.; Tian, X.-J.; Yang, W.; Ehrenberg, B.; Chen, J.-Y. The Conjugates of Gold Nanorods and Chlorin E6 for Enhancing the Fluorescence Detection and Photodynamic Therapy of Cancers. *Phys. Chem. Chem. Phys.* **2013**, *15* (38), 15727. https://doi.org/10.1039/c3cp44227f.
(143) Ke, X.; Wang, D.; Chen, C.; Yang, A.; Han, Y.; Ren, L.; Li, D.; Wang, H. Co-Enhancement of Fluorescence and Singlet Oxygen Generation by Silica-Coated Gold Nanorods Core-Shell Nanoparticle. *Nanoscale Res. Lett.* **2014**, *9* (1), 666. https://doi.org/10.1186/1556-276X-9-666.
(144) Zhao, T.; Yu, K.; Li, L.; Zhang, T.; Guan, Z.; Gao, N.; Yuan, P.; Li, S.; Yao, S. Q.; Xu, Q.-H.; Xu, G. Q. Gold Nanorod Enhanced Two-Photon Excitation Fluorescence of Photosensitizers for Two-Photon Imaging and Photodynamic Therapy. *ACS Appl. Mater. Interfaces* **2014**, *6* (4), 2700–2708. https://doi.org/10.1021/am405214w.
(145) Gui, C.; Cui, D. Functionalized Gold Nanorods for Tumor Imaging and Targeted Therapy. *Cancer Biol. Med.* **2012**, *9* (4), 13.

(146) Choi, W. I.; Sahu, A.; Kim, Y. H.; Tae, G. Photothermal Cancer Therapy and Imaging Based on Gold Nanorods. *Ann. Biomed. Eng.* **2012**, *40* (2), 534–546. https://doi.org/10.1007/s10439-011-0388-0.
(147) Knights, O.; McLaughlan, J. Gold Nanorods for Light-Based Lung Cancer Theranostics. *Int. J. Mol. Sci.* **2018**, *19* (11), 3318. https://doi.org/10.3390/ijms19113318.
(148) Wang, L.; Song, Q.; Liu, Q.; He, D.; Ouyang, J. Plasmon-Enhanced Fluorescence-Based Core-Shell Gold Nanorods as a Near-IR Fluorescent Turn-On Sensor for the Highly Sensitive Detection of Pyrophosphate in Aqueous Solution. *Adv. Funct. Mater.* **2015**, *25* (45), 7017–7027. https://doi.org/10.1002/adfm.201503326.
(149) Wu, X.; Gao, F.; Xu, L.; Kuang, H.; Wang, L.; Xu, C. A Fluorescence Active Gold Nanorod–Quantum Dot Core–Satellite Nanostructure for Sub-Attomolar Tumor Marker Biosensing. *RSC Adv.* **2015**, *5* (118), 97898–97902. https://doi.org/10.1039/C5RA19628K.
(150) Chen, H.; Yuan, F.; Wang, S.; Xu, J.; Zhang, Y.; Wang, L. Aptamer-Based Sensing for Thrombin in Red Region via Fluorescence Resonant Energy Transfer between NaYF4:Yb,Er Upconversion Nanoparticles and Gold Nanorods. *Biosens. Bioelectron.* **2013**, *48*, 19–25. https://doi.org/10.1016/j.bios.2013.03.083.
(151) Qin, L.; He, X.; Chen, L.; Zhang, Y. Turn-on Fluorescent Sensing of Glutathione *S*-Transferase at near-Infrared Region Based on FRET between Gold Nanoclusters and Gold Nanorods. *ACS Appl. Mater. Interfaces* **2015**, *7* (10), 5965–5971. https://doi.org/10.1021/acsami.5b00269.
(152) Yuan, H.; Khatua, S.; Zijlstra, P.; Yorulmaz, M.; Orrit, M. Thousand-Fold Enhancement of Single-Molecule Fluorescence Near a Single Gold Nanorod. *Angew. Chem. Int. Ed.* **2013**, *52* (4), 1217–1221. https://doi.org/10.1002/anie.201208125.
(153) Wientjes, E.; Renger, J.; Cogdell, R.; van Hulst, N. F. Pushing the Photon Limit: Nanoantennas Increase Maximal Photon Stream and Total Photon Number. *J. Phys. Chem. Lett.* **2016**, *7* (9), 1604–1609. https://doi.org/10.1021/acs.jpclett.6b00491.
(154) Zhang, W.; Caldarola, M.; Lu, X.; Pradhan, B.; Orrit, M. Single-Molecule Fluorescence Enhancement of a near-Infrared Dye by Gold Nanorods Using DNA Transient Binding. *Phys. Chem. Chem. Phys.* **2018**, *20* (31), 20468–20475. https://doi.org/10.1039/C8CP03114B.
(155) Kar, A.; Thambi, V.; Paital, D.; Khatua, S. *In Situ* Modulation of Gold Nanorod's Surface Charge Drives the Growth of End-to-End Assemblies from Dimers to Large Networks That Enhance Single-Molecule Fluorescence by 10 000-Fold. *Nanoscale Adv.* **2020**, *2* (7), 2688–2692. https://doi.org/10.1039/D0NA00303D.
(156) Punj, D.; Regmi, R.; Devilez, A.; Plauchu, R.; Moparthi, S. B.; Stout, B.; Bonod, N.; Rigneault, H.; Wenger, J. Self-Assembled Nanoparticle Dimer Antennas for Plasmonic-Enhanced Single-Molecule Fluorescence Detection at Micromolar Concentrations. *ACS Photonics* **2015**, *2* (8), 1099–1107. https://doi.org/10.1021/acsphotonics.5b00152.
(157) Acuna, G. P.; Moller, F. M.; Holzmeister, P.; Beater, S.; Lalkens, B.; Tinnefeld, P. Fluorescence Enhancement at Docking Sites of DNA-Directed Self-Assembled Nanoantennas. *Science* **2012**, *338* (6106), 506–510. https://doi.org/10.1126/science.1228638.
(158) Bidault, S.; Devilez, A.; Maillard, V.; Lermusiaux, L.; Guigner, J.-M.; Bonod, N.; Wenger, J. Picosecond Lifetimes with High Quantum Yields from Single-Photon-Emitting Colloidal Nanostructures at Room Temperature. *ACS Nano* **2016**, *10* (4), 4806–4815. https://doi.org/10.1021/acsnano.6b01729.
(159) Punj, D.; Mivelle, M.; Moparthi, S. B.; van Zanten, T. S.; Rigneault, H.; van Hulst, N. F.; García-Parajó, M. F.; Wenger, J. A Plasmonic 'Antenna-in-Box' Platform for Enhanced Single-Molecule Analysis at Micromolar Concentrations. *Nat. Nanotechnol.* **2013**, *8* (7), 512–516. https://doi.org/10.1038/nnano.2013.98.
(160) Puchkova, A.; Vietz, C.; Pibiri, E.; Wünsch, B.; Sanz Paz, M.; Acuna, G. P.; Tinnefeld, P. DNA Origami Nanoantennas with over 5000-Fold Fluorescence Enhancement and Single-Molecule Detection at 25 μM. *Nano Lett.* **2015**, *15* (12), 8354–8359.

https://doi.org/10.1021/acs.nanolett.5b04045.
(161) Flauraud, V.; Regmi, R.; Winkler, P. M.; Alexander, D. T. L.; Rigneault, H.; van Hulst, N. F.; García-Parajo, M. F.; Wenger, J.; Brugger, J. In-Plane Plasmonic Antenna Arrays with Surface Nanogaps for Giant Fluorescence Enhancement. *Nano Lett.* **2017**, *17* (3), 1703–1710. https://doi.org/10.1021/acs.nanolett.6b04978.
(162) Teixeira, R.; Paulo, P. M. R.; Costa, S. M. B. Gold Nanoparticles in Core–Polyelectrolyte–Shell Assemblies Promote Large Enhancements of Phthalocyanine Fluorescence. *J. Phys. Chem. C* **2015**, *119* (37), 21612–21619. https://doi.org/10.1021/acs.jpcc.5b04667.
(163) Francisco, A. P.; Botequim, D.; Prazeres, D. M. F.; Serra, V. V.; Costa, S. M. B.; Laia, C. A. T.; Paulo, P. M. R. Extreme Enhancement of Single-Molecule Fluorescence from Porphyrins Induced by Gold Nanodimer Antennas. *J. Phys. Chem. Lett.* **2019**, *10* (7), 1542–1549. https://doi.org/10.1021/acs.jpclett.9b00373.
(164) Nordlander, P.; Oubre, C.; Prodan, E.; Li, K.; Stockman, M. I. Plasmon Hybridization in Nanoparticle Dimers. *Nano Lett.* **2004**, *4* (5), 899–903. https://doi.org/10.1021/nl049681c.
(165) Zohar, N.; Chuntonov, L.; Haran, G. The Simplest Plasmonic Molecules: Metal Nanoparticle Dimers and Trimers. *J. Photochem. Photobiol. C Photochem. Rev.* **2014**, *21*, 26–39. https://doi.org/10.1016/j.jphotochemrev.2014.10.002.
(166) Sagle, L. B.; Ruvuna, L. K.; Ruemmele, J. A.; Van Duyne, R. P. Advances in Localized Surface Plasmon Resonance Spectroscopy Biosensing. *Nanomed.* **2011**, *6* (8), 1447–1462. https://doi.org/10.2217/nnm.11.117.
(167) Fong, K. E.; Yung, L.-Y. L. Localized Surface Plasmon Resonance: A Unique Property of Plasmonic Nanoparticles for Nucleic Acid Detection. *Nanoscale* **2013**, *5* (24), 12043. https://doi.org/10.1039/c3nr02257a.
(168) Masson, J.-F. Surface Plasmon Resonance Clinical Biosensors for Medical Diagnostics. *ACS Sens.* **2017**, *2* (1), 16–30. https://doi.org/10.1021/acssensors.6b00763.
(169) Soler, M.; Huertas, C. S.; Lechuga, L. M. Label-Free Plasmonic Biosensors for Point-of-Care Diagnostics: A Review. *Expert Rev. Mol. Diagn.* **2019**, *19* (1), 71–81. https://doi.org/10.1080/14737159.2019.1554435.
(170) Thévenot, D. R.; Toth, K.; Durst, R. A.; Wilson, G. S. Electrochemical biosensors: recommended definitions and classification. *Anal. Lett.* **2001**, *34* (5), 635–659. https://doi.org/10.1081/AL-100103209.
(171) *Encyclopedia of Microfluidics and Nanofluidics: With 152 Tables*; Li, D., Ed.; Springer reference; Springer: New York, NY, 2008.
(172) Chandrasekaran, A. R.; Punnoose, J. A.; Zhou, L.; Dey, P.; Dey, B. K.; Halvorsen, K. DNA Nanotechnology Approaches for MicroRNA Detection and Diagnosis. *Nucleic Acids Res.* **2019**, *47* (20), 10489–10505. https://doi.org/10.1093/nar/gkz580.
(173) Wang, L.; Deng, R.; Li, J. Target-Fueled DNA Walker for Highly Selective MiRNA Detection. *Chem. Sci.* **2015**, *6* (12), 6777–6782. https://doi.org/10.1039/C5SC02784E.
(174) Zheng, J.; Yang, R.; Shi, M.; Wu, C.; Fang, X.; Li, Y.; Li, J.; Tan, W. Rationally Designed Molecular Beacons for Bioanalytical and Biomedical Applications. *Chem. Soc. Rev.* **2015**, *44* (10), 3036–3055. https://doi.org/10.1039/C5CS00020C.
(175) Kricka, L. J.; Fortina, P. Analytical Ancestry: "Firsts" in Fluorescent Labeling of Nucleosides, Nucleotides, and Nucleic Acids. *Clin. Chem.* **2009**, *55* (4), 670–683. https://doi.org/10.1373/clinchem.2008.116152.
(176) Tyagi, S.; Kramer, F. Molecular Beacons: Probes that Fluoresce upon Hybridization. *Nat. Biotechnol.* **1996**, 14, 303–308. https://doi.org/10.1038/nbt0396-303
(177) Heuer-Jungemann, A.; Harimech, P. K.; Brown, T.; Kanaras, A. G. Gold Nanoparticles and Fluorescently-Labelled DNA as a Platform for Biological Sensing. *Nanoscale* **2013**, *5* (20), 9503. https://doi.org/10.1039/c3nr03707j.
(178) Yang, C. J. *Molecular Beacons*; Springer: New York, 2013.

(179) Vietz, C.; Lalkens, B.; Acuna, G. P.; Tinnefeld, P. Synergistic Combination of Unquenching and Plasmonic Fluorescence Enhancement in Fluorogenic Nucleic Acid Hybridization Probes. *Nano Lett.* **2017**, *17* (10), 6496–6500. https://doi.org/10.1021/acs.nanolett.7b03844.
(180) Tyagi, S.; Marras, S. A. E.; Kramer, F. R. Wavelength-Shifting Molecular Beacons. *Nat. Biotechnol.* **2000**, *18* (11), 1191–1196. https://doi.org/10.1038/81192.
(181) Nutiu, R. Tripartite Molecular Beacons. *Nucleic Acids Res.* **2002**, *30* (18), 94e–994. https://doi.org/10.1093/nar/gnf093.
(182) Chen, A. K.; Davydenko, O.; Behlke, M. A.; Tsourkas, A. Ratiometric Bimolecular Beacons for the Sensitive Detection of RNA in Single Living Cells. *Nucleic Acids Res.* **2010**, *38* (14), e148–e148. https://doi.org/10.1093/nar/gkq436.
(183) Zhang, X.; Song, Y.; Shah, A. Y.; Lekova, V.; Raj, A.; Huang, L.; Behlke, M. A.; Tsourkas, A. Quantitative Assessment of Ratiometric Bimolecular Beacons as a Tool for Imaging Single Engineered RNA Transcripts and Measuring Gene Expression in Living Cells. *Nucleic Acids Res.* **2013**, *41* (15), e152–e152. https://doi.org/10.1093/nar/gkt561.
(184) Zhang, X.; Zajac, A. L.; Huang, L.; Behlke, M. A.; Tsourkas, A. Imaging the Directed Transport of Single Engineered RNA Transcripts in Real-Time Using Ratiometric Bimolecular Beacons. *PLoS ONE* **2014**, *9* (1), e85813. https://doi.org/10.1371/journal.pone.0085813.
(185) Fluorescent Nucleic Acid Hybridization Probes. www.Molecular-Beacons.Org/Toto/Marras_fluorescent.html (Accessed: 12 August 2020)
(186) Tsukanov, R.; Tomov, T. E.; Masoud, R.; Drory, H.; Plavner, N.; Liber, M.; Nir, E. Detailed Study of DNA Hairpin Dynamics Using Single-Molecule Fluorescence Assisted by DNA Origami. *J. Phys. Chem. B* **2013**, *117* (40), 11932–11942. https://doi.org/10.1021/jp4059214.
(187) Tsukanov, R.; Tomov, T. E.; Berger, Y.; Liber, M.; Nir, E. Conformational Dynamics of DNA Hairpins at Millisecond Resolution Obtained from Analysis of Single-Molecule FRET Histograms. *J. Phys. Chem. B* **2013**, *117* (50), 16105–16109. https://doi.org/10.1021/jp411280n.
(188) Hartmann, A.; Krainer, G.; Schlierf, M. Different Fluorophore Labeling Strategies and Designs Affect Millisecond Kinetics of DNA Hairpins. *Molecules* **2014**, *19* (9), 13735–13754. https://doi.org/10.3390/molecules190913735.
(189) Wang, H. Label-Free Hybridization Detection of a Single Nucleotide Mismatch by Immobilization of Molecular Beacons on an Agarose Film. *Nucleic Acids Res.* **2002**, *30* (12), 61e–661. https://doi.org/10.1093/nar/gnf061.
(190) Wang, K.; Tang, Z.; Yang, C. J.; Kim, Y.; Fang, X.; Li, W.; Wu, Y.; Medley, C. D.; Cao, Z.; Li, J.; Colon, P.; Lin, H.; Tan, W. Molecular Engineering of DNA: Molecular Beacons. *Angew. Chem. Int. Ed.* **2009**, *48* (5), 856–870. https://doi.org/10.1002/anie.200800370.
(191) Junager, N.; Kongsted, J.; Astakhova, K. Revealing Nucleic Acid Mutations Using Förster Resonance Energy Transfer-Based Probes. *Sensors* **2016**, *16* (8), 1173. https://doi.org/10.3390/s16081173.
(192) Tyagi, S.; Bratu, D.; Kramer, F. Multicolor molecular beacons for allele discrimination. *Nat. Biotechnol.* **1998**, 16, 49–53. https://doi.org/10.1038/nbt0198-49.
(193) Vladimir, D. V. *Fluorescent Energy Transfer Nucleic Acid Probes*; Humana Press: New Jersey, 2006; Vol. 335. https://doi.org/10.1385/1597450693.
(194) Navarro, E.; Serrano-Heras, G.; Castaño, M. J.; Solera, J. Real-Time PCR Detection Chemistry. *Clin. Chim. Acta* **2015**, *439*, 231–250. https://doi.org/10.1016/j.cca.2014.10.017.
(195) Chen, J.; Shi, C.; Kang, X. yue; Shen, X. tong; Lao, X.; Zheng, H. Recent Advances in Fluorescence Resonance Energy Transfer-Based Probes in Nucleic Acid Diagnosis. *Anal Methods* **2020**, *12* (7), 884–893. https://doi.org/10.1039/C9AY02332A.
(196) Lock, L. L.; Cheetham, A. G.; Zhang, P.; Cui, H. Design and Construction of Supramolecular Nanobeacons for Enzyme Detection. *ACS Nano* **2013**, *7* (6), 4924–4932. https://doi.org/10.1021/nn400218a.
(197) Perlette, J.; Tan, W. Real-Time Monitoring of Intracellular mRNA Hybridization Inside

Single Living Cells. *Anal. Chem.* **2001**, *73* (22), 5544–5550. https://doi.org/10.1021/ac010633b.
(198) Bratu, D. P.; Cha, B.-J.; Mhlanga, M. M.; Kramer, F. R.; Tyagi, S. Visualizing the Distribution and Transport of mRNAs in Living Cells. *Proc. Natl. Acad. Sci.* **2003**, *100* (23), 13308–13313. https://doi.org/10.1073/pnas.2233244100.
(199) Santangelo, P. J. Dual FRET Molecular Beacons for mRNA Detection in Living Cells. *Nucleic Acids Res.* **2004**, *32* (6), e57–e57. https://doi.org/10.1093/nar/gnh062.
(200) Ratajczak, K.; Krazinski, B. E.; Kowalczyk, A. E.; Dworakowska, B.; Jakiela, S.; Stobiecka, M. Hairpin–Hairpin Molecular Beacon Interactions for Detection of Survivin mRNA in Malignant SW480 Cells. *ACS Appl. Mater. Interfaces* **2018**, *10* (20), 17028–17039. https://doi.org/10.1021/acsami.8b02342.
(201) Xiang, D.; Zhai, K.; Xiang, W.; Wang, L. Highly Sensitive Fluorescence Quantitative Detection of Specific DNA Sequences with Molecular Beacons and Nucleic Acid Dye SYBR Green I. *Talanta* **2014**, *129*, 249–253. https://doi.org/10.1016/j.talanta.2014.05.040.
(202) Peng, X.-H.; Cao, Z.-H.; Xia, J.-T.; Carlson, G. W.; Lewis, M. M.; Wood, W. C.; Yang, L. Real-Time Detection of Gene Expression in Cancer Cells Using Molecular Beacon Imaging: New Strategies for Cancer Research. *Cancer Res.* **2005**, *65* (5), 1909–1917. https://doi.org/10.1158/0008-5472.CAN-04-3196.
(203) Kang, W. J.; Cho, Y. L.; Chae, J. R.; Lee, J. D.; Choi, K.-J.; Kim, S. Molecular Beacon-Based Bioimaging of Multiple MicroRNAs during Myogenesis. *Biomaterials* **2011**, *32* (7), 1915–1922. https://doi.org/10.1016/j.biomaterials.2010.11.007.
(204) Lee, J. H.; Kim, J. A.; Jeong, S.; Rhee, W. J. Simultaneous and Multiplexed Detection of Exosome MicroRNAs Using Molecular Beacons. *Biosens. Bioelectron.* **2016**, *86*, 202–210. https://doi.org/10.1016/j.bios.2016.06.058.
(205) Lee, J.; Choi, K.-J.; Moon, S. U.; Kim, S. Theragnosis-Based Combined Cancer Therapy Using Doxorubicin-Conjugated MicroRNA-221 Molecular Beacon. *Biomaterials* **2016**, *74*, 109–118. https://doi.org/10.1016/j.biomaterials.2015.09.036.
(206) Du, H.; Disney, M. D.; Miller, B. L.; Krauss, T. D. Hybridization-Based Unquenching of DNA Hairpins on Au Surfaces: Prototypical "Molecular Beacon" Biosensors. *J. Am. Chem. Soc.* **2003**, *125* (14), 4012–4013. https://doi.org/10.1021/ja0290781.
(207) Zhang, X.; Wei, M.; Lv, B.; Liu, Y.; Liu, X.; Wei, W. Sensitive Colorimetric Detection of Glucose and Cholesterol by Using Au@Ag Core–Shell Nanoparticles. *RSC Adv.* **2016**, *6* (41), 35001–35007. https://doi.org/10.1039/C6RA04976A.
(208) Chang, L.; Khan, Y.; Li, L.; Yang, N.; Yin, P.; Guo, L. Colorimetric Detection of HVA by Self-Assembly of Au Nanorods with DNA Double Helices to Give Side-by-Side and End-to-End Structures. *RSC Adv.* **2017**, *7* (23), 13896–13903. https://doi.org/10.1039/C6RA28408F.
(209) McVey, C.; Huang, F.; Elliott, C.; Cao, C. Endonuclease Controlled Aggregation of Gold Nanoparticles for the Ultrasensitive Detection of Pathogenic Bacterial DNA. *Biosens. Bioelectron.* **2017**, *92*, 502–508. https://doi.org/10.1016/j.bios.2016.10.072.
(210) Shawky, S. M.; Awad, A. M.; Allam, W.; Alkordi, M. H.; EL-Khamisy, S. F. Gold Aggregating Gold: A Novel Nanoparticle Biosensor Approach for the Direct Quantification of Hepatitis C Virus RNA in Clinical Samples. *Biosens. Bioelectron.* **2017**, *92*, 349–356. https://doi.org/10.1016/j.bios.2016.11.001.
(211) Piriya V.S, A.; Joseph, P.; Daniel S.C.G., K.; Lakshmanan, S.; Kinoshita, T.; Muthusamy, S. Colorimetric Sensors for Rapid Detection of Various Analytes. *Mater. Sci. Eng. C* **2017**, *78*, 1231–1245. https://doi.org/10.1016/j.msec.2017.05.018.
(212) Xu, L.; Yan, W.; Ma, W.; Kuang, H.; Wu, X.; Liu, L.; Zhao, Y.; Wang, L.; Xu, C. SERS Encoded Silver Pyramids for Attomolar Detection of Multiplexed Disease Biomarkers. *Adv. Mater.* **2015**, *27* (10), 1706–1711. https://doi.org/10.1002/adma.201402244.
(213) Kneipp, J. Interrogating Cells, Tissues, and Live Animals with New Generations of Surface-Enhanced Raman Scattering Probes and Labels. *ACS Nano* **2017**, *11* (2), 1136–1141. https://doi.org/10.1021/acsnano.7b00152.

(214) Laing, S.; Jamieson, L. E.; Faulds, K.; Graham, D. Surface-Enhanced Raman Spectroscopy for in Vivo Biosensing. *Nat. Rev. Chem.* **2017**, *1* (8). https://doi.org/10.1038/s41570-017-0060.
(215) Lenzi, E.; Jimenez de Aberasturi, D.; Liz-Marzán, L. M. Surface-Enhanced Raman Scattering Tags for Three-Dimensional Bioimaging and Biomarker Detection. *ACS Sens.* **2019**. https://doi.org/10.1021/acssensors.9b00321.
(216) Gu, X.; Trujillo, M. J.; Olson, J. E.; Camden, J. P. SERS Sensors: Recent Developments and a Generalized Classification Scheme Based on the Signal Origin. *Annu. Rev. Anal. Chem.* **2018**, *11* (1), 147–169. https://doi.org/10.1146/annurev-anchem-061417-125724.
(217) Plou, J.; García, I.; Charconnet, M.; Astobiza, I.; García-Astrain, C.; Matricardi, C.; Mihi, A.; Carracedo, A.; Liz-Marzán, L. M. Multiplex SERS Detection of Metabolic Alterations in Tumor Extracellular Media. *Adv. Funct. Mater.* **2020**, *30* (17), 1910335. https://doi.org/10.1002/adfm.201910335.
(218) Soares, L.; Csáki, A.; Jatschka, J.; Fritzsche, W.; Flores, O.; Franco, R.; Pereira, E. Localized Surface Plasmon Resonance (LSPR) Biosensing Using Gold Nanotriangles: Detection of DNA Hybridization Events at Room Temperature. *The Analyst* **2014**, *139* (19), 4964–4973. https://doi.org/10.1039/C4AN00810C.
(219) Hammond, J.; Bhalla, N.; Rafiee, S.; Estrela, P. Localized Surface Plasmon Resonance as a Biosensing Platform for Developing Countries. *Biosensors* **2014**, *4* (2), 172–188. https://doi.org/10.3390/bios4020172.
(220) Kaur, B.; Malecka, K.; Cristaldi, D. A.; Chay, C. S.; Mames, I.; Radecka, H.; Radecki, J.; Stulz, E. Approaching Single DNA Molecule Detection with an Ultrasensitive Electrochemical Genosensor Based on Gold Nanoparticles and Cobalt-Porphyrin DNA Conjugates. *Chem. Commun.* **2018**, *54* (79), 11108–11111. https://doi.org/10.1039/C8CC05362F.
(221) Tian, L.; Qian, K.; Qi, J.; Liu, Q.; Yao, C.; Song, W.; Wang, Y. Gold Nanoparticles Superlattices Assembly for Electrochemical Biosensor Detection of MicroRNA-21. *Biosens. Bioelectron.* **2018**, *99*, 564–570. https://doi.org/10.1016/j.bios.2017.08.035.
(222) McArdle, H.; Spain, E.; Keyes, T. E.; Stallings, R. L.; Brennan-Fournet, M.; Forster, R. J. Triangular Silver Nanoplates: Properties and Ultrasensitive Detection of MiRNA. *Electrochem. Commun.* **2017**, *79*, 23–27. https://doi.org/10.1016/j.elecom.2017.04.010.
(223) Chikkaveeraiah, B. V.; Bhirde, A. A.; Morgan, N. Y.; Eden, H. S.; Chen, X. Electrochemical Immunosensors for Detection of Cancer Protein Biomarkers. *ACS Nano* **2012**, *6* (8), 6546–6561. https://doi.org/10.1021/nn3023969.
(224) Liu, L.; Xia, N.; Liu, H.; Kang, X.; Liu, X.; Xue, C.; He, X. Highly Sensitive and Label-Free Electrochemical Detection of MicroRNAs Based on Triple Signal Amplification of Multifunctional Gold Nanoparticles, Enzymes and Redox-Cycling Reaction. *Biosens. Bioelectron.* **2014**, *53*, 399–405. https://doi.org/10.1016/j.bios.2013.10.026.
(225) Huang, H.; Bai, W.; Dong, C.; Guo, R.; Liu, Z. An Ultrasensitive Electrochemical DNA Biosensor Based on Graphene/Au Nanorod/Polythionine for Human Papillomavirus DNA Detection. *Biosens. Bioelectron.* **2015**, *68*, 442–446. https://doi.org/10.1016/j.bios.2015.01.039.
(226) Shahrajabian, M.; Hormozi-Nezhad, M. R. Design a New Strategy Based on Nanoparticle-Enhanced Chemiluminescence Sensor Array for Biothiols Discrimination. *Sci. Rep.* **2016**, *6* (1). https://doi.org/10.1038/srep32160.
(227) Borghei, Y.-S.; Hosseini, M.; Ganjali, M. R.; Ju, H. Colorimetric and Energy Transfer Based Fluorometric Turn-on Method for Determination of MicroRNA Using Silver Nanoclusters and Gold Nanoparticles. *Microchim. Acta* **2018**, *185* (6). https://doi.org/10.1007/s00604-018-2825-3.
(228) Qu, A.; Wu, X.; Xu, L.; Liu, L.; Ma, W.; Kuang, H.; Xu, C. SERS- and Luminescence-Active Au–Au–UCNP Trimers for Attomolar Detection of Two Cancer Biomarkers. *Nanoscale* **2017**, *9* (11), 3865–3872. https://doi.org/10.1039/C6NR09114H.
(229) Babamiri, B.; Salimi, A.; Hallaj, R. Switchable Electrochemiluminescence Aptasensor Coupled with Resonance Energy Transfer for Selective Attomolar Detection of Hg^{2+} via CdTe@CdS/Dendrimer Probe and Au Nanoparticle Quencher. *Biosens. Bioelectron.* **2018**, *102*,

328–335. https://doi.org/10.1016/j.bios.2017.11.034.
(230) Bamrungsap, S.; Treetong, A.; Apiwat, C.; Wuttikhun, T.; Dharakul, T. SERS-Fluorescence Dual Mode Nanotags for Cervical Cancer Detection Using Aptamers Conjugated to Gold-Silver Nanorods. *Microchim. Acta* **2016**, *183* (1), 249–256. https://doi.org/10.1007/s00604-015-1639-9.
(231) Yang, Y.; Zhong, S.; Wang, K.; Huang, J. Gold Nanoparticle Based Fluorescent Oligonucleotide Probes for Imaging and Therapy in Living Systems. *The Analyst* **2019**, *144* (4), 1052–1072. https://doi.org/10.1039/C8AN02070A.
(232) Wang, K.; Huang, J.; Yang, X.; He, X.; Liu, J. Recent Advances in Fluorescent Nucleic Acid Probes for Living Cell Studies. *The Analyst* **2013**, *138* (1), 62–71. https://doi.org/10.1039/C2AN35254K.
(233) Liang, H.; Zhang, X.-B.; Lv, Y.; Gong, L.; Wang, R.; Zhu, X.; Yang, R.; Tan, W. Functional DNA-Containing Nanomaterials: Cellular Applications in Biosensing, Imaging, and Targeted Therapy. *Acc. Chem. Res.* **2014**, *47* (6), 1891–1901. https://doi.org/10.1021/ar500078f.
(234) Xia, Y.; Zhang, R.; Wang, Z.; Tian, J.; Chen, X. Recent Advances in High-Performance Fluorescent and Bioluminescent RNA Imaging Probes. *Chem. Soc. Rev.* **2017**, *46* (10), 2824–2843. https://doi.org/10.1039/C6CS00675B.
(235) He, D.; Wong, K.-W.; Dong, Z.; Li, H.-W. Recent Progress in Live Cell mRNA/microRNA Imaging Probes Based on Smart and Versatile Nanomaterials. *J. Mater. Chem. B* **2018**, *6* (47), 7773–7793. https://doi.org/10.1039/C8TB02285B.
(236) Liu, B.; Liu, J. Methods for Preparing DNA-Functionalized Gold Nanoparticles, a Key Reagent of Bioanalytical Chemistry. *Anal. Methods* **2017**, *9* (18), 2633–2643. https://doi.org/10.1039/C7AY00368D.
(237) Mirkin, C.; Letsinger, R.; Mucic, R.; Storhoff J. A DNA-based method for rationally assembling nanoparticles into macroscopic materials. *Nature* **1996**, 382, 607–609. https://doi.org/10.1038/382607a0.
(238) Alivisatos, A.; Johnsson, K.; Peng, X.; Wilson T.; Loweth C.; Bruchez M.; Schultz P. Organization of 'nanocrystal molecules' using DNA. *Nature* **1996**, 382, 609–611. https://doi.org/10.1038/382609a0.
(239) Seferos, D. S.; Giljohann, D. A.; Hill, H. D.; Prigodich, A. E.; Mirkin, C. A. Nano-Flares: Probes for Transfection and mRNA Detection in Living Cells. *J. Am. Chem. Soc.* **2007**, *129* (50), 15477–15479. https://doi.org/10.1021/ja0776529.
(240) Rosi, N. L. Oligonucleotide-Modified Gold Nanoparticles for Intracellular Gene Regulation. *Science* **2006**, *312* (5776), 1027–1030. https://doi.org/10.1126/science.1125559.
(241) Seferos, D. S.; Prigodich, A. E.; Giljohann, D. A.; Patel, P. C.; Mirkin, C. A. Polyvalent DNA Nanoparticle Conjugates Stabilize Nucleic Acids. *Nano Lett.* **2009**, *9* (1), 308–311. https://doi.org/10.1021/nl802958f.
(242) Choi, C. H. J.; Hao, L.; Narayan, S. P.; Auyeung, E.; Mirkin, C. A. Mechanism for the Endocytosis of Spherical Nucleic Acid Nanoparticle Conjugates. *Proc. Natl. Acad. Sci.* **2013**, *110* (19), 7625–7630. https://doi.org/10.1073/pnas.1305804110.
(243) Wu, X. A.; Choi, C. H. J.; Zhang, C.; Hao, L.; Mirkin, C. A. Intracellular Fate of Spherical Nucleic Acid Nanoparticle Conjugates. *J. Am. Chem. Soc.* **2014**, *136* (21), 7726–7733. https://doi.org/10.1021/ja503010a.
(244) Chenab, K. K.; Eivazzadeh-Keihan, R.; Maleki, A.; Pashazadeh-Panahi, P.; Hamblin, M. R.; Mokhtarzadeh, A. Biomedical Applications of Nanoflares: Targeted Intracellular Fluorescence Probes. *Nanomedicine Nanotechnol. Biol. Med.* **2019**, *17*, 342–358. https://doi.org/10.1016/j.nano.2019.02.006.
(245) Halo, T. L.; McMahon, K. M.; Angeloni, N. L.; Xu, Y.; Wang, W.; Chinen, A. B.; Malin, D.; Strekalova, E.; Cryns, V. L.; Cheng, C.; Mirkin, C. A.; Thaxton, C. S. NanoFlares for the Detection, Isolation, and Culture of Live Tumor Cells from Human Blood. *Proc. Natl. Acad. Sci.* **2014**, *111* (48), 17104–17109. https://doi.org/10.1073/pnas.1418637111.
(246) Yao, J.; Zhang, Z.; Zhao, Y.; Jing, W.; Zuo, G. Double-Stranded Probe Modified AuNPs

for Sensitive and Selective Detection of MicroRNA 30a in Solution and Live Cell. *RSC Adv* **2016**, *6* (45), 38869–38874. https://doi.org/10.1039/C6RA05131F.
(247) Li, J.; Huang, J.; Yang, X.; Yang, Y.; Quan, K.; Xie, N.; Wu, Y.; Ma, C.; Wang, K. Two-Color-Based Nanoflares for Multiplexed MicroRNAs Imaging in Live Cells. *Nanotheranostics* **2018**, *2* (1), 96–105. https://doi.org/10.7150/ntno.22960.
(248) Wu, Q.; Liu, Z.; Su, L.; Han, G.; Liu, R.; Zhao, J.; Zhao, T.; Jiang, C.; Zhang, Z. Sticky-Flares for *in Situ* Monitoring of Human Telomerase RNA in Living Cells. *Nanoscale* **2018**, *10* (19), 9386–9392. https://doi.org/10.1039/C8NR01260A.
(249) Wang, B.; Ren, D.; You, Z.; Yalikun, Y.; Tanaka, Y. Ultrasensitive Detection of Nucleic Acids Based on Dually Enhanced Fluorescence Polarization. *The Analyst* **2018**, *143* (15), 3560–3569. https://doi.org/10.1039/C8AN00952J.
(250) Ning, P.; Wu, Z.; Li, X.; Zhou, Y.; Hu, A.; Gong, X.; He, J.; Xia, Y.; Guo, K.; Zhang, R.; Zhang, X.; Wang, Z. Development of Functionalized Gold Nanoparticles as Nanoflare Probes for Rapid Detection of Classical Swine Fever Virus. *Colloids Surf. B Biointerfaces* **2018**, *171*, 110–114. https://doi.org/10.1016/j.colsurfb.2018.07.024.
(251) Shi, J.; Zhou, M.; Gong, A.; Li, Q.; Wu, Q.; Cheng, G. J.; Yang, M.; Sun, Y. Fluorescence Lifetime Imaging of Nanoflares for mRNA Detection in Living Cells. *Anal. Chem.* **2016**, *88* (4), 1979–1983. https://doi.org/10.1021/acs.analchem.5b03689.
(252) Zhu, D.; Zhao, D.; Huang, J.; Zhu, Y.; Chao, J.; Su, S.; Li, J.; Wang, L.; Shi, J.; Zuo, X.; Weng, L.; Li, Q.; Wang, L. Poly-Adenine-Mediated Fluorescent Spherical Nucleic Acid Probes for Live-Cell Imaging of Endogenous Tumor-Related mRNA. *Nanomedicine Nanotechnol. Biol. Med.* **2018**, *14* (6), 1797–1807. https://doi.org/10.1016/j.nano.2018.05.006.
(253) Yang, Y.; Huang, J.; Yang, X.; Quan, K.; Wang, H.; Ying, L.; Xie, N.; Ou, M.; Wang, K. FRET Nanoflares for Intracellular mRNA Detection: Avoiding False Positive Signals and Minimizing Effects of System Fluctuations. *J. Am. Chem. Soc.* **2015**, *137* (26), 8340–8343. https://doi.org/10.1021/jacs.5b04007.
(254) Vilela, P.; Heuer-Jungemann, A.; El-Sagheer, A.; Brown, T.; Muskens, O. L.; Smyth, N. R.; Kanaras, A. G. Sensing of Vimentin mRNA in 2D and 3D Models of Wounded Skin Using DNA-Coated Gold Nanoparticles. *Small* **2018**, *14* (12), 1703489. https://doi.org/10.1002/smll.201703489.
(255) Yan, R.; Chen, J.; Wang, J.; Rao, J.; Du, X.; Liu, Y.; Zhang, L.; Qiu, L.; Liu, B.; Zhao, Y.; Jiang, P.; Chen, C.; Li, Y. A NanoFlare-Based Strategy for In Situ Tumor Margin Demarcation and Neoadjuvant Gene/Photothermal Therapy. *Small* **2018**, *14* (50), 1802745. https://doi.org/10.1002/smll.201802745.
(256) Wang, B.; Chen, Z.; Ren, D.; You, Z. A Novel Dual Energy Transfer Probe for Intracellular mRNA Detection with High Robustness and Specificity. *Sens. Actuators B Chem.* **2019**, *279*, 342–350. https://doi.org/10.1016/j.snb.2018.10.007.
(257) Prigodich, A. E.; Randeria, P. S.; Briley, W. E.; Kim, N. J.; Daniel, W. L.; Giljohann, D. A.; Mirkin, C. A. Multiplexed Nanoflares: mRNA Detection in Live Cells. *Anal. Chem.* **2012**, *84* (4), 2062–2066. https://doi.org/10.1021/ac202648w.
(258) Kyriazi, M.-E.; Giust, D.; El-Sagheer, A. H.; Lackie, P. M.; Muskens, O. L.; Brown, T.; Kanaras, A. G. Multiplexed mRNA Sensing and Combinatorial-Targeted Drug Delivery Using DNA-Gold Nanoparticle Dimers. *ACS Nano* **2018**, *12* (4), 3333–3340. https://doi.org/10.1021/acsnano.7b08620.
(259) Li, N.; Chang, C.; Pan, W.; Tang, B. A Multicolor Nanoprobe for Detection and Imaging of Tumor-Related mRNAs in Living Cells. *Angew. Chem. Int. Ed.* **2012**, *51* (30), 7426–7430. https://doi.org/10.1002/anie.201203767.
(260) Zheng, D.; Seferos, D. S.; Giljohann, D. A.; Patel, P. C.; Mirkin, C. A. Aptamer Nano-Flares for Molecular Detection in Living Cells. *Nano Lett.* **2009**, *9* (9), 3258–3261. https://doi.org/10.1021/nl901517b.
(261) Chen, L.; Chao, J.; Qu, X.; Zhang, H.; Zhu, D.; Su, S.; Aldalbahi, A.; Wang, L.; Pei, H.

Probing Cellular Molecules with PolyA-Based Engineered Aptamer Nanobeacon. *ACS Appl. Mater. Interfaces* **2017**, *9* (9), 8014–8020. https://doi.org/10.1021/acsami.6b16764.
(262) Chung, C. H.; Kim, J. H.; Jung, J.; Chung, B. H. Nuclease-Resistant DNA Aptamer on Gold Nanoparticles for the Simultaneous Detection of Pb2+ and Hg2+ in Human Serum. *Biosens. Bioelectron.* **2013**, *41*, 827–832. https://doi.org/10.1016/j.bios.2012.10.026.
(263) Yang, Y.; Huang, J.; Yang, X.; Quan, K.; Xie, N.; Ou, M.; Tang, J.; Wang, K. Aptamer-Based FRET Nanoflares for Imaging Potassium Ions in Living Cells. *Chem. Commun.* **2016**, *52* (76), 11386–11389. https://doi.org/10.1039/C6CC05379C.
(264) Yang, X.-J.; Zhang, K.; Zhang, T.-T.; Xu, J.-J.; Chen, H.-Y. Reliable Förster Resonance Energy Transfer Probe Based on Structure-Switching DNA for Ratiometric Sensing of Telomerase in Living Cells. *Anal. Chem.* **2017**, *89* (7), 4216–4222. https://doi.org/10.1021/acs.analchem.7b00267.
(265) Wu, Z.; He, D.; Cui, B. A Fluorometric Assay for Staphylococcal Enterotoxin B by Making Use of Platinum Coated Gold Nanorods and of Upconversion Nanoparticles. *Microchim. Acta* **2018**, *185* (11). https://doi.org/10.1007/s00604-018-3058-1.
(266) Zhang, J.; Wang, L.; Zhang, H.; Boey, F.; Song, S.; Fan, C. Aptamer-Based Multicolor Fluorescent Gold Nanoprobes for Multiplex Detection in Homogeneous Solution. *Small* **2010**, *6* (2), 201–204. https://doi.org/10.1002/smll.200901012.
(267) Wang, J.; Jia, Z. Metal Nanoparticles/Porous Silicon Microcavity Enhanced Surface Plasmon Resonance Fluorescence for the Detection of DNA. *Sensors* **2018**, *18* (2), 661. https://doi.org/10.3390/s18020661.
(268) Li, S.; Xu, L.; Sun, M.; Wu, X.; Liu, L.; Kuang, H.; Xu, C. Hybrid Nanoparticle Pyramids for Intracellular Dual MicroRNAs Biosensing and Bioimaging. *Adv. Mater.* **2017**, *29* (19), 1606086. https://doi.org/10.1002/adma.201606086.
(269) Lu, S.; Wang, S.; Chen, C.; Sun, J.; Yang, X. Enzyme-Free Aptamer/AuNPs-Based Fluorometric and Colorimetric Dual-Mode Detection for ATP. *Sens. Actuators B Chem.* **2018**, *265*, 67–74. https://doi.org/10.1016/j.snb.2018.02.003.
(270) Yu, M.; Yao, Y.; Cui, B.; Sun, C.; Zhao, X.; Wang, Y.; Liu, G.; Cui, H.; Zeng, Z. Metal-Enhanced Near Infrared Fluorescence-Based Sensor with Highly Improved Sensitivity for Adenosine Triphosphate. *ACS Appl. Nano Mater.* **2019**, *2* (1), 48–57. https://doi.org/10.1021/acsanm.8b01583.
(271) Li, C.-H.; Kuo, T.-R.; Su, H.-J.; Lai, W.-Y.; Yang, P.-C.; Chen, J.-S.; Wang, D.-Y.; Wu, Y.-C.; Chen, C.-C. Fluorescence-Guided Probes of Aptamer-Targeted Gold Nanoparticles with Computed Tomography Imaging Accesses for in Vivo Tumor Resection. *Sci. Rep.* **2015**, *5* (1). https://doi.org/10.1038/srep15675.
(272) Li, H.; Wang, M.; Wang, C.; Li, W.; Qiang, W.; Xu, D. Silver Nanoparticle-Enhanced Fluorescence Resonance Energy Transfer Sensor for Human Platelet-Derived Growth Factor-BB Detection. *Anal. Chem.* **2013**, *85* (9), 4492–4499. https://doi.org/10.1021/ac400047d.
(273) Pang, Y.; Rong, Z.; Wang, J.; Xiao, R.; Wang, S. A Fluorescent Aptasensor for H5N1 Influenza Virus Detection Based-on the Core–Shell Nanoparticles Metal-Enhanced Fluorescence (MEF). *Biosens. Bioelectron.* **2015**, *66*, 527–532. https://doi.org/10.1016/j.bios.2014.10.052.
(274) Wu, X.; Gao, F.; Xu, L.; Kuang, H.; Wang, L.; Xu, C. A Fluorescence Active Gold Nanorod–Quantum Dot Core–Satellite Nanostructure for Sub-Attomolar Tumor Marker Biosensing. *RSC Adv.* **2015**, *5* (118), 97898–97902. https://doi.org/10.1039/C5RA19628K.
(275) Deng, Y.-L.; Xu, D.-D.; Pang, D.-W.; Tang, H.-W. Target-Triggered Signal Turn-on Detection of Prostate Specific Antigen Based on Metal-Enhanced Fluorescence of Ag@SiO_2 @SiO_2-RuBpy Composite Nanoparticles. *Nanotechnology* **2017**, *28* (6), 065501. https://doi.org/10.1088/1361-6528/28/6/065501.
(276) Zhang, X.; Liao, N.; Chen, G.; Zheng, A.; Zeng, Y.; Liu, X.; Liu, J. A Fluorescent Turn on Nanoprobe for Simultaneous Visualization of Dual-Targets Involved in Cell Apoptosis and Drug Screening in Living Cells. *Nanoscale* **2017**, *9* (30), 10861–10868.

https://doi.org/10.1039/C7NR03564K.
(277) Huang, J.; Wu, J.; Li, Z. Biosensing Using Hairpin DNA Probes. *Rev. Anal. Chem.* **2015**, *34* (1–2), 1–27. https://doi.org/10.1515/revac-2015-0010.
(278) Peng, H.; Newbigging, A. M.; Wang, Z.; Tao, J.; Deng, W.; Le, X. C.; Zhang, H. DNAzyme-Mediated Assays for Amplified Detection of Nucleic Acids and Proteins. *Anal. Chem.* **2018**, *90* (1), 190–207. https://doi.org/10.1021/acs.analchem.7b04926.
(279) Wu, Y.; Huang, J.; Yang, X.; Yang, Y.; Quan, K.; Xie, N.; Li, J.; Ma, C.; Wang, K. Gold Nanoparticle Loaded Split-DNAzyme Probe for Amplified MiRNA Detection in Living Cells. *Anal. Chem.* **2017**, *89* (16), 8377–8383. https://doi.org/10.1021/acs.analchem.7b01632.
(280) Yang, X.; Tang, Y.; Mason, S. D.; Chen, J.; Li, F. Enzyme-Powered Three-Dimensional DNA Nanomachine for DNA Walking, Payload Release, and Biosensing. *ACS Nano* **2016**, *10* (2), 2324–2330. https://doi.org/10.1021/acsnano.5b07102.
(281) Qu, X.; Zhu, D.; Yao, G.; Su, S.; Chao, J.; Liu, H.; Zuo, X.; Wang, L.; Shi, J.; Wang, L.; Huang, W.; Pei, H.; Fan, C. An Exonuclease III-Powered, On-Particle Stochastic DNA Walker. *Angew. Chem. Int. Ed.* **2017**, *56* (7), 1855–1858. https://doi.org/10.1002/anie.201611777.
(282) Samanta, A.; Banerjee, S.; Liu, Y. DNA Nanotechnology for Nanophotonic Applications. *Nanoscale* **2015**, *7* (6), 2210–2220. https://doi.org/10.1039/C4NR06283C.
(283) Bae, W.; Kocabey, S.; Liedl, T. DNA Nanostructures in Vitro, in Vivo and on Membranes. *Nano Today* **2019**. https://doi.org/10.1016/j.nantod.2019.03.001.
(284) Xu, F.; Dong, H.; Cao, Y.; Lu, H.; Meng, X.; Dai, W.; Zhang, X.; Al-Ghanim, K. A.; Mahboob, S. Ultrasensitive and Multiple Disease-Related MicroRNA Detection Based on Tetrahedral DNA Nanostructures and Duplex-Specific Nuclease-Assisted Signal Amplification. *ACS Appl. Mater. Interfaces* **2016**, *8* (49), 33499–33505. https://doi.org/10.1021/acsami.6b12214.
(285) Hu, J.; Wu, M.; Jiang, L.; Zhong, Z.; Zhou, Z.; Rujiralai, T.; Ma, J. Combining Gold Nanoparticle Antennas with Single-Molecule Fluorescence Resonance Energy Transfer (SmFRET) to Study DNA Hairpin Dynamics. *Nanoscale* **2018**, *10* (14), 6611–6619. https://doi.org/10.1039/C7NR08397A.
(286) Cao, J.; Feng, C.; Liu, Y.; Wang, S.; Liu, F. Highly Sensitive and Rapid Bacteria Detection Using Molecular Beacon–Au Nanoparticles Hybrid Nanoprobes. *Biosens. Bioelectron.* **2014**, *57*, 133–138. https://doi.org/10.1016/j.bios.2014.02.020.
(287) Ochmann, S. E.; Vietz, C.; Trofymchuk, K.; Acuna, G. P.; Lalkens, B.; Tinnefeld, P. Optical Nanoantenna for Single Molecule-Based Detection of Zika Virus Nucleic Acids without Molecular Multiplication. *Anal. Chem.* **2017**, *89* (23), 13000–13007. https://doi.org/10.1021/acs.analchem.7b04082.
(288) Dubertret, B.; Calame, M.; Libchaber, A. J. Single-Mismatch Detection Using Gold-Quenched Fluorescent Oligonucleotides. *Nat. Biotechnol.* **2001**, *19* (4), 365–370. https://doi.org/10.1038/86762.
(289) Maxwell, D. J.; Taylor, J. R.; Nie, S. Self-Assembled Nanoparticle Probes for Recognition and Detection of Biomolecules. *J. Am. Chem. Soc.* **2002**, *124* (32), 9606–9612. https://doi.org/10.1021/ja025814p.
(290) Peng, H.-I.; Strohsahl, C. M.; Leach, K. E.; Krauss, T. D.; Miller, B. L. Label-Free DNA Detection on Nanostructured Ag Surfaces. *ACS Nano* **2009**, *3* (8), 2265–2273. https://doi.org/10.1021/nn900112e.
(291) Uddayasankar, U.; Krull, U. J. Analytical Performance of Molecular Beacons on Surface Immobilized Gold Nanoparticles of Varying Size and Density. *Anal. Chim. Acta* **2013**, *803*, 113–122. https://doi.org/10.1016/j.aca.2013.07.059.
(292) Cheng, Y.; Stakenborg, T.; Van Dorpe, P.; Lagae, L.; Wang, M.; Chen, H.; Borghs, G. Fluorescence Near Gold Nanoparticles for DNA Sensing. *Anal. Chem.* **2011**, *83* (4), 1307–1314. https://doi.org/10.1021/ac102463c.
(293) Beni, V.; Hayes, K.; Lerga, T. M.; O'Sullivan, C. K. Development of a Gold Nano-Particle-Based Fluorescent Molecular Beacon for Detection of Cystic Fibrosis Associated Mutation.

Biosens. Bioelectron. **2010**, *26* (2), 307–313. https://doi.org/10.1016/j.bios.2010.08.043.
(294) Tu, Y.; Wu, P.; Zhang, H.; Cai, C. Fluorescence Quenching of Gold Nanoparticles Integrating with a Conformation-Switched Hairpin Oligonucleotide Probe for MicroRNA Detection. *Chem. Commun.* **2012**, *48* (87), 10718. https://doi.org/10.1039/c2cc35564g.
(295) Qian, R.-C.; Cao, Y.; Long, Y.-T. Binary System for MicroRNA-Targeted Imaging in Single Cells and Photothermal Cancer Therapy. *Anal. Chem.* **2016**, *88* (17), 8640–8647. https://doi.org/10.1021/acs.analchem.6b01804.
(296) Harry, S. R.; Hicks, D. J.; Amiri, K. I.; Wright, D. W. Hairpin DNA Coated Gold Nanoparticles as Intracellular mRNA Probes for the Detection of Tyrosinase Gene Expression in Melanoma Cells. *Chem. Commun.* **2010**, *46* (30), 5557. https://doi.org/10.1039/c001969k.
(297) Jayagopal, A.; Halfpenny, K. C.; Perez, J. W.; Wright, D. W. Hairpin DNA-Functionalized Gold Colloids for the Imaging of mRNA in Live Cells. *J. Am. Chem. Soc.* **2010**, *132* (28), 9789–9796. https://doi.org/10.1021/ja102585v.
(298) Xue, J.; Shan, L.; Chen, H.; Li, Y.; Zhu, H.; Deng, D.; Qian, Z.; Achilefu, S.; Gu, Y. Visual Detection of STAT5B Gene Expression in Living Cell Using the Hairpin DNA Modified Gold Nanoparticle Beacon. *Biosens. Bioelectron.* **2013**, *41*, 71–77. https://doi.org/10.1016/j.bios.2012.06.062.
(299) Deng, D.; Gu, Y.; Li, Y.; Xue, J.; Wang, J.; Ai, G.; Li, X. Gold Nanoparticle-Based Beacon to Detect STAT5b mRNA Expression in Living Cells: A Case Optimized by Bioinformatics Screen. *Int. J. Nanomedicine* **2015**, 3231. https://doi.org/10.2147/IJN.S81754.
(300) Pan, W.; Yang, H.; Li, N.; Yang, L.; Tang, B. Simultaneous Visualization of Multiple mRNAs and Matrix Metalloproteinases in Living Cells Using a Fluorescence Nanoprobe. *Chem. - Eur. J.* **2015**, *21* (16), 6070–6073. https://doi.org/10.1002/chem.201500365.
(301) Pan, W.; Zhang, T.; Yang, H.; Diao, W.; Li, N.; Tang, B. Multiplexed Detection and Imaging of Intracellular mRNAs Using a Four-Color Nanoprobe. *Anal. Chem.* **2013**, *85* (21), 10581–10588. https://doi.org/10.1021/ac402700s.
(302) Rosa, J.; Conde, J.; de la Fuente, J. M.; Lima, J. C.; Baptista, P. V. Gold-Nanobeacons for Real-Time Monitoring of RNA Synthesis. *Biosens. Bioelectron.* **2012**, *36* (1), 161–167. https://doi.org/10.1016/j.bios.2012.04.006.
(303) Conde, J.; Rosa, J.; de la Fuente, J. M.; Baptista, P. V. Gold-Nanobeacons for Simultaneous Gene Specific Silencing and Intracellular Tracking of the Silencing Events. *Biomaterials* **2013**, *34* (10), 2516–2523. https://doi.org/10.1016/j.biomaterials.2012.12.015.
(304) Conde, J.; Larguinho, M.; Cordeiro, A.; Raposo, L. R.; Costa, P. M.; Santos, S.; Diniz, M. S.; Fernandes, A. R.; Baptista, P. V. Gold-Nanobeacons for Gene Therapy: Evaluation of Genotoxicity, Cell Toxicity and Proteome Profiling Analysis. *Nanotoxicology* **2014**, *8* (5), 521–532. https://doi.org/10.3109/17435390.2013.802821.
(305) Bao, C.; Conde, J.; Curtin, J.; Artzi, N.; Tian, F.; Cui, D. Bioresponsive Antisense DNA Gold Nanobeacons as a Hybrid in Vivo Theranostics Platform for the Inhibition of Cancer Cells and Metastasis. *Sci. Rep.* **2015**, *5* (1). https://doi.org/10.1038/srep12297.
(306) Cordeiro, M.; Carvalho, L.; Silva, J.; Saúde, L.; Fernandes, A.; Baptista, P. Gold Nanobeacons for Tracking Gene Silencing in Zebrafish. *Nanomaterials* **2017**, *7* (1), 10. https://doi.org/10.3390/nano7010010.
(307) Wei, G.; Simionesie, D.; Sefcik, J.; Sutter, J. U.; Xue, Q.; Yu, J.; Wang, J.; Birch, D. J. S.; Chen, Y. Revealing the Photophysics of Gold-Nanobeacons via Time-Resolved Fluorescence Spectroscopy. *Opt. Lett.* **2015**, *40* (24), 5738. https://doi.org/10.1364/OL.40.005738.
(308) Liu, J.; Cui, M.; Zhou, H.; Yang, W. DNAzyme Based Nanomachine for *in Situ* Detection of MicroRNA in Living Cells. *ACS Sens.* **2017**, *2* (12), 1847–1853. https://doi.org/10.1021/acssensors.7b00710.
(309) Li, D.; Zhou, W.; Yuan, R.; Xiang, Y. A DNA-Fueled and Catalytic Molecule Machine Lights Up Trace Under-Expressed MicroRNAs in Living Cells. *Anal. Chem.* **2017**, *89* (18), 9934–9940. https://doi.org/10.1021/acs.analchem.7b02247.

(310) Yang, Y.; Huang, J.; Yang, X.; He, X.; Quan, K.; Xie, N.; Ou, M.; Wang, K. Gold Nanoparticle Based Hairpin-Locked-DNAzyme Probe for Amplified MiRNA Imaging in Living Cells. *Anal. Chem.* **2017**, *89* (11), 5850–5856. https://doi.org/10.1021/acs.analchem.7b00174.
(311) Wang, B.; You, Z.; Ren, D. Target-Assisted FRET Signal Amplification for Ultrasensitive Detection of MicroRNA. *The Analyst* **2019**, *144* (7), 2304–2311. https://doi.org/10.1039/C8AN02266F.
(312) Meng, X.; Zhang, K.; Dai, W.; Cao, Y.; Yang, F.; Dong, H.; Zhang, X. Multiplex MicroRNA Imaging in Living Cells Using DNA-Capped-Au Assembled Hydrogels. *Chem. Sci.* **2018**, *9* (37), 7419–7425. https://doi.org/10.1039/C8SC02858C.
(313) Zhao, X.; Xu, L.; Sun, M.; Ma, W.; Wu, X.; Kuang, H.; Wang, L.; Xu, C. Gold-Quantum Dot Core-Satellite Assemblies for Lighting Up MicroRNA In Vitro and In Vivo. *Small* **2016**, *12* (34), 4662–4668. https://doi.org/10.1002/smll.201503629.
(314) Santos, G. M.; Zhao, F.; Zeng, J.; Li, M.; Shih, W.-C. Label-Free, Zeptomole Cancer Biomarker Detection by Surface-Enhanced Fluorescence on Nanoporous Gold Disk Plasmonic Nanoparticles. *J. Biophotonics* **2015**, *8* (10), 855–863. https://doi.org/10.1002/jbio.201400134.
(315) Xu, S.; Jiang, L.; Nie, Y.; Wang, J.; Li, H.; Liu, Y.; Wang, W.; Xu, G.; Luo, X. Gold Nanobipyramids as Dual-Functional Substrates for in Situ "Turn On" Analyzing Intracellular Telomerase Activity Based on Target-Triggered Plasmon-Enhanced Fluorescence. *ACS Appl. Mater. Interfaces* **2018**, *10* (32), 26851–26858. https://doi.org/10.1021/acsami.8b05447.
(316) Niu, C.; Peng, M.; You, Y.; Wang, R.; Jia, Y.; Xie, T.; Wang, J.; Na, N.; Ouyang, J. A Comparative Study of Plasmonic-Enhanced Single-Molecule Fluorescence Induced by Gold Nanoantennas and Its Application for Illuminating Telomerase. *Chem. Commun.* **2017**, *53* (41), 5633–5636. https://doi.org/10.1039/C7CC01330B.
(317) Huang, Y.; Zhao, S.; Liang, H.; Chen, Z.; Liu, Y. Multiplex Detection of Endonucleases by Using a Multicolor Gold Nanobeacon. *Chem. – Eur. J.* **2011**, *17* (26), 7313–7319. https://doi.org/10.1002/chem.201003765.
(318) Dou, X.; Chu, X.; Kong, W.; Luo, J.; Yang, M. A Gold-Based Nanobeacon Probe for Fluorescence Sensing of Organophosphorus Pesticides. *Anal. Chim. Acta* **2015**, *891*, 291–297. https://doi.org/10.1016/j.aca.2015.08.012.
(319) Mei, Z.; Tang, L. Surface-Plasmon-Coupled Fluorescence Enhancement Based on Ordered Gold Nanorod Array Biochip for Ultrasensitive DNA Analysis. *Anal. Chem.* **2017**, *89* (1), 633–639. https://doi.org/10.1021/acs.analchem.6b02797.
(320) Sun, J.; Ji, J.; Sun, Y.; Abdalhai, M. H.; Zhang, Y.; Sun, X. DNA Biosensor-Based on Fluorescence Detection of E. Coli O157:H7 by Au@Ag Nanorods. *Biosens. Bioelectron.* **2015**, *70*, 239–245. https://doi.org/10.1016/j.bios.2015.03.009.
(321) Zhang, Y.; Wei, G.; Yu, J.; Birch, D. J. S.; Chen, Y. Surface Plasmon Enhanced Energy Transfer between Gold Nanorods and Fluorophores: Application to Endocytosis Study and RNA Detection. *Faraday Discuss.* **2015**, *178*, 383–394. https://doi.org/10.1039/C4FD00199K.
(322) Liu, J.; Zhang, L.; Lei, J.; Ju, H. MicroRNA-Responsive Cancer Cell Imaging and Therapy with Functionalized Gold Nanoprobe. *ACS Appl. Mater. Interfaces* **2015**, *7* (34), 19016–19023. https://doi.org/10.1021/acsami.5b06206.
(323) Dai, W.; Dong, H.; Guo, K.; Zhang, X. Near-Infrared Triggered Strand Displacement Amplification for MicroRNA Quantitative Detection in Single Living Cells. *Chem. Sci.* **2018**, *9* (7), 1753–1759. https://doi.org/10.1039/C7SC04243D.
(324) Han, Z.; Chen, L.; Weng, Q.; Zhou, Y.; Wang, L.; Li, C.; Chen, J. Silica-Coated Gold Nanorod@CdSeTe Ternary Quantum Dots Core/Shell Structure for Fluorescence Detection and Dual-Modal Imaging. *Sens. Actuators B Chem.* **2018**, *258*, 508–516. https://doi.org/10.1016/j.snb.2017.11.157.
(325) Wei, G.; Yu, J.; Wang, J.; Gu, P.; Birch, D. J. S.; Chen, Y. Hairpin DNA-Functionalized Gold Nanorods for mRNA Detection in Homogenous Solution. *J. Biomed. Opt.* **2016**, *21* (9), 097001. https://doi.org/10.1117/1.JBO.21.9.097001.

(326) Lio, D. C. S.; Liu, C.; Wiraja, C.; Qiu, B.; Fhu, C. W.; Wang, X.; Xu, C. Molecular Beacon Gold Nanosensors for Leucine-Rich Alpha-2-Glycoprotein-1 Detection in Pathological Angiogenesis. *ACS Sens.* **2018**, *3* (9), 1647–1655. https://doi.org/10.1021/acssensors.8b00321.
(327) Su, F.-X.; Yang, C.-X.; Yan, X.-P. Intracellular Messenger RNA Triggered Catalytic Hairpin Assembly for Fluorescence Imaging Guided Photothermal Therapy. *Anal. Chem.* **2017**, *89* (14), 7277–7281. https://doi.org/10.1021/acs.analchem.7b01348.
(328) Zhu, Z.; Yuan, P.; Li, S.; Garai, M.; Hong, M.; Xu, Q.-H. Plasmon-Enhanced Fluorescence in Coupled Nanostructures and Applications in DNA Detection. *ACS Appl. Bio Mater.* **2018**, *1* (1), 118–124. https://doi.org/10.1021/acsabm.8b00032.
(329) Peng, M.; Sun, F.; Na, N.; Ouyang, J. Target-Triggered Assembly of Nanogap Antennas to Enhance the Fluorescence of Single Molecules and Their Application in MicroRNA Detection. *Small* **2020**, *16* (19), 2000460. https://doi.org/10.1002/smll.202000460.
(330) Singh-Zocchi, M.; Dixit, S.; Ivanov, V.; Zocchi, G. Single-Molecule Detection of DNA Hybridization. *Proc. Natl. Acad. Sci.* **2003**, *100* (13), 7605–7610. https://doi.org/10.1073/pnas.1337215100.
(331) Halpern, A. R.; Wood, J. B.; Wang, Y.; Corn, R. M. Single-Nanoparticle Near-Infrared Surface Plasmon Resonance Microscopy for Real-Time Measurements of DNA Hybridization Adsorption. *ACS Nano* **2014**, *8* (1), 1022–1030. https://doi.org/10.1021/nn405868e.
(332) Baaske, M. D.; Foreman, M. R.; Vollmer, F. Single-Molecule Nucleic Acid Interactions Monitored on a Label-Free Microcavity Biosensor Platform. *Nat. Nanotechnol.* **2014**, *9* (11), 933–939. https://doi.org/10.1038/nnano.2014.180.
(333) Kim, E.; Baaske, M. D.; Vollmer, F. In Situ Observation of Single-Molecule Surface Reactions from Low to High Affinities. *Adv. Mater.* **2016**, *28* (45), 9941–9948. https://doi.org/10.1002/adma.201603153.
(334) Sobek, J.; Rehrauer, H.; Schauer, S.; Fischer, D.; Patrignani, A.; Landgraf, S.; Korlach, J.; Schlapbach, R. Single-Molecule DNA Hybridisation Studied by Using a Modified DNA Sequencer: A Comparison with Surface Plasmon Resonance Data. *Methods Appl. Fluoresc.* **2016**, *4* (1), 015002. https://doi.org/10.1088/2050-6120/4/1/015002.
(335) Gooding, J. J.; Gaus, K. Single-Molecule Sensors: Challenges and Opportunities for Quantitative Analysis. *Angew. Chem. Int. Ed.* **2016**, *55* (38), 11354–11366. https://doi.org/10.1002/anie.201600495.
(336) Lu, X.; Nicovich, P. R.; Gaus, K.; Gooding, J. J. Towards Single Molecule Biosensors Using Super-Resolution Fluorescence Microscopy. *Biosens. Bioelectron.* **2017**, *93*, 1–8. https://doi.org/10.1016/j.bios.2016.10.048.
(337) Taylor, A. B.; Zijlstra, P. Single-Molecule Plasmon Sensing: Current Status and Future Prospects. *ACS Sens.* **2017**, *2* (8), 1103–1122. https://doi.org/10.1021/acssensors.7b00382.
(338) Subramanian, S.; Wu, H.-Y.; Constant, T.; Xavier, J.; Vollmer, F. Label-Free Optical Single-Molecule Micro- and Nanosensors. *Adv. Mater.* **2018**, *30* (51), 1801246. https://doi.org/10.1002/adma.201801246.
(339) Farka, Z.; Mickert, M. J.; Pastucha, M.; Mikušová, Z.; Skládal, P.; Gorris, H. H. Advances in Optical Single-Molecule Detection: En Route to Supersensitive Bioaffinity Assays. *Angew. Chem. Int. Ed.* **2020**, *59* (27), 10746–10773. https://doi.org/10.1002/anie.201913924.
(340) Yan, J.; van Smeden, L.; Merkx, M.; Zijlstra, P.; Prins, M. W. J. Continuous Small-Molecule Monitoring with a Digital Single-Particle Switch. *ACS Sens.* **2020**, *5* (4), 1168–1176. https://doi.org/10.1021/acssensors.0c00220.

Chapter 2

Objectives and Framework of the Research Plan

2. Objectives and framework of the research plan

Biosensors are essential tools for medicine, in clinical diagnostics and therapeutics, by providing detection of disease biomarkers. Indeed, the demand for rapid diagnostic tests towards much-needed point-of-care (POC) tools may benefit the global population by delivering innovative healthcare solutions. In this context, the main objective of this doctoral thesis is the development of fluorescence-based biosensors with high sensitivity in order to push the detection limit of nucleic acids, proposed as model disease biomarkers, in a standalone type of assay. The fluorescence signalling was based on artificial DNA hairpin probes known as molecular beacons (described in Chapter 1). The sensitivity of these probes is often limited by the intensity contrast between the "off"/dark state and the "on"/bright state. To attain increased sensitivity of molecular beacons, an innovative approach was pursued in this thesis by coupling the beacons to gold nanorods, as depicted in Figure 2.1. The latter can perform as optical antennas and enhance fluorescence signals from the beacon's bright state.

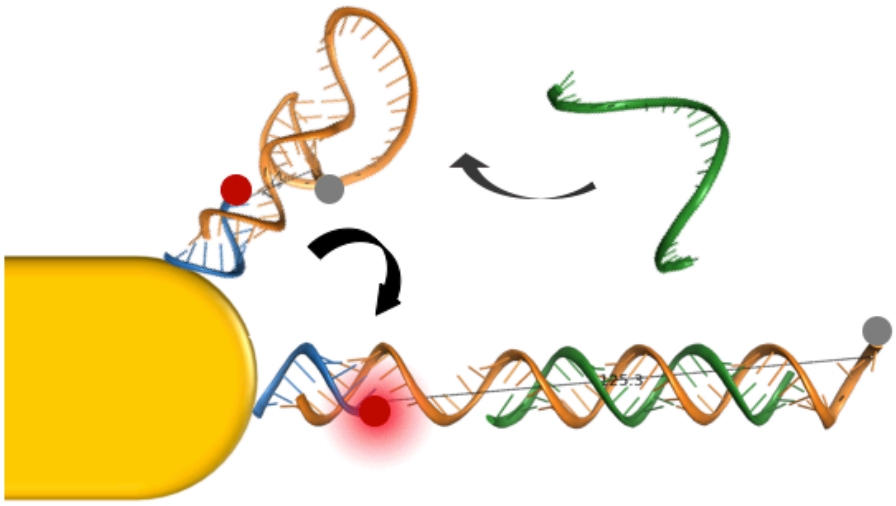

Figure 2.1 - Scheme (not-to-scale) of the nanohybrid biosensors proposed for fluorescent detection of nucleic acids. Molecular beacon probes are conjugated onto a gold nanorod, being on a dark state due to efficient energy transfer between a fluorophore label (donor - red dot) and a quencher (acceptor - grey dot). Upon nucleic acid molecular recognition, molecular beacons undergo a conformational change that increases the distance between the fluorophore and the quencher, thus displaying a bright state (weak energy transfer) with fluorescence signalling that is enhanced by the plasmonic nanorod antenna.

The proposed biosensing platform was envisioned to provide miniaturization, label-free, and real-time detection, holding potential as a fluorescence signalling tool with improved biosensing responses in nucleic acid detection, such as increased sensitivity and specificity. The strategy of increasing sensitivity in a label-free biosensing assay was aimed at dismissing pre-amplification or multi-labeling steps, therefore it is supposed that it can fulfill the current high interest around fast, simpler and reliable alternatives to standard laboratory methods.

The design and characterization of the proposed nanohybrid biosensors was the focus of the research activities in this doctoral thesis, not only because the demonstration of the concept

would add up to other significant advancements in the field of fluorescence-based biosensors, but also because the performance of optical antennas is of general interest for the plasmonics and nanophotonics communities. In this view, the research developed throughout this thesis is framed by four major objectives that are detailed in sections 2.1 to 2.4. The final section of this chapter (§ 2.5) contains a general characterization of the diseases for which target biomarkers were selected for the studies developed in this thesis.

2.1. Enhanced fluorescence of red-emitting dyes by gold nanoantennas

The first objective of this thesis addresses the fluorescence enhancement of organic dyes by using gold nanostructures as optical antennas - Chapter 3. Two types of nanostructures were investigated: a single gold nanorod and a dimer of spherical particles. Both types of structures can provide strong plasmon near-field enhancements upon excitation in the red spectral range and, thus, are able to induce large fluorescence enhancement effects from coupled emitters. The fluorescent dyes chosen for these studies had to present a good spectral overlap for light absorption and emission with the particle's surface plasmon resonance. Again, two examples were tested: Atto-647N and Atto-655 dye. The key objective of these studies was to characterize the range of signal enhancement that could be later explored for sensing purposes. In this view, the experimental design was set to probe the largest enhancement effects in the systems studied by conducting a single-molecule on single-particle type of experiment. The particle is immobilized on a glass substrate and positioned at the centre of the confocal detection volume, while the dye molecule is freely diffusing in solution and, thus, it can probe the entire volume surrounding the particle and eventually interact with the plasmon hot-spots. The evaluation of single-molecule fluorescence events provided an in-depth characterization of the enhancement effect that is free from concentration artefacts. Such information is crucial for the design of fluorescence-based sensors with plasmon-enhanced signalling responses.

2.2. Plasmon-assisted photochemical functionalization of gold nanorods

The interactions between surface plasmons of metal particles and photoactive molecules depend crucially on their relative positions. In order to maximize such interactions, it is desirable to control the surface attachment of organic molecules onto metal particles by directing the former to plasmon hot-spots where the largest near-field enhancements occur. An innovative plasmon-driven photochemical procedure was pursued here to selectively attach molecular components at the tips of gold nanorods - Chapter 4. To demonstrate this strategy, a biotin-derivatized with a photo-crosslinking group was selected for attachment onto surface-immobilized gold nanorods. The photochemical reaction is induced by two-photon absorption using the large near-field enhancement at the nanorods' hot-spots upon light excitation of the longitudinal plasmon. The phenyl azide group is photo-activated to a nitrene that inserts into an organic monolayer coating the gold nanorods. As a result, the gold nanorods

become functionalized with biotin receptors. The functionalization procedure can be tested by monitoring the surface plasmon shift of the gold nanorods upon streptavidin binding, as a model plasmonic sensor for detection of streptavidin protein. This takes advantage of two aspects: the strong affinity of the biotin-streptavidin pair and the localized surface plasmon resonance (LSPR) sensitivity of the gold nanorods to the local refraction index changes that occur upon streptavidin binding. This strategy was devised to be later employed for tip-functionalization of nanorods with molecular beacon probes, in order to maximize the desired fluorescence signalling from the nanobiosensors. The limited success of the plasmon-assisted photochemical functionalization has prompted for a strategy change toward tip-specific attachment of photoactive molecules, as explained next.

2.3. Tip-selective functionalization of gold nanorods with dye-labeled DNAs

Tip-specific functionalization of colloidal gold nanorods has been described in the literature using cetyltrimethylammonium bromide (CTAB) surfactant as a side protective agent. However, it was necessary to demonstrate that this strategy could be employed to maximize plasmon-enhanced fluorescence, which is the main objective of this thesis. For this purpose, the functionalization of gold nanorods with DNA hybrids labeled with Atto-647N dye was optimized comparing two strategies: one directed to the tips, that occurs in the presence of CTAB surfactant protective coatings, and a non-selective one involving ligand-exchange reactions, that results in indiscriminate coverage of the metal particle - Chapter 5. Dye-particle nano-assemblies formed by tip-specific functionalization, which focuses the dye molecules at the rods' hot-spots, afforded fluorescence enhancements of about one order of magnitude in dye's emission, as characterized by ensemble fluorescence spectroscopy. On the contrary, non-selective functionalization produced nano-assemblies without emission enhancement, or even with a minor quenching effect, possibly due to self-quenching of densely packed neighboring dye molecules. Therefore, the loading of dye-labeled oligonucleotides onto the tips of colloidal gold nanorods effectively leads to fluorescence enhancements, which represents a major accomplishment of this work. The replication of this strategy for the attachment of molecular beacon probes onto gold nanorods was explored in the next objective, in order to develop a nanobiosensor with enhanced fluorescence signalling responses.

2.4. Fluorescence signalling of DNA probes functionalized onto gold nanorods

The ultimate goal of this thesis was to demonstrate plasmonic enhancement of the fluorescence signal in molecular recognition assays of nucleic acids as a strategy to improve their detection for biosensing purposes. The molecular beacons were designed to trigger a fluorescence signal by using a Förster Resonance Energy Transfer (FRET) process between a fluorophore label and a quencher. Two donor-acceptor pairs, Atto-647N/Deep Dark Quencher II and Atto-647N/QSY™ 21 were tested. The synthetic nucleic acids that were selected as

targets are three biomarkers with potential interest, respectively, for clinical diagnostics of dengue virus (DENV) and sleeping sickness infections, and cancer/cardiovascular (or other) pathologies (see section 2.5).

The first step was the study of the molecular beacons *per se* in aqueous solution, i.e. in the absence of gold nanorods, by testing the fluorescence signalling mechanism in response to the nucleic acid targets. These studies were performed by confocal fluorescence lifetime microscopy with single-molecule detection sensitivity. Measurements of fluorescence correlation spectroscopy and fluorescence decays by single-photon counting were simultaneously acquired from a microscopic observation volume. Under the experimental conditions tested, the results found in these assays indicate a limited response of the molecular beacons and, as such, a new strategy was devised in which the gold nanorod acts as an energy acceptor instead of an organic quencher molecule. The tip-specific functionalization procedures previously described were also implemented for the conjugation of molecular beacons onto gold nanorods. This approach avoids the dispersion of the target species over surface regions of the nanorod that have a negligible enhancement effect. Fluorescence signalling of the nanobiosensors was characterized in colloidal suspension and in surface-immobilized experiments by means of fluorescence microscopy and single-particle spectroscopy. The performance of the nanohybrids as fluorescence-based biosensors when they are exposed to nucleic acid targets was below the expectations, most likely due to interference in the intra- and intermolecular hybridization interactions required for a proper functioning of the DNA beacon probes. Even though, the ultimate goal of this thesis was not accomplished, the studies performed here have laid the methodological basis and pointed out toward improvements that will contribute to a positive unfolding of future research studies.

2.5. Annexes

Nucleic acids selected as targets were synthetic sequences of RNA from DENV, and DNA from sleeping sickness infections, and microRNA (miRNA) from cancer and cardiovascular diseases. The importance and need of creating diagnostic tools for these diseases are described next, as it is imperative to provide solutions for these public health problems, to lighten healthcare systems worldwide and to allow considerable relief on socioeconomic impacts and on the burden that these diseases instigate.

2.5.1. Dengue virus infection

Dengue, but also and sleeping sickness, are vector-borne diseases that cause significant mortality and morbidity, representing an estimated 17% of the worldwide burden of all infectious diseases.[1] The incidence occur mostly in countries in the tropics and poor communities, hence are classified as neglected tropical diseases. In 2012, several important vector-borne neglected tropical diseases were targeted for elimination by 2020 within the World Health Organization

(WHO) roadmap for these diseases.[2] Unfortunately, however, their burden, including that of dengue and sleeping sickness, will surely continue beyond the ambitious 2020 target.

DENV is a spherical 50 nm virion comprised of three structural proteins, a lipid envelope, and a 10.7 kilobase capped single-stranded positive-sense RNA.[3–5] As small infectious agents, viruses have short genomes that enable them to replicate only inside the living cells of other organisms. They use the machinery and metabolism of the host cell to efficiently usurp and reprogram it, and complete their life cycle.[6] Besides DENV, RNA viruses account for many serious emerging and ongoing threats to public health, like HIV, Ebola, influenza, Zika, chikungunya, and SARS-CoV or SARS-CoV-2 that is causing the 2020 COVID-19 pandemic. Recent DENV infections and epidemics are an important public health problem. In the last 50 years there has been an increasing rise in the infection's incidence with outbreaks of growing frequency and magnitude.[7]

Dengue viruses are a group of four closely related but serologically distinct arboviruses that differ from one another by 25-40% at the amino acid level and are separated into serotypes: DENV-1, DENV-2, DENV-3, and DENV-4.[3,8] These are mosquito-transmitted and cycle in nature between humans and Aedes mosquito vectors, mainly *Aedes aegypti* but also *Aedes albopictus*, through the bites of infected females. Mosquitos become infected with one DENV serotype when they ingest blood from humans during viraemia phase. Infective viral particles pass from the mosquito intestinal tract to the salivary glands and the insect is capable of transmitting the virus to a new host.[9] It replicates primarily in immature dendritic cells and keratinocytes of the skin. Later, cells of the mononuclear lineage become infected, with entry into macrophages and activation of lymphocytes being followed by entry into the bloodstream. This is likely the mechanism for infection of peripheral organs,[7] mainly lymph nodes, spleen, and liver.[3]

DENV serotypes circulate in urban environments throughout the tropics and subtropics of the globe, being widespread in more than 120 countries each year, mainly in the Americas, the Caribbean, Asia and Africa, where conditions of temperature and humidity favor the proliferation of mosquito vectors.[4,7,9] Transmission has increased in the past several decades as a result of the expansion of mosquitos in urban environments (often unplanned and uncontrolled), population growth, global travel, commerce, global warming, difficulty in personal protective measures, but also of a scarcity of mosquito control efforts and programs due to lack of resources and socioeconomic conditions, lack of political will, and/or ineffective and unsustainable implementation.[4,8,10]

According to recent estimates of the WHO, 390 million human dengue infections occur per year, resulting in 96 million clinically apparent infections and around 500 000 people require hospitalization,[7] with the disease causing almost 14000 deaths (2013 data).[11] With an estimated 3.6 billion people - half the world's population - at risk of infection, it is the major cause of arthropod-borne viral disease in the world, causing the highest morbidity and mortality than any other arthropod-borne virus.[3,4,8] In addition to the heavy burden on public health, epidemics have

a huge economic impact on affected countries. The annual economic costs in the countries of Southeast Asia are estimated at 1 billion US dollars[12] and in Latin America/Caribbean at 3 billion US dollars,[13] resulting in a global cost of 8.9 billion US dollars in 2013 prices.[11]

With new outbreaks on the horizon, the demand for innovative detection methods has been renewed. These are aimed to identify the viral pathogen prior to the appearance of symptoms and in an effective timely and accurate manner. This would allow rapid recovery from the symptoms, but also efficient and accurate surveillance and control of outbreaks. In addition, would assist research on prognosis, pathogenesis, vaccine development (the only available, Dengvaxia®, has major weaknesses and showed moderate efficacy in the field),[4,7,14,15] and clinical trials.

Today several detection strategies are available and diagnostic devices, assays and commercial kits are composed of laboratory-based and POC tests. In the laboratory, tests are based on the detection of: i) viral RNA genomes using RT-PCR,[5,10,16] to provide results after several hours; ii) viral antigens, such as the dengue non-structural protein 1 (NS1) using for example Platelia™ Dengue NS1 Ag capture enzyme-linked immunosorbent assay (ELISA) from Bio-Rad;[17–20] or iii) dengue-specific antibodies immunoglobulin M and G (IgM and IgG) using serological assays of the major commercial manufacturers (Panbio, Standard Diagnostics, and Bio-Rad).[19,20] POC tests are usually based on lateral flow immunochromatography,[21,22] being rapid (a few hours) and providing a simple and cheap solution for NS1 or IgM/IgG detection. Unfortunately, reliability, sensitivities and specificities are usually lower than the equivalent laboratory-based ELISA assays.

Weighing the limitations of current testing strategies, it becomes clear that a sequence-specific approach is essential to detect DENV in a practical, rapid (in a question of minutes), and low-cost manner. This would allow detection in mosquito cells and tissues, but also in infected human samples (blood, serum, saliva or urine), with reduced or non-specialized training required. A review article published last year highlights the advances and trends of biosensors for DENV infection diagnostics.[23] These can be categorized into optical and electrochemical or into more advanced technological approaches such as electronic, microfluidic and smartphone-based.

The more important reports used several nanomaterials and techniques to detect all DENV serotypes through antigens, antibodies and viral RNA. In the first two cases, techniques include: voltammetry using carbon nanotubes,[24] and impedance and voltammetry measurements using gold films,[25,26] suction-type[27] and dielectrophoresis[28] microfluidic chips, surface plasmon resonance (SPR) with gold sensor chips,[29–31] long-range surface plasmon waveguides using gold stripes,[32] and optical fibers with gold nanoparticles for LSPR sensing.[33] Detection of viral genomic material comprises: reverse transcription loop-mediated isothermal amplification (RT-LAMP) based on fluorescent paper,[34] colorimetry,[35] optomagnetism,[36] fluorescence (pan-serotype detection),[37] and colorimetric-luminance[38] or fluorescence-based[39] smartphone devices; impedance measurements with nanoporous alumina[40] and pencil graphite;[41] electronic detection with silicon nanowires;[42] colorimetry using DNA-functionalized triangular silver

nanoparticles;[43] quartz crystal microbalance,[44] inductively coupled plasma mass spectrometry[45] and colorimetry[46] with DNA-functionalized gold nanoparticles; fluorescence using gold nanoparticles and quantum dots.[47] The limits of detection of these genosensors range from nano- to a few femtomolar.

2.5.2. Sleeping sickness infection

Human African trypanosomiasis, also known as sleeping sickness, is a vector-borne disease that causes a considerable burden in poor and rural parts of more than 20 countries in sub-Saharan Africa, within the distributional limits of its vector, the tsetse fly.[48,49] Thus, it is an endemic disease placing an estimated 70 million people at risk.[50,51] During the 20th century, it caused devastating epidemics, but the number of reported cases has fallen, reaching a historically low level of fewer than 1000 in 2018.[51–53] This was due to large-scale sustained and coordinated surveillance, and control and treatment efforts over the past 20 years by the WHO, non-government organizations, African governments, the pharmaceutical industry, research charities and Institutions. Although some foci remain above the threshold of 1 case or fewer per 10000 people, the disease is now considered rare. While it would be ideal to eliminate it completely, the more realistic goals of the WHO are to eliminate it by 2020 and to achieve interruption of its transmission by 2030.[2]

Sleeping sickness is a parasitic disease caused by infection with unicellular protozoan parasites called *Trypanosoma* (genus) *brucei* (species) (*T. b.*) and is a medical and veterinary problem. *T. b.* is transmitted by the bite of the blood-feeding tsetse flies of the genus *Glossina* and includes three morphologically indistinguishable sub-species: *T. b. brucei*, that causes animal African trypanosomiasis, known as Nagana,[51] and *T. b. gambiense* and *T. b. rhodesiense* that infect people, causing Gambiense and Rhodesiense human African trypanosomiasis, respectively.[1,53] The latter two sub-species are responsible for syndromes of markedly different geographical range and epidemiology.[48–50,53,54] The majority of cases (currently 98%)[52] are caused by *T. b. gambiense*, which gives rise to the chronic form in Western and Central Africa that has almost exclusively a human reservoir.[48,51] The less common infection with *T. b. rhodesiense* involves humans occasionally (2% of cases)[52] and affects mainly animals (livestock and wildlife).[55] The zoonotic nature of *T. b. rhodesiense* makes it more difficult to control compared to *T. b. gambiense*[56,57] and leads to more acute and severe illness (can lead to death within 6 months)[53] that affects the Eastern and Southern Africa.

The trypanosome parasites are extracellular and independently of the variant, the disease has a first stage - haemolymphatic - where trypanosomes are restricted to the lymph nodes and bloodstream, and over time a second later stage - meningoencephalitic - where they cross the blood-brain barrier and are also seen in brain parenchyma and cerebrospinal fluid (CSF) invading the central nervous system.[52,58] This second stage lasts few weeks (*T. b. rhodesiense*) or several months (*T. b. gambiense*), and involves neurological and psychiatric disturbances,[54] with sleep

disorders being the most typical (hence the name sleeping sickness) accounting for dysregulation of the circadian rhythm of the sleep-wake cycle and disintegration of the sleeping pattern.[59]

Although the prevalence of sleeping sickness has decreased, the disease remains a challenge, because of its clinical features and complex epidemiology. It is still a substantial cause of mortality and morbidity in affected regions, where it also has a considerable effect on livestock production. If infected, livestock will become useless for food and milk production, hence this promotes rural underdevelopment and leads to a 'cycle of poverty' on affected populations.[55] Consequently, the human and animal forms of sleeping sickness cannot be considered in isolation.

Many cases of sleeping sickness certainly are not reported or diagnosed and this may be due to several reasons: i) limited diagnostic capacity response; ii) inaccuracy and inadequacy of current diagnostic methods; iii) diversity and/or lack of specificity of clinical symptoms because first stage symptoms are common to other sub-Saharan Africa infections like malaria, enteric fever, tubercular meningitis and HIV; iv) insufficient staff capacities; v) incomplete community participation; vi) poor access to health facilities and vii) logistical reasons if the disease occurs in remote or unstable/insecure areas of difficult access, i.e. in areas without surveillance.[48,51,53,54] Therefore, diagnostic tests for sleeping sickness are much needed.

Diagnosis is generally based on serological screening of individuals. The long-established Card Agglutination Test for Trypanosomiasis (CATT) is one serological test used in the majority of control programs and at-risk population screening by mobile teams.[50,54,57] It has the advantages of being simple (done with blood, plasma, or serum), cheap and rapid (5 min). However, it has limitations: antigen production is complex, high frequency of false positives and false negatives, limited sensitivity, requires an electricity supply and trained personnel which are difficult to get in the African field.[50,60] Accurate serological tests based on immunofluorescence assays, ELISA and immune trypanolysis also exist for anti-trypanosome antibody detection but are mainly used in non-endemic countries where good laboratory facilities are available.[61–63] Also, lateral flow immunochromatographic devices have been used in rapid diagnostic tests that detect anti-trypanosome antibodies in the blood.[51] These tests, for *T. b. gambiense* infection, were recently developed and introduced in the market: SD Bioline HAT 1.0 and Sero-K-SeT.[64–66]

Molecular diagnostics of sleeping sickness detects the parasite's nucleic acids from body fluids (blood, CSF, urine or saliva). The methods have been the subject of intense research and despite the high number of articles reporting new developments, further standardization and diagnostic validation are needed for the creation of a field-applicable and low-cost DNA or RNA test.

Because serological and molecular tests are not sufficiently specific, parasitological confirmation by observation of trypanosomes in body fluids is generally required by microscopic examination.[49,54] This is cheap but used alone is not sufficient to differentiate sub-species, hence both serological and molecular tests can act as complementary diagnostic tools to provide that distinction.

Overall, currently available diagnostic tools and algorithms for sleeping sickness are complex, expensive, and equipment, resources, and personnel demanding for use in rural sub-Saharan Africa. Thus, research aims to develop more simplified, practical, inexpensive, quicker, reliable and accurate diagnostics tests towards a POC tool that can be incorporated in the public health infrastructure of low-resource settings.[50,51,54,60] Research on biosensors could contribute significantly to develop such POC tools. However, these have not been so much explored by the scientific community, with only a few examples deserving consideration. These used aptamers to detect a glycoprotein at attomolar concentrations[67] or parasites,[68] and another used nucleic acid probes to detect *Trypanosoma* RNA at a limit of 0.5 fmols.[69] Moreover, research of new stage biomarkers with an expansion of the range of antigens and discovery of a new protein, nucleic acid, or metabolite biomarkers, will be vital for the eradication of the disease.

2.5.3. MicroRNAs as clinical biomarkers

Regarding microRNAs, these are a class of single-stranded small (18-25 nucleotides) non-protein-encoded RNAs, which negatively regulate genes' expression at the transcriptional or post-transcriptional level. This is done by direct bind through base pairing with complementary nucleotide sequences or with imperfect complementary sites in the 3'-untranslated regions of the target messenger RNAs, promoting their expression by inducing degradation or repressing translation.[70–73] MiRNAs are endogenous and play essential roles in diverse biological processes including embryogenesis, haematopoiesis, brain morphogenesis, stem cell division, angiogenesis, organ development and cell proliferation, differentiation, apoptosis, metabolism, homeostasis and stress responses.[70–73] They are present in the regulation of these processes both in physiological functions and pathological conditions, having a significant impact on human health.

MiRNAs control critical cellular processes and signalling pathways, so their aberrant expression (increased or decreased) leads to the development and progression of several diseases including cancer, diabetes, viral infections, muscle degenerative diseases, and neurological, cardiovascular, metabolic and ocular disorders.[71,72,74] The study of miRNAs is greater in cancer research where it is prominent nowadays; for example, their de-regulation is considered as a common hallmark of the disease. In general, they are intracellular and their differential expression can be found in a wide range of normal and diseased cells and tissues, that can yield high-quality miRNA suitable for detection.[70,71]

Apart from the tumour microenvironment, miRNAs can also be found in biofluids as the result of apoptosis and necrotic cell death or can be secreted within cell-free lipid carriers such as microvesicles, exosomes, microparticles and apoptotic bodies or bound to protein complexes. This enables them to evade the RNase digestion and remain stable as circulating miRNAs.[70,72,73,75,76] The changes of circulating miRNA expression profiles have been reported to be associated with various physiologic/pathologic conditions, being tissue-specific. Circulating miRNAs have emerged as potential non-invasive and effective biomarkers for different cellular events and disease diagnosis, prognosis, treatment monitoring, classification, staging and

progression.[71,74,75,77] Hence, their global screening could be useful to create a specific signature for a certain disease or cancer type.[78]

Specific miRNAs have been found to be differentially expressed in several human tumours. The miRNA of interest in this doctoral work is miRNA-145 (miR-145), which has a well-characterized tumour-suppressive regulatory role. This role could be explained by its modulation of multiple target oncogenes engaged in invasion and epithelial-to-mesenchymal transition.[79,80] MiR-145 is located on chromosome 5 (5q32-33), a fragile site in the human genome, and is suggested to be co-transcribed with miR-143 forming the 143/145 cluster.[81] It is expressed in normal tissues at significant levels, with the highest expression in the colon and the lowest in the liver and brain. High expression occurs in the prostate, cervix, stomach, uterus and small intestine, while low occurs in the kidney, placenta, testis, spleen and skeletal muscle.[81] But, these levels are commonly downregulated in many types of cancer, suggesting that miR-145 may serve as an important tumour suppressor.[79,82–84] Besides cancer, it was found related to cardiovascular diseases and other illnesses such as atherosclerosis, hypertension, venous thrombosis, fibrosis diseases or pathological retinal angiogenesis.[74,77,85–88]

According to the WHO, cardiovascular diseases are the leading cause of death in the World - 17.9 million deaths in 2016 - with the second biggest being cancer with 9.6 million in 2018.[89,90] Both diseases are also the main causes of morbidity with numbers of affected individuals at risk of rising exponentially, which expands the threats to global health and economic burdens.[91,92] Thus, it is urgent to better manage these diseases, to improve tools for risk prediction, including identification of new accurate biomarkers, to search and develop novel/alternative therapeutics, but also diagnostic methods.[77]

MiRNAs can be a powerful diagnostic tool of diseases, including the above-mentioned, shedding new light on potential treatments. However, detection and quantification are very demanding due to miRNA's intrinsic properties: short length, highly similar sequences in their family that can result in high risk of cross-hybridization, low abundance (a few molecules per cell or low levels in blood), tissue-/stage-specific expression, large variation in base composition and secondary structures. Despite detection being difficult in complex samples, the creation of efficient tools for rapid, simple, label-free, specific, and sensitive sensing of miRNAs would be significant.

For circulating miRNAs' detection in blood, plasma or serum, quantitative Reverse Transcription - Polymerase Chain Reaction (qRT-PCR) and microarrays are the mainstream approaches.[77] Actually, circulating miR-145 was detected using qRT-PCR in body fluids, such as blood, where levels were markedly increased in patients with thyroid cancer;[83] in serum, being a promising biomarker for preoperative diagnosis of ovarian cancer;[93] and also in plasma, in which lower levels were associated with the presence as well as the severity of coronary artery disease.[85] However, the above-mentioned platforms have relative strengths and weaknesses. Nevertheless, for miRNA expression profiles, microarrays have a major advantage in high throughout analysis,

while qRT-PCR is the best choice for quantifying miRNAs with low levels due to its high sensitivity. Other strategies have been developed to improve sensitivity and flexibility of the previous methods, such as rolling circle amplification-based assays[94] and enzymatic assays.[95]

Considering the improvement of sensitivity, needs depend on application, but some realistic limits can be defined for cellular extracts and biological fluids. In the latter, miRNAs are diluted in mL to L scale volumes, resulting in low concentrations, and in clinical results, are measured in the fM range, with some samples reportedly as low as 20 aM and as high as 20 nM. Yet, for biosensing assays, they can be detected not necessarily in their native concentrations, because body fluids collected at the mL scale can be concentrated to the μL scale. So, sensitivity is important but to a certain degree, meaning that sub-fM sensitivity may not be that imperative for detection.

The need for assays to detect low-abundance miRNA and the trend toward miniaturized devices reveal the importance of nanomaterials to accelerate signal transduction and advance towards ultrasensitive detection. In addition, on the basis of the unique optical, electronic, and magnetic properties of nanomaterials, novel biosensors are supposed to be alternative techniques. In fact, several recently published works have shown that biosensor technology can offer rapid results, providing high sensitivity and minimal sample preparation. Optical (besides the ones included in Chapter 1) and electrochemical biosensors are in the spotlight,[96–105] with limits of detection ranging from pico- to femtomolar, including in miR-145 detection.[97,106] Also, techniques such as total internal reflection fluorescence microscopy even allowed detection at the single-molecule level.[107] But obviously, there is still a pressing need to develop analytical platforms for the detection and validation of miRNAs in complex biological samples, ideally without amplification, to provide reliable, portable and inexpensive application in clinic research.

2.6. References

(1) Longbottom, J.; Krause, A.; Torr, S. J.; Stanton, M. C. Quantifying Geographic Accessibility to Improve Efficiency of Entomological Monitoring. *PLoS Negl. Trop. Dis.* **2020**, *14* (3), e0008096. https://doi.org/10.1371/journal.pntd.0008096.
(2) World Health Organization. Accelerating work to overcome the global impact of neglected tropical diseases: a roadmap for implementation. Geneva, 2012.
(3) Begum, F.; Das, S.; Mukherjee, D.; Mal, S.; Ray, U. Insight into the Tropism of Dengue Virus in Humans. *Viruses* **2019**, *11* (12), 1136. https://doi.org/10.3390/v11121136.
(4) Diamond, M. S.; Pierson, T. C. Molecular Insight into Dengue Virus Pathogenesis and Its Implications for Disease Control. *Cell* **2015**, *162* (3), 488–492. https://doi.org/10.1016/j.cell.2015.07.005.
(5) Zou, C.; Huang, C.; Zhang, J.; Wu, Q.; Ni, X.; Sun, J.; Dai, J. Virulence Difference of Five Type I Dengue Viruses and the Intrinsic Molecular Mechanism. *PLoS Negl. Trop. Dis.* **2019**, *13* (3), e0007202. https://doi.org/10.1371/journal.pntd.0007202.
(6) Dethoff, E. A.; Boerneke, M. A.; Gokhale, N. S.; Muhire, B. M.; Martin, D. P.; Sacco, M. T.; McFadden, M. J.; Weinstein, J. B.; Messer, W. B.; Horner, S. M.; Weeks, K. M. Pervasive Tertiary Structure in the Dengue Virus RNA Genome. *Proc. Natl. Acad. Sci.* **2018**, *115* (45), 11513–11518. https://doi.org/10.1073/pnas.1716689115.
(7) World Health Organization. Dengue vaccine: WHO position paper. Geneva, September 2018.

(8) Byk, L. A.; Gamarnik, A. V. Properties and Functions of the Dengue Virus Capsid Protein. *Annu. Rev. Virol.* **2016**, *3* (1), 263–281. https://doi.org/10.1146/annurev-virology-110615-042334.
(9) Ferreira-de-Lima, V. H.; Lima-Camara, T. N. Natural Vertical Transmission of Dengue Virus in Aedes Aegypti and Aedes Albopictus: A Systematic Review. *Parasit. Vectors* **2018**, *11* (1). https://doi.org/10.1186/s13071-018-2643-9.
(10) Johnson, B. W.; Russell, B. J.; Lanciotti, R. S. Serotype-Specific Detection of Dengue Viruses in a Fourplex Real-Time Reverse Transcriptase PCR Assay. *J. Clin. Microbiol.* **2005**, *43* (10), 4977–4983. https://doi.org/10.1128/JCM.43.10.4977-4983.2005.
(11) Shepard, D. S.; Undurraga, E. A.; Halasa, Y. A.; Stanaway, J. D. The Global Economic Burden of Dengue: A Systematic Analysis. *Lancet Infect. Dis.* **2016**, *16* (8), 935–941. https://doi.org/10.1016/S1473-3099(16)00146-8.
(12) Shepard, D. S.; Undurraga, E. A.; Halasa, Y. A. Economic and Disease Burden of Dengue in Southeast Asia. *PLoS Negl. Trop. Dis.* **2013**, *7* (2), e2055. https://doi.org/10.1371/journal.pntd.0002055.
(13) Laserna, A.; Barahona-Correa, J.; Baquero, L.; Castañeda-Cardona, C.; Rosselli, D. Economic Impact of Dengue Fever in Latin America and the Caribbean: A Systematic Review. *Rev. Panam. Salud Pública* **2018**, *42*. https://doi.org/10.26633/RPSP.2018.111.
(14) Thomas, S. J.; Yoon, I.-K. A Review of Dengvaxia®: Development to Deployment. *Hum. Vaccines Immunother.* **2019**, *15* (10), 2295–2314. https://doi.org/10.1080/21645515.2019.1658503.
(15) Villar, L.; Dayan, G. H.; Arredondo-García, J. L.; Rivera, D. M.; Cunha, R.; Deseda, C.; Reynales, H.; Costa, M. S.; Morales-Ramírez, J. O.; Carrasquilla, G.; Rey, L. C.; Dietze, R.; Luz, K.; Rivas, E.; Miranda Montoya, M. C.; Cortés Supelano, M.; Zambrano, B.; Langevin, E.; Boaz, M.; Tornieporth, N.; Saville, M.; Noriega, F. Efficacy of a Tetravalent Dengue Vaccine in Children in Latin America. *N. Engl. J. Med.* **2015**, *372* (2), 113–123. https://doi.org/10.1056/NEJMoa1411037.
(16) Santiago, G. A.; Vázquez, J.; Courtney, S.; Matías, K. Y.; Andersen, L. E.; Colón, C.; Butler, A. E.; Roulo, R.; Bowzard, J.; Villanueva, J. M.; Muñoz-Jordan, J. L. Performance of the Trioplex Real-Time RT-PCR Assay for Detection of Zika, Dengue, and Chikungunya Viruses. *Nat. Commun.* **2018**, *9* (1). https://doi.org/10.1038/s41467-018-03772-1.
(17) Nascimento, E. J. M.; George, J. K.; Velasco, M.; Bonaparte, M. I.; Zheng, L.; DiazGranados, C. A.; Marques, E. T. A.; Huleatt, J. W. Development of an Anti-Dengue NS1 IgG ELISA to Evaluate Exposure to Dengue Virus. *J. Virol. Methods* **2018**, *257*, 48–57. https://doi.org/10.1016/j.jviromet.2018.03.007.
(18) Lima, M. da R. Q.; Nogueira, R. M. R.; Schatzmayr, H. G.; Santos, F. B. dos. Comparison of Three Commercially Available Dengue NS1 Antigen Capture Assays for Acute Diagnosis of Dengue in Brazil. *PLoS Negl. Trop. Dis.* **2010**, *4* (7), e738. https://doi.org/10.1371/journal.pntd.0000738.
(19) Blacksell, S. D.; Jarman, R. G.; Gibbons, R. V.; Tanganuchitcharnchai, A.; Mammen, M. P.; Nisalak, A.; Kalayanarooj, S.; Bailey, M. S.; Premaratna, R.; de Silva, H. J.; Day, N. P. J.; Lalloo, D. G. Comparison of Seven Commercial Antigen and Antibody Enzyme-Linked Immunosorbent Assays for Detection of Acute Dengue Infection. *Clin. Vaccine Immunol.* **2012**, *19* (5), 804–810. https://doi.org/10.1128/CVI.05717-11.
(20) Hunsperger, E. A.; Muñoz-Jordán, J.; Beltran, M.; Colón, C.; Carrión, J.; Vazquez, J.; Acosta, L. N.; Medina-Izquierdo, J. F.; Horiuchi, K.; Biggerstaff, B. J.; Margolis, H. S. Performance of Dengue Diagnostic Tests in a Single-Specimen Diagnostic Algorithm. *J. Infect. Dis.* **2016**, *214* (6), 836–844. https://doi.org/10.1093/infdis/jiw103.
(21) Bonney, J. H. K.; Hayashi, T.; Dadzie, S.; Agbosu, E.; Pratt, D.; Nyarko, S.; Asiedu-Bekoe, F.; Ido, E.; Sarkodie, B.; Ohta, N.; Yamaoka, S. Molecular Detection of Dengue Virus in Patients Suspected of Ebola Virus Disease in Ghana. *PLOS ONE* **2018**, *13* (12), e0208907. https://doi.org/10.1371/journal.pone.0208907.

(22) Choi, J. R.; Yong, K. W.; Tang, R.; Gong, Y.; Wen, T.; Yang, H.; Li, A.; Chia, Y. C.; Pingguan-Murphy, B.; Xu, F. Lateral Flow Assay Based on Paper-Hydrogel Hybrid Material for Sensitive Point-of-Care Detection of Dengue Virus. *Adv. Healthc. Mater.* **2017**, *6* (1), 1600920. https://doi.org/10.1002/adhm.201600920.
(23) Eivazzadeh-Keihan, R.; Pashazadeh-Panahi, P.; Mahmoudi, T.; Chenab, K. K.; Baradaran, B.; Hashemzaei, M.; Radinekiyan, F.; Mokhtarzadeh, A.; Maleki, A. Dengue Virus: A Review on Advances in Detection and Trends – from Conventional Methods to Novel Biosensors. *Microchim. Acta* **2019**, *186* (6). https://doi.org/10.1007/s00604-019-3420-y.
(24) Dias, A. C. M. S.; Gomes-Filho, S. L. R.; Silva, M. M. S.; Dutra, R. F. A Sensor Tip Based on Carbon Nanotube-Ink Printed Electrode for the Dengue Virus NS1 Protein. *Biosens. Bioelectron.* **2013**, *44*, 216–221. https://doi.org/10.1016/j.bios.2012.12.033.
(25) Cavalcanti, I. T.; Guedes, M. I. F.; Sotomayor, M. D. P. T.; Yamanaka, H.; Dutra, R. F. A Label-Free Immunosensor Based on Recordable Compact Disk Chip for Early Diagnostic of the Dengue Virus Infection. *Biochem. Eng. J.* **2012**, *67*, 225–230. https://doi.org/10.1016/j.bej.2012.06.016.
(26) Kim, J. H.; Cho, C. H.; Ryu, M. Y.; Kim, J.-G.; Lee, S.-J.; Park, T. J.; Park, J. P. Development of Peptide Biosensor for the Detection of Dengue Fever Biomarker, Nonstructural 1. *PLOS ONE* **2019**, *14* (9), e0222144. https://doi.org/10.1371/journal.pone.0222144.
(27) Weng, C.-H.; Huang, T.-B.; Huang, C.-C.; Yeh, C.-S.; Lei, H.-Y.; Lee, G.-B. A Suction-Type Microfluidic Immunosensing Chip for Rapid Detection of the Dengue Virus. *Biomed. Microdevices* **2011**, *13* (3), 585–595. https://doi.org/10.1007/s10544-011-9529-3.
(28) Iswardy, E.; Tsai, T.-C.; Cheng, I.-F.; Ho, T.-C.; Perng, G. C.; Chang, H.-C. A Bead-Based Immunofluorescence-Assay on a Microfluidic Dielectrophoresis Platform for Rapid Dengue Virus Detection. *Biosens. Bioelectron.* **2017**, *95*, 174–180. https://doi.org/10.1016/j.bios.2017.04.011.
(29) Kumbhat, S.; Sharma, K.; Gehlot, R.; Solanki, A.; Joshi, V. Surface Plasmon Resonance Based Immunosensor for Serological Diagnosis of Dengue Virus Infection. *J. Pharm. Biomed. Anal.* **2010**, *52* (2), 255–259. https://doi.org/10.1016/j.jpba.2010.01.001.
(30) Jahanshahi, P.; Zalnezhad, E.; Sekaran, S. D.; Adikan, F. R. M. Rapid Immunoglobulin M-Based Dengue Diagnostic Test Using Surface Plasmon Resonance Biosensor. *Sci. Rep.* **2015**, *4* (1). https://doi.org/10.1038/srep03851.
(31) Omar, N. A. S.; Fen, Y. W.; Abdullah, J.; Mustapha Kamil, Y.; Daniyal, W. M. E. M. M.; Sadrolhosseini, A. R.; Mahdi, M. A. Sensitive Detection of Dengue Virus Type 2 E-Proteins Signals Using Self-Assembled Monolayers/Reduced Graphene Oxide-PAMAM Dendrimer Thin Film-SPR Optical Sensor. *Sci. Rep.* **2020**, *10* (1). https://doi.org/10.1038/s41598-020-59388-3.
(32) Wong, W. R.; Sekaran, S. D.; Mahamd Adikan, F. R.; Berini, P. Detection of Dengue NS1 Antigen Using Long-Range Surface Plasmon Waveguides. *Biosens. Bioelectron.* **2016**, *78*, 132–139. https://doi.org/10.1016/j.bios.2015.11.030.
(33) Camara, A. R.; Gouvêa, P. M. P.; Dias, A. C. M. S.; Braga, A. M. B.; Dutra, R. F.; de Araujo, R. E.; Carvalho, I. C. S. Dengue Immunoassay with an LSPR Fiber Optic Sensor. *Opt. Express* **2013**, *21* (22), 27023. https://doi.org/10.1364/OE.21.027023.
(34) Lo, S.-J.; Yang, S.-C.; Yao, D.-J.; Chen, J.-H.; Tu, W.-C.; Cheng, C.-M. Molecular-Level Dengue Fever Diagnostic Devices Made out of Paper. *Lab. Chip* **2013**, *13* (14), 2686. https://doi.org/10.1039/c3lc50135c.
(35) Lau, Y.-L.; Lai, M.-Y.; Teoh, B.-T.; Abd-Jamil, J.; Johari, J.; Sam, S.-S.; Tan, K.-K.; AbuBakar, S. Colorimetric Detection of Dengue by Single Tube Reverse-Transcription-Loop-Mediated Isothermal Amplification. *PLOS ONE* **2015**, *10* (9), e0138694. https://doi.org/10.1371/journal.pone.0138694.
(36) Minero, G. A. S.; Nogueira, C.; Rizzi, G.; Tian, B.; Fock, J.; Donolato, M.; Strömberg, M.; Hansen, M. F. Sequence-Specific Validation of LAMP Amplicons in Real-Time Optomagnetic Detection of Dengue Serotype 2 Synthetic DNA. *The Analyst* **2017**, *142* (18), 3441–3450.

https://doi.org/10.1039/C7AN01023K.
(37) Dauner, A. L.; Mitra, I.; Gilliland, T.; Seales, S.; Pal, S.; Yang, S.-C.; Guevara, C.; Chen, J.-H.; Liu, Y.-C.; Kochel, T. J.; Wu, S.-J. L. Development of a Pan-Serotype Reverse Transcription Loop-Mediated Isothermal Amplification Assay for the Detection of Dengue Virus. *Diagn. Microbiol. Infect. Dis.* **2015**, *83* (1), 30–36. https://doi.org/10.1016/j.diagmicrobio.2015.05.004.
(38) Priye, A.; Bird, S. W.; Light, Y. K.; Ball, C. S.; Negrete, O. A.; Meagher, R. J. A Smartphone-Based Diagnostic Platform for Rapid Detection of Zika, Chikungunya, and Dengue Viruses. *Sci. Rep.* **2017**, *7* (1). https://doi.org/10.1038/srep44778.
(39) Ganguli, A.; Ornob, A.; Yu, H.; Damhorst, G. L.; Chen, W.; Sun, F.; Bhuiya, A.; Cunningham, B. T.; Bashir, R. Hands-Free Smartphone-Based Diagnostics for Simultaneous Detection of Zika, Chikungunya, and Dengue at Point-of-Care. *Biomed. Microdevices* **2017**, *19* (4). https://doi.org/10.1007/s10544-017-0209-9.
(40) Peh, A. E. K.; Li, S. F. Y. Dengue Virus Detection Using Impedance Measured across Nanoporous Aluminamembrane. *Biosens. Bioelectron.* **2013**, *42*, 391–396. https://doi.org/10.1016/j.bios.2012.10.054.
(41) Souza, E.; Nascimento, G.; Santana, N.; Ferreira, D.; Lima, M.; Natividade, E.; Martins, D.; Lima-Filho, J. Label-Free Electrochemical Detection of the Specific Oligonucleotide Sequence of Dengue Virus Type 1 on Pencil Graphite Electrodes. *Sensors* **2011**, *11* (6), 5616–5629. https://doi.org/10.3390/s110605616.
(42) Zhang, G.-J.; Zhang, L.; Huang, M. J.; Luo, Z. H. H.; Tay, G. K. I.; Lim, E.-J. A.; Kang, T. G.; Chen, Y. Silicon Nanowire Biosensor for Highly Sensitive and Rapid Detection of Dengue Virus. *Sens. Actuators B Chem.* **2010**, *146* (1), 138–144. https://doi.org/10.1016/j.snb.2010.02.021.
(43) Vinayagam, S.; Rajaiah, P.; Mukherjee, A.; Natarajan, C. DNA-Triangular Silver Nanoparticles Nanoprobe for the Detection of Dengue Virus Distinguishing Serotype. *Spectrochim. Acta. A. Mol. Biomol. Spectrosc.* **2018**, *202*, 346–351. https://doi.org/10.1016/j.saa.2018.05.047.
(44) Chen, S.-H.; Chuang, Y.-C.; Lu, Y.-C.; Lin, H.-C.; Yang, Y.-L.; Lin, C.-S. A Method of Layer-by-Layer Gold Nanoparticle Hybridization in a Quartz Crystal Microbalance DNA Sensing System Used to Detect Dengue Virus. *Nanotechnology* **2009**, *20* (21), 215501. https://doi.org/10.1088/0957-4484/20/21/215501.
(45) Hsu, I.-H.; Chen, W.-H.; Wu, T.-K.; Sun, Y.-C. Gold Nanoparticle-Based Inductively Coupled Plasma Mass Spectrometry Amplification and Magnetic Separation for the Sensitive Detection of a Virus-Specific RNA Sequence. *J. Chromatogr. A* **2011**, *1218* (14), 1795–1801. https://doi.org/10.1016/j.chroma.2011.02.005.
(46) Carter, J. R.; Balaraman, V.; Kucharski, C. A.; Fraser, T. S.; Fraser, M. J. A Novel Dengue Virus Detection Method That Couples DNAzyme and Gold Nanoparticle Approaches. *Virol. J.* **2013**, *10* (1). https://doi.org/10.1186/1743-422X-10-201.
(47) Dutta Chowdhury, A.; Ganganboina, A. B.; Nasrin, F.; Takemura, K.; Doong, R.; Utomo, D. I. S.; Lee, J.; Khoris, I. M.; Park, E. Y. Femtomolar Detection of Dengue Virus DNA with Serotype Identification Ability. *Anal. Chem.* **2018**, *90* (21), 12464–12474. https://doi.org/10.1021/acs.analchem.8b01802.
(48) Malvy, D.; Chappuis, F. Sleeping Sickness. *Clin. Microbiol. Infect.* **2011**, *17* (7), 986–995. https://doi.org/10.1111/j.1469-0691.2011.03536.x.
(49) Merritt, M. W.; Sutherland, C. S.; Tediosi, F. Ethical Considerations for Global Health Decision-Making: Justice-Enhanced Cost-Effectiveness Analysis of New Technologies for Trypanosoma Brucei Gambiense. *Public Health Ethics* **2018**. https://doi.org/10.1093/phe/phy013.
(50) Kennedy, P. G. Clinical Features, Diagnosis, and Treatment of Human African Trypanosomiasis (Sleeping Sickness). *Lancet Neurol.* **2013**, *12* (2), 186–194. https://doi.org/10.1016/S1474-4422(12)70296-X.
(51) Bonnet, J.; Boudot, C.; Courtioux, B. Overview of the Diagnostic Methods Used in the Field

for Human African Trypanosomiasis: What Could Change in the Next Years? *BioMed Res. Int.* **2015**, *2015*, 1–10. https://doi.org/10.1155/2015/583262.
(52) World Health Organization. WHO Interim Guidelines for the Treatment of Gambiense Human African Trypanosomiasis.; 2019.
(53) Büscher, P.; Cecchi, G.; Jamonneau, V.; Priotto, G. Human African Trypanosomiasis. *The Lancet* **2017**, *390* (10110), 2397–2409. https://doi.org/10.1016/S0140-6736(17)31510-6.
(54) Kennedy, P. G. E.; Rodgers, J. Clinical and Neuropathogenetic Aspects of Human African Trypanosomiasis. *Front. Immunol.* **2019**, *10*. https://doi.org/10.3389/fimmu.2019.00039.
(55) Mableson, H. E.; Okello, A.; Picozzi, K.; Welburn, S. C. Neglected Zoonotic Diseases—The Long and Winding Road to Advocacy. *PLoS Negl. Trop. Dis.* **2014**, *8* (6), e2800. https://doi.org/10.1371/journal.pntd.0002800.
(56) Hasker, E.; Mpanya, A.; Makabuza, J.; Mbo, F.; Lumbala, C.; Kumpel, J.; Claeys, Y.; Kande, V.; Ravinetto, R.; Menten, J.; Lutumba, P.; Boelaert, M. Treatment Outcomes for Human African Trypanosomiasis in the Democratic Republic of the Congo: Analysis of Routine Program Data from the World's Largest Sleeping Sickness Control Program. *Trop. Med. Int. Health* **2012**, *17* (9), 1127–1132. https://doi.org/10.1111/j.1365-3156.2012.03042.x.
(57) Control and Surveillance of Human African Trypanosomiasis: Report of a WHO Expert Committee; World Health Organization: Geneva, 2013.
(58) Ponte-Sucre, A. An Overview of Trypanosoma Brucei Infections: An Intense Host–Parasite Interaction. *Front. Microbiol.* **2016**, *7*. https://doi.org/10.3389/fmicb.2016.02126.
(59) Rijo-Ferreira, F.; Carvalho, T.; Afonso, C.; Sanches-Vaz, M.; Costa, R. M.; Figueiredo, L. M.; Takahashi, J. S. Sleeping Sickness Is a Circadian Disorder. *Nat. Commun.* **2018**, *9* (1). https://doi.org/10.1038/s41467-017-02484-2.
(60) Wastling, S. L.; Welburn, S. C. Diagnosis of Human Sleeping Sickness: Sense and Sensitivity. *Trends Parasitol.* **2011**, *27* (9), 394–402. https://doi.org/10.1016/j.pt.2011.04.005.
(61) Sullivan, L.; Wall, S. J.; Carrington, M.; Ferguson, M. A. J. Proteomic Selection of Immunodiagnostic Antigens for Human African Trypanosomiasis and Generation of a Prototype Lateral Flow Immunodiagnostic Device. *PLoS Negl. Trop. Dis.* **2013**, *7* (2), e2087. https://doi.org/10.1371/journal.pntd.0002087.
(62) Lejon, V.; Büscher, P.; Magnus, E.; Moons, A.; Wouters, I.; Van Meirvenne, N. A Semi-Quantitative ELISA for Detection of Trypanosoma Brucei Gambiense Specific Antibodies in Serum and Cerebrospinal Fluid of Sleeping Sickness Patients. *Acta Trop.* **1998**, *69* (2), 151–164. https://doi.org/10.1016/S0001-706X(97)00137-X.
(63) Camara, O.; Camara, M.; Lejon, V.; Ilboudo, H.; Sakande, H.; Léno, M.; Büscher, P.; Bucheton, B.; Jamonneau, V. Immune Trypanolysis Test with Blood Spotted on Filter Paper for Epidemiological Surveillance of Sleeping Sickness. *Trop. Med. Int. Health* **2014**, *19* (7), 828–831. https://doi.org/10.1111/tmi.12316.
(64) Büscher, P.; Gilleman, Q.; Lejon, V. Rapid Diagnostic Test for Sleeping Sickness. *N. Engl. J. Med.* **2013**, *368* (11), 1069–1070. https://doi.org/10.1056/NEJMc1210373.
(65) Büscher, P.; Mertens, P.; Leclipteux, T.; Gilleman, Q.; Jacquet, D.; Mumba-Ngoyi, D.; Pyana, P. P.; Boelaert, M.; Lejon, V. Sensitivity and Specificity of HAT Sero-K-SeT, a Rapid Diagnostic Test for Serodiagnosis of Sleeping Sickness Caused by Trypanosoma Brucei Gambiense: A Case-Control Study. *Lancet Glob. Health* **2014**, *2* (6), e359–e363. https://doi.org/10.1016/S2214-109X(14)70203-7.
(66) Bisser, S.; Lumbala, C.; Nguertoum, E.; Kande, V.; Flevaud, L.; Vatunga, G.; Boelaert, M.; Büscher, P.; Josenando, T.; Bessell, P. R.; Biéler, S.; Ndung'u, J. M. Sensitivity and Specificity of a Prototype Rapid Diagnostic Test for the Detection of Trypanosoma Brucei Gambiense Infection: A Multi-Centric Prospective Study. *PLoS Negl. Trop. Dis.* **2016**, *10* (4), e0004608. https://doi.org/10.1371/journal.pntd.0004608.
(67) Zelada-Guillén, G. A.; Tweed-Kent, A.; Niemann, M.; Göringer, H. U.; Riu, J.; Rius, F. X. Ultrasensitive and Real-Time Detection of Proteins in Blood Using a Potentiometric

Carbon-Nanotube Aptasensor. *Biosens. Bioelectron.* **2013**, *41*, 366–371. https://doi.org/10.1016/j.bios.2012.08.055.
(68) Knieß, R.; Wagner, C. B.; Ulrich Göringer, H.; Mueh, M.; Damm, C.; Sawallich, S.; Chmielak, B.; Plachetka, U.; Lemme, M. Towards the Development of THz-Sensors for the Detection of African Trypanosomes. *Frequenz* **2018**, *72* (3–4), 101–111. https://doi.org/10.1515/freq-2018-0011.
(69) Wang, Y.; Fill, C.; Nugen, S. R. Development of Chemiluminescent Lateral Flow Assay for the Detection of Nucleic Acids. *Biosensors* **2012**, *2* (1), 32–42. https://doi.org/10.3390/bios2010032.
(70) Pritchard, C. C.; Cheng, H. H.; Tewari, M. MicroRNA Profiling: Approaches and Considerations. *Nat. Rev. Genet.* **2012**, *13* (5), 358–369. https://doi.org/10.1038/nrg3198.
(71) Dong, H.; Lei, J.; Ding, L.; Wen, Y.; Ju, H.; Zhang, X. MicroRNA: Function, Detection, and Bioanalysis. *Chem. Rev.* **2013**, *113* (8), 6207–6233. https://doi.org/10.1021/cr300362f.
(72) Hayes, J.; Peruzzi, P. P.; Lawler, S. MicroRNAs in Cancer: Biomarkers, Functions and Therapy. *Trends Mol. Med.* **2014**, *20* (8), 460–469. https://doi.org/10.1016/j.molmed.2014.06.005.
(73) Faruq, O.; Vecchione, A. MicroRNA: Diagnostic Perspective. *Front. Med.* **2015**, *2*. https://doi.org/10.3389/fmed.2015.00051.
(74) de Lucia, C.; Komici, K.; Borghetti, G.; Femminella, G. D.; Bencivenga, L.; Cannavo, A.; Corbi, G.; Ferrara, N.; Houser, S. R.; Koch, W. J.; Rengo, G. MicroRNA in Cardiovascular Aging and Age-Related Cardiovascular Diseases. *Front. Med.* **2017**, *4*. https://doi.org/10.3389/fmed.2017.00074.
(75) Filipów, S.; Łaczmański, Ł. Blood Circulating MiRNAs as Cancer Biomarkers for Diagnosis and Surgical Treatment Response. *Front. Genet.* **2019**, *10*. https://doi.org/10.3389/fgene.2019.00169.
(76) Schwarzenbach, H.; Nishida, N.; Calin, G. A.; Pantel, K. Clinical Relevance of Circulating Cell-Free MicroRNAs in Cancer. *Nat. Rev. Clin. Oncol.* **2014**, *11* (3), 145–156. https://doi.org/10.1038/nrclinonc.2014.5.
(77) Faccini, J.; Ruidavets, J.-B.; Cordelier, P.; Martins, F.; Maoret, J.-J.; Bongard, V.; Ferrières, J.; Roncalli, J.; Elbaz, M.; Vindis, C. Circulating MiR-155, MiR-145 and Let-7c as Diagnostic Biomarkers of the Coronary Artery Disease. *Sci. Rep.* **2017**, *7* (1). https://doi.org/10.1038/srep42916.
(78) Chandrasekaran, A. R.; Punnoose, J. A.; Zhou, L.; Dey, P.; Dey, B. K.; Halvorsen, K. DNA Nanotechnology Approaches for MicroRNA Detection and Diagnosis. *Nucleic Acids Res.* **2019**, *47* (20), 10489–10505. https://doi.org/10.1093/nar/gkz580.
(79) Wang, C.; Tao, W.; Ni, S.; Chen, Q.; Zhao, Z.; Ma, L.; Fu, Y.; Jiao, Z. Tumor-Suppressive MicroRNA-145 Induces Growth Arrest by Targeting SENP1 in Human Prostate Cancer Cells. *Cancer Sci.* **2015**, *106* (4), 375–382. https://doi.org/10.1111/cas.12626.
(80) Zeinali, T.; Mansoori, B.; Mohammadi, A.; Baradaran, B. Regulatory Mechanisms of MiR-145 Expression and the Importance of Its Function in Cancer Metastasis. *Biomed. Pharmacother.* **2019**, *109*, 195–207. https://doi.org/10.1016/j.biopha.2018.10.037.
(81) Das, A. V.; Pillai, R. M. Implications of MiR Cluster 143/145 as Universal Anti-OncomiRs and Their Dysregulation during Tumorigenesis. *Cancer Cell Int.* **2015**, *15* (1). https://doi.org/10.1186/s12935-015-0247-4.
(82) Cui, S.-Y.; Wang, R.; Chen, L.-B. MicroRNA-145: A Potent Tumour Suppressor That Regulates Multiple Cellular Pathways. *J. Cell. Mol. Med.* **2014**, *18* (10), 1913–1926. https://doi.org/10.1111/jcmm.12358.
(83) Boufraqech, M.; Zhang, L.; Jain, M.; Patel, D.; Ellis, R.; Xiong, Y.; He, M.; Nilubol, N.; Merino, M. J.; Kebebew, E. MiR-145 Suppresses Thyroid Cancer Growth and Metastasis and Targets AKT3. *Endocr. Relat. Cancer* **2014**, *21* (4), 517–531. https://doi.org/10.1530/ERC-14-0077.
(84) Tang, L.; Wei, D.; Yan, F. MicroRNA-145 Functions as a Tumor Suppressor by Targeting

Matrix Metalloproteinase 11 and Rab GTPase Family 27a in Triple-Negative Breast Cancer. *Cancer Gene Ther.* **2016**, *23* (8), 258–265. https://doi.org/10.1038/cgt.2016.27.
(85) Gao, H.; Guddeti, R. R.; Matsuzawa, Y.; Liu, L.-P.; Su, L.-X.; Guo, D.; Nie, S.-P.; Du, J.; Zhang, M. Plasma Levels of MicroRNA-145 Are Associated with Severity of Coronary Artery Disease. *PLOS ONE* **2015**, *10* (5), e0123477. https://doi.org/10.1371/journal.pone.0123477.
(86) Sahu, A.; Jha, P. K.; Prabhakar, A.; Singh, H. D.; Gupta, N.; Chatterjee, T.; Tyagi, T.; Sharma, S.; Kumari, B.; Singh, S.; Nair, V.; Goel, S.; Ashraf, M. Z. MicroRNA-145 Impedes Thrombus Formation via Targeting Tissue Factor in Venous Thrombosis. *EBioMedicine* **2017**, *26*, 175–186. https://doi.org/10.1016/j.ebiom.2017.11.022.
(87) Yang, J.; Liu, Q.; Cao, S.; Xu, T.; Li, X.; Zhou, D.; Pan, L.; Li, C.; Huang, C.; Meng, X.; Zhang, L.; Wang, X. MicroRNA-145 Increases the Apoptosis of Activated Hepatic Stellate Cells Induced by TRAIL through NF-KB Signaling Pathway. *Front. Pharmacol.* **2018**, *8*. https://doi.org/10.3389/fphar.2017.00980.
(88) Liu, C.-H.; Wang, Z.; Huang, S.; Sun, Y.; Chen, J. MicroRNA-145 Regulates Pathological Retinal Angiogenesis by Suppression of TMOD3. *Mol. Ther. - Nucleic Acids* **2019**, *16*, 335–347. https://doi.org/10.1016/j.omtn.2019.03.001.
(89) Cardiovascular Diseases. https://www.who.int/News-Room/Fact-Sheets/Detail/Cardiovascular-Diseases-(Cvds) (Accessed: 20 August 2020)
(90) Cancer. https://www.who.int/News-Room/Fact-Sheets/Detail/Cancer (Accessed: 20 August 2020).
(91) Khavjou O.; Phelps D.; Leib A. Projections of Cardiovascular Disease Prevalence and Costs: 2015–2035. Technical Report. RTI International, 2016.
(92) Stewart, B. W.; Wild, C. International Agency for Research on Cancer; World Health Organization. *World Cancer Report 2014*; 2014.
(93) Kim, S.; Choi, M. C.; Jeong, J.-Y.; Hwang, S.; Jung, S. G.; Joo, W. D.; Park, H.; Song, S. H.; Lee, C.; Kim, T. H.; An, H.-J. Serum Exosomal MiRNA-145 and MiRNA-200c as Promising Biomarkers for Preoperative Diagnosis of Ovarian Carcinomas. *J. Cancer* **2019**, *10* (9), 1958–1967. https://doi.org/10.7150/jca.30231.
(94) Zhou, Y.; Huang, Q.; Gao, J.; Lu, J.; Shen, X.; Fan, C. A Dumbbell Probe-Mediated Rolling Circle Amplification Strategy for Highly Sensitive MicroRNA Detection. *Nucleic Acids Res.* **2010**, *38* (15), e156–e156. https://doi.org/10.1093/nar/gkq556.
(95) Su, X.; Teh, H. F.; Lieu, X.; Gao, Z. Enzyme-Based Colorimetric Detection of Nucleic Acids Using Peptide Nucleic Acid-Immobilized Microwell Plates. *Anal. Chem.* **2007**, *79* (18), 7192–7197. https://doi.org/10.1021/ac0709403.
(96) Liu, L.; Xia, N.; Liu, H.; Kang, X.; Liu, X.; Xue, C.; He, X. Highly Sensitive and Label-Free Electrochemical Detection of MicroRNAs Based on Triple Signal Amplification of Multifunctional Gold Nanoparticles, Enzymes and Redox-Cycling Reaction. *Biosens. Bioelectron.* **2014**, *53*, 399–405. https://doi.org/10.1016/j.bios.2013.10.026.
(97) Jolly, P.; Batistuti, M. R.; Miodek, A.; Zhurauski, P.; Mulato, M.; Lindsay, M. A.; Estrela, P. Highly Sensitive Dual Mode Electrochemical Platform for MicroRNA Detection. *Sci. Rep.* **2016**, *6* (1). https://doi.org/10.1038/srep36719.
(98) Azzouzi, S.; Mak, W. C.; Kor, K.; Turner, A. P. F.; Ali, M. B.; Beni, V. An Integrated Dual Functional Recognition/Amplification Bio-Label for the One-Step Impedimetric Detection of Micro-RNA-21. *Biosens. Bioelectron.* **2017**, *92*, 154–161. https://doi.org/10.1016/j.bios.2017.02.014.
(99) Khakbaz, F.; Mahani, M. Micro-RNA Detection Based on Fluorescence Resonance Energy Transfer of DNA-Carbon Quantum Dots Probes. *Anal. Biochem.* **2017**, *523*, 32–38. https://doi.org/10.1016/j.ab.2017.01.025.
(100) Fang, S.; Lee, H. J.; Wark, A. W.; Corn, R. M. Attomole Microarray Detection of MicroRNAs by Nanoparticle-Amplified SPR Imaging Measurements of Surface Polyadenylation Reactions. *J. Am. Chem. Soc.* **2006**, *128* (43), 14044–14046. https://doi.org/10.1021/ja065223p.

(101) Nasheri, N.; Cheng, J.; Singaravelu, R.; Wu, P.; McDermott, M. T.; Pezacki, J. P. An Enzyme-Linked Assay for the Rapid Quantification of MicroRNAs Based on the Viral Suppressor of RNA Silencing Protein P19. *Anal. Biochem.* **2011**, *412* (2), 165–172. https://doi.org/10.1016/j.ab.2011.01.030.
(102) Driskell, J. D.; Seto, A. G.; Jones, L. P.; Jokela, S.; Dluhy, R. A.; Zhao, Y.-P.; Tripp, R. A. Rapid MicroRNA (MiRNA) Detection and Classification via Surface-Enhanced Raman Spectroscopy (SERS). *Biosens. Bioelectron.* **2008**, *24* (4), 917–922. https://doi.org/10.1016/j.bios.2008.07.060.
(103) Driskell, J. D.; Tripp, R. A. Label-Free SERS Detection of MicroRNA Based on Affinity for an Unmodified Silver Nanorod Array Substrate. *Chem. Commun.* **2010**, *46* (19), 3298. https://doi.org/10.1039/c002059a.
(104) Xu, Z.; Chang, Y.; Chai, Y.; Wang, H.; Yuan, R. Ultrasensitive Electrochemiluminescence Biosensor for Speedy Detection of MicroRNA Based on a DNA Rolling Machine and Target Recycling. *Anal. Chem.* **2019**, *91* (7), 4883–4888. https://doi.org/10.1021/acs.analchem.9b00728.
(105) He, X.; Zeng, T.; Li, Z.; Wang, G.; Ma, N. Catalytic Molecular Imaging of MicroRNA in Living Cells by DNA-Programmed Nanoparticle Disassembly. *Angew. Chem. Int. Ed.* **2016**, *55* (9), 3073–3076. https://doi.org/10.1002/anie.201509726.
(106) Ribes, À.; Santiago-Felipe, S.; Aviñó, A.; Candela-Noguera, V.; Eritja, R.; Sancenón, F.; Martínez-Máñez, R.; Aznar, E. Design of Oligonucleotide-Capped Mesoporous Silica Nanoparticles for the Detection of MiRNA-145 by Duplex and Triplex Formation. *Sens. Actuators B Chem.* **2018**, *277*, 598–603. https://doi.org/10.1016/j.snb.2018.09.026.
(107) Chan, H.-M.; Chan, L.-S.; Wong, R. N.-S.; Li, H.-W. Direct Quantification of Single-Molecules of MicroRNA by Total Internal Reflection Fluorescence Microscopy. *Anal. Chem.* **2010**, *82* (16), 6911–6918. https://doi.org/10.1021/ac101133x.

Chapter 3

Enhanced Fluorescence of Red-emitting Dyes By Gold Nanoantennas

3. Enhanced fluorescence of red-emitting dyes by gold nanoantennas

This chapter is dedicated to the fluorescence enhancement of red-emitting organic dyes by two types of optical nanoantennas: a single gold nanorod or a dimer of gold nanospheres. These nanostructures can provide intense plasmon near-fields upon excitation in the red to infrared spectral ranges and, hence, are capable of inducing large enhancement of fluorescence from coupled emitters. The main motivation of these studies was to characterize the range of signal enhancement that could be later explored for nucleic acid sensing.

3.1. Introduction

Two examples of fluorescent dyes were tested: Atto-647N and Atto-655 dye, that were chosen to allow for a good spectral overlap in light absorption and emission with the surface plasmon resonances of the gold nanoantennas.[1] In order to probe the largest enhancement effects in the systems studied, an experimental scheme based on a single-molecule on single-particle type of measurement was performed. The experimental details are described in sections 3.2 and 3.3. Evaluation of single-molecule fluorescence events provided a detailed characterization of the top emission enhancements. The comparison of experimental results with theoretical simulations provided valuable insights for a better comprehension of the fluorescence enhancement effect. This combined approach is essential to properly design fluorescence-based sensors with plasmon-enhanced signalling responses.

3.2. Fluorescence enhancement of Atto-647N by single gold nanorods

Gold nanorods can act as plasmonic nanoantennas to enhance fluorescence of dyes when excited by light due to the strong near-field enhancements at their tips. This effect can be appreciated from theoretical DDA simulations of gold nanorods with a size of 25 nm × 60 nm (width × length), as used in the experiments (Figure 3.1).

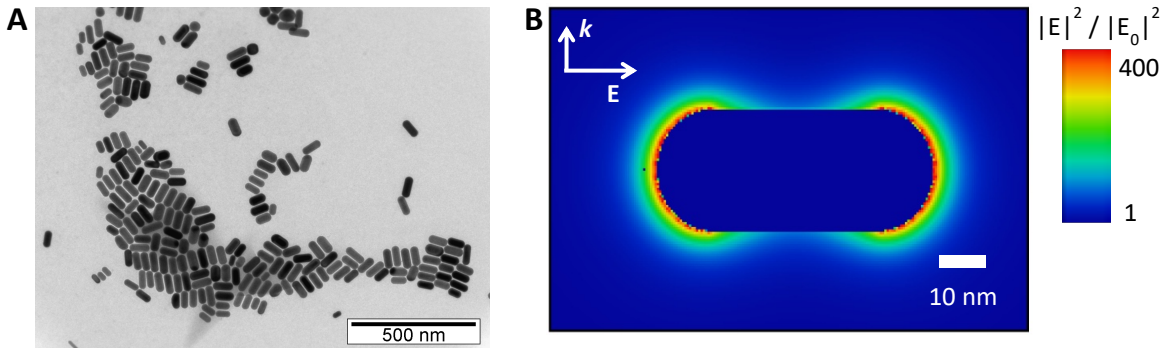

Figure 3.1 - Gold nanorods (25 nm × 60 nm) used as plasmonic nanoantennas for enhanced fluorescence. (A) Transmission electron microscopy (TEM) image. (B) DDA simulated map of the plasmonic near-field around a nanorod (25 nm × 61 nm) excited at an incident wavelength of 639 nm and assuming a medium with the refraction index of water (1.33).

The dye Atto-647N was selected because of its brightness (high molar absorption coefficient and fluorescence quantum yield, Φ_F = 0.65), photostability, good spectral and chemical properties (Figure 3.2A).[2] For these reasons, it is commonly used for labeling nucleic acids in biophysical studies. In the studies of fluorescence enhancement, Atto-647N was also used as a label of a single-stranded DNA (ssDNA) sequence, that was hybridized with a complementary sequence, forming a double-stranded DNA (dsDNA) with 10 base pairs. Because Atto-647N has an absorption peak at 646 nm and an emission peak at 664 nm,[2] it assures a good spectral match with the longitudinal surface plasmon (LSP) peak wavelength of the gold nanorods (Figure 3.2B). Moreover, it is also slightly red-shifted in relation to the LSP peak, which is a favorable condition for the enhancement of fluorescence emission.[1]

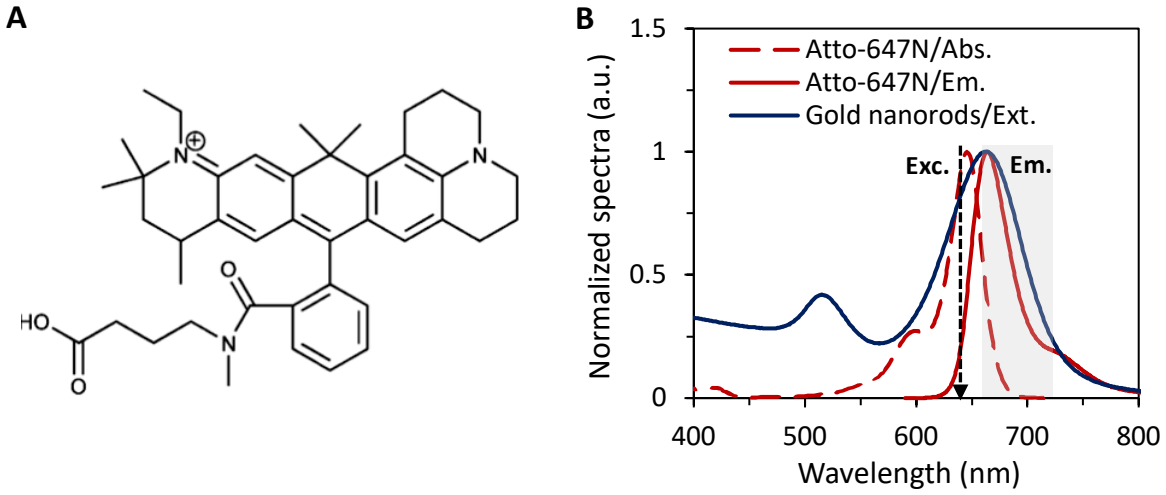

Figure 3.2 - Characteristics of Atto-647N dye and of the gold nanorods used. (A) Chemical structure of Atto-647N dye. (B) Spectral overlap between absorption (dashed red line) and emission (red line) of Atto-647N and the localized surface plasmon resonance (blue line) of the gold nanorods, with indication of the excitation wavelength at 639 nm and the detection range of the bandpass emission filter (grey rectangle).

Gold nanorods were immobilized at low surface density on a glass coverslip that had been previously silanized with (3-mercaptopropyl)-trimethoxysilane (MPTMS) to create a surface functionalized with thiol groups in order to attach covalently the gold nanorods. When excited using a laser of wavelength 482 nm, the optical microscopy image shows bright diffraction-limited spots with a narrow dispersion of emission intensity (Figure 3.3A). The photoluminescence spectrum collected from these spots was used for differentiating between single particles and aggregates, in order to select only the former ones for single-particle experiments. In each experiment at least 30 nanoparticles were selected from those that were clearly identified as individual ones from their emission spectra, as seen in Figure 3.3B. In the spectra, a Full Width at Half Maximum (FWHM) below 100 meV was used to identify individual nanorods.[3] The spectra of the particles exemplified in the figure had LSP peak wavelengths between 630 and 704 nm, which shows the heterogeneity of the sample.

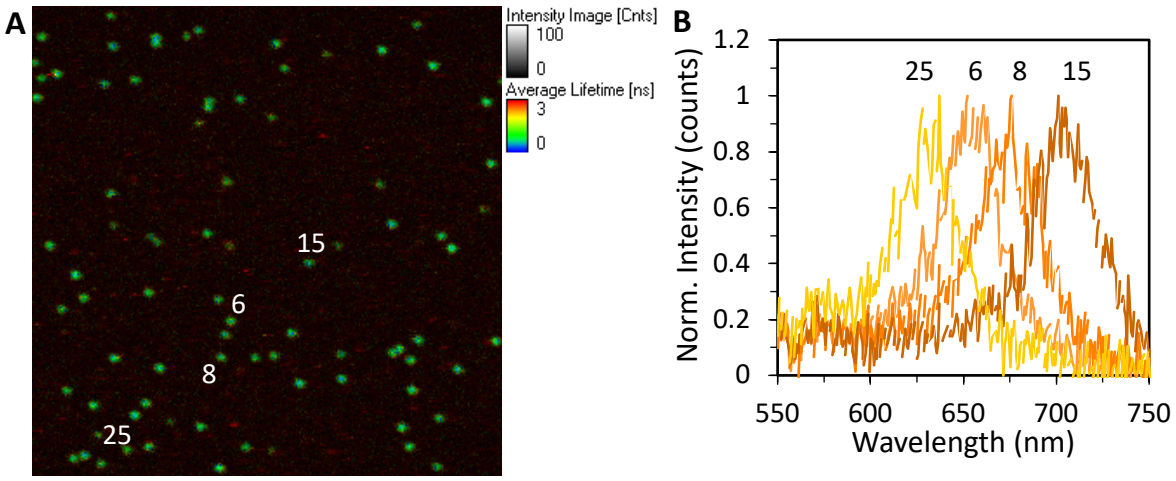

Figure 3.3 - Selection of single gold nanorods immobilized on a glass substrate. (A) Photoluminescence image of the particles, while irradiated with a laser excitation wavelength of 482 nm. (B) Emission spectra of four single nanorods identified as spots 6, 8, 15 and 25 in image (A), with distinct LSP bands, indicative of the sample's heterogeneity.

For fluorescence enhancement experiments, schematically illustrated in Figure 3.4A, a nanomolar solution of fluorescently-labeled oligonucleotide hybrids was used to immerse the gold nanorods, which were excited with a laser wavelength of 639 nm. This excitation wavelength simultaneously excites the dye's and the longitudinal plasmon band of the particles. The position of individual nanorods can be pinpointed on the surface from their photoluminescence emission (Figure 3.4B). Once immersed in a dilute dye solution, the individual molecules diffuse in the solution volume around the particle, and eventually one passes close to the hot-spot regions, thus experiencing the nanoantenna effect on its emission. By recording the fluorescence signalling in one of the nanorod spots, strong and discrete fluorescence emission bursts were observed in the emission intensity time traces (bottom panel of Figure 3.4C). These bursts are attributed to the stochastic interactions of single dye molecules with the hot-spot regions of the nanorods, thus confirming the particle's antenna effect. Control measurements were also performed, in which the intense emission events did not occur when measuring the emission from single nanorods in the absence of the dye, neither in regions of the surface where there was no nanorod particle - only free dye-labeled hybrids diffusing or adsorbed to the glass (Figure 3.4C).

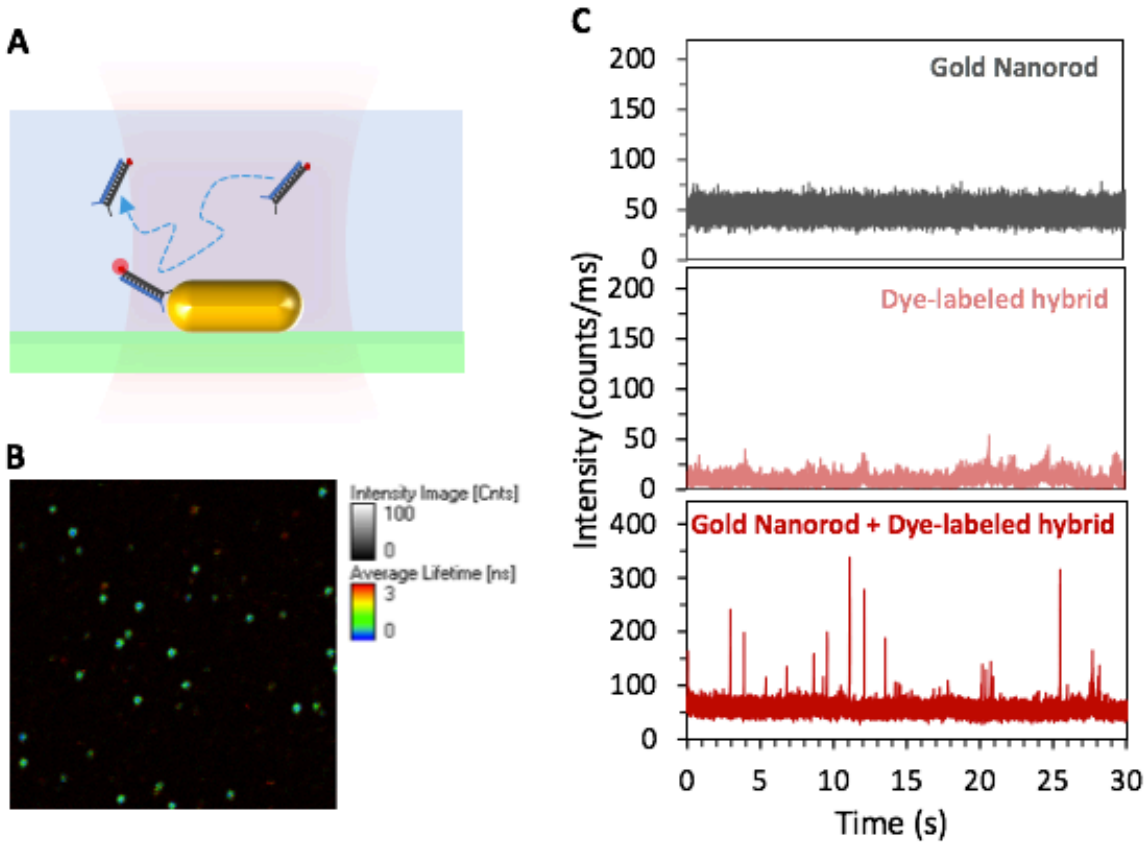

Figure 3.4 - Single dye molecule on a single gold nanorod experiment. (A) Scheme that illustrates the experiment. Oligonucleotide hybrids labeled with Atto-647N dye (red dot) diffusing in solution around a gold nanorod and eventually exploring the hot-spot regions. (B) Photoluminescence of the particles with excitation at 639 nm. (C) Fluorescence intensity time traces measured from an individual gold nanorod in the absence of dye-labeled oligonucleotides (in gray), from a region of the surface without any particle, but in the presence of dye-labeled hybrids (in pink) in nanomolar concentrations and from a single gold nanorod in the presence of the dye-labeled hybrids (in red), in the same concentration as before.

This experiment allowed to probe the largest enhancement effects that could be achieved with the gold nanorods. Analyzing the strongest fluorescence bursts in each time trace, top fluorescence enhancement factors were calculated (Figure 3.5A). These are the ratio between enhanced and non-enhanced emissions for that event, meaning that they correspond to the maximum burst intensity corrected for the background signal and normalized to the average intensity of a non-enhanced Atto-647N dye. The latter was determined through fluorescence correlation spectroscopy (FCS) measurements and was about 1.83 counts/ms for the same conditions of the enhancement experiment (see section 3.7.1 of Annexes). Top fluorescence enhancements of about two orders of magnitude and reaching up to almost 300-fold were obtained.

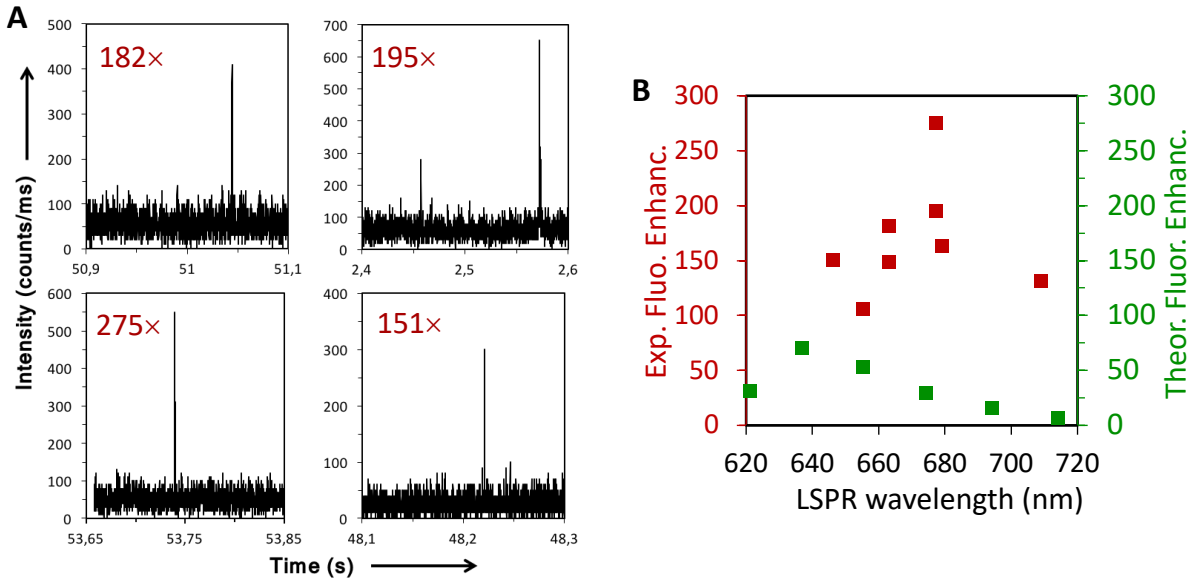

Figure 3.5 - Fluorescence enhancement factors for Atto-647N dye molecule interacting with the hot-spot regions of single gold nanorod antennas. (A) Examples of intense fluorescence bursts from dye's emission enhanced by the particles - the enhancement factor for each burst is indicated. (B) Comparison between experimental results and theoretical simulations performed by DDA.

The experimental results were compared with theoretical simulations performed by DDA (Figure 3.5B). The calculated enhancement factors were below the experimental ones, in particular at longer wavelengths. One plausible explanation for this could be that the random selection of nanorods is biased toward larger and more bright objects (due to limited sampling), which will contribute for larger fluorescence enhancements than the ones simulated (for which the nominal size from the manufacturer were assumed). It is also possible that the simplicity of the theoretical model and the numerical accuracy of DDA simulations could contribute to the mismatch in the enhancement factors. Nevertheless, the important outcome highlighted here is the feasibility of using gold nanorods as plasmonic antennas to enhance the fluorescence of a red-emitting dye such as Atto-647N.

3.3. Enhanced fluorescence of Atto-655 dye on DNA-assembled gold nanodimers

Most of the content of this section (and also parts of the annexes) was published in the following reference: Paulo, P. M. R.; *Botequim, D.*; Jóskowiak, A.; Martins, S.; Prazeres, D. M. F.; Zijlstra, P.; Costa, S. M. B. Enhanced Fluorescence of a Dye on DNA-Assembled Gold Nanodimers Discriminated by Lifetime Correlation Spectroscopy. *J. Phys. Chem. C* **2018**, *122* (20), 10971–10980. https://doi.org/10.1021/acs.jpcc.7b12622.

The fabrication of dimer nanostructures can be accomplished by nanolithography, but precise control of gap distances down to only a few nanometers is still challenging using these methods. Alternatively, wet-chemistry synthesis and supramolecular assembly approaches give access to dimers of gold nanoparticles with narrow interparticle distances. One successful approach is the use of DNA-directed self-assembly to produce dimer nanoparticles that perform efficiently as

plasmonic antennas.[4–8] Nevertheless, these methods generally require quite elaborate molecular arrangements of DNA (e.g., singly DNA-functionalized particles or DNA origami templates) that make the full process expensive and complex to replicate. On the other hand, the spontaneous aggregation of gold nanoparticles upon surface immobilization has also been shown to produce dimers that can be used as plasmonic antennas.[9] Although this is a very simple way to produce dimers, the process is intrinsically not selective for dimers, which then appear on the surface mixed with single particles and large aggregates.

In this work, a DNA-directed approach was adapted to assemble gold nanoparticles into dimers,[10] which is simple and does not rely on exactly one dsDNA in the gap, while being selective for dimer assembly contrasting to spontaneous particle aggregation. The performance of these dimer particles as plasmonic antennas for emission enhancement of a red-emitting dye, Atto-655, was investigated by single-molecule fluorescence microscopy, with the purpose to probe the largest enhancement factors that could be attained. The dimers used in fluorescence enhancement experiments were produced by bridging two nanoparticles with a DNA-based linker formed by hybridizing two thiolated oligonucleotides. These short linkers contain a central, double-stranded region of less than 60 base pairs and overhanging single-strand segments with 10 nucleotides (see Figure 3.14 of section 3.5.1 of Annexes for details).

The dimers produced displayed interparticle gaps of a few nanometers that can be observed in TEM images (Figure 3.6A,B). The gap distances are shorter than the length of the double-stranded region because of the single-strand segments on both ends of the DNA linker. The single-strand segments confer flexibility to the DNA linker and allow for the rigid double-strand segment to be positioned at a tilted angle within the gap, which would explain why the interparticle separation is shorter than the length of the double-stranded region. Another fundamental difference regarding this dimerization protocol relative to other described in the literature is that the DNA linkers are previously hybridized and only then added to the citrate-stabilized nanoparticles. In this way, it is possible that initially one (or few) DNA linker connects two particles at a tilted angle, before the particles get extensively coated, thereby, locking them at a separation distance smaller than the fully extended size of the linker.

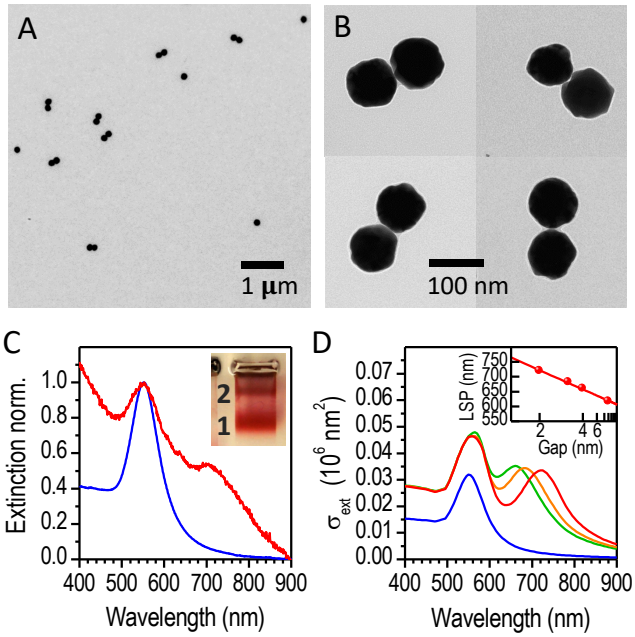

Figure 3.6 - DNA-directed approach used to assemble gold nanoparticles into dimers. (A) Electron microscopy images of dimers of gold nanoparticles with a diameter of 80 nm assembled by a DNA linker with a 60-bp double-stranded region. (B) Magnification of TEM images of four selected examples of dimer nanoparticles. (C) Extinction spectrum of dimers of gold nanoparticles (red curve) extracted from the gel band no. 2, and that of gold nanoparticles functionalized with DNA, but not dimerized (blue curve), separated from gel band no. 1 - the inset shows a photograph of the gel with bands indicated. (D) Calculated extinction spectra from DDA simulations of a single gold nanoparticle of 80 nm (blue curve) and that of dimer nanoparticles with a gap separation of 2, 3, and 4 nm (red, orange, and green curves, respectively) - the inset shows the peak wavelength of the LSP band, as a function of the gap separation considered in DDA simulations.

The fraction of dimer particles obtained after purification by gel electrophoresis, as observed from TEM images, was on average 68%, whereas single particles represent 23% of the analyzed samples. Single particles are present as smear in the gel and end up as a contamination in the dimer sample when extracted from the respective gel band (inset of Figure 3.6C). Gold nanoparticles that are only citrate-stabilized show a gel without any bands; only a smear is visible, which emphasizes the role of thiolated DNA linkers in particle assembly (Figure 3.16 of the Annexes).

The optical extinction spectrum of dimer particles features two surface plasmon bands instead of the single band that is characteristic of single gold nanoparticles (Figure 3.6C). This occurs because of plasmon coupling between the individual modes in neighboring particles of the dimer which gives rise to two optically active hybridized plasmon modes.[11] The surface plasmon band appearing at longer wavelengths corresponds to the bonding mode, and it generates strong local fields across the interparticle gap that are interesting for fluorescence enhancement. The resonance wavelength of the longitudinal plasmon mode depends strongly on the gap separation. For instance, at shorter gap distances, the plasmon coupling is stronger and this energy-stabilizing interaction induces a shift of the LSP band toward longer wavelengths. This effect is illustrated in Figure 3.6D that shows the calculated extinction spectra for dimers of gold particles of 80 nm simulated with gap distances of 2, 3, and 4 nm - red, orange, and green curves, respectively.

Using this plasmon ruler obtained from simulated spectra (inset of Figure 3.6D), estimation from the experimental spectrum of the dimer sample resulted in average interparticle distances around 2-3 nm, which matches well with results from TEM (Table 3.2 of the Annexes).

The dimer particles were further characterized by their optical spectrum measured at the single-particle level. For this purpose, dimer samples were immobilized onto glass coverslips at low surface density. The optical microscopy images show diffraction-limited spots with a narrow dispersion of emission intensity (Figure 3.7A,B). The photoluminescence spectrum was collected from several of these spots on each image. The spectrum of dimer particles typically features two bands: one more intense at around 550 nm accompanied by another band or shoulder at longer wavelengths (Figure 3.7C). It is clearly different from the spectrum of single particles that show only one band at 550 nm with a Lorentzian line shape - as exemplified in spectrum no. 6 of Figure 3.7C. Also, the emission intensity from dimer particles is approximately twice that of single particles, and in addition, the emission from single particles is non-polarized, whereas the dimers emission displays polarization in the sample plane. These features allow to easily distinguish the emission of individual dimers from that of a minor fraction of single particles that is always present even after purification by gel electrophoresis.

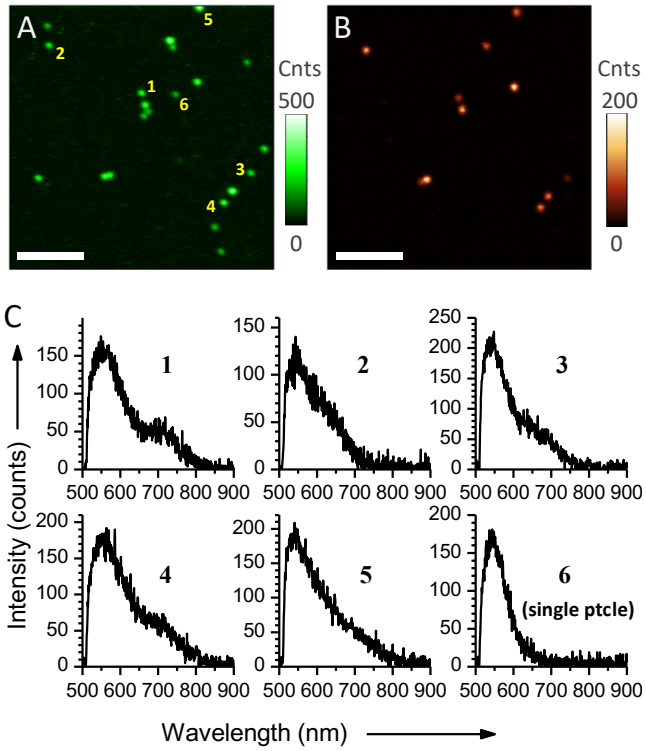

Figure 3.7 - Characterization of dimer nanoparticles by their optical spectrum measured at the single-particle level**.** (A) Optical microscopy image obtained with excitation at 482 nm (~50 kW/cm²) and detection with a longpass filter above 510 nm. Each spot on the image is a single dimer nanoparticle or an individual particle of size 80 nm - the scale bar is 5 μm. (B) Same area scan as shown in image (A) obtained with excitation at 639 nm (~4 kW/cm²) and detection with a bandpass filter centered at 695 nm with a transmission window of 55 nm. (C) Photoluminescence spectrum of single dimer particles identified as spots 1-5 in image (A) and one example of an individual gold nanoparticle labeled no. 6.

The emission spectrum of dimer particles changes slightly from particle to particle within each sample. In fact, the flexible ends of the DNA oligonucleotide linkers allow for some variation in the gap distance between paired particles, which strongly affects the LSP band of the dimer spectrum. This variation in the gap distance was first noticed in the TEM images of dimer samples (Figure 3.18 of the Annexes). Another contribution to heterogeneity in the emission spectrum of individual dimers arises from deviations from the spherical shape of the gold nanoparticles. Nevertheless, we have used the plasmon ruler shown in the inset of Figure 3.6D to infer about the approximate interparticle gap distance of dimer particles from their single particle spectra.

3.3.1. Single-molecule fluorescence enhancement of Atto-655 dye

The measurement of fluorescence enhancement in the emission of Atto-655 dye was performed by collecting light from one spot, at a time, from spots where an individual dimer is found. For this purpose, the dimer sample was immersed in a nanomolar solution of Atto-655 dye. During the measurement, the Atto-655 molecules diffuse and explore the space surrounding the individual dimer and eventually interact with the interparticle gap (Figure 3.8A). The interparticle gap is the hot-spot for fluorescence enhancement because of the large local field created there by the bonding plasmon mode. The broad spectral distribution of this plasmon mode, ranging from 600 to 800 nm, is suitable for fluorescence enhancement of red-emitting dyes. The emission of Atto-655 is well-matched with the longitudinal mode in dimers' spectra (Figure 3.8B), and for this reason, this dye was chosen to illustrate fluorescence enhancement.

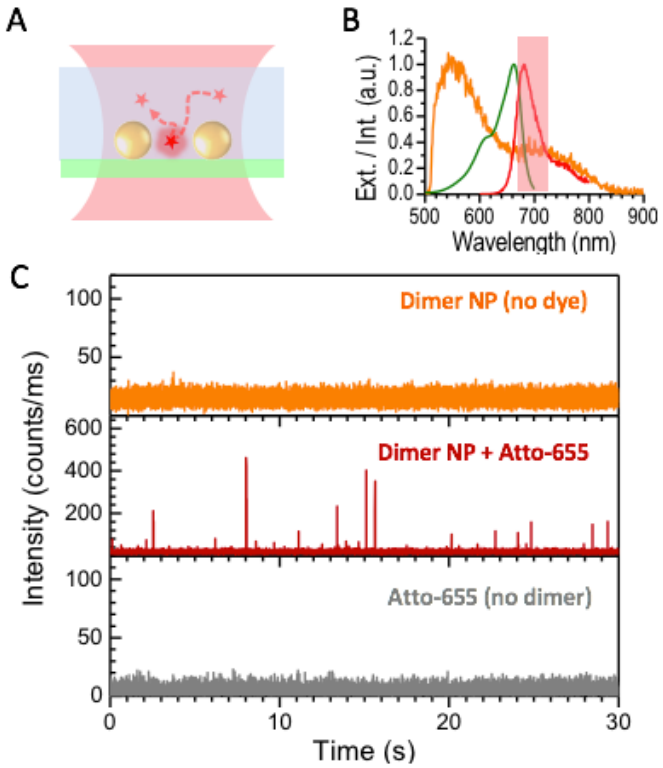

Figure 3.8 - Single-molecule fluorescence enhancement of Atto-655 dye. (A) Scheme of the enhancement experiment showing a single Atto-655 dye molecule (red star) diffusing through the gap (hot-spot) of a dimer nanoparticle. (B) Photoluminescence spectrum of an individual dimer nanoparticle (orange curve)

overlapped with the absorption and emission spectra of Atto-655 dye (green and red curves, respectively), and the detection range of the bandpass emission filter (light pink rectangle). (C) Emission intensity time traces measured from the spot of an individual dimer nanoparticle in the absence of Atto-655 dye in solution (top, orange curve); emission time trace from the same spot as before, but in the presence of Atto-655 dye in nanomolar concentrations (middle, red curve); emission time trace from a region of the surface without any particle, but in the presence of Atto-655 dye in the same concentration as previous (bottom, gray curve).

The enhancement effect was measured by using laser excitation at 639 nm, which addresses both the dye's absorption and the longitudinal plasmon band of the dimer nanoparticles (Figure 3.8B). The signal collected from the dimer nanoparticles when the dye is present in solution shows strong emission bursts in the time traces (red trace in Figure 3.8C). These events are several orders of magnitude more intense than the dimers' background signal. On the other hand, the signal from the dimer nanoparticles alone (in the absence of Atto-655) is steady over long observation times (orange trace in Figure 3.8C). The emission of Atto-655 molecules in solution, when collected from a surface region free of dimer nanoparticles, is also free of emission bursts (gray trace in Figure 3.8C). Therefore, strong fluorescence bursts are only detected from spots where dimers are immobilized and when Atto-655 molecules are present in solution.

The intense fluorescence bursts are attributed to the exploration of hot-spot regions on the surface of dimer nanoparticles by Atto-655 molecules diffusing in solution and transiently interacting with the DNA. The gap region is a very small volume, on the order of zeptoliters, when compared to the confocal detection volume which is around 4 fL. For the typical concentrations of Atto-655 used in the measurements, the dye's occupation number in the confocal detection volume varies between 1 and 10 and thus, the occupation probability of the gap region is several orders of magnitude lower, as further discussed below. For this reason, the probability of multiple occupancy of the gap region is negligible and each burst is ascribed to the exploration of the interparticle gap by only one dye molecule.

The duration and intensity of each fluorescence burst are closely related to the trajectory of the Atto-655 molecule as it diffuses across the interparticle gap. In this region, the plasmon's near-field changes rapidly. Likewise, the enhancement of the dye's excitation and emission varies as the dye's position changes in the gap. The spatial dependence of the emission enhancement effect together with the randomness of the dye's trajectory explains the intensity variations observed from burst to burst within each time trace collected for several dimers. In order to characterize the enhancement effect, this discussion will focus on the most intense event of each time trace. Some examples of intense bursts observed for dimers of 80 nm gold particles are presented in Figure 3.9A-D. As previously mentioned (§ 3.2), it was assumed that if the observation time is long enough, then the most intense event should correspond to the molecular trajectory through the region of largest fluorescence enhancement. The top enhancement factor is then calculated from the maximum burst intensity corrected for the background signal and normalized to the average

intensity of a non-enhanced Atto-655 dye. The latter was determined to be 0.35 counts/ms for the same conditions of the enhancement experiment (Figure 3.19 of the Annexes).

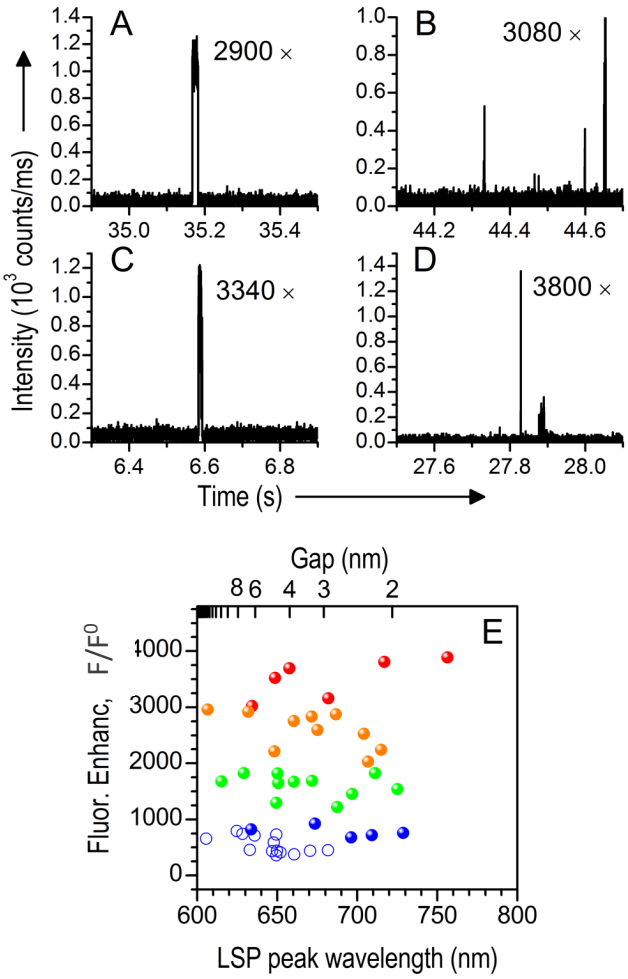

Figure 3.9 - Determination of emission enhancement factors and their relation with the LSP peak wavelength. (A-D) Examples of intense fluorescence bursts from Atto-655 emission enhanced by dimers of gold nanoparticles - the emission enhancement factor corresponding to each burst is indicated inside the figure. (E) Top emission enhancement factors for single-molecule fluorescence of Atto-655 dye plotted against the LSP peak wavelength of the individual dimer nanoparticles used for fluorescence enhancement. Each symbol represents a measurement on a different dimer nanoparticle within a total of 32 dimers analyzed. The symbols are color-coded according to the enhancement factor: blue, <1000; green, 1000-2000; orange, 2000-3000; and red, >3000. The open and closed symbols show enhancement factors obtained for dimers of 40 and 80 nm particles, respectively.

Dimers of gold particles with 40 nm were found to give maximum enhancement factors between 500- and 1000-fold (open symbols in Figure 3.9E). On the other hand, dimers of 80 nm particles are able to enhance the emission of Atto-655 by more than a 1000-fold, and in several examples, the top enhancements reach almost 4000-fold (closed symbols in Figure 3.9E). As expected, the emission enhancement increases with the dimer particle size because the radiative efficiency of the plasmon also increases. The range of enhancement factors is comparable for different linker sizes, which are shown together in Figure 3.9E, because the dimerization protocol

resulted in similar gap distances among samples. Surprisingly, a fraction of 16% of the dimers of 80 nm particles does not show any enhancement events in the sampled time interval of 60 s. This is tentatively attributed to an obstruction of dimer gaps with an excess of DNA linkers that prevents the dye to access the hot-spot region. Nevertheless, about 71% out from a total of 32 dimers analyzed shows events with top enhancements above 1000-fold, and out of these, about 16% is above 3000-fold.

The top enhancement factors reported here match up the largest known values from the literature for plasmonic emission enhancement of single-molecule fluorescence.[1,12,13] Recently, enhancement factors of 5000-fold on the emission of Atto-655 were reported with a system that uses complex nanostructures of DNA origami to assemble dimers of gold nanoparticles.[8] Another work reported on fluorescence enhancement using dimers spontaneously assembled by particle aggregation upon surface immobilization, which resulted in enhancement factors of more than 1000-fold.[9] In comparison, the dimer antennas used in this work deliver comparable or better enhancement factors, but using a DNA-directed assembly approach that is considerably more simple and affordable than those based on DNA origami, while being selective for dimer assembly which is not possible with spontaneous aggregation. This approach was further developed by separately functionalizing two samples of 80 nm gold nanospheres with complementary ssDNA sequences to assemble through hybridization both particle samples into a dimer.[14] The dimer nanospheres allowed, for weak emitters (porphyrins), unprecedented top fluorescence enhancement factors of 10^5 to 1 million.[14]

The plot of top enhancement factors *versus* the peak wavelength of the LSP band does not show any particular trend between these two experimental observables (Figure 3.9E), in contrast to other examples of plasmonic nanoparticles used for fluorescence enhancement, such as single gold nanorods.[1] A plausible explanation for this lack of correlation is that the molecular congestion of gaps with DNA linkers may limit or obstruct the dye's access to the central region of the hotspot by randomly occupying the interparticle volume. In Ref. 9, it was demonstrated that upon attaching bulky thiolated PEG chains onto the surface of dimer particles, the respective enhancement factors decrease, in agreement with an exclusion effect of the dye due to molecular crowding of the interparticle gap. Even though, in this work, the dimers are extensively coated with DNA, these linkers do not seem to have such a detrimental effect, and large enhancement factors above 1000-fold were measured in 71% of the dimers analyzed. Actually, it was hypothesized that the DNA linkers may increase the residence time of Atto-655 in the hot-spot, as supported by a simple argument based on the hot-spot volume and its expected occupancy. For this purpose, it was first determined from DDA simulations that the decay length of the plasmon field is around 10 nm in a direction perpendicular to the interparticle axis (for a dimer of 80 nm particles with a gap of 10 nm). Assuming that the hot-spot is approximately cylindrical with a radius and height of 10 nm × 10 nm gives a volume of 3.1 zL, for which an average dye concentration around 4 nM gives an occupancy of 7.6×10^{-6} molecules in the hot-spot. Another way to analyze this volume

occupancy results from multiplying it by the duration of time traces and calculate the estimated occupation time of one molecule in the hot-spot. For time traces with a duration of 60 s, this would correspond to one molecule being present in the hot-spot for about 450 μs during the time trace interval. The frequency of burst events observed ranges from 20 events up to several hundred per trace with an average burst duration around 120 μs (Figure 3.10). The total duration of enhanced emission events per time trace is generally much larger than the estimated occupation time of 450 μs. Thus, it was hypothesized that the dye's interaction with the DNA somehow favors the occupancy of the hot-spot and the observation of fluorescence enhancement from the dimer particles.

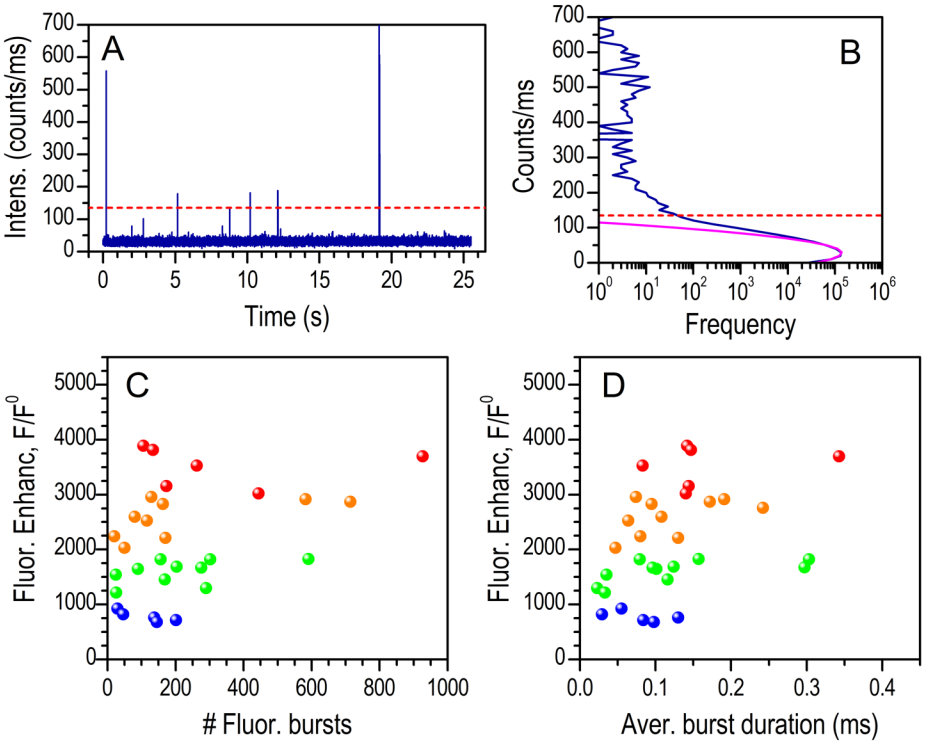

Figure 3.10 - Details of the intensity time traces. (A) Emission intensity time trace showing enhanced fluorescence bursts - the red-dashed line shows the threshold used to discriminate intense events of enhanced single-molecule fluorescence. An intensity threshold of $\mu + 6\sigma$ was used, as proposed in Ref. 7, where μ is the average background signal and σ is the standard deviation. (B) Photon count rate histogram from the emission trace shown in (A) and the normal distribution fitted to the background emission (magenta curve). This fitting was used to find the average background signal and its standard deviation (μ and σ, respectively). The number and duration of events with intensity above $\mu + 6\sigma$ were counted on each time trace for the 32 dimers analyzed. (C) Top emission enhancement factors for single-molecule fluorescence of Atto-655 dye plotted against the number of fluorescence bursts during the time trace. The symbols and respective colors represent the same enhancement factors shown in Figure 3.9E. (D) Similar plot using the average burst duration to represent the top enhancement factors. The weak correlation found in the plots (C,D) suggests that dimers with more available gaps, that is, showing a higher number of bursts or of longer duration, can reach higher enhancement factors.

Model simulations of gold nanoparticle dimers were performed to compare theoretical predictions of fluorescence enhancement with experimental results. The model dimers were defined for a particle size of 80 nm and the interparticle gap was varied between 2 and 10 nm.

Even for a gap separation of 10 nm, the near-field enhancement corresponds to an intensity increase of almost 1000-fold along the interparticle axis, but it decays within approx. 10 nm (Figure 3.11A). It was assumed three fixed positions of the dye in the gap, in order to evaluate how the fluorescence enhancement changes with the position (right side of Figure 3.11A). The enhancement of fluorescence emission results from the combined changes in the excitation, radiative, and non-radiative decay rates of the dye induced by interaction with the nanoparticle antenna. The enhancement factor of excitation rate (γ_{exc}) and fluorescence quantum yield (Φ_m/Φ_F) were calculated separately (see section 3.5.6 of the Experimental section). Here, the discussion will be focused on the overall emission enhancement, that is, $F/F_0 = \gamma_{exc} \times (\Phi_m/\Phi_F)$, and on the reduced fluorescence lifetime, that is, $\tau = 1/(K_r + K_{nr})$.

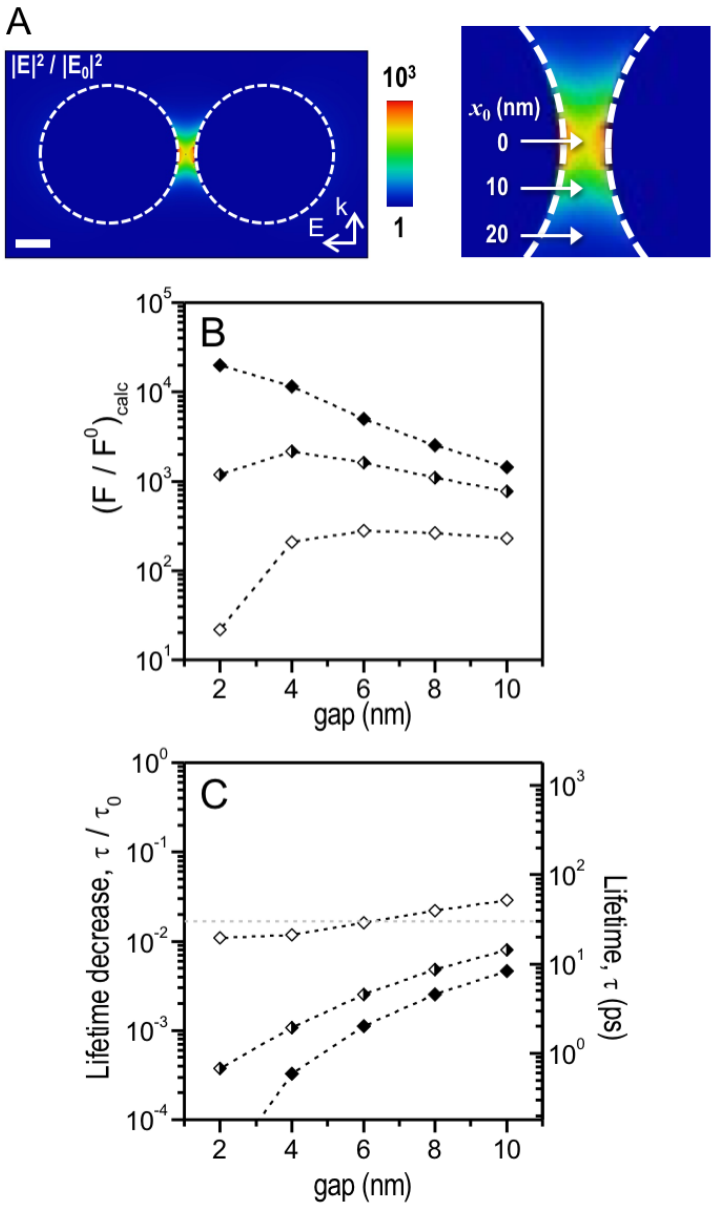

Figure 3.11 - Model simulations of gold nanoparticle dimers. (A) Near-field maps calculated from DDA simulations of a dimer of gold nanoparticles with a size of 80 nm and a gap separation of 10 nm for an

incident wavelength of 639 nm polarized across the interparticle axis - the scale bar is 20 nm. The near-field map on the right shows a magnification of the interparticle gap where the positions considered for the point-like dipole of the emitting dye molecule were fixed - the number shown is the displacement in nanometers away from the interparticle axis. (B) Enhancement factor calculated for the overall fluorescence emission F/F^0 for the interaction of Atto-655 dye with a dimer of gold nanoparticles of size 80 nm at different gap separations - closed symbols correspond to a dye molecule positioned at the interparticle joining axis, semifilled, and open symbols are for a position 10 and 20 nm away from the axis. (C) Fluorescence lifetime decrease (τ/τ_0) calculated for the same conditions described before, where τ_0 is the decay time of Atto-655 in water (1.8 ns).

The overall emission enhancements calculated for the central position of the gap yielded values ranging from 1000- to 10 000-fold increase in the dye's emission (Figure 3.11B). This result compares well with the experimental top enhancement factors which range from 1000- to almost 4000-fold. The comparison is made on the basis of the top enhancement values, assuming that these correspond to the dye being close to gap' s center, where the largest enhancements are expected. Actually, the absolute maximum is probably at some position along the interparticle axis shifted away from the center, where there is an optimal radiative over non-radiative decay rate enhancements.[7] On the other hand, the intensity distribution of each fluorescence burst experimentally measured is affected by the trajectory and residence time of the dye in the gap. The position dependence of the enhancement effect can be evaluated from the values of F/F_0 for positions away from the gap center (semifilled and open symbols in Figure 3.11B). The enhancement effect decreases by orders of magnitude over a few tens of nanometers, as it closely follows a similar distance dependence of the excitation rate enhancement. As previously hypothesized, the lack of correlation between top enhancements and the LSP peak wavelength of dimer particles may be explained by molecular hindrance of DNA linkers that limits the dye's access to the central region of the hot-spot. The strong spatial dependence of the overall emission enhancement, as seen in the calculations, suggests that this is a plausible explanation.

The interparticle distance has a pronounced effect in the LSP peak wavelength, as well as in the fluorescence enhancement although in two opposite ways. Short interparticle distances induce larger near-fields in the gap, which favor the dye's excitation and radiative decay rate enhancements, but the close proximity of the metal surface also favors the non-radiative decay through energy transfer and Ohmic losses. The interplay between these opposing factors reduces the variation of emission enhancement with the LSP peak wavelength (or conversely, the gap distance) in dimer particles. On the other hand, the effect on the fluorescence lifetime from the acceleration of radiative and non-radiative decay rates is always characterized by a pronounced lifetime decrease (Figure 3.11C). The predicted decay rates in the hot-spot region are in the picosecond and sub-picosecond timescales, which is below the time resolution of the setup (gray-dashed line). Indeed, the fluorescence decays retrieved from strong burst events show a decay profile that approximately coincides with the instrument response function (Figure 3.20 of the Annexes).

3.3.2. Analysis by Fluorescence Lifetime Correlation Spectroscopy

The fluorescence emission time traces contain detected photons from both enhanced and non-enhanced dye molecules within the confocal detection volume (Figure 3.12). As previously discussed, the emission decay time is strongly accelerated by plasmonic effects, which provides a way to distinguish from non-enhanced emission. This feature was explored here to discriminate enhanced from non-enhanced emission in the analysis of time traces using the method of Fluorescence Lifetime Correlation Spectroscopy (FLCS).[15,16] To the best of our knowledge, this approach had only been reported once for a similar purpose.[17] Other approaches for discriminating between enhanced and non-enhanced emissions typically involve at least two polarization-resolved measurements,[1,7,9] whereas FLCS approach can be performed from a single measurement.

The accelerated decay time associated with plasmon-enhanced fluorescence allows to clearly define a distinct fluorescence decay pattern that can be used in FLCS analysis to filter the correlation function of enhanced (and non-enhanced) emission. The fluorescence decays recorded simultaneously with each emission trace show multi-exponential decay profiles, which can be decomposed in short and long decay components, as shown in Figure 3.12B (red and blue curves, respectively). The short decay components are attributed to the enhanced decay rates of the dye together with some background signal from the dimer particle. It can be described by two exponential components with average decay times of 70 ps (84.5%) and 1.08 ns (3.5%). The long lifetime of 2.44 ns is similar to the lifetime of Atto-655 in aqueous solution (1.8 ns), although it is slightly longer probably because of adsorption onto the polymer-glass substrate. The FLCS analysis uses the decay components previously defined from decay analysis to build mathematical filters (Figure 3.12C), which are then used to weigh the detected photons in order to retrieve separate correlation functions for each decay component (Figure 3.12D). In this work, the FLCS analysis was used to distinguish between the correlation function of photons from enhanced dye molecules, which are associated with short decay times, from that of non-enhanced molecules (red and blue curves in Figure 3.12D).

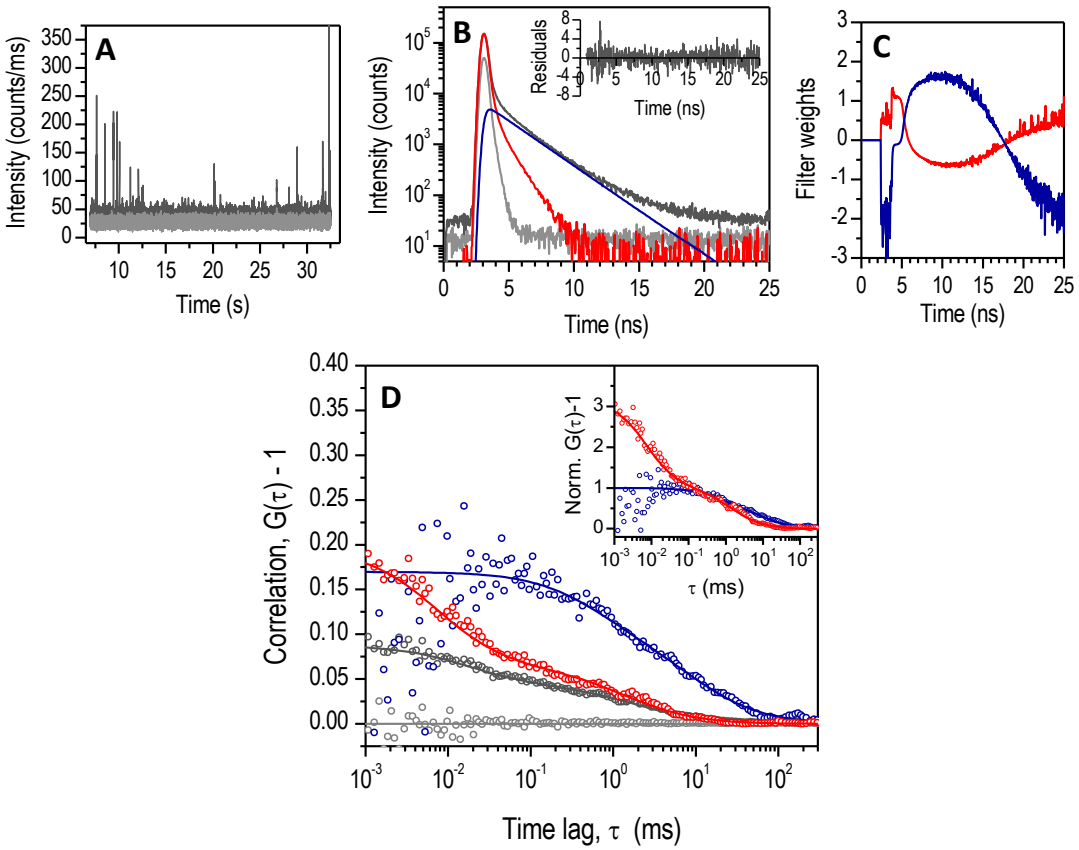

Figure 3.12 - Discrimination between enhanced and non-enhanced emission in the analysis of time traces using FLCS. (A) Emission intensity time trace showing intense fluorescence bursts from Atto-655 enhanced emission (dark gray) and background signal from the dimer particle alone (light gray). (B) Fluorescence decay of the same emission trace (dark gray) decomposed into short and long decay components shown as red and blue curves, respectively (IRF is depicted in light gray, and the inset shows the weighed residuals from a triexponential fit). (C) Filter weights obtained by FLCS analysis based on the short and long decay components defined to separate the enhanced and non-enhanced emissions (red and blue curves, respectively). (D) Correlation curve of enhanced and non-enhanced emissions (red and blue curves, respectively) obtained by FLCS analysis, and non-filtered correlation curve of the emission trace (dark gray) and of the background signal (light gray), as shown in (A).

The main difference between the correlation function of enhanced and non-enhanced emissions is that the first one shows an additional decay at short times that is not present in the latter. This trend was confirmed by performing the FLCS analysis of other emission traces showing substantial enhancement effects (Figure 3.21 of the Annexes). The correlation functions were fitted with the commonly used free-diffusion model, which afforded reasonable fits using two diffusion terms. The free-diffusion model was used here just to extract relaxation times, which are then compared to calculated diffusion times, in order to discuss the possible origin of the several decay components observed in the correlation function. As it will later become obvious, the free diffusion picture is not adequate to explain the results. The fast decay component that is only present in the correlation function of enhanced emission has an average relaxation time of 20 μs, and it can be associated with the short and very intense fluorescence bursts observed in emission traces. Assuming that these events correspond to dye molecules crossing the hot-spot in the gap region, the expected free-diffusion time would be in the sub-microsecond time scale because of the small

volume of the hot-spot. The estimated diffusion time would be 0.22 μs for an Atto-655 molecule diffusing in water across the transverse dimension of 10 nm calculated for the near-field in the gap region. The retrieved relaxation time of 20 μs could be tentatively explained by transient sticking of the dye to DNA linkers, or simply, by the limited time resolution of the correlation curves that allows only to measure a relaxation tail of the fast decay component.

On the other hand, the long decay component occurs on a similar time scale for the correlation function of enhanced and non-enhanced emissions (inset of Figure 3.12D). The average relaxation time of this long component is around 2.7 ms and is attributed to the dye's adsorption/desorption on the surface surrounding the dimer particle. A similar behavior has been previously reported for emission enhancement of single-molecule fluorescence using surface-immobilized gold nanorods.[1,18] The slower motion of dye molecules due to sticking onto the surface, or due to interaction with DNA linkers, seems to be corroborated by intense emission events that last longer than a few milliseconds, which are seldomly observed in emission traces (Figure 3.21 of the Annexes). Alternatively, it is possible to retrieve separate correlation functions for enhanced and non-enhanced emissions by using the polarization properties of the LSP mode.[9] Here, it was used the emission polarization of dimer particles to select those that are aligned in such a way that emission along the LSP mode, or perpendicular to it, was divided by the beam-splitter analyzer into two detection channels (Figure 3.13). The correlation function of the enhanced emission shows at short times an additional relaxation component that is not present in the correlation of non-enhanced emission, similarly to the FLCS analysis. The comparable results between these approaches validate the use of FLCS to separate enhanced from non-enhanced emission in plasmon-coupled fluorescence, as shown here.

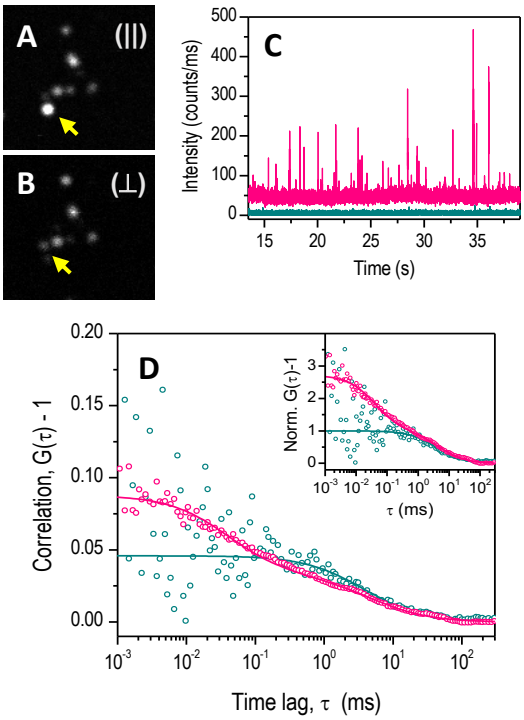

Figure 3.13 - Separation of correlation functions for enhanced and non-enhanced emissions by using the polarization properties of the LSP mode. (A, B) Optical microscopy images of dimer particles obtained with

excitation at 639 nm and emission analyzed by a beam-splitter cube into two mutually perpendicular polarizations, which are labeled as (||) and (⊥). The arrow indicates a dimer particle with emission from LSP mode aligned mostly with the polarization selected in the first channel (||) - the scale bar is 2 μm. (C) Emission intensity traces of Atto-655 dye in aqueous solution measured at the dimer particle indicated by the arrow in "A", or "B", showing that fluorescence bursts are only detected in the polarization of channel (||), which is aligned with the emission from LSP mode (pink trace), while the perpendicular polarization (⊥) does not show evidence of bursts (blue trace). (D) Correlation curves of the emission traces shown in (C) for the enhanced and non-enhanced emission (pink and blue symbols and curves, respectively) - the inset show normalized curves for the long decay components of the correlation.

3.4. Remarks

The performance of gold nanorods and gold nanodimers as plasmonic antennas for emission enhancement of Atto-647N and Atto-655 dyes, respectively, was investigated by single-molecule fluorescence microscopy. It was confirmed that both, rods and dimers, make efficient plasmonic antennas for fluorescence enhancement of red-emitting dyes. Gold nanorods with their hot-spot regions at the tips provided fluorescence enhancements of Atto-647N of two orders of magnitude, reaching in some cases, top enhancement factors of almost 300-fold.

Regarding the dimers of gold particles, produced by DNA self-assembly, the combination of large-sized nanoparticles having a diameter of 80 nm with nanometric gaps, generated hot-spots with intense near-fields in the interparticle region, that afforded enhanced fluorescence of Atto-655 dye by more than 1000-fold, whereas in some cases, top emission enhancements reached almost 4000-fold, which are comparable to the largest enhancement factors reported so far using colloidal methods.[8,9] It was further shown that fluorescence lifetime correlation spectroscopy can be used to separate plasmon-enhanced from non-enhanced emission. This analysis revealed a short relaxation component in the correlation curves that is exclusive of the enhanced emission, and it is tentatively attributed to dye interactions with the gap hot-spots. Further studies using this approach would enable to explore its potential in extracting more information from plasmon-enhanced fluorescence. The DNA-directed assembly approach used here is selective for dimer assembly, which is not possible with spontaneous particle aggregation, and is considerably simpler and more affordable than approaches based on DNA origami templates. These two features of dimer particles, that is, large fluorescence enhancements and preparation by affordable self-assembly colloidal methods, render these plasmonic antennas promising for applications in optical imaging or sensing.

3.5. Experimental section

3.5.1. Materials

Gold nanorods coated with cetyltrimethylammonium bromide (CTAB) with an approximate size of 25 nm × 60 nm and with a LSP peak wavelength of 664 nm (product no. A12-25-650-CTAB) were acquired from Nanopartz Inc. as aqueous suspensions with an optical density (OD) of 1. Gold nanoparticles with sizes of 80 and 40 nm, stabilized by a citrate coating,

were from Nanopartz Inc. as aqueous suspensions with an OD of 1 (product no. A11-80 and A11-40).

DNA oligonucleotides purified by high-performance liquid chromatography were purchased from STAB Vida (Monte da Caparica, Portugal). For fluorescence enhancement purposes using gold nanorods, thiolated DNA strands with the following sequences were used: a dye-labeled strand, (Atto-647N)-5'-GAGTCTGGAC-(C6-SH)-3' and a non-labeled complementary strand, 3'-CTCAGACCTG-(C6-SH)-5'. Considering gold nanoparticles dimer assembly, DNA strands with (n + 10) nucleotides and having the general sequence 5'-SH-$A_{10}N_n$-3' were used. Two oligonucleotides were designed for "n" equal to 15, 30, or 60, in such a way as to form hybrids by base pairing of the N_{15}, N_{30}, and N_{60} sequences, respectively (see diagram below). These oligonucleotides are modified at the 5' end with a thiol group that is linked through a C6 alkyl chain to a segment of ten adenines. When hybridized, the A10 segment of each oligonucleotide remains single stranded.

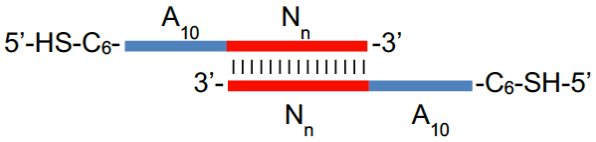

Figure 3.14 - Schematic diagram of the oligonucleotide pairs used to bridge gold nanoparticles.

The sequences of the oligonucleotides used in this work are shown below in Table 3.1.

Table 3.1 - Single stranded DNA oligonucleotide sequences used for preparation of dimers of gold nanoparticles.

Labels	Oligonucleotide sequences
SA15	5'-AAA AAA AAA ACG TAG GAG TCT GGA C-3'
PA15	5'-AAA AAA AAA AGT CCA GAC TCC TAC G-3'
SA30	5'-AAA AAA AAA AGT AAC GTC AAT GAG CAA AGG TAT TAA CTT T-3'
PA30	5'-AAA AAA AAA AAA AGT TAA TAC CTT TGC TCA TTG ACG TTA C-3'
SA60	5'-AAA AAA AAA AGA TTT CAC ATC TGA CTT AAC AAA CCG CCT GCG TGC GCT TTA CGC CCA GTA ATT CCG ATT A-3'
PA60	5'-AAA AAA AAA ATA ATC GGA ATT ACT GGG CGT AAA GCG CAC GCA GGC GGT TTG TTA AGT CAG ATG TGA AAT C-3'

CTAB was purchased from Sigma with a purity of ≥99%. (3-mercaptopropyl)-trimethoxysilane (MPTMS) was from Aldrich with 95% purity. Phosphate-buffered saline (PBS) buffer as tablets from Sigma was dissolved in ultrapure water (18.2 MΩ·cm). Tris base (Eurobio, molecular biology grade), boric acid (Fisher Chemical, assay 100%), and ethylenediaminetetraacetic acid (TCI Europe, 98%) were used to prepare TBE buffer. Sodium citrate tribasic dihydrate (Sigma-Aldrich, ≥ 99.5%) and hydrochloric acid (Sigma-Aldrich, 37%) were used to prepare citrate buffer. Agarose with an electrophoresis purity degree was purchased from NZYTech. Polyethylenimine, branched polymer

with an average $M_w \approx 25\,000$, was purchased from Aldrich. Ultrapure water was obtained with a Milli-Q purification system (Merck-Millipore) and used in all experiments. Microscope round coverslips of ∅ 22 mm were produced by Menzel-Gläser (Gerhard Menzel GmbH).

3.5.2. Instrumentation

Extinction spectra were measured in an UV/vis spectrophotometer from PerkinElmer, model Lambda 35. Transmission electron microscopy characterization was performed on a Hitachi H-8100 electron microscope operating at 200 kV. Glass surfaces were cleaned using an UV/ozone chamber model PSD-UV3 from Novascan. Single-molecule fluorescence experiments were performed on a confocal fluorescence lifetime microscope, MicroTime 200 (PicoQuant GmbH). Details of the microscope setup are described next. A pulsed laser source is coupled to an inverted optical microscope Olympus IX-71. For image acquisition, the laser excitation wavelength was 639 nm (LDH 635-b, PicoQuant) with a pulse repetition rate of 20 MHz. For single spectra acquisition, the laser excitation wavelength was 482 nm (LDH 485, PicoQuant) at 40 MHz. The objective is a 60× water immersion lens with a numerical aperture (NA) of 1.2 (UPLSAPO 60XW, Olympus). Sample emission passes through an excitation wavelength specific dichroic mirror and filter, followed by a 50 μm pinhole. The filter for the 639 nm laser was 695AF55 (Omega, bandpass filter centered at 695 nm with a 55 nm transmission window); the filter for the 482 nm laser was 510ALP (Omega, longpass filter). For image acquisition, the collimated emission continues through a 50/50 beam splitter for detection in two SPAD (single-photon avalanche diode) detectors (SPCM-AQR from PerkinElmer) and the signal is processed at a TimeHarp 200 TCSPC (Time-Correlated Single Photon Counting) PC board by PicoQuant, operating in time-tagged time-resolved mode (TTTR). For single spectra acquisition, sample emission is collected on a QE Pro (Ocean Optics) spectrometer, that was fiber coupled to the confocal microscope. The SymPhoTime software, version 5.3.2.2, from PicoQuant GmbH (Germany) was used for data acquisition and analysis. This program was also used to carry out data analysis by FLCS.[15,19]

3.5.3. Preparation of gold nanoparticle dimers

The first step was the hybridization of the thiolated DNA oligonucleotides to form a DNA linker with two thiol moieties, one at each end of the double strand (see previous Figure 3.14). Then, the double-stranded DNA linkers were used to assemble gold nanoparticles into dimers and larger aggregates in an approach similar to that described in Ref. 10. The concentration of DNA used was always more than a two-fold excess relative to the theoretical maximum number of thiolated oligos per particle, that is, approx. 1400 and 430 chains for gold particles with 80 and 40 nm, respectively.[20] The solution of pre-hybridized DNA linkers was mixed with citrate stabilized gold nanoparticles following the low pH protocol of Zhang et al.[21]. Briefly, DNA hybridization was performed by mixing the complementary sequences (8 μL each) with Tris-borate-EDTA (TBE) buffer (0.5×, 4 μL) containing added NaCl salt (200 mM). The mixture was heated up to

80 ºC for 15 min, then cooled down to room temperature, and left to rest overnight. The gold nanoparticles were concentrated by centrifugation from a volume of ~1000 μL of the solution supplied (OD~1) and collecting a volume of 26 μL from the pellet. This volume of particles was added to the DNA hybridization mixture under vigorous stirring and left to pre-incubate for 30 mins. Afterwards, a citrate buffer solution was added to the hybridization mixture. The citrate buffer solution was prepared according to the low pH protocol of Zhang et al.[21] and was added gradually by mixing 2 μL of buffer solution each time, followed by stirring and resting for 10 min before the next addition, up to a total of 4 addition steps. The final incubation time was 60 min. The reaction was halted by washing off the excess of DNA by centrifugation and replacing the supernatant with 0.5× TBE buffer. The large excess of DNA linkers and the low pH protocol were used to obtain an extensive surface functionalization of gold nanoparticles with oligonucleotides.

Gel electrophoresis was used to separate single particles from dimers and higher aggregates. The concentrations of agarose gels used were 0.7 and 1.5% for particles sized 80 and 40 nm, respectively. All gels were run at 120 V in 0.5× TBE buffer. Two red bands were typically obtained after 30 min. These particle-containing agarose fractions were cut from the gel and placed in a microtube filled with approx. 0.5 mL of 0.5× TBE buffer. The particles were allowed to diffuse from the gel pieces for at least one week. Samples containing the extracted gold nanoparticles were characterized by TEM, showing that the fraction extracted from the slowest migrating band contained mostly dimers.

3.5.4. Immobilization of gold nanoparticles on glass substrates

For the fixation of gold nanorods on glass substrates, round coverslips were cleaned by sonication in methanol during 30 min, followed by rinsing with water, drying in an oven and UV/ozone treatment for 60 min. After, silanization of the glass was performed by immersion of the clean slides in a 5% (v/v) solution of MPTMS in methanol for 30 min, then rinsing thoroughly with methanol to remove unbound silane from the glass surface, sonication for 10 min in methanol and blow drying with nitrogen. This procedure creates a glass surface functionalized with thiol groups, that is used to attach the particles covalently. Diluted solutions (OD = 1) of these particles were washed, to reduce the CTAB concentration and facilitate surface adhesion, through centrifugation (6000 rpm, 20 min) with supernatant substitution with an aqueous solution of CTAB (0.1 mM) at least two times. The washed suspension of nanoparticles (0.1 nM) was drop-casted on the silanized glass by leaving a 100 μL drop in contact with the glass for 20 min. Then, the glass surface was rinsed copiously with water, placed in 1× PBS for 45 min, washed again with water and blow dried with nitrogen.

Regarding immobilization of nanoparticle dimers, round glass coverslips were cleaned by sonication in aqueous solution of RBS50 detergent 5% (v/v) during 30 min, followed by another sonication in absolute ethanol and rinsing with water after each step. The dried coverslips were then irradiated for 2 h in the UV/ozone chamber. Before particle immobilization, the glass surface was coated with polyethyleneimine.[22] First, the coverslips were dipped in a cold piranha bath for

10 min to improve the surface wettability, then rinsed copiously with water, and dried. The polymer coating was deposited by covering the surface with an aqueous solution of polyethyleneimine 0.2% (w/v) during 20 min, then rinsing with water, and nitrogen blow drying. The gold nanoparticle dimers were immobilized by spin-coating 10 μL from a dilute (sub-nM) aqueous solution of these particles.

3.5.5. Details on fluorescence enhancement experiments

The surface immobilization conditions were previously optimized to obtain microscopy images showing well-dispersed diffraction-limited spots. The glass coverslips with immobilized nanorods or dimers were first observed in the confocal microscope under laser excitation at 482 nm using a power of approximately 50 kW/cm^2 to scan an area of 40 × 40 μm^2 (384 pixels per side) in the case of the nanorods, and 20 × 20 μm^2 (256 pixels per side) for the dimers, both with an integration time of 0.6 ms/pixel. Concerning the rods, they were immersed in 1× PBS, that was replaced three times to clean the glass surface. Then, the photoluminescence spectrum was collected out of a total of 30 particles selected per image, and each single nanorod was inferred by the LSP band. The dimer particles were immersed in ultrapure water during this kind of measurements and the photoluminescence spectrum was also collected for each dimer particle within a total of 10-15 particles selected per image. The LSP band was used to infer the gap separation using a plasmon ruler relation determined from the simulation results.

The laser excitation was changed to 639 nm, and the same area was scanned with an excitation power of ca. 4.8 (for nanorods) and 4 kW/cm^2 (for nanodimers). The diffraction-limited spots in the new image were matched to the previously identified nanorods or dimers. The fluorescence intensity time trace was measured at 639 nm using an excitation power of ca. 1.6 or 0.4 kW/cm^2 respectively for each nanorod or dimer. At this point, the nanorods or the dimers were immersed in PBS or in ultrapure water, respectively. The purpose of measuring intensity time traces was to characterize the background signal from the nanoparticle(s) photoluminescence emission and to confirm the absence of fluorescence bursts later attributed to the enhanced fluorescence from dye molecules interacting with the plasmonic nanostructures. Then, in the case of the gold nanorods, the PBS solution was replaced with a nanomolar solution of Atto-647N labeled dsDNA - hybridization between the dye-labeled (10 nM) and the non-labeled (20 nM) DNA strands was performed in 1× PBS during 2 hours at room temperature. $NiCl_2$ (5 mM) was used in the DNA mixture to cause photobleaching of the surface-adsorbed dye. As for the dimers, the water drop covering them was replaced with a diluted aqueous solution of Atto-655 dye with a concentration of a few nanomolar. The exact concentration of Atto-655 was determined for each experiment by performing a FCS measurement at a depth of 10 μm inside the dye solution, which afforded values of dye concentration in the range of 0.7-4.8 nM. The emission intensity time trace of each nanorod and dimer was remeasured, at powers of 1.6 and 0.4 kW/cm^2, respectively, now in the presence of Atto-647N labeled hybrid or Atto-655 dye in aqueous solution. During the 60 s' time acquisition, it was possible to observe, in most cases, from tens to hundreds of strong fluorescence emission

events. The fluorescence enhancement factors for each particle were evaluated by comparing with the non-enhanced average emission of the single dye, as determined from FCS measurements at the same excitation power, similarly to other studies reported in the literature.[1,7,18]

3.5.6. Discrete dipole approximation simulations

Simulations of discrete dipole approximation were performed at the host laboratory in order to obtain the near-field intensity maps from model nanostructures. The free software implementation A-DDA was used for running these simulations,[23] using the subroutine for near-field included in the software package.[24] The theoretical formalism described by D'Agostino et al. was used for calculating the enhanced radiative and non-radiative decay rates, as detailed below.[25] The overall emission enhancement (F/F^0) can be estimated as the product of the excitation rate enhancement (γ_{exc}) and the relative emission quantum yield of the dye as modified by the metal nanoparticle(s) (Φ_m/Φ_F). The excitation rate enhancement is obtained from $\gamma_{exc} = |\boldsymbol{E}|^2/|\boldsymbol{E_0}|^2$, which is the near-field enhancement at the incident wavelength (639 nm) in the position assumed for the dye molecule. The fluorescent dye is modelled as a point-like dipole (p_0) emitting at a specific wavelength. The near-field of the emitting dipole excites the surface plasmon of the nearby metal particle(s) and the scattered field (E_{scat}) at the dipole's position accelerates its spontaneous decay rate.[25] This rate is expressed as the sum of the metal enhanced radiative (K_r) and non-radiative decay rates (K_{nr}) that appears in the numerator of the *l.h.s.* of the following equation,

$$\frac{K_{\mathrm{r}} + K_{\mathrm{nr}}}{k_r} = 1 + \frac{6\pi\varepsilon_0\varepsilon_{\mathrm{B}}}{k^3|\mathbf{p}_0|^2}\,\mathrm{Im}[\mathbf{p}_0^{*}\cdot\mathbf{E}_{\mathrm{scat}}(\mathbf{r}_0)] \tag{1}$$

where r_0 is the position of the dye molecule, k_r is the intrinsic radiative decay rate, ε_0 and ε_B are the dielectric constants of vacuum and background medium, and k is the wavenumber of emitted light. The metal enhanced non-radiative decay rate can be estimated from the time-averaged power absorbed by the metal nanoparticles:

$$K_{\mathrm{nr}} = \frac{P_{\mathrm{abs}}}{\hbar\omega} \approx \frac{\varepsilon_0}{2\hbar}\,\mathrm{Im}(\varepsilon)\sum_{i=1}^{N}\left|\mathbf{E}_{\mathrm{local},i}\right|^2 \times V_c \tag{2}$$

where ε is the dielectric function of gold, $\mathbf{E}_{\mathrm{local.i}}$ is the internal electric field at the position of the i^{th} dipole, and V_c is the volume of the cubic elements. From the accelerated K_r and K_{nr}, rates calculated by using equations 1 and 2, the modified quantum-yield of the dye can be found,

$$\phi = \frac{K_{\mathrm{r}}}{K_{\mathrm{r}} + k_{\mathrm{r}}(1/\phi^0 - 1) + K_{\mathrm{nr}}} \tag{3}$$

The overall emission enhancement, F/F_0, was obtained from the spectral average of enhancement factors, $f(\lambda)/f^0$, calculated at several wavelengths across the emission range selected

by the detection filter and weighed by the normalized emission spectrum, $S(\lambda)$, of Atto-655 dye, i.e. $F/F^0 = \int f(\lambda)/f^0 \times S(\lambda)d\lambda$. The overall emission enhancement resulting from spectral averaging reflects the fact that different spectral components of the emission spectrum of the dye are enhanced by different amounts, as discussed in Ref. 1. The enhancement factors F/F^0 given in this work were calculated between 670 and 720 nm with intervals of 10 nm. The details on the position of the dye within the gap of the dimer nanoparticle are described in section 3.3.1 of the main text. The dye's transition dipole moment was fixed in a parallel orientation relative to the interparticle joining axis, in order to maximize the calculated enhancement effect. In the experiment, the orientation of dye molecule is not fixed and assuming a fast and free rotation of the dye molecule, it would be more fair a comparison with orientationally averaged theoretical enhancement factors. Nevertheless, the calculated enhancements considering the fixed parallel orientation serve the purpose of comparing the maximum emission enhancements obtained both experimentally and theoretically.

3.6. References

(1) Khatua, S.; Paulo, P. M. R.; Yuan, H.; Gupta, A.; Zijlstra, P.; Orrit, M. Resonant Plasmonic Enhancement of Single-Molecule Fluorescence by Individual Gold Nanorods. *ACS Nano* **2014**, *8* (5), 4440–4449. https://doi.org/10.1021/nn406434y.
(2) Atto-647N manufacturer. https://www.atto-tec.com/fileadmin/user_upload/Katalog_Flyer_Support/Catalogue_2009_2010.pdf (Accessed: 02 August 2020).
(3) Sönnichsen, C.; Franzl, T.; Wilk, T.; von Plessen, G.; Feldmann, J.; Wilson, O.; Mulvaney, P. Drastic Reduction of Plasmon Damping in Gold Nanorods. *Phys. Rev. Lett.* **2002**, *88* (7). https://doi.org/10.1103/PhysRevLett.88.077402.
(4) Busson, M. P.; Rolly, B.; Stout, B.; Bonod, N.; Bidault, S. Accelerated Single Photon Emission from Dye Molecule-Driven Nanoantennas Assembled on DNA. *Nat. Commun.* **2012**, *3* (1). https://doi.org/10.1038/ncomms1964.
(5) Acuna, G. P.; Moller, F. M.; Holzmeister, P.; Beater, S.; Lalkens, B.; Tinnefeld, P. Fluorescence Enhancement at Docking Sites of DNA-Directed Self-Assembled Nanoantennas. *Science* **2012**, *338* (6106), 506–510. https://doi.org/10.1126/science.1228638.
(6) Bidault, S.; Devilez, A.; Maillard, V.; Lermusiaux, L.; Guigner, J.-M.; Bonod, N.; Wenger, J. Picosecond Lifetimes with High Quantum Yields from Single-Photon-Emitting Colloidal Nanostructures at Room Temperature. *ACS Nano* **2016**, *10* (4), 4806–4815. https://doi.org/10.1021/acsnano.6b01729.
(7) Zhang, T.; Gao, N.; Li, S.; Lang, M. J.; Xu, Q.-H. Single-Particle Spectroscopic Study on Fluorescence Enhancement by Plasmon Coupled Gold Nanorod Dimers Assembled on DNA Origami. *J. Phys. Chem. Lett.* **2015**, *6* (11), 2043–2049. https://doi.org/10.1021/acs.jpclett.5b00747.
(8) Puchkova, A.; Vietz, C.; Pibiri, E.; Wünsch, B.; Sanz Paz, M.; Acuna, G. P.; Tinnefeld, P. DNA Origami Nanoantennas with over 5000-Fold Fluorescence Enhancement and Single-Molecule Detection at 25 μM. *Nano Lett.* **2015**, *15* (12), 8354–8359. https://doi.org/10.1021/acs.nanolett.5b04045.
(9) Punj, D.; Regmi, R.; Devilez, A.; Plauchu, R.; Moparthi, S. B.; Stout, B.; Bonod, N.; Rigneault, H.; Wenger, J. Self-Assembled Nanoparticle Dimer Antennas for Plasmonic-Enhanced Single-Molecule Fluorescence Detection at Micromolar Concentrations. *ACS Photonics* **2015**, *2* (8), 1099–1107. https://doi.org/10.1021/acsphotonics.5b00152.
(10) Lan, X.; Chen, Z.; Liu, B.-J.; Ren, B.; Henzie, J.; Wang, Q. DNA-Directed Gold Nanodimers

with Tunable Sizes and Interparticle Distances and Their Surface Plasmonic Properties. *Small* **2013**, *9* (13), 2308–2315. https://doi.org/10.1002/smll.201202503.
(11) Nordlander, P.; Oubre, C.; Prodan, E.; Li, K.; Stockman, M. I. Plasmon Hybridization in Nanoparticle Dimers. *Nano Lett.* **2004**, *4* (5), 899–903. https://doi.org/10.1021/nl049681c.
(12) Kinkhabwala, A.; Yu, Z.; Fan, S.; Avlasevich, Y.; Müllen, K.; Moerner, W. E. Large Single-Molecule Fluorescence Enhancements Produced by a Bowtie Nanoantenna. *Nat. Photonics* **2009**, *3* (11), 654–657. https://doi.org/10.1038/nphoton.2009.187.
(13) Yuan, H.; Khatua, S.; Zijlstra, P.; Yorulmaz, M.; Orrit, M. Thousand-Fold Enhancement of Single-Molecule Fluorescence Near a Single Gold Nanorod. *Angew. Chem. Int. Ed.* **2013**, *52* (4), 1217–1221. https://doi.org/10.1002/anie.201208125.
(14) Francisco, A. P.; Botequim, D.; Prazeres, D. M. F.; Serra, V. V.; Costa, S. M. B.; Laia, C. A. T.; Paulo, P. M. R. Extreme Enhancement of Single-Molecule Fluorescence from Porphyrins Induced by Gold Nanodimer Antennas. *J. Phys. Chem. Lett.* **2019**, *10* (7), 1542–1549. https://doi.org/10.1021/acs.jpclett.9b00373.
(15) Gregor, I.; Enderlein, J. Time-Resolved Methods in Biophysics. 3. Fluorescence Lifetime Correlation Spectroscopy. *Photochem Photobiol Sci* **2007**, *6* (1), 13–18. https://doi.org/10.1039/B610310C.
(16) Ghosh, A.; Karedla, N.; Thiele, J. C.; Gregor, I.; Enderlein, J. Fluorescence Lifetime Correlation Spectroscopy: Basics and Applications. *Methods* **2018**, *140–141*, 32–39. https://doi.org/10.1016/j.ymeth.2018.02.009.
(17) Ray, K.; Zhang, J.; Lakowicz, J. R. Fluorescence Lifetime Correlation Spectroscopic Study of Fluorophore-Labeled Silver Nanoparticles. *Anal. Chem.* **2008**, *80* (19), 7313–7318. https://doi.org/10.1021/ac8009356.
(18) Khatua, S.; Yuan, H.; Orrit, M. Enhanced-Fluorescence Correlation Spectroscopy at Micro-Molar Dye Concentration around a Single Gold Nanorod. *Phys. Chem. Chem. Phys.* **2015**, *17* (33), 21127–21132. https://doi.org/10.1039/C4CP03057E.
(19) Kapusta, P.; Macháň, R.; Benda, A.; Hof, M. Fluorescence Lifetime Correlation Spectroscopy (FLCS): Concepts, Applications and Outlook. *Int. J. Mol. Sci.* **2012**, *13* (12), 12890–12910. https://doi.org/10.3390/ijms131012890.
(20) Hill, H. D.; Millstone, J. E.; Banholzer, M. J.; Mirkin, C. A. The Role Radius of Curvature Plays in Thiolated Oligonucleotide Loading on Gold Nanoparticles. *ACS Nano* **2009**, *3* (2), 418–424. https://doi.org/10.1021/nn800726e.
(21) Zhang, X.; Gouriye, T.; Göeken, K.; Servos, M. R.; Gill, R.; Liu, J. Toward Fast and Quantitative Modification of Large Gold Nanoparticles by Thiolated DNA: Scaling of Nanoscale Forces, Kinetics, and the Need for Thiol Reduction. *J. Phys. Chem. C* **2013**, *117* (30), 15677–15684. https://doi.org/10.1021/jp403946x.
(22) Teixeira, R.; Paulo, P. M. R.; Viana, A. S.; Costa, S. M. B. Plasmon-Enhanced Emission of a Phthalocyanine in Polyelectrolyte Films Induced by Gold Nanoparticles. *J. Phys. Chem. C* **2011**, *115* (50), 24674–24680. https://doi.org/10.1021/jp209605v.
(23) Yurkin, M. A.; Hoekstra, A. G. The Discrete-Dipole-Approximation Code ADDA: Capabilities and Known Limitations. *J. Quant. Spectrosc. Radiat. Transf.* **2011**, *112* (13), 2234–2247. https://doi.org/10.1016/j.jqsrt.2011.01.031.
(24) D'Agostino, S.; Pompa, P. P.; Chiuri, R.; Phaneuf, R. J.; Britti, D. G.; Rinaldi, R.; Cingolani, R.; Della Sala, F. Enhanced Fluorescence by Metal Nanospheres on Metal Substrates. *Opt. Lett.* **2009**, *34* (15), 2381. https://doi.org/10.1364/OL.34.002381.
(25) D'Agostino, S.; Della Sala, F.; Andreani, L. C. Dipole-Excited Surface Plasmons in Metallic Nanoparticles: Engineering Decay Dynamics within the Discrete-Dipole Approximation. *Phys. Rev. B* **2013**, *87* (20). https://doi.org/10.1103/PhysRevB.87.205413.
(26) *Single Molecule Detection in Solution: Methods and Applications*, 1st ed.; Zander, C., Enderlein, J., Keller, R. A., Eds.; Wiley-VCH: Berlin, 2002.

3.7. Annexes

3.7.1. Emission brightness of a non-enhanced Atto-647N dye

The determination of the single-molecule fluorescence emission from non-enhanced Atto-647N dye labeled onto the dsDNA was performed by FCS measurements with a laser excitation of 639 nm (Figure 3.15A). From the experimental autocorrelation function that was fitted with a single-species 3D Brownian diffusion model (Figure 3.15B), the average number of molecules in the detection volume, N, was obtained. By dividing the average fluorescence intensity (Figure 3.15C), discounted from the background noise, over N, it resulted a value of 1.83 counts/ms for the brightness of a single Atto-647N dye (non-enhanced).

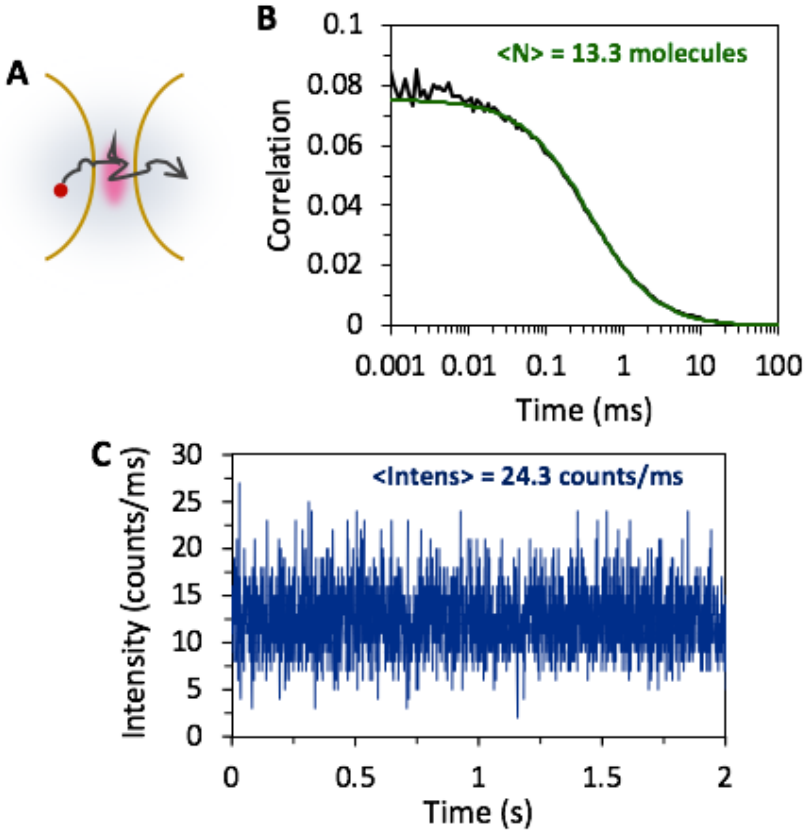

Figure 3.15 - Determination of the emission brightness of a non-enhanced Atto-647N dye. (A) Scheme of the fluorescence correlation spectroscopy experiment implemented to determine the average number, N, of Atto-647N dye molecules (labeled onto DNA hybrids; red dot) in the detection volume of the microscope, while irradiating at a laser excitation of 639 nm. (B) Experimental autocorrelation function (black curve) and single-exponential fitting (green curve) that afforded N equal to 13.3 molecules. (C) Fluorescence intensity time trace from Atto-647N dye in aqueous solution for the same excitation power and detection conditions used in the single-molecule and single-particle experiment. The average intensity of 24.3 counts/ms was discounted from the background noise (0.39 counts/ms measured in PBS) and divided by the average number of 13.3 molecules, being obtained an emission intensity of 1.83 counts/ms for single Atto-647N dye non-enhanced.

3.7.2. Characterization of spherical gold nanodimers

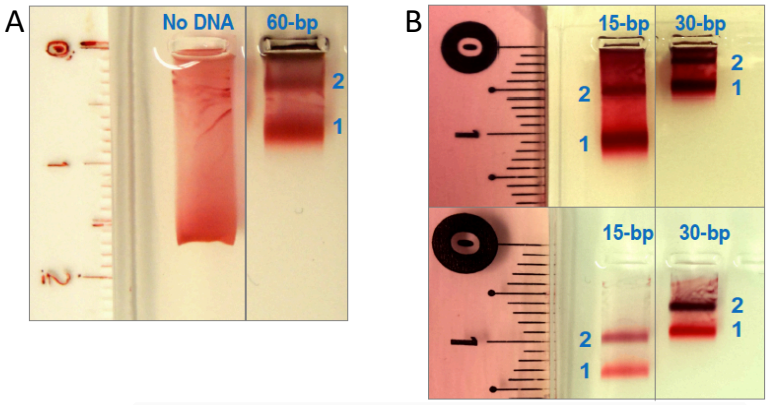

Figure 3.16 - Agarose gel electrophoresis used for purification of dimer nanoparticles. (A) Comparison of a gel from a sample of gold nanoparticles of 80 nm that are only citrate-stabilized ("No DNA") with a sample that has been functionalized with an oligonucleotide pair with N_{60} sequence ("60-bp"). The former gel does not show bands, while the later shows two bands: no. 1 is mostly formed by single particles and no. 2 contains dimer particles. (B) Purification gel of a sample of gold nanoparticles of 40 nm that has been functionalized with oligonucleotide pairs with N_{15} and N_{30} sequences ("15-bp" and "30-bp", respectively). Also, band no. 1 is mostly formed by single particles and no. 2 contains dimer particles. The bottom image shows re-purification gels of the material extracted from band no. 2 of the gels in the top image.

Samples of dimer particles extracted from band no. 2 in the purification gels were evaporated onto a Formvar coated copper grid and imaged by transmission electron microscopy. Two types of images were collected: low magnification (approx. 6 × 8 μm^2) images that were used to estimate the fraction of dimers of the sample; and high magnification (approx. 400 × 530 nm^2) images that were used to measure the gap separation between dimer particles (Figure 3.17).

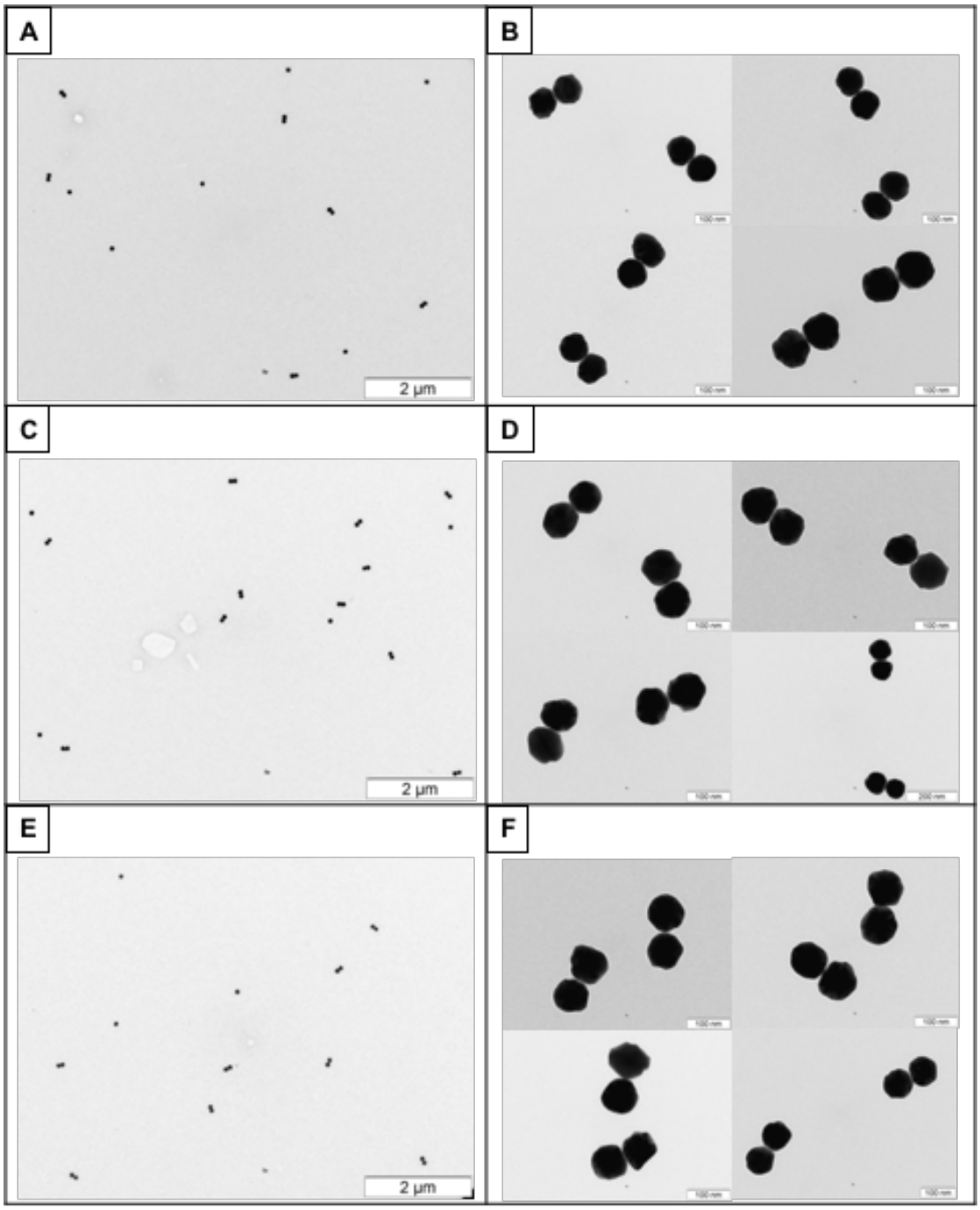

Figure 3.17 - Transmission electron microscopy (TEM) images of dimers of gold nanoparticles with a size of 80 nm. Assembly by DNA linkers with: (A, B) N_{15} sequence; (C, D) N_{30} sequence and; (E, F) N_{60} sequence. The images on the left (A, C, E) show low magnification (or large area) images used to determine the fraction of dimer particles after purification, while the images on the right (B, D, F) show high magnification images used to measure gap separation distances (see Table 3.2).

The analyzed samples of dimers assembled with DNA linkers N_{15}, N_{30} and N_{60} show that the major fraction is that of dimer particles, respectively 55.0, 74.8 and 76.4 % (Table 3.2). In the chapter's main text, it is only mentioned the average fraction of dimers of 68% obtained from the several samples listed in this table. The high magnification images show that the separation between dimer particles is very short. The measured gap distances of dimer samples assembled with DNA linkers N_{15}, N_{30} and N_{60} resulted in average values of 2.8, 2.7 and 2.3 nm, respectively.

Table 3.2 - Results from analysis of TEM images of dimer particle samples assembled with DNA linkers N_{15}, N_{30} and N_{60}. The fraction of particles identified as single (n = 1), dimers (n = 2) and larger aggregates (n > 2) from low magnification images comprising more than 500 particles analyzed per type of linker. The average gap distance is measured for a subset of dimer particles from the high magnification images.

	% of particles assembled						Gap measurements		
DNA linker	No. samples	No. images	No. ptcls	n=1 (single)	n=2 (dimer)	n>2 (large aggs.)	No. images	No. dimers	Average gap/nm
N_{15}	2	23	618	32.0	55.0	13.0	6	11	2.8
N_{30}	2	27	580	18.7	74.8	6.5	10	17	2.7
N_{60}	2	27	588	19.8	76.4	3.8	8	15	2.3

The large particle size when compared with gap distances makes it complicated to evaluate precisely the gap distance, particularly, because the particles are not perfectly spherical. Moreover, it is also possible that artifacts from sample preparation and measurement (in vacuum conditions) could affect the gap separation of dimers evaporated onto the TEM grid (Figure 3.18). Nonetheless, the gap distances determined from TEM images agree with that inferred from optical spectra (see main text). In this work, preference was given to gap distances inferred from single-particle spectra using a plasmon ruler relation, because these can be directly related to the fluorescence enhancement effect observed for a particular dimer particle.

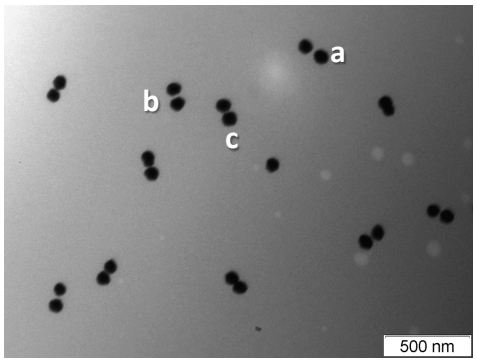

Figure 3.18 - Electron microscopy image of dimers of gold nanoparticles with a size of 80 nm assembled by a DNA linker with a 60-bp double-stranded region. The selected examples "a" to "c" illustrate dimer nanoparticles that show diverse gap separations, as it can be visually perceived from this TEM image. In most cases, the gap separation is practically unperceivable, such as the example of dimer "c", which represents the majority of dimer particles observed. Nevertheless, even in those cases there could be small gap variations at the nanometer scale from particle to particle that significantly affect their optical spectra, in particular the longitudinal plasmon component at longer wavelengths (see Figure 3.6D of the main text).

3.7.3. Emission brightness of single non-enhanced Atto-655 dye

The average intensity of a non-enhanced Atto-655 dye was determined from a FCS measurement similarly to that described in section 3.7.1 (Figure 3.19A,B). From such a measurement, the average number of molecules in the detection volume (Figure 3.19C), and their

average emission intensity (Figure 3.19C) were acquired, being obtained a value of 0.35 counts/ms for the brightness of single Atto-655 dye (non-enhanced).

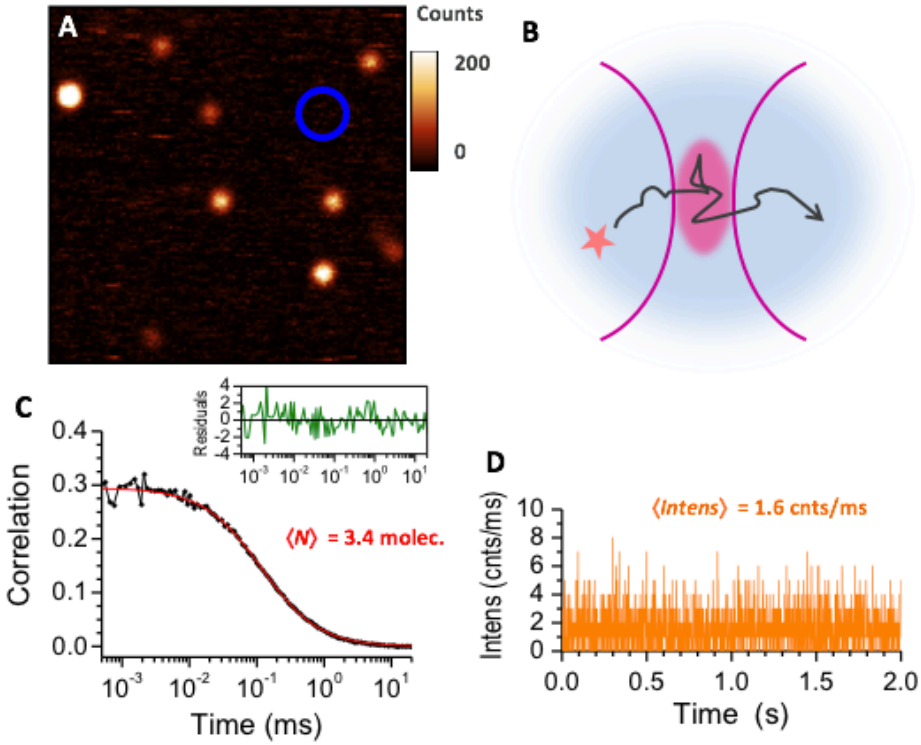

Figure 3.19 - Determination of the emission brightness of a non-enhanced Atto-655 dye. (A) Optical microscopy image of individual dimer nanoparticles obtained with laser excitation at 639 nm used for fluorescence enhancement of Atto-655 dye - the blue circle illustrates a surface region without any dimer nanoparticles that was used to assess the emission intensity of Atto-655 alone. (B) Scheme of the fluorescence correlation spectroscopy experiment performed to determine the average number <N> of dye molecules in the detection volume. (C) Experimental fluorescence correlation curve and fit with a single-species Brownian diffusion model (red curve) that afforded the average number of dye molecules in each set of experiments of fluorescence enhancement - the inset shows the residuals from the curve fit. (D) Emission time trace from the Atto-655 dye in aqueous solution for the same excitation power and detection conditions used in the fluorescence enhancement experiments. In the example shown here, the average intensity of 1.6 counts/ms was discounted from the background noise (0.39 counts/ms measured in pure water) and divided by the average number of 3.4 molecules in the detection volume to give the emission intensity of 0.35 counts/ms for single Atto-655 not enhanced.

The fluorescence decay of enhanced emission was retrieved from emission time traces (Figure 3.20A), by using an intensity threshold that selected only the most intense events. The decay profile of enhanced emission is approximately coincident with the instrument response function because the plasmonic effects on the acceleration of decay rates is likely to decrease the decay times down to ps or sub-ps timescales (Figure 3.20B).

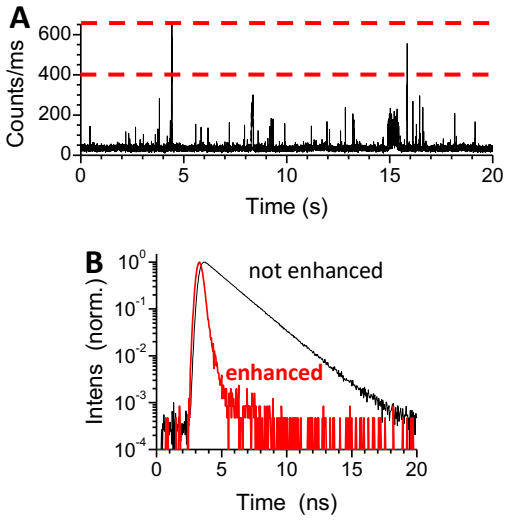

Figure 3.20 - Fluorescence decay of enhanced emission. (A) Emission intensity time traces measured from an experiment of fluorescence enhancement of Atto-655 dye showing events of intense fluorescence emission. (B) Fluorescence decays of Atto-655 dye in aqueous solution from emission not enhanced (black curve) and enhanced by dimer nanoparticles of 80 nm (red curve) - the decay curve for the enhanced emission was obtained from the photon counting histogram of the fluorescence bursts shown between the red dashed lines in the emission time trace. This fluorescence decay practically coincides with the instrument response function. i.e. the enhanced emission decays faster than the time resolution (~30 ps) of the time-correlated single-photon counting system of the fluorescence lifetime microscope.

3.7.4. Fluorescence Lifetime Correlation Spectroscopy analysis

As described in the main text, the correlation functions filtered by FLCS analysis for enhanced emission show two relaxation components. In order to extract the relaxation times associated with these components the correlation curves were fitted with the free-diffusion model for two species,[26]

$$G(t) - 1 = \sum_{i=1}^{n} \rho_i \left(1 + \frac{\tau}{\tau_i}\right)^{-1} \left(1 + \frac{\tau}{\kappa^2 \cdot \tau_i}\right)^{-1/2} \quad (4)$$

Even though this model affords reasonable fits, the relaxation times retrieved are not amenable with a free-diffusion picture, as further explained in the main text. For this reason, the free-diffusion model is used as a phenomenological fitting function with the sole purpose of extracting relaxation times. The values of fast (τ_1) and slow (τ_2) relaxation times obtained from fitting Eq. 4 to the correlation curves of enhanced emission are given in Table 3.3 for selected examples of time traces showing a large number of enhanced fluorescence bursts. The variability observed in τ_1 is most likely due to sample heterogeneity related to molecular congestion of the gap volume with DNA linkers. The slow relaxation time, τ_2, also varies from dimer to dimer because of the stochastic process of dye's adsorption onto solid surfaces. In the main text, the values given of τ_1 and τ_2, respectively of 20 μs and 2.7 ms, are the average of the values in Table 3.3 for these components. For comparison purposes, it is also shown in Table 3.3 the corresponding values of the slow relaxation time τ_1 from fitting Eq. 4 to the correlation curves of non-enhanced emission.

Table 3.3 - Relaxation times of the fast (τ_1) and slow (τ_2) components obtained from fitting Eq. 4 to correlation curves filtered by FLCS for enhanced emission (columns labeled "Enhanced"). Relaxation time (τ_1) obtained from fitting Eq. 4 to correlation curves of non-enhanced emission (column labeled "Non-enhanced").

		Enhanced		**Non-enhanced**
DNA linker	Dimer #	τ_1 (ms)	τ_2 (ms)	τ_1 (ms)
N_{15}	2	0.011	6.397	4.745
N_{30}	1	0.007	1.442	5.463
	3	0.044	1.454	4.193
	4	0.037	0.517	2.485
	9	0.013	0.670	5.931
	13	0.042	5.548	3.542
N_{60}	3	0.014	5.404	0.927
	6	0.009	0.987	2.162
	8	0.007	0.956	1.535
	13	0.012	3.295	1.856

Intense emission events that last longer than a few milliseconds are occasionally observed in emission traces (Figure 3.21), indicative of the slower motion because of the sticking onto the glass substrate, or due to interaction with DNA linkers.

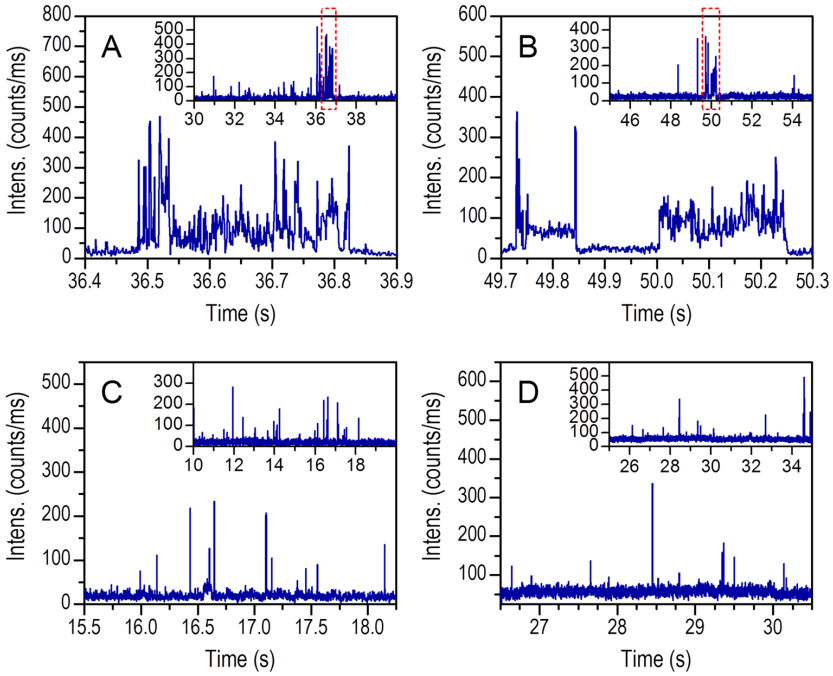

Figure 3.21 - Intense emission events that last longer than a few milliseconds. (A, B) Examples of emission intensity time traces showing enhanced fluorescence emission during time intervals of several ms, which are attributed to the dye's adsorption/desorption on the surface surrounding the dimer particle, or to the interaction with DNA linkers - the inset shows an extended interval of the emission time trace with the event signaled by a red box. (C, D) Examples of emission intensity time traces showing for comparison purposes enhanced fluorescence bursts of short duration.

Chapter 4

Plasmon-assisted Photochemical functionalization of Gold Nanorods

4. Plasmon-assisted photochemical functionalization of gold nanorods

The aim of this chapter was to develop a functionalization procedure that would allow to specifically attach photoactive molecules at the plasmon hot-spots of gold nanorods. This strategy was pursued here in order to maximize plasmonic effects on fluorescence enhancement that could be explored for signalling of biomarker detection with improved sensitivity. However, before proceeding to photochemical functionalization with fluorescent DNA probes, the photocrosslinking reaction was tested for biotin attachment onto gold nanorods. The strategy devised relies in the capability of plasmonic nanoparticles to trigger chemical reactions on the nanoscale when they interact with light. But also on how these interactions could be explored to achieve a tip-specific functionalization of gold nanorods with biotin receptors that could enable to specifically bind streptavidin. The binding triggers a red-shift of the nanorods' surface plasmon resonance that can be optically detected. This approach is the basis of plasmonic sensors, which are introduced next.

4.1. Introduction to plasmonic sensors

The importance given to metal nanoparticles is in part owned to their distinctive spectral extinction peaks at visible and near-infrared frequencies, which result from strong light absorption and scattering at these wavelengths. In turn, these optical properties are due to the phenomenon of localized surface plasmon resonance (LSPR), as previously described in Chapter 1. The LSPR wavelength depends on the plasmon mode and in turn on the particle shape, size and composition. Also, it depends on changes in the local refractive index (RI) in the surroundings of the particle. In the dipolar approximation of Mie theory, this dependence for a spherical particle is given by,

$$\lambda_{max} = \lambda_p \sqrt{2n^2 + 1} \qquad (1)$$

where λ_{max} is the LSPR peak wavelength, λ_p is the wavelength corresponding to the plasma oscillation frequency of the bulk metal and n is the refractive index of the surrounding medium.[1] It also has been experimentally shown that, in general, the LSPR peak wavelength shift for spheroidal particles is approximately linear with the RI, which is also predicted by the dipolar approximation of Mie-Gans theory (see Figure 4.1).

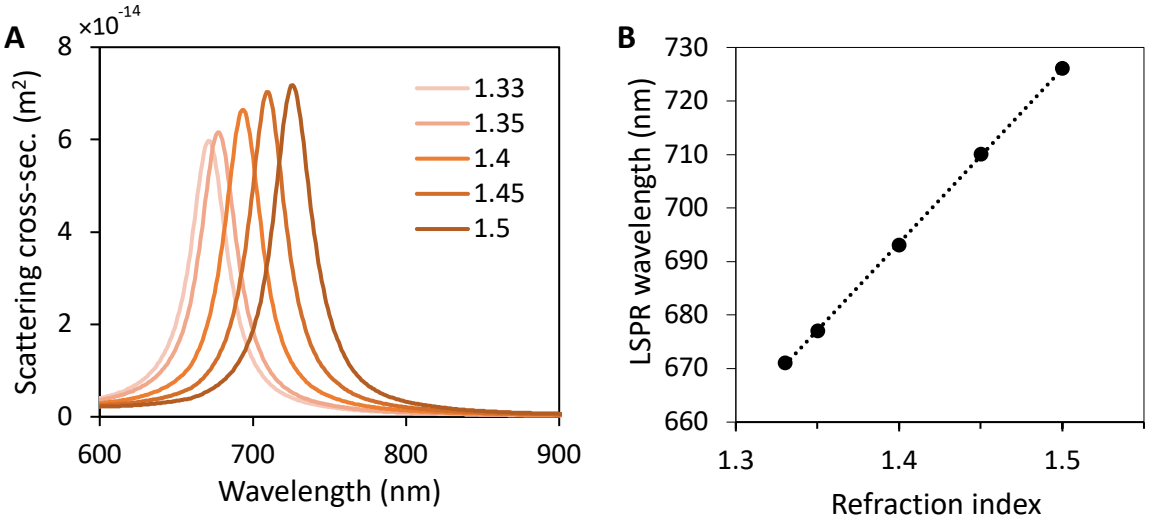

Figure 4.1 - Plasmonic particles exhibit a dependence of the LSPR peak wavelength in relation to the medium's refractive index. (A) LSPR peak wavelength calculated from the dipolar approximation of Mie-Gans theory for an ellipsoidal particle of aspect ratio 3, while changing the refraction index between 1.33 and 1.5. (B) Linear dependence of the LSPR peak wavelength with respect to the refraction index.

Therefore, molecular interactions near the particle's surface that change the local refractive index can induce a plasmon shift in the LSPR peak wavelength, that once monitored, e.g. as a function of time, can be explored to probe molecular binding events. Consequently, LSPR can be the basis for sensing molecular interactions by directly measuring minute changes in the particle's dielectric environment.[2] The RI sensitivity of a specific nanoparticle is normally reported in terms of peak shift expressed in nanometers per refractive index unit, i.e. nm/RIU. Generally, for metal particles of anisotropic shape, increasing their aspect ratio (length/width) shifts the surface plasmon resonance (across the long dimension) toward lower energies (or frequencies), and the electromagnetic field decay length also increases.[3] The plasmon's enhanced electric field decays rapidly with respect to the distance from the particle surface, so spectral LSPR only probes a nanoscale region around the particle. Moreover, because the near-field distribution is not homogeneous across the particle's surface,[4] but instead it depends on the mode profile and so on the particle geometry. The regions of large plasmon-enhanced near-field, such as the sharp tips of elongated particle shapes, are preferred for plasmonic sensing. These regions, named hot-spots, have high RI sensitivities localized in nanometric volumes. Thus, particles with elongated shapes have been more employed for plasmonic biosensing, such as gold nanorods,[5–16] gold[17–20] and silver[21–23] nanotriangles, silver nanocubes[24] or gold nanobipyramids.[25–27] Plasmonic sensors have been exploited for chemical (e.g. gas and pH sensors) and biological optical detection, topics that have been reviewed extensively and to which the reader is referred for a detail description.[1,2,28–33]

As seen, gold nanoparticles are often preferable to silver for plasmonic sensors, because of their accessible synthesis, chemical stability, single-crystalline nature and narrow plasmon resonance. But silver structures are also considered due to sharper resonances and higher refractive index sensitivity. Despite their enormous potential as a highly-sensitive and selective platform,

plasmon-based biosensors are still in a proof-of-concept state, mainly for the detection of biomolecules (e.g., enzymes, proteins, nucleic acids, antigens or antibodies). Low molecular weight compounds with dimensions between 2 and 20 nm, comparable to those of plasmonic nanostructures, makes them structurally compatible, and that is why the first stage of the design of a LSPR biosensor is the successful preparation of an appropriate and stable biomolecule-nanostructure conjugate.

Being label-free is one of the most relevant characteristics of a nanoplasmonic sensor, allowing continuous measurement of the target concentration on the sensor and analysis of thermodynamic and real-time binding kinetics. These have contributed, along with molecular concentrations and conformational changes studies, to the establishment of LSPR-based biomolecular assays in academia. The assays have been based on highly specific biological molecular recognition interactions, as demonstrated by the conjugation of metal particles to biotin-streptavidin[5,7–9,13,21,34,35] and antibody-antigen (immunoassays)[10,14,19,20,22,25,26] interactions, both having high selectivity for the receptor-analyte binding. In addition, nucleic acid hybridization,[17] microRNA sensing[18,36] and aptamer-protein interaction[37] were also reported.

The ultimate detection limit in biology and analytic chemistry is single-molecule detection. Plasmonic nanoparticles, contrary to fluorophores, do not bleach or blink, providing virtually unlimited photons for molecular binding observation over arbitrarily long-time intervals. This binding of molecules results in an optical signal, i.e. a LSPR spectrum, that can be measured by either transmission spectroscopy or dark-field light scattering spectroscopy. Technical developments in the measurement of optical signals from LSPR phenomena have gradually improved in detection sensitivity, reaching up the single-molecule detection using single particles,[7,15,26,38] a hot-topic area that was recently reviewed.[39] For that purpose, either photothermal, dark-field or total internal reflection microscopies have been employed.[7,15] The proof-of-concept has been done on the detection of proteins, because these biomacromolecules with molecular weights in the range of tens to hundreds of kDa, give enough contrast of local refractive index for single-molecule detection. Zijlstra et al.[7] demonstrated that using photothermal microscopy it is possible to detect single-molecule binding events of proteins as small as streptavidin, with only 53 kDa, by using short biotin-thiolated receptors that were specifically functionalized onto the tips of gold nanorods. In the follow-up, single-particle LSPR-sensors based on hundreds of gold nanorods with single-molecule sensitivity were developed, in which the particles were simultaneously monitored in real-time.[38] The authors stated that this ability would theoretically allow to lower detection limits, providing a sensor with a dynamic range of 7 decades in concentration. These features can be further exploited for device miniaturization, multiplexing or to achieve lower detection limits. In fact, some works reported multiplexed sensors using surface-immobilized individual gold nanorods in a microfluidic flow cell,[37] and arrays of gold nanorods in a parallel LSPR lab-on-a-chip[40] and in a LSPR with microfluidics on-a-chip.[41] Due to these

advances, LSPR sensing is now considered a powerful addition to the current toolbox of single-molecule detection methods.

Specificity in plasmonic biosensors is built-in by the particles' surface chemical functionalization for correctly attach selective biorecognition elements that capture only the targeted analyte with high affinity, while preventing non-specific adsorptions by using blocking agents typically forming hydrophilic self-assembled monolayers (SAMs). Also, the surface-functionalization procedure must optimize the receptor density so that steric hindrance issues are minimized, e.g. when capturing large analytes. Latest reports have demonstrated site-specific functionalization of some of the nanoparticles' shapes mentioned above, with the goal of maximizing the sensitivity.[7,16,19,20,42–45] Some of these studies used the plasmon hot-spots of gold nanorods and showed that an adequate density of receptors in a tip-specific functionalization approach, is crucial to develop plasmonic sensors with improved performance by capturing the target species at the most sensitive regions of the particle's surface.[7,16] Besides, in contrast to full particle's surface coverage, tip-specific functionalization preserves the quality factor of the plasmonic sensor, by avoiding line broadening due to chemical interface damping.[42] To summarize, the functionalization of the sensor surface is a key aspect and represents a critical challenge for the development of plasmonic biosensors.

The next section provides an overview of plasmon-mediated photochemical reactions for surface functionalization, and later in section 4.3, the photochemistry of phenyl azides, which was the photocrosslinker used in this work, is briefly described.

4.1.1. Plasmon-mediated photochemical reactions for surface functionalization

The first report on a plasmon-assisted photochemical reaction of nanoparticles is from 1983,[46] and several reports have explored this field showing its great potential, which can be seen by recent reviews.[47–52] Plasmon-mediated chemistry takes in consideration the plasmonic antenna effect of metal nanostructures, that through the highly intense and near-field enhancement, efficiently triggers and controls photochemical reactions on the nanoparticle surface. For instance, in the metal's hot-spots the enormous increase of the available number of photons per unit volume increases the conversion of photochemical reactions.

One example of plasmon-induced photoreactions is photopolymerization. In 2008, Ueno et al. demonstrated that in the nanogap between coupled gold nanoblocks, the large field enhancement was strong enough to reach regimes that activated non-linear two-photon absorption (2PA), and subsequent site-selective polymerization across the nanogaps was achieved.[53] For the first time, instead of using tightly focused beams of powerful lasers, 2PA was triggered by a low-intensity incoherent light source. Other examples of photopolymerization reactions in plasmonic nanostructures have followed up on this pioneering work.[54–57] Photopolymerization of biomolecules in plasmonic nanoparticles was achieved recently, in which the researchers used single gold nanotriangles for metal-enhanced two-photon absorption, and consequent polymerization of a bovine serum albumin hydrogel in the triangles' hot-spot tips by controlling the polarization and intensity of the incident laser.[58]

In 2016, Nguyen et al. reported on plasmon-mediated chemical surface functionalization through aryl film grafting (derived from a diazonium salt), covalently bond at the surface of gold lithographic nanostripes. The aryl film (ca. 30 nm) was specifically grafted in few seconds in hot-spot areas of maximum near-field enhancement, under laser irradiation for LSPR excitation.[59] The energy dose of the incident light and the LSPR wavelength were central for the grafting yield and the aryl film thickness. Next, the same group used the process for regioselective functionalization of lithographically designed gold nanorods arrays with aryl diazonium salt. The layer formation (40-60 nm) was very fast, 10 s, using the polarized light of a laser with the wavelength matching the maximum of extinction of the longitudinal surface plasmon (LSP) band of the rods.[60]

A different approach, but equally interesting, consists in exploring hot electrons in plasmonic materials.[61] These have the ability for nanoscale patterning of surface chemistry on those materials by positioning molecules in highly reactive regions. Studies by the previous group on adjacent gold spheres or at the corners of triangular particles suggested that the growth of an organic layer was due to the generation, upon LSPR excitation, of hot electrons on the surfaces of the particles.[62] This principle was also applied to the surface multi-functionalization of lithographic gold disk arrays with aryl diazonium salts along the Y and X directions.[63] In another work, hot electrons locally reduced the terminal group of a self-assembled molecular layer in hot-spot regions of silver bowtie structures.[45] Due to the hot electrons dynamics the field of plasmon photochemistry have evolved greatly in recent years.[64] In fact, these have been used for real-time and real-space observation of a plasmon-induced chemical reaction at the single-molecule[65] and at the single-particle level,[66] and for nanoscale control of molecular self-assembly.[67] Other applications have been developed lately like photocatalysis,[68,69] and the case of water splitting.[70]

Clearly, this plasmonic-based approach offers an innovative way for the regioselective functionalization of gold nanorods. Moreover, it can provide an all-purpose strategy to attach biomolecules into the nanorods' hot-spot regions and further improve their detection for biosensing applications. This chapter addresses a proof of this concept in which a plasmon-assisted photochemical procedure was implemented for tip-specific functionalization of nanorods with biotin receptors. The biotin-functionalized nanorods were then tested as a model plasmonic sensor for the detection of streptavidin. Furthermore, the functionalization route here pursued would be in principle generalizable for any type of plasmonic particle that provides well-defined plasmon hot-spots and for any type of receptors, or biomolecule, that could be derivatized with a photo-activatable group, as later discussed.

4.2. Experimental design for the functionalization and testing of a model plasmonic sensor

In this section, the general scheme for photochemical site-selective surface functionalization of immobilized gold nanorods is outlined, together with the monitorization tests that were carried out

for evaluating the sensor response of these biotin-functionalized nanorods for streptavidin detection. The present experimental implementation comprises five major preparation steps, as represented in Figure 4.2.

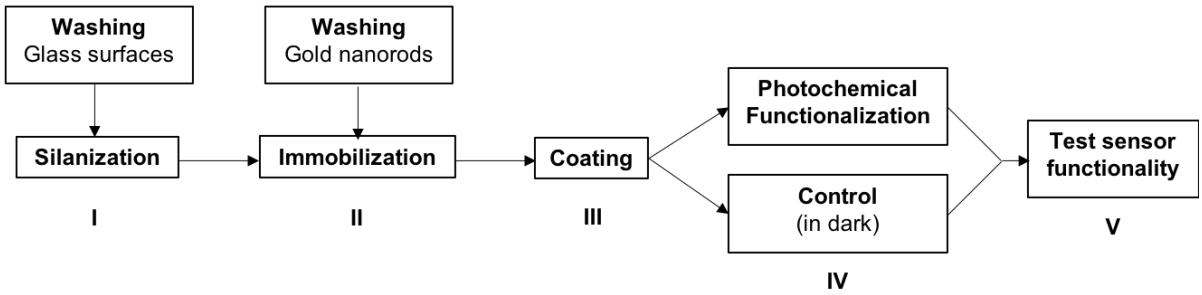

Figure 4.2 - Scheme of the experimental procedures implemented for the preparation of the plasmonic sensor. The method comprises five sequential steps: I. Silanization of the glass substrates; II. Immobilization of gold nanorods on the silanized glass substrates; III. Coating of the nanorods' surface with thiolated self-assembled monolayers; IV. Plasmon-induced photochemical reactions for tip-specific functionalization of nanorods with biotin ligands; V. Testing of sensor functionality with streptavidin binding assays.

The details concerning each of the five steps involved in the experimental design are described throughout the next sub-sections.

I - Silanization of glass substrates

The first step consisted in a silanization process on glass substrates for the formation of organosilane monolayers.[71] Therefore, the surface of glass coverslips was modified with a self-assembled monolayer that forms a well-ordered chemical matrix of an alkoxysilane, (3-mercaptopropyl) trimethoxysilane (MPTMS). It has functional groups at both terminals: one surface reactive silanol group (Si-OCH_3) for glass attachment and a functional thiol group (-SH) for immobilization of gold particles. After hydroxylation of the glass substrate with HCl (conversion of the surface SiO_2 into Si-OH groups), the silanol group of MPTMS is expected to form stable Si-O-Si bonds. This is due to the hydroxyl groups that are adequate anchors, creating an interface with protruding mercaptopropyl moieties. The thiol group acts as a suitable linker for gold atoms, because upon exposure the sulfur atom strongly chemisorbs to the metal surface, forming a Au-S interface.[72–74] A monolayer based on this chemical group is considered so far the best option for plasmonics.[75]

II - Immobilization of gold nanorods

The surface preparation continued by drop-casting a solution of gold nanorods onto the glass substrates previously silanized for covalent immobilization through formation of Au-S bonds. The nanorods' suspensions had a concentration corresponding to an optical density (OD) of 5 at the LSP peak wavelength (i.e. approx. 1 nM). This particle concentration was chosen to guarantee an adequate density of the immobilized particles on the glass coverslips, while avoiding stains on the glass that could result from particle aggregation (as seen in Figure 4.21 of the Annexes - section

4.10). Extinction spectra from the surface-immobilized nanorods show narrow longitudinal peaks that suggest well-dispersed nanoparticles (Figure 4.3).

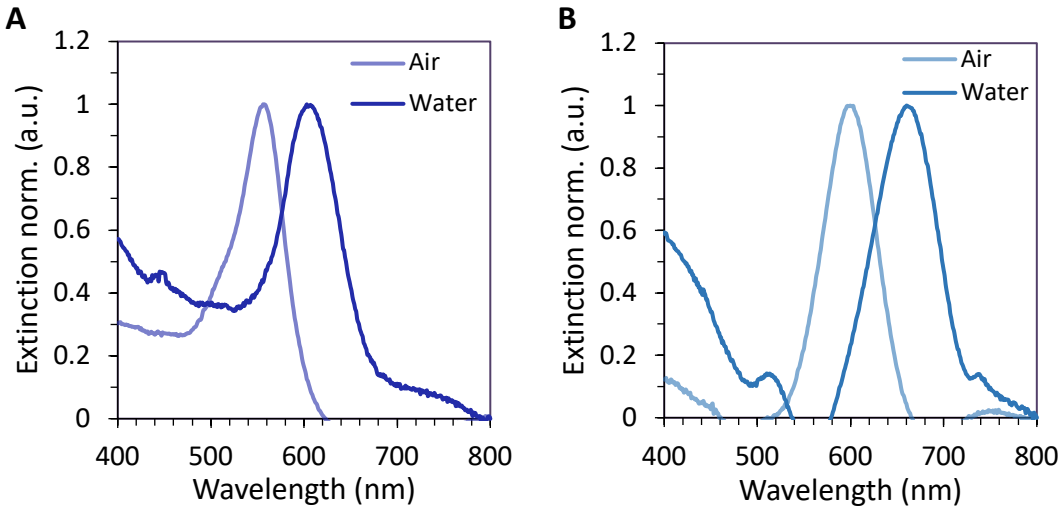

Figure 4.3 - Examples of typical extinction spectra obtained in air and water for glass-immobilized (A) 25/600 and (B) 25/650 gold nanorods.

The optical densities of these surfaces at the longitudinal peak were usually between 0.002 and 0.01, considering the difference between the peak maximum OD and the baseline on the long wavelength range. The characteristic extinction maximums, i.e. the LSP peak wavelengths, occurred at approximately 550 and 600 nm for 25/600 and 25/650 nanorods, respectively, because these spectra were taken in air, while those of the same surfaces immersed in water are red-shifted by about 50 nm. Overall, the glass surfaces with appropriate optical densities and well-dispersed covalently attached gold nanorods were used for the subsequent particle's surface chemistry.

III - Coating of gold nanorods' surface with an organic monolayer

In order for the photochemical functionalization procedure to work (see sub-section IV), it requires that an organic monolayer is previously assembled at the gold nanorod's surface. Briefly, the photoactive group in biotin derivatives is a phenyl azide that upon irradiation is converted to a nitrene that can perform a N-H or C-H insertion (see Figure 4.6). For this purpose, the nanorods have to be previously coated with a monolayer of an organic short chain compound that can provide such chemical moieties for nitrene coupling.

Here, cysteamine (CEA) or 11-amine-1-undecanethiol (AUT) alkanethiols were used. These alkane chain molecules with a terminal thiol group firmly attach to gold by chemisorption, and owing to hydrophobic and van der Waals interactions between the carbon chains, they form a stable monolayer. The terminal primary amine in these monolayers was intended as a site for photochemically triggered insertion of nitrene, because of its nucleophilicity. Alternatively, a methyl-PEG-thiol with four monomers of chain length was used, $MT(PEG)_4$. This molecule forms less organized monolayers than alkanethiols, such as AUT, but being flexible and highly

hydrophilic, i.e. by attracting water molecules that form a layer of hydration, it can repeal proteins or other compounds. This antifouling character was demonstrated to be useful for minimizing non-specific bindings[76] and is an improved version of conventional alkanethiol SAMs.

IV - Photochemical tip-specific functionalization of gold nanorods

The photochemical reaction employed here for plasmon-mediated functionalization of hot-spots is based on the photochemistry of phenyl azides. For the proof-of-concept, a biotin derivative with a PEG spacer and a phenyl azide photoactivatable group, TFPA-PEG_3-Biotin, hereafter named TFPA-Bt, or a nitro-substituted phenyl azide, hereafter named NPA-Bt, were used. The photochemistry of phenyl azides is detailed in section 4.3. Here, a brief description is given in the scope of the functionalization strategy toward achieving a tip-specific attachment of biotin receptors onto gold nanorods. The phenyl azide group in TFPA-Bt is perfluorinated and upon irradiation in the ultraviolet (UV, below ca. 300 nm) it is converted to a nitrene group that can perform N-H or C-H insertion by reaction with an organic monolayer. This also occurs in nitrophenyl azides, that instead can be irradiated with long-UV light (e.g, 365 nm; 300 to 460 nm), which is an advantage when compared to perfluorophenyl azides, because the damage caused by short-wave UV to biomolecules is minimized.

However, this direct approach would afford an indiscriminate surface functionalization of gold nanorods. Instead, the employed approach was to drive the photochemical reaction by two-photon absorption using the strong near-field enhancement at the nanorods' tips upon excitation of the LSP at around 600 nm (see Figure 4.4). The light sources were a pulsed diode (NanoLED594nm) or a light-emitting diode (LED595nm), with peak wavelengths of 594 nm and 595 nm, respectively. Similar strategies have been successfully demonstrated for obtaining spatial control of photopolymerization onto metal nanostructures.[53–57] The rationale for anchoring biotin receptors onto nanorods was to validate the surface attachment by using these particles as plasmonic sensors for the corresponding target biomolecule, streptavidin (SA). This approach was envisioned for creating plasmonic sensors with improved performance by concentrating the receptor units at the plasmon hot-spots.

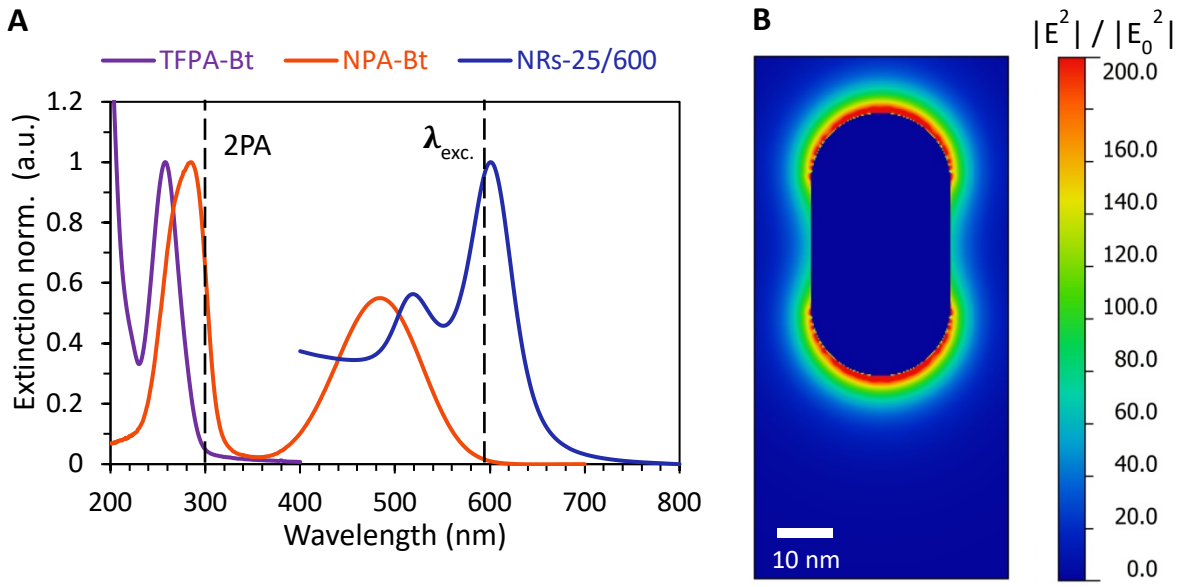

Figure 4.4 - Photochemical tip-specific functionalization of gold nanorods. (A) Extinction spectra of 25/600 (dark blue) nanorods, and of photoreactants TFPA-Bt (purple) and NPA-Bt (orange). Excitation wavelength ($\lambda_{exc.}$) is either 594 (NanoLED594nm) or 595 nm (LED595nm) to induce 2PA of photoreactants. (B) Simulated maps of the plasmonic near-field using discrete dipole approximation method for gold nanorods (25 nm × 47 nm, LSP of 597 nm) excited at an incident wavelength of 600 nm and considering the RI of water (1.33).

V - Test sensor functionality

The interaction between streptavidin (53 kDa) and biotin is one of the strongest non-covalent biological interactions found in nature having a binding constant in the order of 10^{15} M^{-1}.[77] For this reason, this interaction is widely employed when one wants to develop biological assays, and many reagents based on it are commercially available for bioconjugation techniques. The biotin-streptavidin pair is particularly well suited for LSPR sensing because biotin can be conjugated into the nanoparticle surface, while the RI of the larger streptavidin is detected. In principle, because of its binding constant of 10^{15} M^{-1}, it would allow for detection limits down to femtomolar. However, reported examples of plasmonic sensors are typically more modest with detection limits in the range from micromolar to picomolar. The effects of conjugation of biotin to the nanoparticle surface via a molecular tether, which includes steric hindrance and limited mobility, are described as possible explanations for the reduced affinity that is measured.[1]

Here, single-immobilized gold nanorods coated with an organic layer were photochemically functionalized with biotin, as represented in the schematic illustration of Figure 4.5A. The change in the local refraction index close to the nanorod's surface, induced by streptavidin binding, is transduced into a longitudinal plasmon peak shift that can be monitored by transmission spectroscopy (Figure 4.5B). As control assays, nanorods were exposed to the photochemical reactants, but without being irradiated, and therefore their surface should be free from biotin.

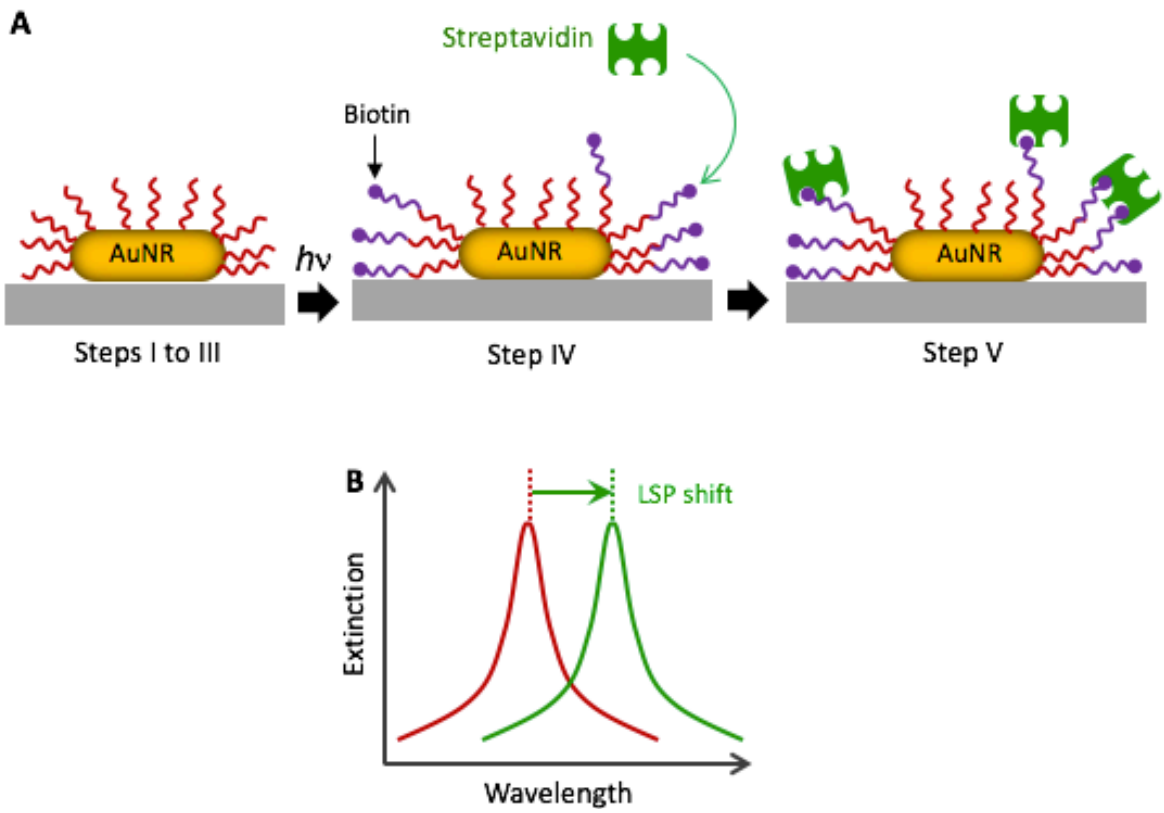

Figure 4.5 - Scheme of the plasmonic sensor immobilized on a glass substrate via a MPTMS monolayer. (A) A monolayer (red) of alkanethiols (AUT or CEA) or oligo(ethylene glycol) ($MT(PEG)_4$) is formed on the surface of the gold nanorods (steps I-III). Under irradiation, the photochemical functionalization occurs at the rods' tips (step IV), using a derivatized biotin of TFPA-Bt or NPA-Bt photoreactants (purple symbols). Binding of streptavidin to the biotinylated nanorods' surface occurs (step V). (B) Illustration of the plasmonic wavelength shift that represents the sensing principle employed. The binding of streptavidin to a photochemically tip-functionalized nanorod causes a shift of the LSP peak that is monitored via real-time extinction spectra.

4.3. Photochemistry of phenyl azides

Organic phenyl azides have been widely used in synthetic organic chemistry and generally in some biology research applications for effective and reliable photoaffinity labeling (a technique for marking the binding sites of proteins), and photocrosslinking of proteins, biomolecules and biopolymers. Numerous specific forms of phenyl azide compounds are available, differing slightly in terms of efficiency, stability and absorbance maximum. However, their reaction mechanism is triggered by a common step, so for better elucidation, the photochemistry and possible reaction pathways of phenyl azides can be presented in the unified scheme of Figure 4.6.

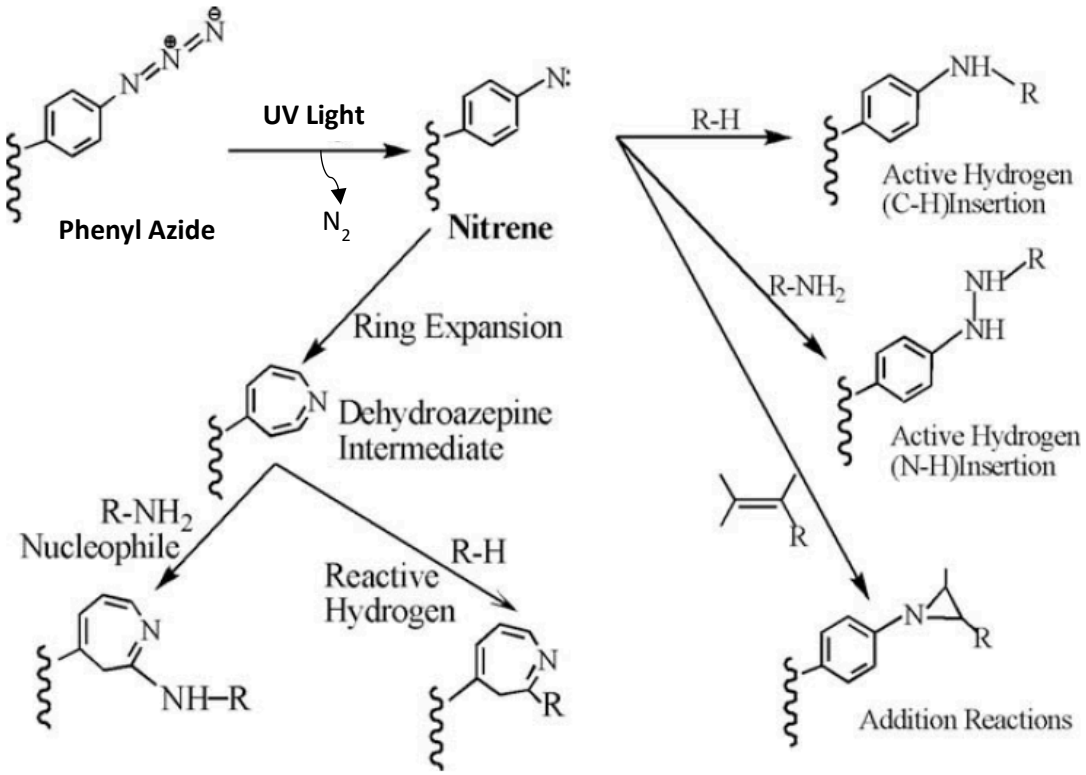

Figure 4.6 - Scheme of aryl azides possible reaction pathways for light-activated photochemical conjugation with surrounding molecules. R can represent any molecule that contains nucleophilic or active hydrogen groups (C-H or N-H). Adapted from Ref. 78.

Once a photoreactive phenyl azide is exposed to ultraviolet light, photoactivation occurs and the azide decomposes releasing nitrogen gas to give the singlet biradical phenyl nitrene. This is a highly reactive intermediate that can undergo reactions indiscriminately with a large variety of organic functional groups.[79] Covalent bonds with neighboring molecules are possible to occur by several pathways: active hydrogen insertion into C-H and N-H sites, addition reactions with double C=C bonds, or ring expansion.[80,81]

Photolysis of aryl azides leads to formation of singlet aryl nitrene at ambient temperature, but the photobehavior of this species depends on temperature and phase conditions. In solution at room temperature (or higher temperatures), phenyl nitrene immediately vibrationally deactivates and ring expansion, to form an dehydroazepine intermediate, is very fast (10-100 ps range)[82] with a 3 kcal/mol barrier.[83,84] The use of fast, pulsed lasers as light sources allowed the direct detection of short-lived intermediates and enabled the detailed study of their reactions.[85]

Besides dependence on temperature, the rate of phenyl nitrene ring expansion to dehydroazepines is also strongly dependent on the effects of ring substituents. This influences significantly the electronic structure of phenyl nitrene. In fact, aryl azides substituted with various groups, for example, nitro-, fluoro-, imino-, can provide different outcomes, being actually proposed as better photoaffinity labeling reagents. In the scope of this thesis, two types of substitution are more pertinent, fluoro- and nitro- aryl azides, which correspond to the

photoactivatable groups present in the biotin derivates used for particle functionalization. These examples are described in more detail below.

An important finding in the photochemistry of phenyl azides was the introduction of halogen atoms (F or Cl) on the aromatic ring.[86,87] The fluoro- substituents in perfluorinated aryl azides greatly suppress the ring expansion reaction and thus increase the yields of insertion reactions with C-H (to form secondary amines or ISC to triplet nitrenes) and N-H bonds (of nucleophiles), or with C=C bonds (in addition reactions), establishing stable covalent chemical bonds.[81,86–88] The major difference between the photochemistry of fluorinated and non-fluorinated phenyl azides is the raise of the barrier for ring expansion of singlet (tetrafluorophenyl) nitrene (8 kcal/mol)[87,89] when compared to that of singlet phenyl nitrene (3 kcal/mol).[84] This increases singlet nitrene lifetime into the range of tens or hundreds of nanoseconds at ambient temperature. The increased lifetime of the singlet nitrene and the improved coupling chemistry of fluorinated azides is appropriate for a wide range of molecules and materials and is therefore highly general and versatile. Polyfluorinated aryl azides have long been proposed as superior reagents for photoaffinity labeling studies.[77] They are also used in covalent functionalization of various types of unreactive targets, like solid surfaces and nanoparticles of hydrocarbon-based materials such as carbon nanotubes[90] or graphene;[91,92] and in immobilization of proteins,[93] small molecules, carbohydrates, enzymes, and synthetic polymers.[77,94–96]

Like every technique, the perfluorophenyl azide coupling chemistry is not without shortcomings. Because the coupling reaction applies to C-H, N-H, and C=C bonds, the method therefore lacks specificity for certain functional groups. Generally, short-wavelength UV light (e.g., 254 nm; 265 to 275 nm) is needed to efficiently activate perfluorophenyl azides (or simple phenyl azides) as they all have UV absorption maxima around 260 nm. This is other disadvantage because it is also the region where biopolymers (proteins and nucleic acids) have absorption. Fortunately, photolysis tends to be complete before any appreciable photolytic damage of these biopolymers takes place. Nitro-substituted phenyl azides better solve this issue and also find widespread use as photoaffinity labeling agents of biological macromolecules.

4.4. Functionalization and testing of gold nanorods coated with an amine-alkanethiol monolayer

The first set of results described in this chapter concern the functionalization of gold nanorods using a biotin derivatized with a perfluorinated aryl azide. In order to accomplish its photochemical coupling, the nanorods were previously coated with an amine alkanethiol layer. The rationale behind the choice of an amine-terminated alkanethiol layer was that the reaction with the nitrene group, formed upon photochemical conversion of the perfluorinated aryl azide, would proceed mainly by N-H insertion (although C-H insertion could also take place with neighboring methylene chain groups). The perfluorinated aryl azide that was used is the commercially available

TFPA-PEG_3-Biotin, or TFPA-Bt (Figure 4.7). The PEG spacer is a hydrophilic chain group that for an extended conformation of TFPA-Bt has a spacer arm length of 3.4 nm.[2]

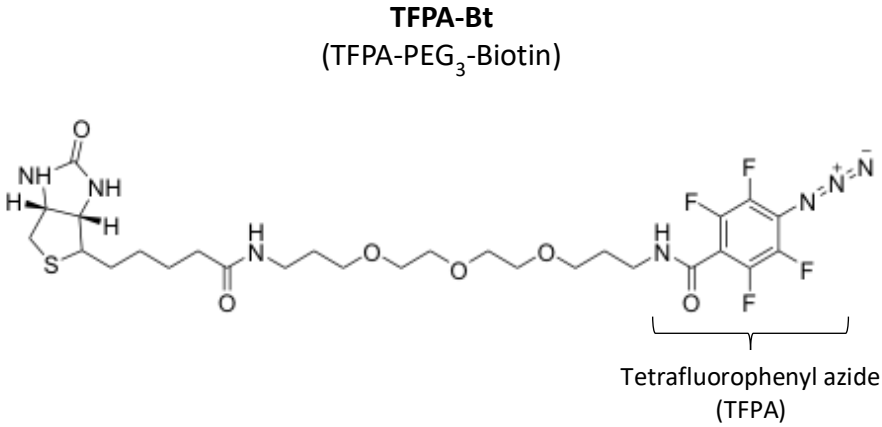

Figure 4.7 - Chemical structure of TFPA-Bt photoreactant with indication of the photoactive tetrafluorophenyl azide group.

Two amine-terminated alkanethiols were used for previous coating of nanorods that differ only in the alkane chain length, with CEA and AUT having chain lengths of 2 and 11 carbon atoms, respectively (Figure 4.8). The rationale behind testing two chain lengths was to evaluate the plasmonic response of the biotin-functionalized nanorods upon streptavidin binding due to the known distance dependence of plasmon sensitivity. The capture of the target biomolecule at distances closer to the nanorods' surface should correspond to a larger sensor response due to the greater sensibility to the refraction index. Figure 4.8 shows one of the possible insertion products from the photochemical reaction of TFPA-Bt with either CEA or AUT. The represented products would give the longest distances between biotin receptor and the gold surface. However, the extended representation may be misleading because the PEG spacers are flexible. On the other hand, the alkanethiol spacer should form a compact monolayer on the nanorod's surface and this monolayer has a different thickness between CEA and AUT.

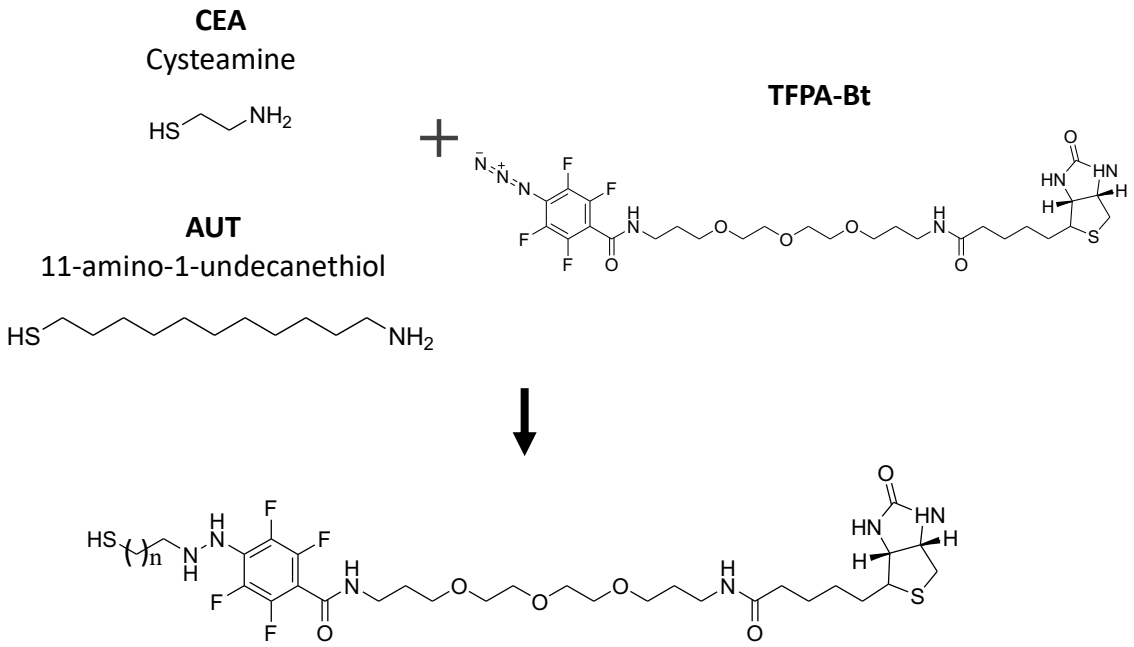

Figure 4.8 - Photochemical reactions between CEA or AUT and TFPA-Bt. Upon irradiation, covalent bonding occurs through N-H insertion into the phenyl nitrene intermediate of TFPA-Bt. One of the possible reaction products is represented, considering CEA when n=1 and AUT when n=10.

The first study presented here aimed at evaluating the efficacy of the photochemical reactions on AUT-coated nanorods simply by monitoring LSP peak shifts that could eventually be induced by attachment of the biotin derivative. In this assay, the nanorods' surface was immersed in aqueous solutions of the photoreactant and irradiation was performed over an interval of 2 hours, while monitoring the transmission spectrum of the irradiated nanorods. For control purposes, the nanorods' surface was kept in the dark for 2 hours before any irradiation took place and monitored for non-specific interactions. The light source used in this assay was the LED595nm selected for an intensity level of 6, which for the irradiation arrangement used corresponds to an irradiance of 1.80 mW/cm^2. A similar test with NanoLED594nm, that gives an irradiance of 0.11 mW/cm^2, yielded equivalent results (not shown here). The nanorods exhibited negligible LSP shifts while kept in the dark (90 min) or after under irradiation for 2 h (Figure 4.9). This unexpected result does not necessarily mean that TFPA-Bt did not react with the AUT monolayer on the nanorods. Instead, it might simply be that the attachment of biotin linkers did not afford a large enough variation in the organic layer thickness to give a contrast of index of refraction to be measured by transmission. There are literature examples of relevant LSP peak shifts detected in similar experiments, but these involve a much thicker and compact grafted layer formed by plasmon-induced photo-conversion of diazonium salts on gold nanoparticles.[62]

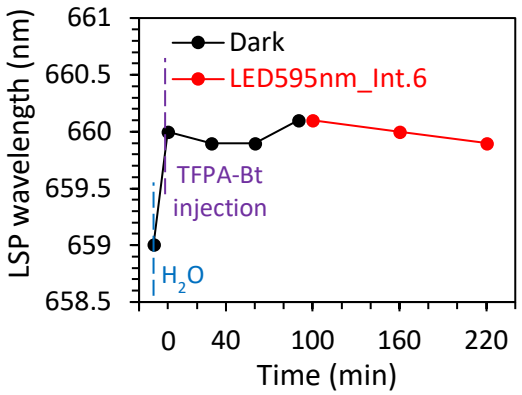

Figure 4.9 - Test to monitor the photochemical reaction of TFPA-Bt with AUT-coated gold nanorods. The surface was filled with water, then water was replaced by TFPA-Bt solution (1 mM) and the surface was kept in the dark for 90 min (black symbols). Afterward, it was irradiated with LED595nm at intensity level 6 for 2 hours.

Since it was not possible to directly confirm the attachment of TFPA-Bt onto the nanorods, the surface functionalization with biotin receptors was evaluated indirectly by performing streptavidin sensing assays. In this type of assay, the nanorods are exposed to an aqueous solution of streptavidin and the LSP wavelength is monitored in response to streptavidin binding. In most assays performed, two nanorod samples are compared: one that was irradiated, and it should be biotin-functionalized; and, another, that was kept in the dark and that serves as a control sample for non-specific adsorption.

The first set of results presented here from streptavidin sensing assays concern an evaluation of the irradiance power on the extent of biotin functionalization in the nanorods. Actually, a question that often arises with respect to aryl azide linkers is what should be the optimal wavelength and intensity of light for photoactivation. The LED595nm source allows to vary the irradiation power that was selected in separate assays at levels 1, 3 and 6, that correspond to 0.03, 0.18 and 1.80 mW/cm^2, respectively (while keeping the irradiation time constant at 2 hours). The irradiated nanorod samples were then subjected to streptavidin sensing assays by monitoring the LSP peak every minute, which allows to describe a binding kinetic curve (Figure 4.10A). The kinetic curves show an initial red-shift of the LSP peak wavelength, and after some time it stabilizes, as expected for a situation of chemical equilibrium. The difference between the final and initial peak wavelengths give a total LSP peak shift that was compared between assays to evaluate biotin functionalization of the nanorods. In Figure 4.10B, the average LSP peak shifts for several replicas of sensing assays performed for the several irradiation powers used (starting from the non-irradiated control assays) are displayed in a column plot. Unfortunately, only a minor increase of less than 1 nm, in comparison to non-irradiated control samples, was observed with the increment of the irradiance.

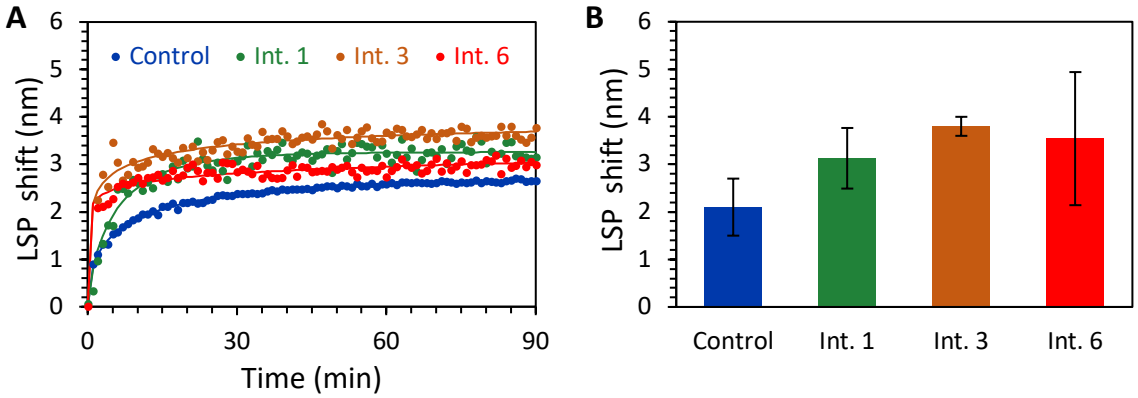

Figure 4.10 - Plasmonic sensing using streptavidin in the presence of AUT-coated gold nanorods that were photochemically tip-functionalized with TFPA-Bt. (A) Examples of kinetic traces showing the LSP shift of TFPA-Bt photochemically functionalized nanorods using LED595nm at intensity level 1 (green symbols), 3 (orange symbols) and 6 (red symbols), and a control assay (blue symbols), in response to streptavidin (100 nM) binding. The filled lines are the fits performed with a stretched exponential. (B) Average LSP shifts in response to streptavidin binding. Error bars correspond to the standard deviation.

The results presented graphically in Figure 4.10 are given in more detail in Table 4.1. Although nanorods functionalized with biotin respond to streptavidin, the difference of response between controls and irradiated samples' sensing responses was not significant enough for unequivocal validation of the tip-selective functionalization approach when using AUT-coated particles. These results could be indicative that the photochemical reaction of TFPA-Bt with AUT may be impaired to some extent, as later discussed.

Table 4.1 - LSP shifts (Δλ) measured for streptavidin sensing (100 nM) using AUT-coated 25/650 nanorods tip-functionalized with photoreactant TFPA-Bt (0.1 mM) using LED595nm irradiation with intensities 1, 3 and 6. Control corresponds to non-irradiated surfaces. The column on the right stands for the average ± standard deviation of N=3 (except Int. 3).

	Δλ/nm (100 nM SA)	
Control	1.5 2.2 2.7	2.1 ± 0.6
Int. 1	3.8 2.2 3.3 3.3	3.1 ± 0.6
Int. 3	3.6 3.9	3.8 ± 0.2
Int. 6	5.2 3.0 2.4	3.5 ± 1.4

In order to increase the peak-shift response, the streptavidin target was replaced with an antibiotin antibody, since a bulkier protein may elicit larger sensing responses from the biotin-functionalized nanorods. The kinetic time traces of Figure 4.11 represent the LSP peak shifts

measured for a non-irradiated control and an irradiated sample. The values of 3.4 and 4.3 nm for the control and the irradiated sample, respectively, are comparable. The lack of a significant difference between sample and control confirmed that the photochemical reaction between AUT and TFPA-Bt was not a promising strategy for tip-specific functionalization of gold nanorods.

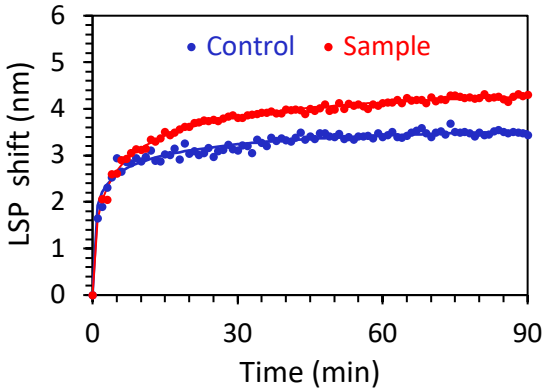

Figure 4.11 - Kinetic traces showing the LSP peak shift of 25/650 gold nanorods coated with AUT and irradiated with TFPA-Bt (red symbols), and of a control assay (blue symbols), in response to antibiotin antibody. The curves shown correspond to the fits performed with a stretched exponential function.

Alternatively, the photochemical reaction with TFPA-Bt was also tested on CEA-coated nanorods. As it was previously done with AUT-coated particles, an initial assay was done simply by monitoring LSP shifts that could eventually be induced by attachment of the biotin derivative onto CEA-coated nanorods. For this purpose, immobilized nanorods with an LSP peak at 600 nm were used and the influence of irradiation with LED595nm at intensity level 6 was also tested. The nanorods showed insignificant LSP shifts after being kept in the dark for 30 min or when irradiated, both for 30 min, with LED595nm (Figure 4.12). As previously observed with AUT-coated nanorods, the plasmon peak shifts were negligible when compared to control experiments, so the attachment of TFPA-Bt onto the nanorods was again not directly confirmed.

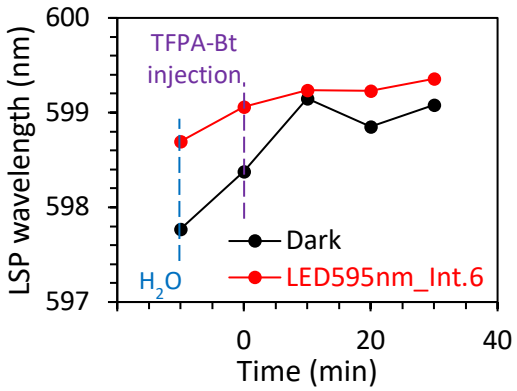

Figure 4.12 - Monitorization of the photochemical reaction of TFPA-Bt with CEA-coated nanorods. Two surfaces were filled with water and then water was replaced by TFPA-Bt solution (1 mM). One surface was kept in the dark for 30 min (black symbols), while the other was irradiated with LED595nm at intensity level 6 also 30 min.

As previously done with AUT-coated particles, the next step was to test the efficacy of the photochemical reaction between CEA and TFPA-Bt by performing SA binding assays. These assays were performed with 25/600 CEA-coated nanorods that were exposed to TFPA-Bt (0.1 mM) while irradiated with NanoLED594nm (samples) or kept in the dark (controls). Table 4.2 presents the LSP shifts measured for these controls and irradiated samples. The small differences found between the non-irradiated controls and the irradiated samples make these assays inconclusive.

Table 4.2 - Partial and total LSP shifts (Δλ) measured for streptavidin sensing (100 and 1000 nM) using CEA-coated 25/600 nanorods tip-functionalized with photoreactant TFPA-Bt (0.1 mM) through irradiation with NanoLED594nm. For each set of LSP shifts the column of the right corresponds to the average ± standard deviation considering N=7.

	Δλ/nm (100 nM SA)		**Δλ/nm (1000 nM SA)**		**Δλ/nm (Total)**	
Controls	1.9	1.3 ± 0.7	1.6	0.9 ± 0.4	3.5	2.3 ± 1.1
	1.2		0.9		2.1	
	2.7		1.3		4.0	
	1.4		0.9		2.3	
	0.9		0.6		1.5	
	1.1		0.4		1.5	
	0.9		0.4		1.3	
Samples	4.1	1.7 ± 1.2	1.5	1.0 ± 0.6	5.6	2.5 ± 1.2
	1.3		1.6		2.9	
	1.6		1.3		2.9	
	2.3		1.1		3.4	
	1.0		0.5		1.5	
	0.8		0.4		1.2	
	0.9		0.3		1.2	

An important aspect of the SA sensing assays with biotin functionalized AUT- and CEA-coated nanorods is the comparison between the LSP shifts measured on these particles with the ones obtained for the non-specific interactions of the bare nanorods. First, the average LSP shifts measured for a concentration of SA of 100 nM were between 3.1 and 3.5 nm for biotin functionalized AUT-coated nanorods, which are higher values than those obtained, 1.1 nm, for the non-specific interactions of SA with bare nanorods with the same characteristics (see section 4.10.2 of Annexes). Moreover, for biotin functionalized CEA-coated nanorods the average values of the LSP peak shifts in the presence of 100 nM of SA vary between 1.3 to 1.7 nm, being smaller than the 2.6 nm obtained with identical 25/600 bare nanorods (see also 4.10.2 of Annexes). These results follow an opposite trend of what was intended by testing compounds of different chain length.

Using AUT and CEA alkyl-thiols terminated with an amine group, streptavidin assays showed that the plasmonic response observed in non-irradiated controls is comparable to the one obtained with irradiated samples. This represents an undesirable effect that did not allow to take more definitive conclusions about the functionalization process *via* photochemical reactions.

The eventual failure of the photochemical reaction in these conditions could be tentatively explained by the protonation of the amine groups of AUT or CEA at the pH of the reaction medium. The loss of nucleophilicity from the amines, once they are protonated, would compromise the reactivity of AUT and CEA with the phenyl nitrene group of TFPA-Bt. In fact, the amines' pKa of AUT is 7.5, even in SAMs,[97] while for CEA this value is 10.8, so one can assume that the monolayers are partially or totally protonated, respectively.[98]

Research was then redirected to find alternative organic coatings to amine-alkanethiol SAMs. Hence, PEG-thiol molecules were used in the coating of nanorods, as presented in the next section.

4.5. Functionalization and testing of gold nanorods coated with a methyl-PEG-thiol monolayer

The photochemical biotin functionalization of nanorods was also performed on particles coated with a monolayer of oligo (ethylene glycol) thiols terminated by a methyl group. The chemical structure of this thiol compound, $MT(PEG)_4$, is shown in Figure 4.13. In this molecule, the photochemical reaction of the phenyl nitrene intermediate of TFPA-Bt could occur by covalent insertion with the C-H bounds of the terminal methyl group, as shown in Figure 4.13, or the C-H bonds of the methylene groups of the chain.

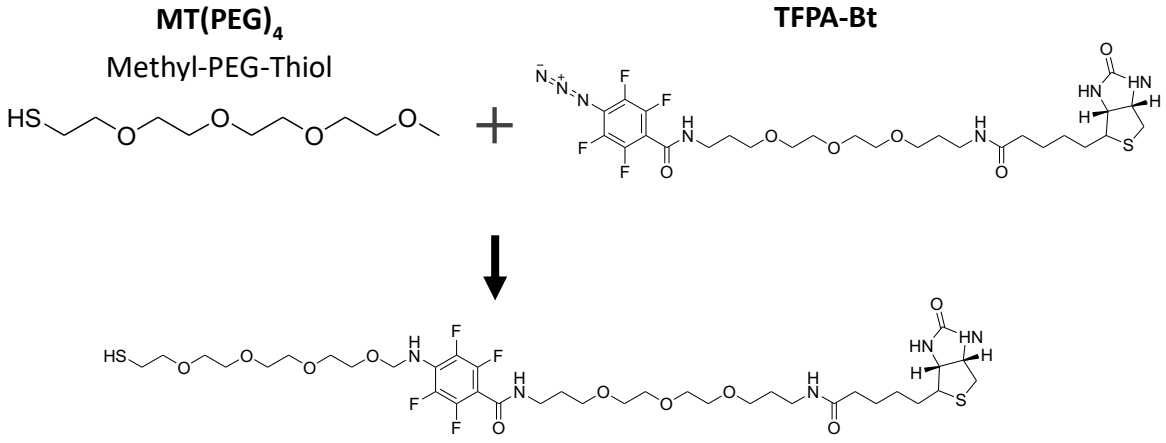

Figure 4.13 - Photochemical reaction between $MT(PEG)_4$-coated gold nanorods and TFPA-Bt. Covalent bonding occurs, upon irradiation, through C-H insertion into the phenyl nitrene intermediate of TFPA-Bt. One of the possible reaction products is represented.

In order to evaluate the efficiency of the photochemical reaction, two conditions were tested on glass-immobilized nanorods (25/600) that were either: i) exposed to TFPA-Bt with a concentration of 0.1 mM and using an irradiance power of 0.18 mW/cm^2 (LED595nm, intensity level 3), or; ii) exposed to TFPA-Bt with concentrations of 1 mM and using an irradiance power of 1.80 mW/cm^2 (LED595nm, level 6). Then, the sensing capability of these biotin-functionalized nanorod samples was evaluated from kinetic measurements of streptavidin binding. The results presented on Table 4.3 are the monitored LSP shifts obtained for non-irradiated controls and for irradiated samples, for both conditions tested. The observed shifts were almost 2-fold greater for

irradiated samples than for controls, that were also exposed with TFPA-Bt but not irradiated. In the latter, the response is only due to the non-specific adsorption of SA onto the nanorods. However, in the irradiated samples, the plasmon peak shift to streptavidin binding is larger than the non-specific response level. This strongly suggests that the photochemical reaction resulted in the successful functionalization of nanorods with biotin *via* the reaction of TFPA-Bt with the methyl-PEG thiol monolayer on the nanorods. In order to further characterize if biotin functionalization is tip-specific as intended, it would be required to examine this samples by a microscopy technique with nanometric spatial resolution, such as Atomic Force Microscopy (AFM) or Scanning Electron Microscopy (SEM).

Table 4.3 - LSP shifts ($\Delta\lambda$) measured for streptavidin sensing (100 nM) using MT(PEG)$_4$-coated nanorods functionalized with photoreactant TFPA-Bt (0.1 mM) using intensity 3 of LED595nm, and with 1 mM irradiating at intensity 6 of LED595nm. The right column corresponds to the average ± standard deviation considering N=4.

	TFPA-Bt/mM	LED595nm intensity level	Δλ/nm (100 nM SA)	
Controls	0.1	no	1.1 1.3	1.2 ± 0.1
	1	no	1.0 1.2	
Samples	0.1	3	2.3 2.3	2.1 ± 0.3
	1	6	1.7 2.1	

Some of the replicates of Table 4.3 are represented by the kinetic time traces of Figure 4.14. The nanorods' LSP peak red-shifts represent the response obtained for SA concentrations of 100 nM (region I) and 1000 nM (region II).

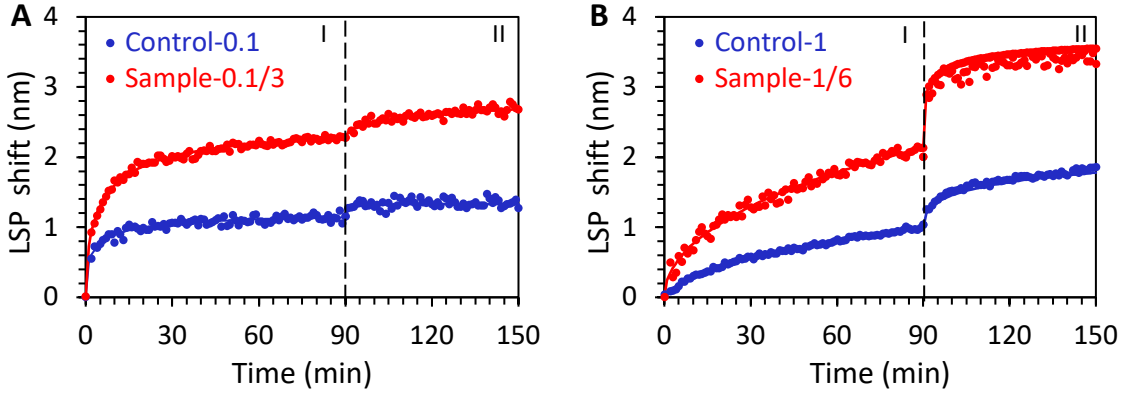

Figure 4.14 - Kinetic traces of the binding of streptavidin to nanorods coated with MT(PEG)$_4$ and tip-functionalized with (A) TFPA-Bt (0.1 mM) using intensity 3 of LED595nm, and with (B) 1 mM at intensity 6 of LED595nm (red symbols in both situations). Blue symbols correspond to the controls, i.e. surfaces that were not irradiated. Monitorization of the LSP shifts was performed with streptavidin solutions of 100 nM (region I) and 1000 nM (region II). The filled lines are the fits using a stretched exponential.

When using 0.1 mM of TFPA-Bt and an irradiance power of 0.18 mW/cm^2 (LED595nm, level 3), the time traces in region I show that, after several minutes, the LSP shifts slow down earlier for the control than for the irradiated sample (Figure 4.14A). If the protein concentration is increased up to 1000 nM (region II), the LSP shift increases again and it also stabilizes more rapidly in the control than in the irradiated sample. The same trend is observed for 1 mM of TFPA-Bt and an irradiance power of 1.80 mW/cm^2 (LED595nm, level 6) - Figure 4.14B. However, in region I, the LSP shifts do not reach a stable plateau and, in region II, the LSP shifts are higher in the irradiated sample than in the control.

It is worth mentioning that the photoreactant does not absorb in the visible spectral range, but instead at wavelengths inferior to 300 nm (Figure 4.26 of Annexes). So, in correspondence to the experimental design, the photochemical reaction may have been triggered from a two-photon absorption that is induced in the regions of strong near-field enhancement at the nanorods' tips. The near-field enhancement effect is stronger for irradiation with a wavelength (595 nm) close to the resonance frequency of the plasmon band (600 nm).

The results of photochemical functionalization obtained with nanorods coated with a MT(PEG)$_4$ monolayer are strikingly different than those previously shown for rods with AUT or CEA monolayers (section 4.4). Two possible explanations for this improvement are highlighted: i) methyl groups of MT(PEG)$_4$ are not vulnerable to protonation as are the amine groups of AUT and CEA, and so the reactivity of methyl-terminated SAMs is better via a C-H insertion of the nitrene group of TFPA-Bt; ii) passivation of glass substrates with methyl-terminated molecules is known to reduce the effect of non-specific adsorption *via* introduction of hydrophilic units,[21] and therefore, streptavidin is more prone to bind with the sparse biotin functionalized in the rod's tips.

Although the results shown in this section indicate the photochemical attachment of biotin receptors onto the nanorods, the marginal improvement of only 2-fold increase of the LSP shift of the irradiated samples relatively to the controls, has led to research other possible photoreactants, as described in the sections below.

4.6. Functionalization and sensing assays with photoreactant NPA-Bt

The other photoreactant tested was NPA-Bt, in which the photoreactive group is now a nitrophenyl azide (NPA). This molecule was obtained from a coupling reaction between the commercially available Sulfo-SANPAH and Amine-PEG$_2$-Biotin compounds, as illustrated in Figure 4.15. Sulfo-SANPAH is a well-known heterobifunctional photocrosslinker that has a spacer arm length of 1.82 nm terminated with a sulfo N-hydroxysuccinimide NHS-ester group that can be used to couple amine-derivatized molecules.

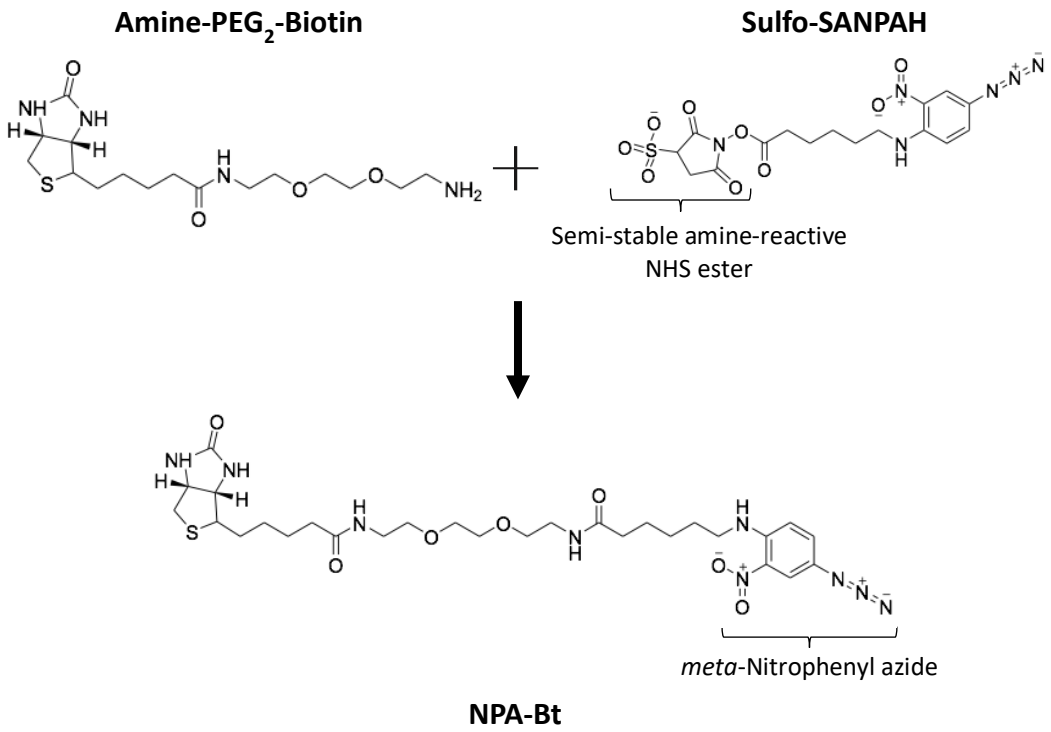

Figure 4.15 - Coupling reaction between Sulfo-SANPAH and Amine-PEG_2-Biotin to produce NPA-Bt photoreactant. *Meta*-nitrophenyl azide photoactive group is indicated.

NPA is a nitro-substituted phenyl azide, and as previously shown, the photoreactivity of nitrene is non-specific to virtually all hydrocarbon backbones of polymers. So, sulfo-SANPAH has successfully been used to introduce NHS active ester groups to polymeric surfaces.[99,100] It has also been applied to conjugate peptides, proteins or aminated biomolecules, such as DNA and polysaccharides, to most polymeric materials.[78,99–101] The use of this photoreactant was envisioned in the scope of this thesis as a way to link NPA-Bt to DNA probes, such as molecular beacons, that would be modified with an amine group at one end of the chain.

Another feature of NPA is that its UV absorption band extends to longer wavelengths than TFPA, with measurable absorption up to 320 nm. In principle, this effect of the nitro- substituent could make NPA more photoreactive in a plasmon-assisted 2PA process using irradiation at 595 nm. In Figure 4.16A it is shown the absorption spectrum of NPA displaying a band close to 300 nm, useful for 2PA, and a broad band between 400-600 nm. The latter band was not described in the product specifications, and it was not clear if it could interfere with the desired photochemical reaction. For this reason, this section is opened with results from an irradiation study of NPA-Bt compound in bulk solution. When broadband irradiation from a mercury lamp was used with a filter that excludes the UV range (Figure 4.16B), then no changes in the spectrum were observable. However, when the filter was removed, the shape of the absorption bands at ca. 300 nm and 400-600 nm changed and an additional increase in absorbance at longer wavelengths was visible for both bands. The changes in the absorption band at ca. 300 nm of NPA-Bt upon UV-irradiation is tentatively attributed to the loss of N_2 and the formation of a

phenyl nitrene group that mostly likely then suffers solvolysis or self-polymerization. This assumption can be sustained because under visible light irradiation with an incoherent source (LED595nm at intensity level 6) the spectrum remained unchanged (see Figure 4.27B of Annexes). Hence, the photochemical reaction in the absence of a plasmon near-field seems to be triggered only by UV irradiation, because irradiation of NPA's absorption band between 400-600 nm does not change its spectrum.

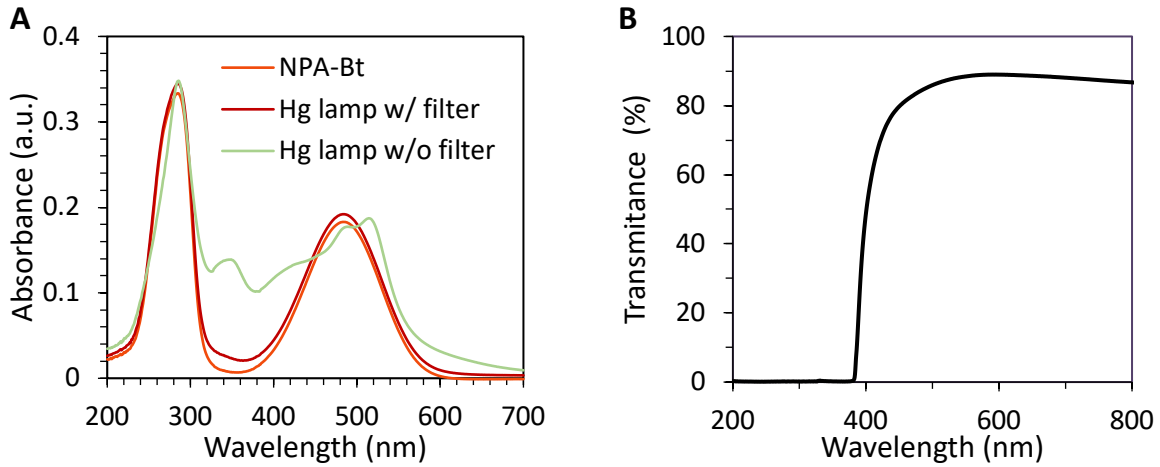

Figure 4.16 - Irradiation of photoreactant NPA-Bt with LED595nm at intensity level 6. (A) Absorption spectra of photoreactant before (orange line), and after exposure to a mercury lamp (30 min) using a filter that excludes the UV range (red line) and without the filter after more 30 min irradiation (green line). (B) Filter with a transmission window that excludes UV light.

To assess the ability of NPA-Bt as a viable reactant for the photochemical attachment of biotin onto nanorods, three samples of particles coated with AUT, CEA and MT(PEG)$_4$ were first exposed to 0.1 mM of the molecule under irradiation with NanoLED594nm. After, the particles' functionalization with biotin was evaluated by streptavidin binding assays. The kinetic measurements provided the LSP shifts for irradiated samples that were compared with non-irradiated controls, which should not be functionalized with biotins. These results are presented in Table 4.4.

Table 4.4 - Partial and total LSP shifts (Δλ) measured for streptavidin sensing (100 nM) with AUT-coated 25/650 nanorods, and CEA- and MT(PEG)$_4$-coated 25/600 nanorods, tip-functionalized photochemically with NPA-Bt.

		Δλ/nm (100 nM SA)
AUT	Control	3.4
	Sample	3.9
CEA	Control	1.4
	Sample	1.7
MT(PEG)$_4$	Control	0.6
	Sample	6.5

For AUT- and CEA-coated nanorods the plasmon shifts obtained in the controls and in the irradiated samples are mostly comparable. Besides, the results resemble those obtained with the photoreactant TFPA-Bt, as discussed in previous sections, and can be attributed mainly to non-specific binding of SA. Likewise, these assays also confirm the inefficacy of amine-terminated monolayers for photochemical reactions in nanorods. This has also been reported in a work that claims that Sulfo-SANPAH (precursor of NPA-Bt) bonds preferentially to the -OH groups of chitosan.[78] The bonding occurs by insertion of H atoms on the phenyl nitrene intermediate, in detriment of the amines that were protonated in acidic conditions resulting in weakened nucleophilicity.

Regarding MT$(PEG)_4$-coated nanorods, the irradiated sample showed a 10-fold increase in the LSP shift when compared to a not irradiated control. This preliminary result showed that NPA-Bt photoreactant can be more suitable than TFPA-Bt (only 2-fold increment) for the photochemical attachment of biotin receptors onto the nanorod's surface. This is attributed to the higher absorption overlap that is achieved in the plasmon-induced 2PA of NPA-Bt when compared to TFPA-Bt (see Figure 4.4).

The performed assays can be examined in more detail from the kinetic time traces of Figure 4.17. The LSP peak shifts in response to a SA concentration of 100 nM show that for AUT-coated nanorods the control and irradiated sample have the same sensing response (Figure 4.17A). But interestingly in CEA-coated particles there is a remarkable difference between the plasmon peak shifts of the irradiated sample and the control (Figure 4.17B). This effect is more pronounced in the beginning of the assays, maybe because, despite of the lower reactivity of amine-terminated monolayers, some biotins still got attached by photochemical reaction providing receptors for SA binding. The strange behavior of the irradiated sample can be attributed to a spurious perturbation of the streptavidin layer adsorbed on the particles' surface.

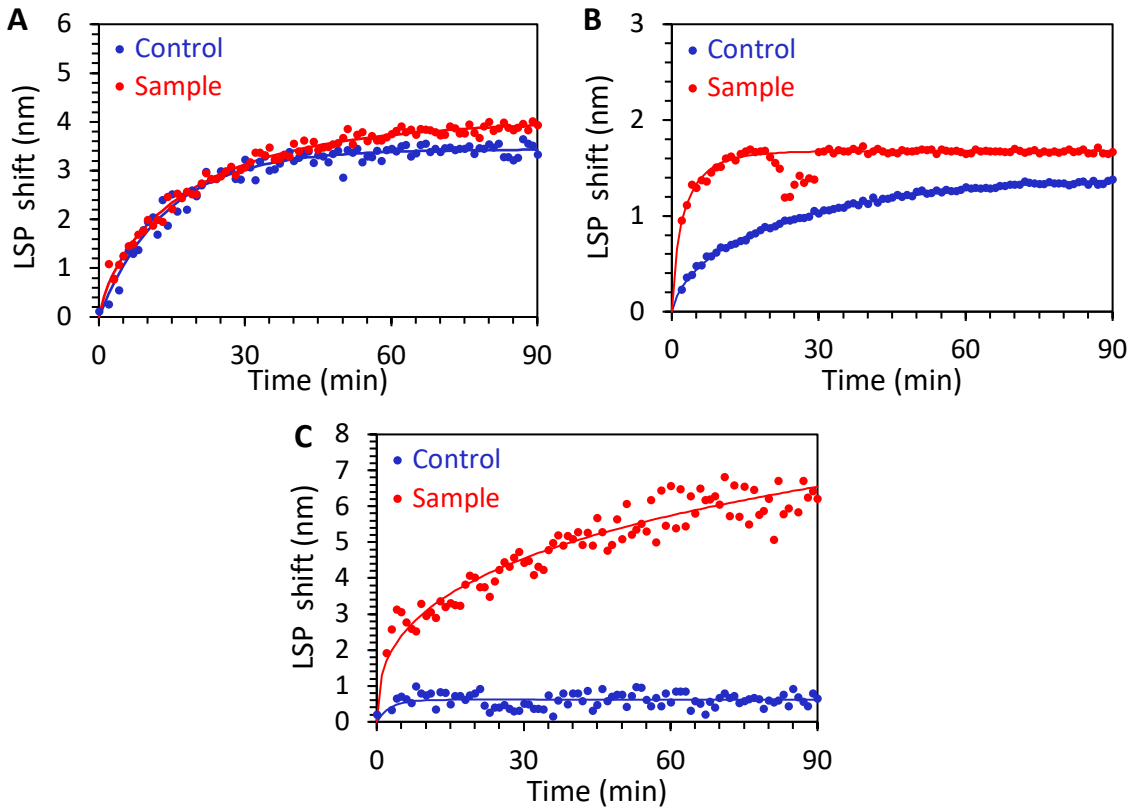

Figure 4.17 - Kinetic traces showing the LSP shift of 25/650 gold nanorods coated with (A) AUT, and of 25/600 nanorods coated with (B) CEA and (C) $MT(PEG)_4$, in response to streptavidin binding (100 nM). Photochemical tip-functionalization was performed with NPA-Bt (red symbols), and controls correspond to non-irradiated surfaces (blue symbols). The filled lines are fits performed with a stretched exponential.

In the assays with $MT(PEG)_4$-coated nanorods (Figure 4.17C) the marginal response of the non-irradiated control is only due to the non-specific adsorption of SA to the nanorods. This response is significantly lower to the non-specific interactions verified in the amine-terminated coatings. Once again, this is justified by the hydrophilic monolayer formed by $MT(PEG)_4$ molecules on the surface of the nanorods that prevents the adsorption of SA. This highlights the importance of using pegylated compounds as anti-fouling agents in LSPR assays.

4.7. Remarks and follow-up

The performance of label-free biosensors depends strongly on the biomolecular interactions between the target analyte and specific bioreceptors and, in this perspective, the development of novel receptors is important (e.g. aptamers, peptamers, nanobodies, etc.), as it may lead to better detection sensitivities and lower concentration limits. A complementary strategy is to improve the transduction component of a biosensor, in order to achieve larger responses from a low number of recognition events. In this sense, it is crucial to position receptors at the most sensitive regions of the sensing component. This feature is well illustrated by the work developed in this chapter. The implementation of an innovative photoactivated process to yield specific functionalization of the tip hot-spots at gold nanorods was aimed at improving the response of plasmonic sensors,

because this strategy could be employed for selective attachment of receptors at the hot-spots of other plasmonic nanostructures.

The proof-of-concept was developed here with a gold nanorod functionalized with biotin receptors for the development of a model plasmonic biosensor for streptavidin detection. An improvement in the sensing assays with methyl-terminated coated nanorods photochemically functionalized with NPA-Bt was found. However, this improvement is not that much relevant when compared to chemical functionalization approaches used for streptavidin LSPR sensing (annex 4.10.3). Therefore, the idealized generalization of photochemical functionalization to other type of bioreceptors, e.g. nucleic acids, was not pursued in the follow-up of this thesis. Alternatively, the well-established strategy of thiol conjugation was used for attaching fluorescently-labeled DNA probes, such as molecular beacons, onto the tips of gold nanorods, as discussed later in Chapters 5 and 6. Some possible sources of interference and methodological limitations were identified, and these will be discussed throughout this section.

The glass substrates' preparation could have interfered with the efficacy of the photochemical reaction, because the propyl chain of the MPTMS layer probably gets inserted to some extent into the nitrene group of the photoreactants, therefore competing with the N-H or C-H bonds present in the organic coatings of the nanorods. This could have been aggravated by the weakened nucleophilicity of the terminal amine groups of AUT and CEA due to their protonation. This was partially overcome by replacing these organic layers with methyl-terminated SAMs on the surface of the nanorods using $MT(PEG)_4$.

The photochemical reactions were not evaluated directly in the surface of the nanorods. In fact, the insertion of the photoreactant into the organic layer on the nanorods' surface did not produce significant shifts in the LSP band due to detectable changes in the RI around the particles. However, possible alternatives for direct assessment of the efficiency of the photochemical reactions could be implemented: i) perform the reactions between the photoactivatable molecules and AUT, CEA or $MT(PEG)_4$ in solution and quantify the resultant outcome by mass, Nuclear Magnetic Resonance (NMR) or Raman spectroscopies in search of reaction products;[63] ii) at the metal particle surface, to determine the formation of organic layers of photoreactant, X-Ray Photoelectron Spectroscopy (XPS) or Reflection Adsorption Infrared Spectroscopy (RAIRS) can be used to identify chemical elements or groups, while AFM can also be used to indirectly assess the localization of functionalization sites through the detection of bound streptavidin.[16]

Experimental variables such as the irradiation energy and time (2 hours), and the distance between the light source and the photoreactants placed in contact with immobilized nanorods were not optimized. So, these conditions could have been inadequate for effective photoactivation and succeeding reactions. The irradiance of the light source can be higher if a coherent laser source, that normally reaches 10^6-10^9 W/cm^2, is chosen instead of the sources used.[53]

The loss of thiols from the nanorods' surface due to extensive washing before the sensing assays is another experimental aspect that may have caused interferences. Since the Au-S bonds between the organic coating and the nanorods are labile,[74] there is a possibility for their desorption under certain circumstances. For example, the phosphate buffered saline (PBS) buffer overnight immersion step that proceeds SA sensing. Modification of the procedures can include a minimal PBS immersion of 30 min or 1 hour instead of long periods of time such as overnight.

Other plausible limitation can be the limited RI sensibility of the chosen gold nanorods. This corresponds to a shift in the plasmonic band of about 200 nm/RIU. To overcome this weakness, there could be employed gold nanoparticles with other shapes, or even of different materials, such as silver, that could allow for a higher sensibility to the RI. As the suggested approach intrinsically targets the regions of high near-field enhancement at the plasmon hot-spots, it can be generalized to any particle shape. Thus, bypiramids, triangles, cubes and stars, that hold sharp tips that create localized sensing volumes and offer high RI sensibilities, are an alternative to rods.[1]

Further studies using dark-field microscopy for single-particle and/or single-molecule detection could clarify about the sources of heterogeneity in molecular interactions that occur in the surfaces used for plasmonic sensing. Also, single-molecule plasmon sensing experiments could allow statistical analysis of the number of proteins that bind to biotin functionalized onto gold nanorods. In this regard, some exploratory efforts were conducted using gold nanorods immobilized on a microfluidic channel, with their surface functionalized *in situ* with thiolated biotin receptors, and further monitoring the plasmon response upon exposure to streptavidin. The work was developed in the Molecular Biosensing for Medical Diagnostics group of the Eindhoven University of Technology, under the supervision of Dr. Peter Zijlstra.

It is clear that further work is needed on the plasmonic sensor optimization and functionalization to improve reproducibility and sensibility. Many of the improvements suggested are challenging, specially from a surface functionalization point of view, because the sensor surface exposes different materials to the protein target, i.e. glass and gold. Novel methods that reduce time-consuming steps, enable simple and spatially localized particle's functionalization, and yield specific binding with high affinity to the nanorod's surface while reducing non-specific binding are therefore highly desirable.

4.8. Experimental section

4.8.1. Materials

Gold nanorods coated with cetyltrimethylammonium bromide (CTAB) with an approximate size of 25 nm × 57 nm or 25 nm × 60 nm with a LSP peak wavelength of 600 or 650 nm (products no. A12-25-600-CTAB (25/600) or A12-25-650-CTAB (25/650)), respectively, and of 10 nm × 30 nm with a LSP wavelength of 700 nm (product no. A12C-NR10-700 (10/700)), were acquired from Nanopartz Inc. as aqueous suspensions with an optical density of 1. CTAB was

purchased from Sigma with a purity of ≥99%. (3-mercaptopropyl)-trimethoxysilane (MPTMS) was from Aldrich with 95% purity. Hydrochloric acid 37% (HCl) was from Sigma-Aldrich. EZ-Link NHS-Biotin and EZ-Link NHS-PEG_4-Biotin were from ThermoFisher Scientific.

The surface coating reagents: 11-amino-1-undecanethiol hydrochloride (AUT, 99%) was from Aldrich, cysteamine (CEA, 98%) was from Sigma, and methyl-PEG-thiol (MT$(PEG)_4$) was from ThermoFisher Scientific. Photocrosslinkers biotinamido-[tri(ethylene glycol)]-azido-2,3,5,6-tetrafluorobenzamide (EZ-Link TFPA-PEG_3-Biotin, TFPA-Bt), sulfosuccinimidyl 6-(4'-azido-2'-nitrophenylamino)hexanoate (Sulfo-SANPAH) were from ThermoFisher Scientific; N-Succinimidyl 4-Azido-2,3,5,6-tetrafluorobenzoate (ATFB-SE) was from Molecular Probes. EZ-Link Amine-PEG_2-Biotin, (+)-biotinyl-3,6-dioxaoctanediamine, was supplied from ThermoFisher Scientific. Anhydrous sodium carbonate (Na_2CO_3) from Baker and sodium bicarbonate ($NaHCO_3$) from Merck were used to prepare carbonate-bicarbonate buffer. Streptavidin from *Streptomyces avidinii* was from Sigma, already affinity purified and lyophilized from 10 mM potassium phosphate. Monoclonal antibiotin antibody produced in mouse, ELISA 1:4000, was from Sigma. Phosphate-buffered saline buffer was acquired as tablets from Sigma and dissolved in ultrapure water (18.2 MΩ·cm); before use it was filtered in 0.22 μm PVDF filters. Ethanol absolute anhydrous was from Panreac and methanol was from Riedel-de-Haën (>99.8%). Ultrapure water was obtained with a Milli-Q purification system (Merck-Millipore) and used in all preparations. Glass slides of rectangular shape (25 × 36 mm^2 and 25 × 50 mm^2 in area) with thicknesses #1 and #1.5 were acquired from Menzel-Gläser, Deltalab or Normax.

4.8.2. Instrumentation

Absorption/extinction spectra were measured with a UV/vis spectrophotometer from PerkinElmer, model Lambda 35. Glass surfaces were cleaned using a UV/ozone chamber, model PSD-UV3, from Novascan. Incoherent light sources for irradiation were a pulsed diode NanoLED-590, with a peak wavelength of 594 nm (NanoLED594nm) and ca. 1.33 mW of power, from Horiba Scientific, and a mounted high-power LED M595L3 from Thorlabs with a peak wavelength of 595 nm (LED595nm) and six power levels available, as shown in Figure 4.18. The intensity of each level was measured considering a distance of 3 cm between the source and a lens (focus ~ 8 cm), plus a sample holder 12 cm from the lens.

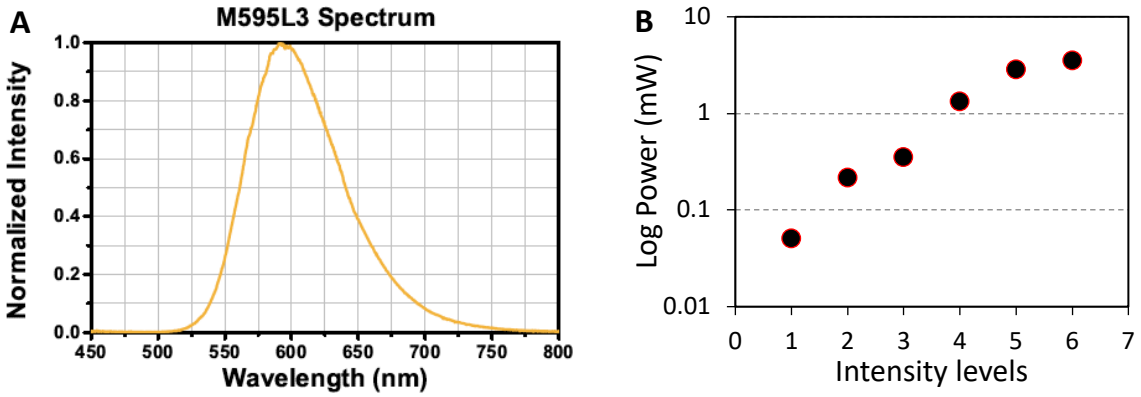

Figure 4.18 - Characteristics of the high-power LED, LED595nm, used as incoherent light source irradiation to trigger the photochemical reactions. (A) Visible spectrum with maximum wavelength at 595 nm. (B) Power measured as a function of the intensity levels available in the instrument.

The irradiated areas corresponded to a 1.9 cm × 2.1 cm ellipse, in the case of NanoLED594nm, and a circle-shaped region with 1.25 cm of radius when using LED595nm. Table 4.5 displays the light irradiance intensities of both irradiation sources.

Table 4.5 - Light intensities measured for the irradiation sources NanoLED594nm and LED595nm (with the six intensity levels available in the instrument).

		Intensity (mW/cm^2)
NanoLED594nm		0.11
LED595nm Intensity levels	1	0.03
	2	0.11
	3	0.18
	4	0.68
	5	1.44
	6	1.80

4.8.3. Glass substrates silanization and gold nanorods immobilization

Glass coverslips (24 × 50 mm^2 in area and of thicknesses #1 or #1.5) were cleaned by performing a UV/ozone treatment for 60 min. After, a TLC chamber was used to hold the slides, where they were immersed in HCl (1 M) for 30 min, then rinsed copiously with water, and sonicated in water and methanol for 10 min with intermediate steps of N_2 blow drying. For silanization, the clean slides were immersed in a 5% (v/v) solution of MPTMS in ethanol or methanol for 30 min, rinsed thoroughly with ethanol to remove unbound silane from the glass surface, sonicated for 10 min in methanol and blow dried with N_2. Alternatively, silanization was also performed considering a mixture of 5% (v/v) HCl (1 M) and 5% (v/v) MPTMS in ethanol.

Diluted gold nanorod solutions (OD = 1) were concentrated 5-fold by washing the particles. This procedure reduced the CTAB concentration and facilitated surface adhesion through centrifugation (6000 rpm, 20 min) with supernatant replacement with an aqueous solution of CTAB (0.1 mM) at least three times. The washed suspension of nanorods was drop-casted on the

silanized glass coverslips over an area of approximately 1-1.5 cm^2 by leaving a 200 μL drop in contact with the glass for 20 min. Then, the solution was removed, and the glass surface was rinsed copiously with water, and blow dried with N_2. This process was repeated 3 to 5 times until the particle density on the glass surface, measured by UV/vis spectroscopy, reached an OD of 0.002 to 0.01.

4.8.4. Gold nanorods' surface coating

To achieve a full surface coating layer of the nanorods with AUT, CEA or $MT(PEG)_4$, CTAB was not added to the coating solutions. Instead, glass surfaces with immobilized nanorods were exposed to aqueous solutions of the coating molecules (200 μL, 1 mM) for 90 min. The surface was thoroughly rinsed with water, immersed 2 h in PBS buffer, rinsed again with water and blow dried with N_2. Removal of any reactant residues or CTAB detergent must be efficient to avoid interferences during the photochemical reactions and/or the sensing assays.

4.8.5. Photochemical functionalization of coated gold nanorods

A biotin-derivatized photoreactant with an azide group was prepared by a coupling reaction between the photocrosslinker Sulfo-SANPAH (0.1 mM) and Amine-PEG_2-Biotin (1 mM) in carbonate-bicarbonate buffer at pH 7.9 (adjusted with a solution of 1 M of HCl). The coupling reaction was allowed to proceed for 1 h and the final mixture, with ca. 0.1 mM, was kept in the dark at -20 ºC without purification until further use. The resulting coupling product was named NPA-Bt in accordance to the nitrophenyl azide group in the photocrosslinker precursor and the derivatized biotin moiety. TFPA-Bt photoreactant was also named after the azide group, tetrafluorophenyl, and the biotin part. Stock solutions (3 mM) of this photoreactant were prepared by dissolving it in ethanol and freezing at -20 ºC in the dark until further use.

Glass slides containing fully-coated nanorods were assembled into a home-made liquid cell (Figure 4.19) by attaching over each one, using a melted thin frame of Parafilm M, a clean glass slide of 25 × 36 mm^2 in area and thickness #1.5 from Menzel-Gläser. The liquid cells were about 1 mm thick and hold approximately 500 μL of solution.

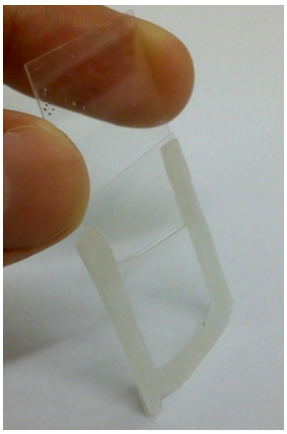

Figure 4.19 - Example of home-made liquid cell where the gold nanorods were immobilized and that was used to perform photochemical reactions and/or streptavidin sensing assays.

For photochemical reactions the liquid cells were filled with solutions of TFPA-Bt (0.1 or 1 mM) or NPA-Bt (ca. 0.1 mM), both in water. Liquid cells were irradiated with both light sources for 2 h under ambient conditions. In the irradiations with LED595nm, a lens was placed 3 cm from the source and a sample holder 12 cm from the lens (Figure 4.20).

Figure 4.20 - Experimental setup used for irradiating samples with LED595nm. A lens was placed 3 cm from the source and a sample holder 12 cm from the lens.

Controls were liquid cells filled with solutions of photoreactants that were kept in the dark, i.e. were not irradiated, also during 2 h. All liquid cells were thoroughly rinsed with water and filled with PBS buffer overnight. This last step was required before the sensing experiments in order to remove unreacted photoreactant and any additional residues that could cause interferences.

Control assays to monitor the photochemical reaction of TFPA-Bt (1 mM in water) with bare (uncoated) and with AUT- and CEA-coated nanorods were employed. For bare nanorods, water was first injected in liquid cells and extinction spectra were recorded. Water was then removed, replaced by a photoreactant solution and extinction spectra were again measured. Next, one liquid cell was irradiated with LED595nm at intensity level 6 and another one was kept in the dark, i.e. was not irradiated, while obtaining alternately extinction spectra of both samples at defined times over a period of 90 min. Concerning AUT-coated nanorods, the extinction spectra of one liquid cell filled with water was recorded and afterwards water was exchanged by a TFPA-Bt solution, maintaining the liquid cell in the dark during 90 min, before irradiating it for 2 h with LED595 nm at intensity level 6; spectra were obtained at pre-established time points. For CEA-coated nanorods, experiments were analogous to the previous ones with AUT-coated nanorods, with a difference on irradiating one liquid cell and keeping other in the dark, and recording alternately extinction spectra of both cells every 10 min during 30 min.

Evaluation of the photoreactivity of NPA-Bt (ca. 2.5 μM) and TFPA-Bt (ca. 10 μM in water), both in water, was performed by positioning a 250 W mercury lamp 10 cm from a quartz cuvette containing the solutions. Absorption spectra of the photoreactants were recorded before irradiation and every 5 min until 30 min of irradiation in the case of NPA-Bt, and after 30 min

exposure when using TFPA-Bt. NPA-Bt photoactivity was also assessed using the mercury lamp with a filter and LED595nm at intensity level 6.

ATFB-SE photoreaction with bare nanorods consisted in filling the liquid cell with water, recording the extinction spectra and replacing the water by a solution of photoreactant (1 mM in water). The cell was kept in the dark for 90 min and irradiated after with LED595nm at intensity level 6 for another 90 min, while obtaining spectra at defined time intervals.

Worth's mentioning that when using TFPA-Bt solutions, special care was taken to keep the ethanol content as low as possible in the liquid cells, since placing ethanol would break the parafilm seal and the cells would need to be assembled again.

4.8.6. Sensor functionality assays using photochemically functionalized gold nanorods

Stock solutions of streptavidin were prepared by dissolving 1 mg of protein in 1 mL of PBS buffer. This solution was diluted in PBS to attain the final concentrations of streptavidin used for sensing, i.e. 100 nM and 1 μM. Next, PBS that was kept overnight in the liquid cells, was replaced by a novel PBS solution, to ensure cleanness of the surfaces. To monitor the streptavidin sensing, on a liquid cell filled with PBS the extinction spectra was recorded at a speed of 240 nm/min to obtain the initial peak position of LSP. Then, the PBS buffer was replaced with a 100 nM SA solution, and successive spectra were recorded at a speed of 120 nm/min each minute, during 90 min (occasionally was 60 min), over a wavelength span of 100 nm around the LSP position. After this kinetic run, the extinction spectrum of the liquid cell containing the 100 nM of streptavidin was recorded at a speed of 240 nm/min to obtain the LSP position. Then, the 100 nM SA solution was replaced with another of higher concentration (1 μM) to perform another kinetic run of 60 min with the same wavelength span and speed as before. After this second kinetic run, the extinction spectrum of the liquid cell filled with 1 μM of streptavidin was again recorded at a speed of 240 nm/min to obtain the LSP position at the end of the sensing assay.

Kinetic traces were created from a time series of extinction spectra, in which each LSP position was fitted with a Gaussian function, and the maximum wavelength obtained from the fit was represented as a function of time. After, kinetic traces were also fitted, using a stretched exponential function, as described in Ref. 16, being the quality of the fits evaluated from the residuals plot. Partial plasmon peak shifts, for 100 nM and 1 μM SA concentrations, were evaluated as the difference between the values of the fitted exponential function at the end and initial peak positions of the 100 nM streptavidin sensing trace, and the end and initial peak position of the 1 μM streptavidin sensing trace, respectively. Total LSP shifts, when considered, correspond to the sum of the partial plasmon shifts.

Antibiotin sensing assays were also performed by diluting the protein directly from the flask in PBS buffer and monitoring it by a kinetic run of 90 min, following the same procedures implemented for streptavidin sensing.

There were cases in which the liquid cell was remade for any reason, e.g. broken coverslip, leak or appearance of an interference pattern. In such situations, the liquid cells were disassembled by

filling them with ethanol and letting them sit for ca. 1 min. Then, the front and back glass slides were gently separated, and the liquid cell mounted again.

4.8.7. Tip-specific chemical functionalization of gold nanorods

The procedures listed next were employed to chemically functionalize gold nanorods at their tips. First, biotin thiol linkers were prepared by coupling reactions, following an established protocol from Ref. 16. Briefly, 10 mM of the EZ Link precursors reacted with 1 mM of cysteamine in PBS buffer. The coupling reaction was allowed to proceed for 30 min and the final mixture was used without purification in the next functionalization steps. The biotin thiol linkers, hereafter termed PEG0 and PEG4, were named accordingly to the length of the oligoethylene glycol spacer in the precursor, i.e. NHS-Biotin and NHS-PEG_4-Biotin, respectively.

Glass slides with immobilized nanorods were cleaned with UV/ozone treatment for 10 min and then rinsed with water and blow dried with N_2. To start the tip-specific chemical functionalization, the area with immobilized particles was incubated with a CTAB solution (200 μL, 1 mM) for 10 min. This solution was then removed by draining it out of the surface and replacing it with a solution of biotin thiol linker (10 μM) and 1 mM of CTAB. PEG0 and PEG4 were used to functionalize 10/700 and 25/600 or 25/650 gold nanorods, respectively. This thiol attachment reaction was allowed to continue for 90 min. Lastly, the surface was thoroughly rinsed with water, immersed 2 h in PBS buffer, rinsed again with water and blow dried with N_2. Again, removal of any reactant residues or CTAB is important to avoid interferences during the sensing assays.

4.9. References

(1) Mayer, K. M.; Hafner, J. H. Localized Surface Plasmon Resonance Sensors. *Chem. Rev.* **2011**, *111* (6), 3828–3857. https://doi.org/10.1021/cr100313v.
(2) Anker, J. N.; Hall, W. P.; Lyandres, O.; Shah, N. C.; Zhao, J.; Van Duyne, R. P. Biosensing with Plasmonic Nanosensors. *Nat. Mater.* **2008**, *7* (6), 442–453. https://doi.org/10.1038/nmat2162.
(3) Miller, M. M.; Lazarides, A. A. Sensitivity of Metal Nanoparticle Surface Plasmon Resonance to the Dielectric Environment. *J. Phys. Chem. B* **2005**, *109* (46), 21556–21565. https://doi.org/10.1021/jp054227y.
(4) Lu, G.; Hou, L.; Zhang, T.; Li, W.; Liu, J.; Perriat, P.; Gong, Q. Anisotropic Plasmonic Sensing of Individual or Coupled Gold Nanorods. *J. Phys. Chem. C* **2011**, *115* (46), 22877–22885. https://doi.org/10.1021/jp2081066.
(5) Chen, C.-D.; Cheng, S.-F.; Chau, L.-K.; Wang, C. R. C. Sensing Capability of the Localized Surface Plasmon Resonance of Gold Nanorods. *Biosens. Bioelectron.* **2007**, *22* (6), 926–932. https://doi.org/10.1016/j.bios.2006.03.021.
(6) Marinakos, S. M.; Chen, S.; Chilkoti, A. Plasmonic Detection of a Model Analyte in Serum by a Gold Nanorod Sensor. *Anal. Chem.* **2007**, *79* (14), 5278–5283. https://doi.org/10.1021/ac0706527.
(7) Zijlstra, P.; Paulo, P. M. R.; Orrit, M. Optical Detection of Single Non-Absorbing Molecules Using the Surface Plasmon Resonance of a Gold Nanorod. *Nat. Nanotechnol.* **2012**, *7* (6), 379–382. https://doi.org/10.1038/nnano.2012.51.
(8) Nusz, G. J.; Curry, A. C.; Marinakos, S. M.; Wax, A.; Chilkoti, A. Rational Selection of Gold Nanorod Geometry for Label-Free Plasmonic Biosensors. *ACS Nano* **2009**, *3* (4), 795–806. https://doi.org/10.1021/nn8006465.

(9) Baciu, C. L.; Becker, J.; Janshoff, A.; Sönnichsen, C. Protein–Membrane Interaction Probed by Single Plasmonic Nanoparticles. *Nano Lett.* **2008**, *8* (6), 1724–1728. https://doi.org/10.1021/nl080805l.
(10) Yu, C.; Irudayaraj, J. Multiplex Biosensor Using Gold Nanorods. *Anal. Chem.* **2007**, *79* (2), 572–579. https://doi.org/10.1021/ac061730d.
(11) Becker, J.; Trügler, A.; Jakab, A.; Hohenester, U.; Sönnichsen, C. The Optimal Aspect Ratio of Gold Nanorods for Plasmonic Bio-Sensing. *Plasmonics* **2010**, *5* (2), 161–167. https://doi.org/10.1007/s11468-010-9130-2.
(12) Li, C.; Wu, C.; Zheng, J.; Lai, J.; Zhang, C.; Zhao, Y. LSPR Sensing of Molecular Biothiols Based on Noncoupled Gold Nanorods. *Langmuir* **2010**, *26* (11), 9130–9135. https://doi.org/10.1021/la101285r.
(13) Nusz, G. J.; Marinakos, S. M.; Curry, A. C.; Dahlin, A.; Höök, F.; Wax, A.; Chilkoti, A. Label-Free Plasmonic Detection of Biomolecular Binding by a Single Gold Nanorod. *Anal. Chem.* **2008**, *80* (4), 984–989. https://doi.org/10.1021/ac7017348.
(14) Mayer, K. M.; Lee, S.; Liao, H.; Rostro, B. C.; Fuentes, A.; Scully, P. T.; Nehl, C. L.; Hafner, J. H. A Label-Free Immunoassay Based Upon Localized Surface Plasmon Resonance of Gold Nanorods. *ACS Nano* **2008**, *2* (4), 687–692. https://doi.org/10.1021/nn7003734.
(15) Ament, I.; Prasad, J.; Henkel, A.; Schmachtel, S.; Sönnichsen, C. Single Unlabeled Protein Detection on Individual Plasmonic Nanoparticles. *Nano Lett.* **2012**, *12* (2), 1092–1095. https://doi.org/10.1021/nl204496g.
(16) Paulo, P. M. R.; Zijlstra, P.; Orrit, M.; Garcia-Fernandez, E.; Pace, T. C. S.; Viana, A. S.; Costa, S. M. B. Tip-Specific Functionalization of Gold Nanorods for Plasmonic Biosensing: Effect of Linker Chain Length. *Langmuir* **2017**, *33* (26), 6503–6510. https://doi.org/10.1021/acs.langmuir.7b00422.
(17) Soares, L.; Csáki, A.; Jatschka, J.; Fritzsche, W.; Flores, O.; Franco, R.; Pereira, E. Localized Surface Plasmon Resonance (LSPR) Biosensing Using Gold Nanotriangles: Detection of DNA Hybridization Events at Room Temperature. *The Analyst* **2014**, *139* (19), 4964–4973. https://doi.org/10.1039/C4AN00810C.
(18) Joshi, G. K.; Deitz-McElyea, S.; Liyanage, T.; Lawrence, K.; Mali, S.; Sardar, R.; Korc, M. Label-Free Nanoplasmonic-Based Short Noncoding RNA Sensing at Attomolar Concentrations Allows for Quantitative and Highly Specific Assay of MicroRNA-10b in Biological Fluids and Circulating Exosomes. *ACS Nano* **2015**, *9* (11), 11075–11089. https://doi.org/10.1021/acsnano.5b04527.
(19) Beeram, S. R.; Zamborini, F. P. Selective Attachment of Antibodies to the Edges of Gold Nanostructures for Enhanced Localized Surface Plasmon Resonance Biosensing. *J. Am. Chem. Soc.* **2009**, *131* (33), 11689–11691. https://doi.org/10.1021/ja904387j.
(20) Beeram, S. R.; Zamborini, F. P. Effect of Protein Binding Coverage, Location, and Distance on the Localized Surface Plasmon Resonance Response of Purified Au Nanoplates Grown Directly on Surfaces. *J. Phys. Chem. C* **2011**, *115* (15), 7364–7371. https://doi.org/10.1021/jp2010869.
(21) Haes, A. J.; Van Duyne, R. P. A Nanoscale Optical Biosensor: Sensitivity and Selectivity of an Approach Based on the Localized Surface Plasmon Resonance Spectroscopy of Triangular Silver Nanoparticles. *J. Am. Chem. Soc.* **2002**, *124* (35), 10596–10604. https://doi.org/10.1021/ja020393x.
(22) Haes, A. J.; Chang, L.; Klein, W. L.; Van Duyne, R. P. Detection of a Biomarker for Alzheimer's Disease from Synthetic and Clinical Samples Using a Nanoscale Optical Biosensor. *J. Am. Chem. Soc.* **2005**, *127* (7), 2264–2271. https://doi.org/10.1021/ja044087q.
(23) Sherry, L. J.; Jin, R.; Mirkin, C. A.; Schatz, G. C.; Van Duyne, R. P. Localized Surface Plasmon Resonance Spectroscopy of Single Silver Triangular Nanoprisms. *Nano Lett.* **2006**, *6* (9), 2060–2065. https://doi.org/10.1021/nl061286u.
(24) Galush, W. J.; Shelby, S. A.; Mulvihill, M. J.; Tao, A.; Yang, P.; Groves, J. T. A Nanocube Plasmonic Sensor for Molecular Binding on Membrane Surfaces. *Nano Lett.* **2009**, *9* (5), 2077–2082. https://doi.org/10.1021/nl900513k.

(25) Lee, S.; Mayer, K. M.; Hafner, J. H. Improved Localized Surface Plasmon Resonance Immunoassay with Gold Bipyramid Substrates. *Anal. Chem.* **2009**, *81* (11), 4450–4455. https://doi.org/10.1021/ac900276n.
(26) Mayer, K. M.; Hao, F.; Lee, S.; Nordlander, P.; Hafner, J. H. A Single Molecule Immunoassay by Localized Surface Plasmon Resonance. *Nanotechnology* **2010**, *21* (25), 255503. https://doi.org/10.1088/0957-4484/21/25/255503.
(27) Peters, S. M. E.; Verheijen, M. A.; Prins, M. W. J.; Zijlstra, P. Strong Reduction of Spectral Heterogeneity in Gold Bipyramids for Single-Particle and Single-Molecule Plasmon Sensing. *Nanotechnology* **2016**, *27* (2), 024001. https://doi.org/10.1088/0957-4484/27/2/024001.
(28) Sagle, L. B.; Ruvuna, L. K.; Ruemmele, J. A.; Van Duyne, R. P. Advances in Localized Surface Plasmon Resonance Spectroscopy Biosensing. *Nanomed.* **2011**, *6* (8), 1447–1462. https://doi.org/10.2217/nnm.11.117.
(29) Fong, K. E.; Yung, L.-Y. L. Localized Surface Plasmon Resonance: A Unique Property of Plasmonic Nanoparticles for Nucleic Acid Detection. *Nanoscale* **2013**, *5* (24), 12043. https://doi.org/10.1039/c3nr02257a.
(30) Hammond, J.; Bhalla, N.; Rafiee, S.; Estrela, P. Localized Surface Plasmon Resonance as a Biosensing Platform for Developing Countries. *Biosensors* **2014**, *4* (2), 172–188. https://doi.org/10.3390/bios4020172.
(31) Masson, J.-F. Surface Plasmon Resonance Clinical Biosensors for Medical Diagnostics. *ACS Sens.* **2017**, *2* (1), 16–30. https://doi.org/10.1021/acssensors.6b00763.
(32) Malekzad, H.; Sahandi Zangabad, P.; Mohammadi, H.; Sadroddini, M.; Jafari, Z.; Mahlooji, N.; Abbaspour, S.; Gholami, S.; Ghanbarpour Houshangi, M.; Pashazadeh, R.; Beyzavi, A.; Karimi, M.; Hamblin, M. R. Noble Metal Nanostructures in Optical Biosensors: Basics, and Their Introduction to Anti-Doping Detection. *TrAC Trends Anal. Chem.* **2018**, *100*, 116–135. https://doi.org/10.1016/j.trac.2017.12.006.
(33) Soler, M.; Huertas, C. S.; Lechuga, L. M. Label-Free Plasmonic Biosensors for Point-of-Care Diagnostics: A Review. *Expert Rev. Mol. Diagn.* **2019**, *19* (1), 71–81. https://doi.org/10.1080/14737159.2019.1554435.
(34) Raschke, G.; Kowarik, S.; Franzl, T.; Sönnichsen, C.; Klar, T. A.; Feldmann, J.; Nichtl, A.; Kürzinger, K. Biomolecular Recognition Based on Single Gold Nanoparticle Light Scattering. *Nano Lett.* **2003**, *3* (7), 935–938. https://doi.org/10.1021/nl034223+.
(35) Marinakos, S. M.; Chen, S.; Chilkoti, A. Plasmonic Detection of a Model Analyte in Serum by a Gold Nanorod Sensor. *Anal. Chem.* **2007**, *79* (14), 5278–5283. https://doi.org/10.1021/ac0706527.
(36) Gu, Y.; Song, J.; Li, M.-X.; Zhang, T.-T.; Zhao, W.; Xu, J.-J.; Liu, M.; Chen, H.-Y. Ultrasensitive MicroRNA Assay via Surface Plasmon Resonance Responses of Au@Ag Nanorods Etching. *Anal. Chem.* **2017**, *89* (19), 10585–10591. https://doi.org/10.1021/acs.analchem.7b02920.
(37) Rosman, C.; Prasad, J.; Neiser, A.; Henkel, A.; Edgar, J.; Sönnichsen, C. Multiplexed Plasmon Sensor for Rapid Label-Free Analyte Detection. *Nano Lett.* **2013**, *13* (7), 3243–3247. https://doi.org/10.1021/nl401354f.
(38) Beuwer, M. A.; Prins, M. W. J.; Zijlstra, P. Stochastic Protein Interactions Monitored by Hundreds of Single-Molecule Plasmonic Biosensors. *Nano Lett.* **2015**, *15* (5), 3507–3511. https://doi.org/10.1021/acs.nanolett.5b00872.
(39) Taylor, A. B.; Zijlstra, P. Single-Molecule Plasmon Sensing: Current Status and Future Prospects. *ACS Sens.* **2017**, *2* (8), 1103–1122. https://doi.org/10.1021/acssensors.7b00382.
(40) Aćimović, S. S.; Ortega, M. A.; Sanz, V.; Berthelot, J.; Garcia-Cordero, J. L.; Renger, J.; Maerkl, S. J.; Kreuzer, M. P.; Quidant, R. LSPR Chip for Parallel, Rapid, and Sensitive Detection of Cancer Markers in Serum. *Nano Lett.* **2014**, *14* (5), 2636–2641. https://doi.org/10.1021/nl500574n.
(41) Yavas, O.; Aćimović, S. S.; Garcia-Guirado, J.; Berthelot, J.; Dobosz, P.; Sanz, V.; Quidant, R. Self-Calibrating On-Chip Localized Surface Plasmon Resonance Sensing for Quantitative and Multiplexed Detection of Cancer Markers in Human Serum. *ACS Sens.* **2018**, *3* (7), 1376–1384.

https://doi.org/10.1021/acssensors.8b00305.
(42) Zijlstra, P.; Paulo, P. M. R.; Yu, K.; Xu, Q.-H.; Orrit, M. Chemical Interface Damping in Single Gold Nanorods and Its Near Elimination by Tip-Specific Functionalization. *Angew. Chem. Int. Ed.* **2012**, *51* (33), 8352–8355. https://doi.org/10.1002/anie.201202318.
(43) Feuz, L.; Jonsson, M. P.; Höök, F. Material-Selective Surface Chemistry for Nanoplasmonic Sensors: Optimizing Sensitivity and Controlling Binding to Local Hot Spots. *Nano Lett.* **2012**, *12* (2), 873–879. https://doi.org/10.1021/nl203917e.
(44) Fang, A.; White, S. L.; Masitas, R. A.; Zamborini, F. P.; Jain, P. K. One-to-One Correlation between Structure and Optical Response in a Heterogeneous Distribution of Plasmonic Constructs. *J. Phys. Chem. C* **2015**, *119* (42), 24086–24094. https://doi.org/10.1021/acs.jpcc.5b09292.
(45) Cortés, E.; Xie, W.; Cambiasso, J.; Jermyn, A. S.; Sundararaman, R.; Narang, P.; Schlücker, S.; Maier, S. A. Plasmonic Hot Electron Transport Drives Nano-Localized Chemistry. *Nat. Commun.* **2017**, *8* (1). https://doi.org/10.1038/ncomms14880.
(46) Chen, C. J.; Osgood, R. M. Direct Observation of the Local-Field-Enhanced Surface Photochemical Reactions. *Phys. Rev. Lett.* **1983**, *50* (21), 1705–1708. https://doi.org/10.1103/PhysRevLett.50.1705.
(47) Ueno, K.; Misawa, H. Surface Plasmon-Enhanced Photochemical Reactions. *J. Photochem. Photobiol. C Photochem. Rev.* **2013**, *15*, 31–52. https://doi.org/10.1016/j.jphotochemrev.2013.04.001.
(48) Zhou, X.; Soppera, O.; Plain, J.; Jradi, S.; Wei Sun, X.; Volkan Demir, H.; Yang, X.; Deeb, C.; Gray, S. K.; Wiederrecht, G. P.; Bachelot, R. Plasmon-Based Photopolymerization: Near-Field Probing, Advanced Photonic Nanostructures and Nanophotochemistry. *J. Opt.* **2014**, *16* (11), 114002. https://doi.org/10.1088/2040-8978/16/11/114002.
(49) Baffou, G.; Quidant, R. Nanoplasmonics for Chemistry. *Chem. Soc. Rev.* **2014**, *43* (11), 3898. https://doi.org/10.1039/c3cs60364d.
(50) Linic, S.; Aslam, U.; Boerigter, C.; Morabito, M. Photochemical Transformations on Plasmonic Metal Nanoparticles. *Nat. Mater.* **2015**, *14* (6), 567–576. https://doi.org/10.1038/nmat4281.
(51) Wang, Z.; Ai, B.; Möhwald, H.; Zhang, G. Colloidal Lithography Meets Plasmonic Nanochemistry. *Adv. Opt. Mater.* **2018**, *6* (18), 1800402. https://doi.org/10.1002/adom.201800402.
(52) Lacroix, J.; van Nguyen, Q.; Ai, Y.; van Nguyen, Q.; Martin, P.; Lacaze, P. From Active Plasmonic Devices to Plasmonic Molecular Electronics. *Polym. Int.* **2019**, *68* (4), 607–619. https://doi.org/10.1002/pi.5756.
(53) Ueno, K.; Juodkazis, S.; Shibuya, T.; Yokota, Y.; Mizeikis, V.; Sasaki, K.; Misawa, H. Nanoparticle Plasmon-Assisted Two-Photon Polymerization Induced by Incoherent Excitation Source. *J. Am. Chem. Soc.* **2008**, *130* (22), 6928–6929. https://doi.org/10.1021/ja801262r.
(54) Ueno, K.; Juodkazis, S.; Shibuya, T.; Mizeikis, V.; Yokota, Y.; Misawa, H. Nanoparticle-Enhanced Photopolymerization. *J. Phys. Chem. C* **2009**, *113* (27), 11720–11724. https://doi.org/10.1021/jp901773k.
(55) Gao, S.; Ueno, K.; Misawa, H. Plasmonic Antenna Effects on Photochemical Reactions. *Acc. Chem. Res.* **2011**, *44* (4), 251–260. https://doi.org/10.1021/ar100117w.
(56) Haggui, M.; Dridi, M.; Plain, J.; Marguet, S.; Perez, H.; Schatz, G. C.; Wiederrecht, G. P.; Gray, S. K.; Bachelot, R. Spatial Confinement of Electromagnetic Hot and Cold Spots in Gold Nanocubes. *ACS Nano* **2012**, *6* (2), 1299–1307. https://doi.org/10.1021/nn2040389.
(57) Zhou, X.; Deeb, C.; Kostcheev, S.; Wiederrecht, G. P.; Adam, P.-M.; Béal, J.; Plain, J.; Gosztola, D. J.; Grand, J.; Félidj, N.; Wang, H.; Vial, A.; Bachelot, R. Selective Functionalization of the Nanogap of a Plasmonic Dimer. *ACS Photonics* **2015**, *2* (1), 121–129. https://doi.org/10.1021/ph500331c.
(58) Rajeeva, B. B.; Hernandez, D. S.; Wang, M.; Perillo, E.; Lin, L.; Scarabelli, L.; Pingali, B.; Liz-Marzán, L. M.; Dunn, A. K.; Shear, J. B.; Zheng, Y. Regioselective Localization and Tracking of Biomolecules on Single Gold Nanoparticles. *Adv. Sci.* **2015**, *2* (11), 1500232. https://doi.org/10.1002/advs.201500232.

(59) Nguyen, M.; Lamouri, A.; Salameh, C.; Lévi, G.; Grand, J.; Boubekeur-Lecaque, L.; Mangeney, C.; Félidj, N. Plasmon-Mediated Chemical Surface Functionalization at the Nanoscale. *Nanoscale* **2016**, *8* (16), 8633–8640. https://doi.org/10.1039/C6NR00744A.
(60) Nguyen, M.; Kherbouche, I.; Gam-Derouich, S.; Ragheb, I.; Lau-Truong, S.; Lamouri, A.; Lévi, G.; Aubard, J.; Decorse, P.; Félidj, N.; Mangeney, C. Regioselective Surface Functionalization of Lithographically Designed Gold Nanorods by Plasmon-Mediated Reduction of Aryl Diazonium Salts. *Chem Commun* **2017**, *53* (82), 11364–11367. https://doi.org/10.1039/C7CC05974D.
(61) Zayats, A. V.; Maier, S. Hot-Electron Effects in Plasmonics and Plasmonic Materials. *Adv. Opt. Mater.* **2017**, *5* (15), 1700508. https://doi.org/10.1002/adom.201700508.
(62) Nguyen, V.-Q.; Ai, Y.; Martin, P.; Lacroix, J.-C. Plasmon-Induced Nanolocalized Reduction of Diazonium Salts. *ACS Omega* **2017**, *2* (5), 1947–1955. https://doi.org/10.1021/acsomega.7b00394.
(63) Tijunelyte, I.; Kherbouche, I.; Gam-Derouich, S.; Nguyen, M.; Lidgi-Guigui, N.; de la Chapelle, M. L.; Lamouri, A.; Lévi, G.; Aubard, J.; Chevillot-Biraud, A.; Mangeney, C.; Felidj, N. Multi-Functionalization of Lithographically Designed Gold Nanodisks by Plasmon-Mediated Reduction of Aryl Diazonium Salts. *Nanoscale Horiz.* **2018**, *3* (1), 53–57. https://doi.org/10.1039/C7NH00113D.
(64) Li, G.-C.; Zhang, Q.; Maier, S. A.; Lei, D. Plasmonic Particle-on-Film Nanocavities: A Versatile Platform for Plasmon-Enhanced Spectroscopy and Photochemistry. *Nanophotonics* **2018**, *7* (12), 1865–1889. https://doi.org/10.1515/nanoph-2018-0162.
(65) Kazuma, E.; Jung, J.; Ueba, H.; Trenary, M.; Kim, Y. Real-Space and Real-Time Observation of a Plasmon-Induced Chemical Reaction of a Single Molecule. *Science* **2018**, *360* (6388), 521–526. https://doi.org/10.1126/science.aao0872.
(66) Simoncelli, S.; Pensa, E. L.; Brick, T.; Gargiulo, J.; Lauri, A.; Cambiasso, J.; Li, Y.; Maier, S. A.; Cortés, E. Monitoring Plasmonic Hot-Carrier Chemical Reactions at the Single Particle Level. *Faraday Discuss.* **2019**, *214*, 73–87. https://doi.org/10.1039/C8FD00138C.
(67) Simoncelli, S.; Li, Y.; Cortés, E.; Maier, S. A. Nanoscale Control of Molecular Self-Assembly Induced by Plasmonic Hot-Electron Dynamics. *ACS Nano* **2018**, *12* (3), 2184–2192. https://doi.org/10.1021/acsnano.7b08563.
(68) Cortés, E. Activating Plasmonic Chemistry. *Science* **2018**, *362* (6410), 28–29. https://doi.org/10.1126/science.aav1133.
(69) Gargiulo, J.; Berté, R.; Li, Y.; Maier, S. A.; Cortés, E. From Optical to Chemical Hot Spots in Plasmonics. *Acc. Chem. Res.* **2019**, *52* (9), 2525–2535. https://doi.org/10.1021/acs.accounts.9b00234.
(70) Sigle, D. O.; Zhang, L.; Ithurria, S.; Dubertret, B.; Baumberg, J. J. Ultrathin CdSe in Plasmonic Nanogaps for Enhanced Photocatalytic Water Splitting. *J. Phys. Chem. Lett.* **2015**, *6* (7), 1099–1103. https://doi.org/10.1021/acs.jpclett.5b00279.
(71) Glass, N. R.; Tjeung, R.; Chan, P.; Yeo, L. Y.; Friend, J. R. Organosilane Deposition for Microfluidic Applications. *Biomicrofluidics* **2011**, *5* (3), 036501. https://doi.org/10.1063/1.3625605.
(72) Pensa, E.; Cortés, E.; Corthey, G.; Carro, P.; Vericat, C.; Fonticelli, M. H.; Benítez, G.; Rubert, A. A.; Salvarezza, R. C. The Chemistry of the Sulfur–Gold Interface: In Search of a Unified Model. *Acc. Chem. Res.* **2012**, *45* (8), 1183–1192. https://doi.org/10.1021/ar200260p.
(73) Xue, Y.; Li, X.; Li, H.; Zhang, W. Quantifying Thiol–Gold Interactions towards the Efficient Strength Control. *Nat. Commun.* **2014**, *5* (1). https://doi.org/10.1038/ncomms5348.
(74) Bürgi, T. Properties of the Gold–Sulphur Interface: From Self-Assembled Monolayers to Clusters. *Nanoscale* **2015**, *7* (38), 15553–15567. https://doi.org/10.1039/C5NR03497C.
(75) Gothe, P. K.; Gaur, D.; Achanta, V. G. MPTMS Self-Assembled Monolayer Deposition for Ultra-Thin Gold Films for Plasmonics. *J. Phys. Commun.* **2018**, *2* (3), 035005. https://doi.org/10.1088/2399-6528/aaaedd.
(76) Zheng, M.; Davidson, F.; Huang, X. Ethylene Glycol Monolayer Protected Nanoparticles for Eliminating Nonspecific Binding with Biological Molecules †. *J. Am. Chem. Soc.* **2003**, *125* (26),

7790–7791. https://doi.org/10.1021/ja0350278.
(77) Yan, M.; Cai, S. X.; Wybourne, M. N.; Keana, J. F. W. N-Hydroxysuccinimide Ester Functionalized Perfluorophenyl Azides as Novel Photoactive Heterobifunctional Crosslinking Reagents. The Covalent Immobilization of Biomolecules to Polymer Surfaces. *Bioconjug. Chem.* **1994**, *5* (2), 151–157. https://doi.org/10.1021/bc00026a007.
(78) Yang, Y.; Liu, X.; Yu, W.; Zhou, H.; Li, X.; Ma, X. Homogeneous Synthesis of GRGDY Grafted Chitosan on Hydroxyl Groups by Photochemical Reaction for Improved Cell Adhesion. *Carbohydr. Polym.* **2010**, *80* (3), 733–739. https://doi.org/10.1016/j.carbpol.2009.12.019.
(79) Schnapp, K. A.; Poe, R.; Leyva, E.; Soundararajan, N.; Platz, M. S. Exploratory Photochemistry of Fluorinated Aryl Azides. Implications for the Design of Photoaffinity Labeling Reagents. *Bioconjug. Chem.* **1993**, *4* (2), 172–177. https://doi.org/10.1021/bc00020a010.
(80) Panov, M. S. Early Events in Photochemistry of Aryl Azides Used as Photoaffinity Labeling Agents. **2011**, 241.
(81) Liu, L.-H.; Yan, M. Perfluorophenyl Azides: New Applications in Surface Functionalization and Nanomaterial Synthesis. *Acc. Chem. Res.* **2010**, *43* (11), 1434–1443. https://doi.org/10.1021/ar100066t.
(82) Michalak, J.; Zhai, H. B.; Platz, M. S. The Photochemistry of Various Para-Substituted Tetrafluorophenyl Azides in Acidic Media and the Formation of Nitrenium Ions. *J. Phys. Chem.* **1996**, *100* (33), 14028–14036. https://doi.org/10.1021/jp961100n.
(83) Schrock, A. K.; Schuster, G. B. Photochemistry of Phenyl Azide: Chemical Properties of the Transient Intermediates. *J. Am. Chem. Soc.* **1984**, *106* (18), 5228–5234. https://doi.org/10.1021/ja00330a032.
(84) Leyva, Elisa.; Platz, M. S.; Persy, Gabriele.; Wirz, Jakob. Photochemistry of Phenyl Azide: The Role of Singlet and Triplet Phenylnitrene as Transient Intermediates. *J. Am. Chem. Soc.* **1986**, *108* (13), 3783–3790. https://doi.org/10.1021/ja00273a037.
(85) Schuster, G. B.; Platz, M. S. Photochemistry of Phenyl Azide. In *Advances in Photochemistry*; Volman, D. H., Hammond, G. S., Neckers, D. C., Eds.; John Wiley & Sons, Inc.: Hoboken, NJ, USA, 2007; pp 69–143. https://doi.org/10.1002/9780470133484.ch2.
(86) Keana, J. F. W.; Cai, S. X. New Reagents for Photoaffinity Labeling: Synthesis and Photolysis of Functionalized Perfluorophenyl Azides. *J. Org. Chem.* **1990**, *55* (11), 3640–3647. https://doi.org/10.1021/jo00298a048.
(87) Poe, R.; Schnapp, K.; Young, M. J. T.; Grayzar, J.; Platz, M. S. Chemistry and Kinetics of Singlet (Pentafluoropheny1)Nitrene. **1992**, 14.
(88) Morawietz, J.; Sander, W. Photochemistry of Fluorinated Phenyl Nitrenes: Matrix Isolation of Fluorinated Azirines. *J. Org. Chem.* **1996**, *61* (13), 4351–4354. https://doi.org/10.1021/jo960093w.
(89) Platz, M. Comparison of Phenylcarbene and Phenylnitrenel. **1995**, 6.
(90) Pastine, S. J.; Okawa, D.; Kessler, B.; Rolandi, M.; Llorente, M.; Zettl, A.; Fréchet, J. M. J. A Facile and Patternable Method for the Surface Modification of Carbon Nanotube Forests Using Perfluoroarylazides. *J. Am. Chem. Soc.* **2008**, *130* (13), 4238–4239. https://doi.org/10.1021/ja8003446.
(91) Liu, L.-H.; Yan, M. Simple Method for the Covalent Immobilization of Graphene. *Nano Lett.* **2009**, *9* (9), 3375–3378. https://doi.org/10.1021/nl901669h.
(92) Liu, L.-H.; Zorn, G.; Castner, D. G.; Solanki, R.; Lerner, M. M.; Yan., M. A Simple and Scalable Route to Wafer-Size Patterned Graphene. *J. Mater. Chem.* **2010**, *20* (24), 5041. https://doi.org/10.1039/c0jm00509f.
(93) Pandurangi, R. S. High Efficiency Photolabeling of Human Serum Albumin and Human Y-Globulinwith [14C]Methyl4-Azido-2,3,5,6-Tetrafluoro- Benzoate. **1995**, 5.
(94) Bartlett, M. A.; Yan, M. Fabrication of Polymer Thin Films and Arrays with Spatial and Topographical Controls. *Adv. Mater.* **2001**, *13* (19), 1449–1451. https://doi.org/10.1002/1521-4095(200110)13:19<1449::AID-ADMA1449>3.0.CO;2-M.
(95) McVerry, B. T.; Wong, M. C. Y.; Marsh, K. L.; Temple, J. A. T.; Marambio-Jones, C.; Hoek,

E. M. V.; Kaner, R. B. Scalable Antifouling Reverse Osmosis Membranes Utilizing Perfluorophenyl Azide Photochemistry. *Macromol. Rapid Commun.* **2014**, *35* (17), 1528–1533. https://doi.org/10.1002/marc.201400226.
(96) Luetzow, K.; Hommes-Schattmann, P. J.; Neffe, A. T.; Ahmad, B.; Williams, G. R.; Lendlein, A. Perfluorophenyl Azide Functionalization of Electrospun Poly(*Para* -dioxanone). *Polym. Adv. Technol.* **2019**, *30* (5), 1165–1172. https://doi.org/10.1002/pat.4331.
(97) Lim, C.; Ko, J.; Jeon, D.; Song, Y.; Park, J.; Ryu, J.; Lee, D. W. Probing Molecular Mechanisms of M13 Bacteriophage Adhesion. *Commun. Chem.* **2019**, *2* (1). https://doi.org/10.1038/s42004-019-0198-0.
(98) Szefczyk, B.; Franco, R.; Gomes, J. A. N. F.; Cordeiro, M. N. D. S. Structure of the Interface between Water and Self-Assembled Monolayers of Neutral, Anionic and Cationic Alkane Thiols. *J. Mol. Struct. THEOCHEM* **2010**, *946* (1–3), 83–87. https://doi.org/10.1016/j.theochem.2009.11.021.
(99) Chung, T.-W.; Lu, Y.-F.; Wang, S.-S.; Lin, Y.-S.; Chu, S.-H. Growth of Human Endothelial Cells on Photochemically Grafted Gly–Arg–Gly–Asp (GRGD) Chitosans. *Biomaterials* **2002**, *23* (24), 4803–4809. https://doi.org/10.1016/S0142-9612(02)00231-4.
(100) Li, B.; Chen, J.; Wang, J. H.-C. RGD Peptide-Conjugated Poly(Dimethylsiloxane) Promotes Adhesion, Proliferation, and Collagen Secretion of Human Fibroblasts. *J. Biomed. Mater. Res. A* **2006**, *79A* (4), 989–998. https://doi.org/10.1002/jbm.a.30847.
(101) Connelly, J. T.; Petrie, T. A.; García, A. J.; Levenston, M. E. Fibronectin- and Collagen-Mimetic Ligands Regulate BMSC Chondrogenesis in 3D Hydrogels. **2016**, 14.
(102) Pramod, P.; Joseph, S. T. S.; Thomas, K. G. Preferential End Functionalization of Au Nanorods through Electrostatic Interactions. *J. Am. Chem. Soc.* **2007**, *129* (21), 6712–6713. https://doi.org/10.1021/ja071536o.
(103) Caswell, K. K.; Wilson, J. N.; Bunz, U. H. F.; Murphy, C. J. Preferential End-to-End Assembly of Gold Nanorods by Biotin−Streptavidin Connectors. *J. Am. Chem. Soc.* **2003**, *125* (46), 13914–13915. https://doi.org/10.1021/ja037969i.
(104) Pan, B.; Ao, L.; Gao, F.; Tian, H.; He, R.; Cui, D. End-to-End Self-Assembly and Colorimetric Characterization of Gold Nanorods and Nanospheres via Oligonucleotide Hybridization. *Nanotechnology* **2005**, *16* (9), 1776–1780. https://doi.org/10.1088/0957-4484/16/9/061.
(105) Wang, Y.; DePrince, A. E.; Gray, S. K.; Lin, X.-M.; Pelton, M. Solvent-Mediated End-to-End Assembly of Gold Nanorods. *J. Phys. Chem. Lett.* **2010**, *1* (18), 2692–2698. https://doi.org/10.1021/jz1010048.
(106) Zijlstra, P.; Paulo, P. M. R.; Orrit, M. Optical Detection of Single Non-Absorbing Molecules Using the Surface Plasmon of a Gold Nanorod. *Nat. Nanotechnol.* **2012**, *7* (6), 379–382. https://doi.org/10.1038/nnano.2012.51.

4.10. Annexes

4.10.1. Immobilization of gold nanorods on glass surfaces

Gold nanorods (e.g. 25/600) solutions with an OD of 10 were used but the outcome rendered stains on the glass coverslips (Figure 4.21A). After extinction spectra measurement, this revealed aggregation of the particles, pictured by the appearance of a band between 600-700 nm or a spectrum with an undefined shape, in which the distinctive longitudinal plasmon band of the nanorods was absent (Figure 4.21B).

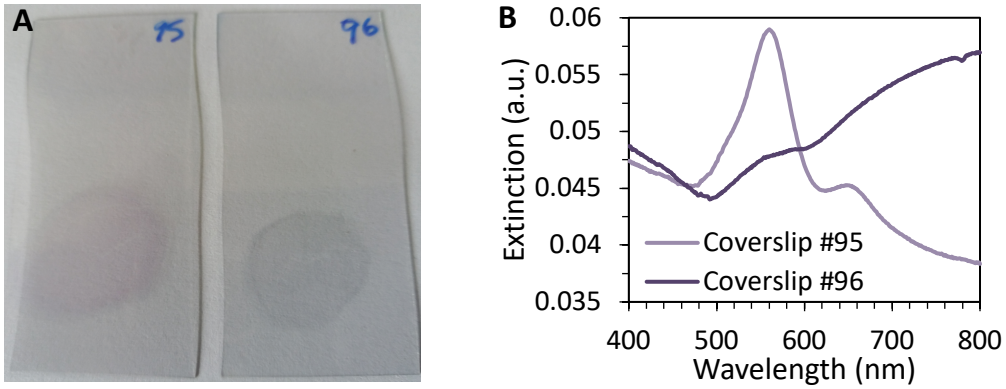

Figure 4.21 - Immobilization of 25/600 gold nanorods on silanized glass substrates through the formation of Au-S bonds. (A) Example of an immobilization rendering nanorod's stains in the glass coverslips, (B) that corresponded to aggregation of the particles as revealed in the extinction spectra.

4.10.2. Control assays I: evaluation of non-specific adsorption

To first assess the non-specific binding of streptavidin to the gold nanorod's surface, a set of control experiments was performed. Bare nanorods, i.e. particles that were not functionalized with biotin, were exposed to streptavidin solutions. Red-shifts in the particles' plasmon peak position were then monitored, as seen in regions I (100 nM of SA) and II (1000 nM of SA) of the examples of Figure 4.22.

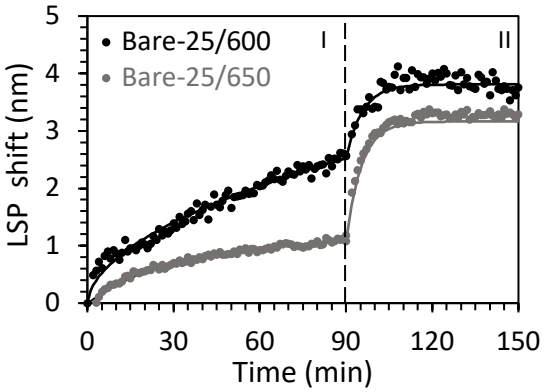

Figure 4.22 - Kinetic traces showing the LSP peak shifts of bare 25/600 (black) and 25/650 (grey) gold nanorods in response to streptavidin binding using solutions of 100 nM (region I) and 1000 nM (region II). The filled lines represent the fits performed with a stretched exponential.

The LSP shifts of 25/600 nanorods are slightly greater than the ones obtained with 25/650 nanorods. This tendency is confirmed in Table 4.6 in which the total plasmon shifts were about 3.6 and 3.2 nm for 25/600 and 25/650 nanorods, respectively. These values correspond to the non-specific adsorption of streptavidin to bare nanorods and were assumed as the lower limit for defining a specific sensor response. The higher response of 25/600 gold nanorods, particularly to 100 nM of SA, is not in agreement with the expected sensitivities of these two nanorod samples.

Table 4.6 - Partial and total LSP shifts (Δλ) measured for streptavidin sensing (100 and 1000 nM) using bare 25/600 and 25/650 nanorods. Average ± standard deviation of N=3.

NRs	Δλ/nm (100 nM SA)		Δλ/nm (1000 nM SA)		Δλ/nm (Total)	
25/600	2.3 2.5 3.0	2.6 ± 0.4	0.9 1.3 0.7	1.0 ± 0.3	3.2 3.8 3.7	3.6 ± 0.3
25/650	1.1	-	2.1	-	3.2	-

4.10.3. Control assays II: gold nanorods functionalized by thiol attachment evaluation of non-specific adsorption

The effect of tip-selective functionalization with the photochemical strategy was compared to another strategy that uses thiol attachment in the presence of CTAB detergent that acts as a side-protective coating. The role of CTAB in this tip-functionalization of gold nanorods with thiol-derivatized molecules has long been recognized in the literature.[102,103–105] It implies that CTAB molecules create a bilayer coating over the nanorods that is more compact over the particles' sides, thus directing thiol attachment to the tips.

Nanorods were tip-functionalized using a protocol previously demonstrated to be site-selective.[42,106] Two biotin-linker thiols of different length, PEG0 and PEG4, were prepared by coupling reactions (see section 4.8.7) following a published protocol.[7] Briefly, both linkers were prepared by mixing an excess of NHS-Biotin or NHS-PEG4-Biotin with cysteamine (Figure 4.23A). The NHS-activated biotin reacts with the primary amine of cysteamine forming a stable amide bond. The spacer arms that separates biotin from the thiol group has an end-to-end distance, at an extended conformation (biotin not included), of about 0.5 nm and 2.4 nm for PEG0 and PEG4, respectively. To attach the desired biotin functionality on the nanorods, biotinylation was performed in a home-made flow cell by incubation of the particles with a solution of CTAB. This established a bilayer of CTAB on the sides of the nanorod, preventing the thiolated biotin from binding there and favoring thiol attachment at the nanorods' tips for streptavidin detection (Figure 4.23B).

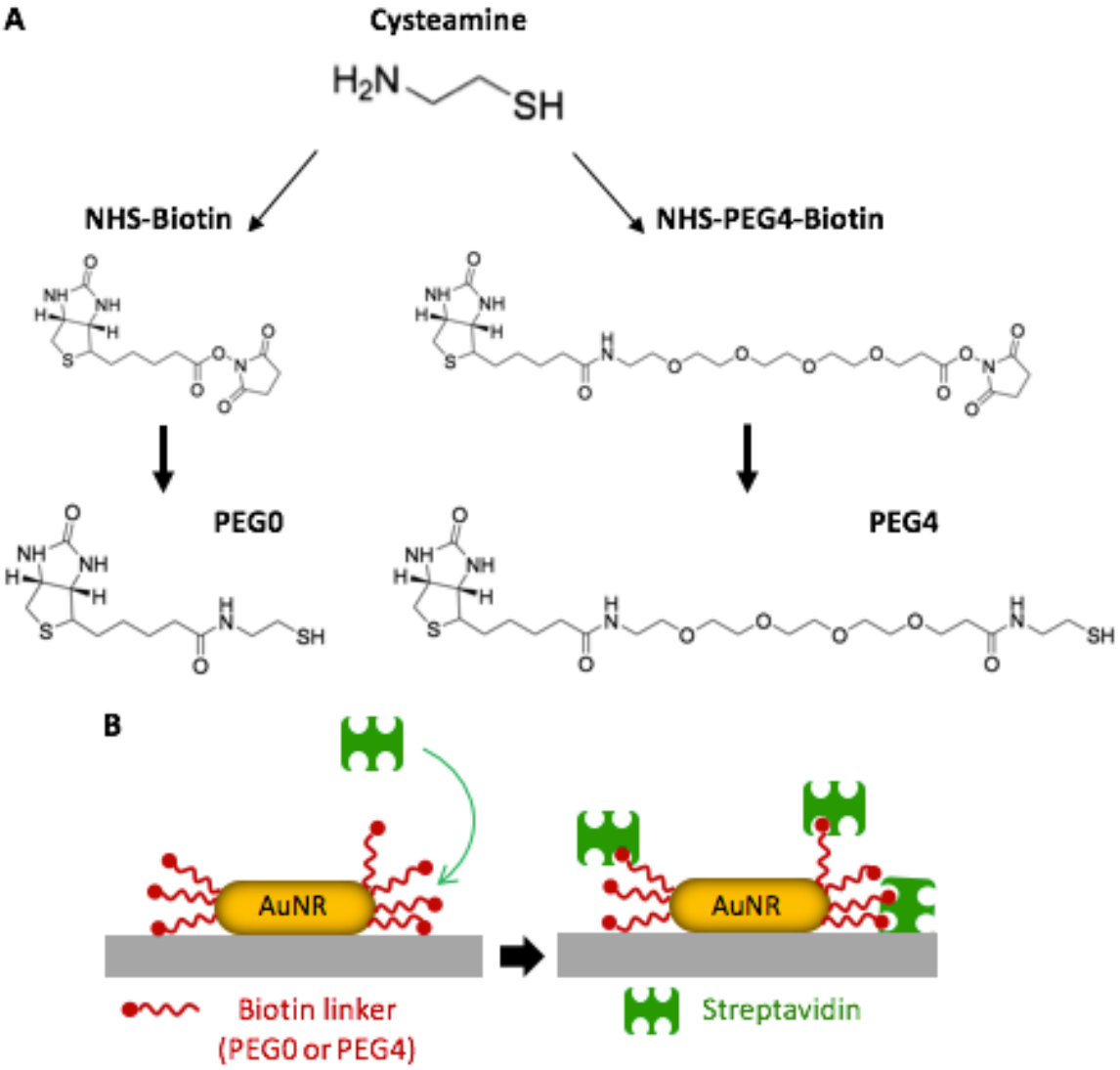

Figure 4.23 - Biotin thiol linkers prepared by coupling reactions. (A) Cysteamine and NHS-Biotin produced PEG0, and cysteamine and NHS-PEG4-Biotin produced PEG4. (B) Scheme of the chemical tip-functionalization of glass-immobilized gold nanorods using the coupling reactions' products (PEG0 or PEG4) rendering biotinylated nanorods, that act as plasmonic sensors of streptavidin binding.

For the chemical tip-functionalization of 25/600 and 25/650 nanorods the longer biotin-linker thiol PEG4 was used. In sensing assays, the nanorods' LSP peak red-shifts were monitored (Figure 4.24) for SA concentrations of 100 nM (region I) and 1000 nM (region II).

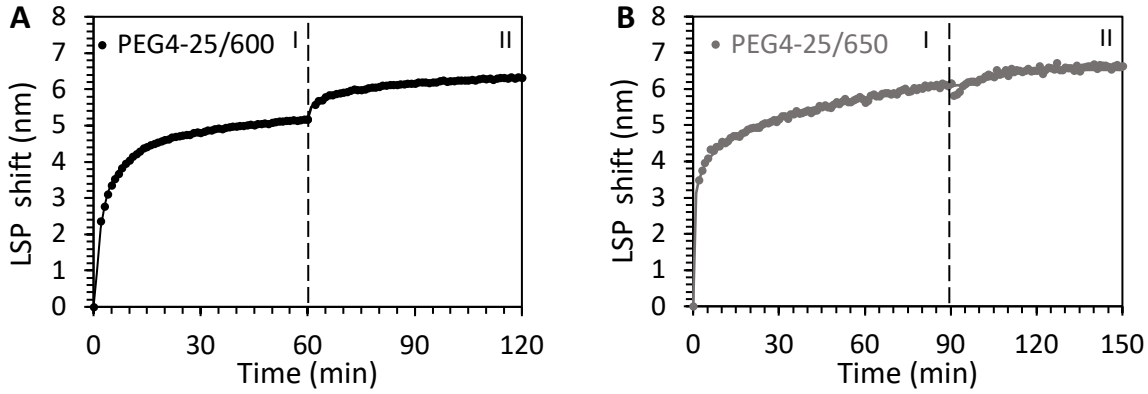

Figure 4.24 - Kinetic traces showing the change over time in the LSP peak position of (A) 25/600 and (B) 25/650 gold nanorods chemically tip-functionalized with PEG4 linker, in response to streptavidin binding (100 nM in region I and 1000 nM in region II). The filled lines correspond to the fits performed with a stretched exponential.

For both 25/600 and 25/650 nanorods the total LSP shifts were comparable, with values of about 6.3 and 6.5 nm, respectively (Table 4.7). These values are well-above the threshold obtained for the non-specific adsorption in bare nanorods, as would be expected for a response measured in biotin-functionalized nanorods due to specific adsorption. The results also illustrate the highest response to streptavidin that can be acquired with tip-specific chemical functionalization of the nanorods.

Table 4.7 - Partial and total LSP shifts (Δλ) measured for streptavidin sensing (100 and 1000 nM) using 25/600 and 25/650 nanorods chemically functionalized with PEG4 at their tips.

NRs	Δλ/nm (100 nM SA)	Δλ/nm (1000 nM SA)	Δλ/nm (Total)
25/600	5.2	1.1	6.3
25/650	6.1	0.4	6.5

The maximum response to streptavidin that could be attained with a chemical tip-specific functionalization was further tested. To this end, smaller nanorods with a width of 10 nm and with an LSP peak at 700 nm (10/700) were used (Figure 4.25A,B). Smaller particles are advantageous because the smaller surface area reduces non-specific interactions and allows more target binding. Also, when compared to previous bigger nanorods, they produce plasmon near-fields at their tips that are one order of magnitude higher (Figure 4.25C), thus being more sensitive.

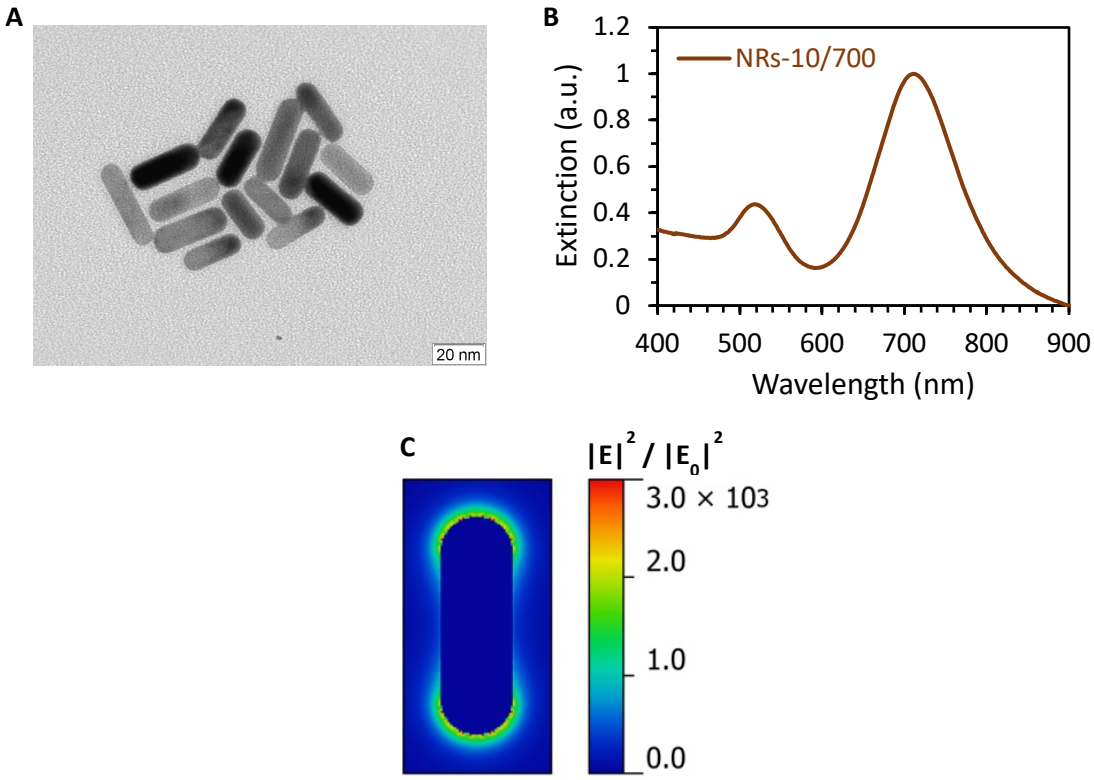

Figure 4.25 - Characteristics of the 10 nm × 30 nm gold nanorods used. (A) TEM image. (B) Extinction spectrum. (C) Plasmon near-field map calculated for a nanorod with the dimensions mentioned and excited at the LSP peak wavelength (700 nm) of the nanorods.

The nanorods were tip-functionalized with PEG0 due to the higher sensitivity of the smaller particles in a close distance to their surface. The evaluation of the sensing response to streptavidin resulted on an averaged value of 7.6 nm (Table 4.8). The particles were also tested for the detection of antibiotin antibodies and the LSP shift was about 14 nm (Table 4.8).[27]

Table 4.8 - LSP shifts (Δλ) measured for streptavidin (100 nM) and antibiotin, using 10/700 nanorods chemically functionalized with PEG0 at their tips. For SA, the right column corresponds to the average ± standard deviation of N=3.

	Δλ/nm	
100 nM SA	7.6 7.9 7.2	7.6 ± 0.4
Antibiotin 100-fold	14	-

Despite the better sensitivity and increased response of the 10/700 smaller particles to both streptavidin and antibiotin binding, the possibility of using these nanorods to achieve two-photon reactivity seemed unlikely. This was due to the mismatch between the LSP peak at 700 nm and the requirement of irradiating the photoreaction at wavelengths close to 300 nm.

4.10.4. Irradiation of TFPA-Bt and NPA-Bt photoreactants

The photoreactant TFPA-Bt was tested under UV-light exposure as a control measurement of its behavior (Figure 4.26). It was seen that the bulk reactant has a band with maximum at ca. 260 nm (useful for 2PA) and has almost no absorption above 300 nm. However, when broadband irradiation from a mercury lamp was used, absorption decreased with an additional increase in absorbance at longer wavelengths. The change in the absorption spectrum upon UV-irradiation can be attributed possibly to the loss of N_2 and the formation of a phenyl nitrene group, so the reactant was in appropriate conditions to be photoactivated.

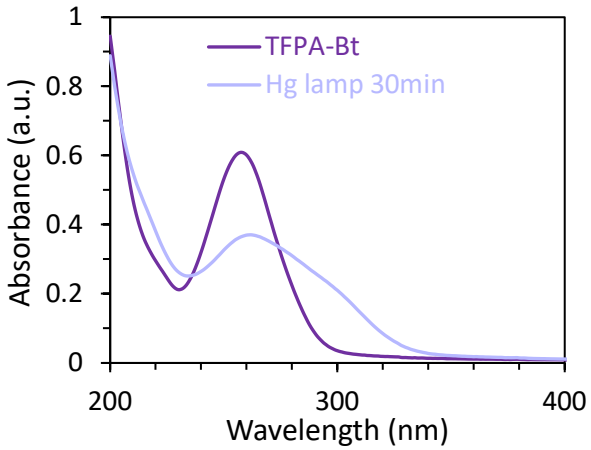

Figure 4.26 - Absorption spectra of TFPA-Bt photoreactant before (dark purple) and after exposure with a mercury lamp during 30 min (light purple).

As for NPA-Bt, UV-light exposure showed changes in the absorption band at ca. 300 nm and a clear isosbestic point forming at 440 nm (Figure 4.27A), possibly due to the loss of N_2 and the formation of a phenyl nitrene group that eventually suffers solvolysis or self-polymerization. Irradiation with LED595nm at intensity level 6 did not changed the absorption bands of the photoreactant (Figure 4.27B).

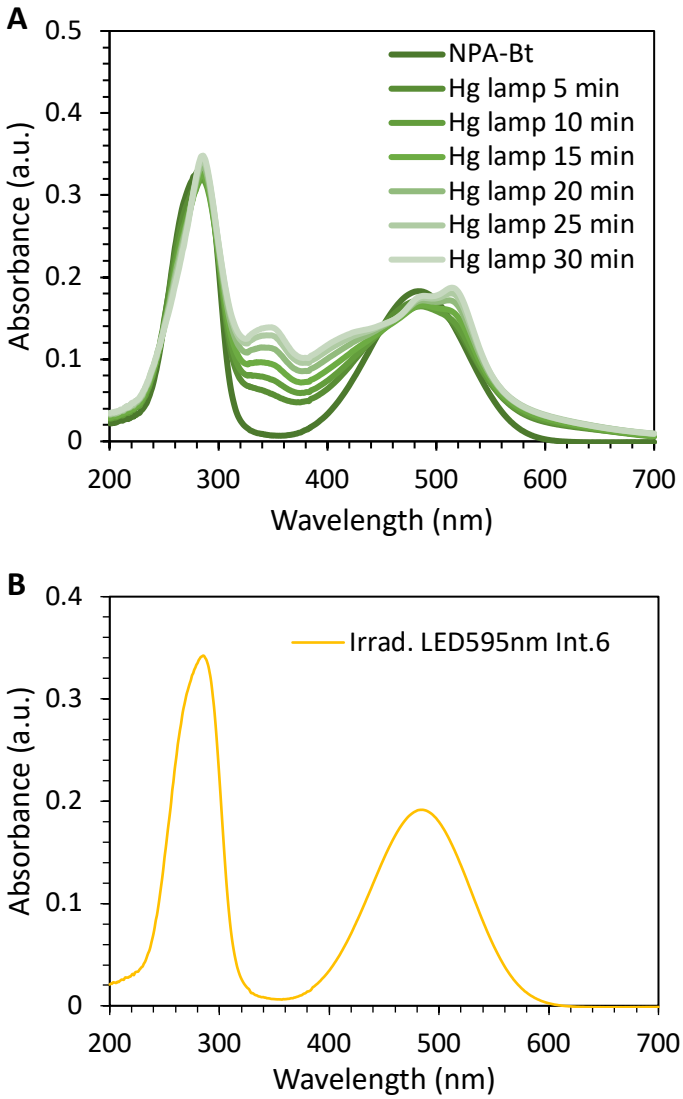

Figure 4.27 - Absorption spectra of NPA-Bt photoreactant. (A) Before (dark green) and during 30 min irradiation with a mercury lamp, considering intervals of 5 minutes. (B) Irradiation using LED595nm at intensity level 6.

4.10.5. Control assays III: Irradiation of bare gold nanorods

Control experiments were performed to evaluate the photoreaction of TFPA-BT with the surface of bare 25/600 nanorods, that were placed in contact with water, and after exposed to aqueous solutions of TFPA-Bt at 1 mM, in the dark or using LED595nm irradiating at intensity level 6 (Figure 4.28).

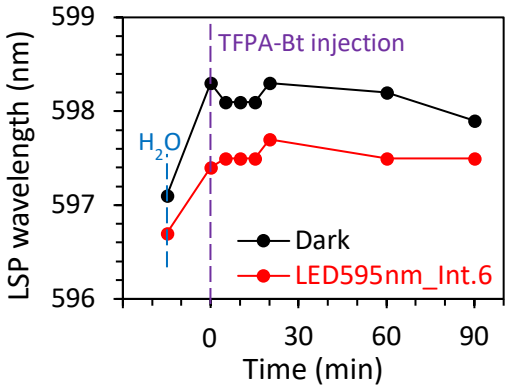

Figure 4.28 - Test to monitor the photochemical reaction of TFPA-Bt with bare nanorods. Surfaces were water injected, then replaced with a TFPA-Bt solution (1 mM). One surface was irradiated with LED595nm at intensity level 6 (red symbols) and the other was kept in the dark (black symbols), both during 90 min.

After TFPA-Bt injection, a LSP shift of ca. 1 nm was observed in both situations, due to the changes of the photoreactant solution (small fraction of ethanol) in the medium's RI. But in the absence or in the presence of light irradiation, it was clearly depicted that the LSP shifts decreased or increased marginally, keeping a constant behavior. This indicates that the perfluorophenyl azide do not bond *per se* to metal surfaces, and TFPA-Bt could not be applied directly for biotin functionalization of nanorods.

4.10.6. Experiments with photoreactant ATFB-SE

An alternative photoreactant to TFPA-Bt that was considered was N-Succinimidyl 4-Azido-2,3,5,6-tetrafluorobenzoate, ATFB-SE - chemical structure in Figure 4.29. This heterobifunctional molecule is also a perfluorophenyl azide and the NHS-ester functionality was envisioned as a potential route for linkage with molecular beacons.

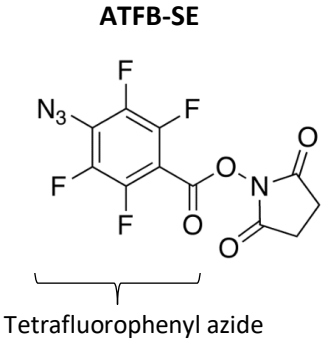

Figure 4.29 - Chemical structure of ATFB-SE photoreactant.

The possibility of polymerizing ATFB-SE directly in the nanorods' tips was tested using 25/600 bare uncoated nanorods and LED595nm at intensity level 6. The nanorods were placed in contact with water and after exposed to an aqueous solution (1 mM) of photoreactant, first in the dark and then using light irradiation, both during 90 min (Figure 4.30). It was clearly shown that in both

situations the LSP peak wavelength varied only slightly (values below 0.7 nm), and a constant tendency was kept, so the photoreactant was not further applied.

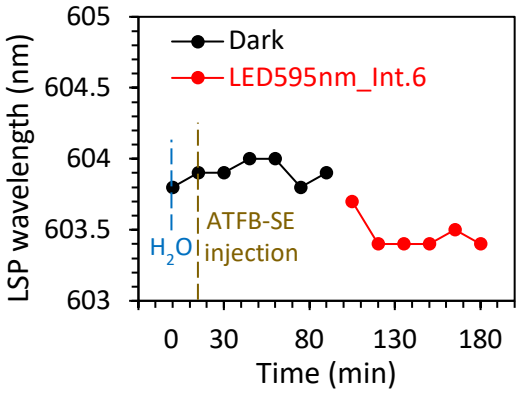

Figure 4.30 - Test of the photochemical reaction between ATFB-SE and bare gold nanorods. The surface was filled with water and then water was replaced by ATFB-SE solution (1 mM). The surface was then kept in the dark (black symbols) and later irradiated with LED595nm at intensity level 6 (red symbols).

Chapter 5

Tip-specific Functionalization of Gold Nanorods with Dye-labeled DNAs

5. Tip-specific functionalization of gold nanorods with dye-labeled DNAs

The validation of a tip-specific functionalization of gold nanorods with fluorescently-labeled oligonucleotides in order to achieve an effective fluorescence enhancement in ensemble emission was a crucial development in the scope of this doctoral thesis. The functionalization of gold nanorods was optimized by comparing two strategies: one specific to the tips, that is carried out in the presence of a surfactant protective coating, and a non-selective one that involves ligand-exchange reactions and results in indiscriminate cover of the particle. The content of this chapter were published in: *Botequim, D.*; Silva, I. I. R.; Serra, S. G.; Melo, E. P.; Prazeres, D. M. F.; Costa, S. M. B.; Paulo, P. M. R. Fluorescent Dye Nano-Assemblies by Thiol Attachment Directed to the Tips of Gold Nanorods for Effective Emission Enhancement. *Nanoscale* **2020**, *12* (11), 6334–6345. https://doi.org/10.1039/D0NR00267D.

5.1. Introduction

The assembly of nano-objects composed of fluorescent dyes, or other emitters, and metal nanoparticles is a promising approach for the development of multifunctional probes. In most of the early reports, the overall emission of these nano-assemblies is less than, or at most comparable to, that of the same amount of fluorescent dye loaded onto the nanoparticle.[1,2] Therefore, the plasmonic antenna effect of gold nanorods is not being explored for enhancing the bioimaging functionality in these systems. In fact, there are only a limited number of reports in which an effective fluorescence enhancement is clearly demonstrated.[3–5] Furthermore, in these nano-assemblies, the dye molecules are indiscriminately attached over the whole surface of the gold nanorods, instead of being concentrated at the tips, where plasmon hot-spots for emission enhancement are located.[6]

The colloidal stabilization of gold nanorods by a cetyltrimethylammonium bromide (CTAB) surfactant bilayer offers a straightforward approach for tip-specific functionalization using thiol-derivatized molecules. The role of CTAB detergent as a side-protective reagent that directs thiol attachment toward the nanorods' tips has long been reported in the literature and explored for controlled end-to-end nanorod assembly.[7–9] Later, it was also explored for selectively attaching dye molecules mediated by biotin-streptavidin binding onto the tips of gold nanorods, which yielded enhancements of about 40-fold from single-molecule fluorescence emission.[10] The ability of gold nanorods to perform as optical antennas that afford large fluorescence enhancements has been demonstrated for a diversity of emitters using single-molecule fluorescence detection,[11–13] with overall enhancement factors that surpassed a 1000-fold emission increase of weakly fluorescent molecules for resonant plasmonic enhancement of fluorescence.[11] On the other hand, the large enhancement factors observed for dye-particle systems that are prepared, or selected, in single-molecule experiments may be difficult to achieve in ensemble conditions. The enhancement

factors are more modest for dye-nanorod assemblies, typically in the range of 10-fold emission increase, due to sample averaging over many dye molecules positioned randomly, instead of being concentrated at the plasmon hot-spots.[14–17] In this view, the optimization of dye-particle attachment in such nano-assemblies is critical to maximize the enhancement effect of the gold nanorod antenna.

The modification of gold nanoparticles with thiolated oligonucleotides has enabled the use of DNA-directed assembly to achieve precise positioning of particles or molecular components in the development of nano-composite materials. In this work, the interest was in exploring DNA linkers as a spacer between the metal surface of a gold nanorod and a fluorescent dye, in order to develop dye-particle nano-assemblies with enhanced emission properties. Two functionalization strategies were compared to prepare dye-particle nano-assemblies using thiol attachment of dye-labeled double-stranded DNA (dsDNA) oligonucleotides onto gold nanorods. The nano-assemblies were prepared either by a tip-specific approach using a CTAB side-protective bilayer, or by a non-selective approach, that consists of a two-step ligand exchange process. The emission properties of these dye-particle nano-assemblies were investigated by ensemble spectroscopy and single-particle fluorescence microscopy.

5.2. Tip- and non-selective functionalization of nanorods with dye-labeled DNAs

The double-stranded DNA linker used is assembled by combining two complementary 10-nt sequences that are terminated with thiol groups. The opposite side of one of the oligonucleotides is labeled with one Atto-647N dye molecule (Figure 5.1). The length of this sequence, which is ca. 3.4 nm, was chosen to approximately match the optimal distance for emission enhancement at the nanorod's tips, as estimated from model simulations using discrete dipole approximation (DDA) method (Figure 5.10 of section 5.12 - Annexes). The initial aim was to maximize the thiol attachment at the nanorod tips which would concentrate dye molecules in the hot-spot regions. As previously mentioned, the colloidal stabilization of gold nanorods by a CTAB bilayer has been widely employed for achieving tip-selective functionalization of these particles with thiolated molecules.[7–10,18,19] However, in the case of DNA oligonucleotides, which are strongly negatively charged, their attachment onto CTAB-stabilized gold particles may be facilitated by the addition of salt and/or co-surfactants, such as sodium dodecyl sulfate (SDS), Tween or polyvinylpyrrolidone (PVP). In some examples, this process is carried out in two steps so that CTAB is first completely replaced by another surface agent before binding of the thiolated oligonucleotides.[20,21] Even though this approach allows for a better control over particle stability, it usually implies the loss of the CTAB side-protective role that directs the tip attachment of thiols and, thus, it results in the functionalization of the particle surface in a non-selective fashion.

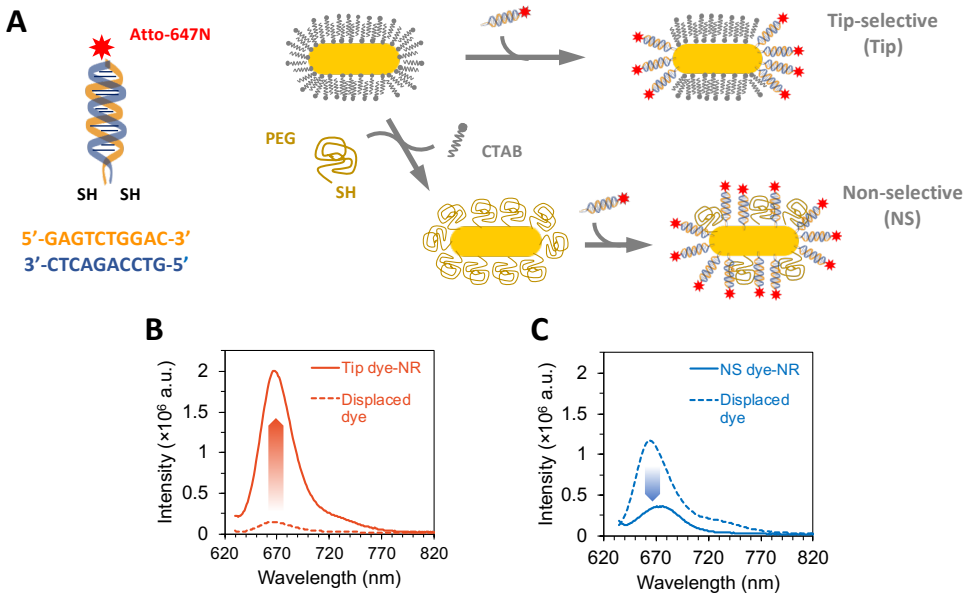

Figure 5.1 - Functionalization of gold nanorods with dye-labeled DNAs. (A) Scheme of a dye-labeled dsDNA oligonucleotide and preparation of dye-particle nano-assemblies using two functionalization methods: (top) tip-selective or "Tip" is based on the CTAB protective role of the nanorods' side walls; (bottom) non-selective or "NS" is a two-step coating process in which CTAB is first replaced with thiolated PEG and then by fluorescently-labeled DNA oligonucleotides. (B) Emission spectra of tip-functionalized nano-assemblies (solid line) and of the dye-labeled oligonucleotides from the same sample displaced into solution by ligand exchange with 2-mercaptoethanol (dashed line). (C) Emission spectra of NS-functionalized nano-assemblies (solid line) and of its displaced dye-labeled oligonucleotides (dashed line). Excitation wavelength was 620 nm in both parts (B) and (C).

It was chosen to compare two approaches for the functionalization of gold nanorods with thiolated oligonucleotides: a non-selective coating via a two-step ligand exchange, hereafter termed "NS" functionalization, and a tip-selective approach using the CTAB as a directing reagent through its side protective role, hereafter termed "tip" functionalization (Figure 5.1A). The latter approach was validated by performing hybridization between gold nanorods tip-functionalized with a thiolated single-stranded DNA (ssDNA) sequence and gold nanospheres coated with a complementary sequence, as shown in the transmission electron microscopy (TEM) images of Figure 5.2.

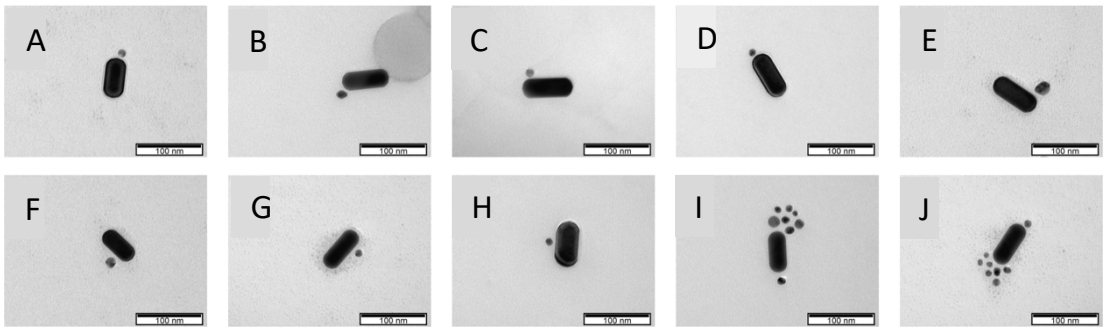

Figure 5.2 - Validation of tip-selective functionalization by promoting hybridization between tip-functionalized gold nanorods with a thiolated ssDNA of 24 nts and gold nanospheres coated with the complementary sequence: 5'-CAG CCC CAT AGA TTG CTC CGA AAA-3'-SH. Examples of TEM

images showing: (A-E) tip assembly, and (F-H) side assembly. From a total of 39 nanorods evaluated with 68 nanospheres assembled, the ratio of 40:28 was obtained for a tip:side classification, showing that the majority of assembled nanospheres are at the nanorods' tips. A non-negligible fraction of side-assembled particles has also been reported in previous studies from the literature.[22–24] In this work, it is plausible that some additional side assembly could have been promoted by electrostatic adsorption between positively charged sides of nanorods and negatively charged nanospheres. Besides tip-selective assembly, it was also noticed self-aggregation of nanospheres (images I and J) even after washing by two cycles of centrifugation and resuspension in aqueous CTAB solution.

The comparison between the two approaches provided a demonstration of the critical role of surface chemistry in the outcome properties of these systems - both resulted in strongly emitting dye-particle nano-assemblies, but only tip-functionalization showed evidence of an effective antenna effect, in which the emission from the assembly is larger than its isolated components.

5.3. Fluorescence enhancement in tip-functionalized nano-assemblies

The fluorescence enhancement effect was experimentally assessed by comparing the emission spectrum from a sample of dye-particle nano-assemblies with that from the same sample after displacing the dye molecules into solution by ligand exchange with 2-mercaptoethanol.[25] For tip-functionalized samples, this method consistently afforded larger emission intensities for dye-particle nano-assemblies than for displaced dye molecules, thus, showing an effective emission enhancement (Figure 5.1B). On the other hand, the dye-particle nano-assemblies obtained by NS-functionalization often show more emission from its displaced dye into solution, which means that overall, the dye's emission is suppressed in these nano-assemblies (Figure 5.1C).

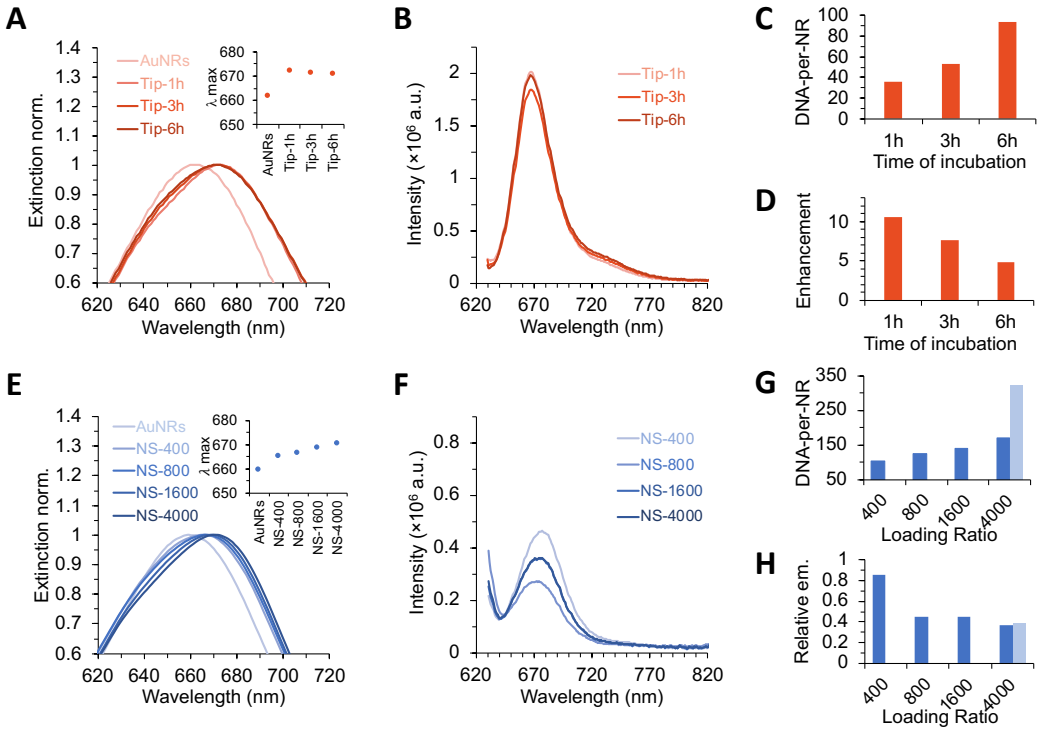

Figure 5.3 - Evaluation of fluorescence enhancement in dye-particle nano-assemblies. (A,B) Extinction and emission spectra of tip-selective functionalized gold nanorod samples for several incubation times - the inset

in part (A) shows the extinction peak wavelength (λ_{max}). (C) Number of dye-labeled DNA chains per nanorod ("DNA-per-NR"). (D) Experimental fluorescence enhancement factor of tip-functionalized gold nanorods determined for excitation at 620 nm. (E,F) Extinction and emission spectra of non-selective functionalized gold nanorod samples for various DNA loading ratios - the inset in part (E) shows the extinction peak wavelength (λ_{max}). (G) Number of dye-labeled DNA chains per nanorod ("DNA-per-NR"). (H) Experimental relative emission showing quenching in non-selective functionalized gold nanorods determined for excitation at 620 nm. The light blue bars in parts (G) and (H) refer to a non-selective functionalization sample prepared with an overnight incubation time.

This subject was further investigated by evaluating how the amount of dye loaded per particle affects the fluorescence enhancement in tip-functionalized nano-assemblies (Figure 5.3). The emission intensity of displaced dye increases proportionally to the incubation time during their functionalization, which indicates that larger amounts of dye are being loaded onto the nanorods (Figure 5.11 in the Annexes). The dye-per-particle ratio corresponds on average to approximately 36, 53 and 93 dye molecules for incubation times of 1, 3 and 6 hours, respectively (Figure 5.3C). These values are well below the theoretical maximum of 412 oligos estimated from the empirical footprint of a short ssDNA chain, as proposed in Ref. 26, and are also below those determined experimentally by other authors for fully coated gold nanorods of similar size.[24,27] Thus, it is reasonable to assume that the surface of gold nanorods is not saturated even for an incubation time of 6 hours. However, as more dye is added by extending the incubation time, it is also likely that insertion at the nanorod side becomes more relevant. As discussed further ahead (section 5.5), the loading of dye molecules on the particle side should have a negative contribution to the average emission enhancement, as these surface regions provide little or no enhancement effect. Indeed, the largest enhancement factor was evaluated for an incubation of 1 hour and the trend shows a decrease of enhancement factors as incubation time increases (Figure 5.3D). The apparent effect of emission saturation is tentatively explained if the tip surface becomes saturated already at the lowest dye-per-particle ratio and the dye molecules that are further loaded by increasing dye-per-particle ratio become inserted in the side regions, thus giving a negligible contribution to the overall dye-particle emission.

The extinction spectrum of tip-functionalized nano-assemblies compared to that of the original CTAB-stabilized gold nanorods shows that the plasmon peak wavelength is red-shifted by about 10 nanometers (inset of Figure 5.3A) and, also the spectral lineshape broadens. These effects may result from a combination of factors. First, the replacement of CTAB surfactant molecules by DNA oligonucleotide chains is likely to contribute with a change of local refraction index in the tip regions, which could account for the peak shift of the surface plasmon resonance, while particle-to-particle variability in the number of attached DNA chains may contribute as a source of inhomogeneous line broadening. Second, the dye-particle extinction also includes a contribution from plasmon-enhanced absorption of light by its coupled dye molecules. It is not straightforward to separate the above-mentioned two effects on the overall extinction spectrum, in order to experimentally assess only the enhancement factor on the dye's absorption.

The samples prepared by NS-functionalization can also be tuned in terms of the amount of dye-labeled DNA attached per particle (Figure 5.3E,F). By keeping the incubation time fixed at 1 hour, it was possible to gradually increase the number of DNA chains attached per particle from about 102 up to 170 by successively increasing the loading ratio from 400 to 4000 during incubation (Figure 5.3G). In the latter case, it was further possible to almost double the number of the attached chains up to 327 by extending the incubation time from 1 hour to overnight (light blue-coloured bar). However, the emission intensity from NS-functionalized samples is at most comparable to that of the displaced dye into solution, and more frequently than not, it is actually less intense (Figure 5.3F and Figure 5.11B in the Annexes). So, the average emission from dye molecules in the nano-assemblies prepared by NS-functionalization is suppressed (Figure 5.3H). The absence of an effective emission enhancement, or antenna effect, in these ensemble measurements does not mean that the dye-particle nano-assemblies are not strongly emissive as individual objects, a fact that was confirmed by fluorescence microscopy (section 5.7).

The non-selective functionalization seems to produce nano-assemblies in which there is a compensation between the antenna effect known for dye molecules positioned at the rod tips and quenching processes that may result from the predominance of non-radiative decay enhancement at the particle sides or from self-quenching interactions due to close packing of dye molecules on the particle surface.

5.4. Excitation wavelength dependence of the enhancement effect

It was also investigated the dependence of emission enhancement on the excitation wavelength. It could be anticipated that emission enhancement increases as the excitation wavelength is brought closer to the longitudinal surface plasmon resonance, because the induced plasmon near-field becomes stronger, thus, producing larger accelerations in the dye's excitation rate. This feature was explored by selecting excitation wavelengths on the high energy side of the longitudinal surface plasmon band until the dye's Stokes shift allowed the measurement of the maximum emission peak, as illustrated here for tip-functionalized nano-assemblies with an incubation time of 1 hour (Figure 5.4). It was possible to confirm that the emission enhancement increases from a factor of about 7 up to 17-fold when the excitation wavelength varies from 600 to 650 nm, as it approaches the longitudinal surface plasmon peak of these gold nanorods. In the samples prepared with incubation times of 3 and 6 hours, we have observed the same trend (Figure 5.17 and Table 5.3 of the Annexes), although the enhancement factors are smaller in magnitude, as previously discussed. The dependence of the enhancement factor on the excitation wavelength, as shown here, qualitatively supports the role of plasmon-enhanced fluorescence in the emission from these dye-particle nano-assemblies.

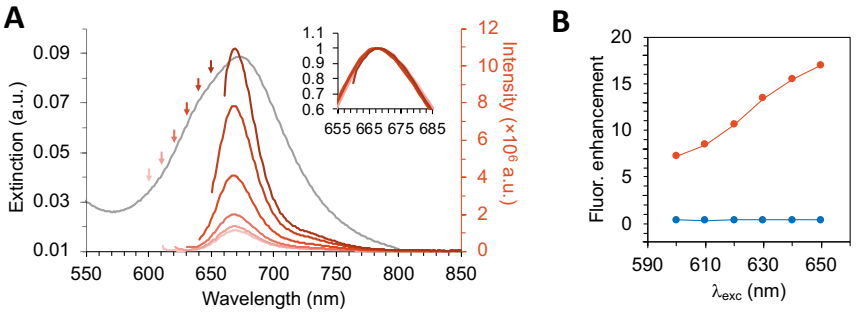

Figure 5.4 - Evaluation of fluorescence enhancement of tip-functionalized gold nanorods and its dependence on the excitation wavelength. (A) Extinction spectrum of dye-particle nano-assemblies for the "Tip-1h" sample (grey curve) and emission spectra of the same sample for several excitation wavelengths (red curves) indicated by the arrows over the extinction spectrum - the inset is an overlay of the normalized emission spectra showing that the lineshape practically does not change. (B) Experimental fluorescence enhancement factor of dye-particle nano-assemblies for the "Tip-1h" sample (red symbols) and comparison with non-selectively functionalized gold nanorods for the "NS-4000" sample (blue symbols).

Intriguingly, no significant changes were observed in the lineshape of the enhanced emission spectra, as inferred from a comparison between the normalized emission from dye-particle nano-assemblies and that of the displaced dye molecules (inset of Figure 5.4A and Figure 5.12 of the Annexes). The apparent absence of spectral reshaping in the plasmon-coupled emission of our dye-particle assemblies may result from a good spectral overlap between the dye's emission and the longitudinal surface plasmon band, as suggested from the simulated spectra shown in Figure 5.12B and C of the Annexes.

The spectral dependence of NS-functionalized samples shows a distinct behaviour relatively to tip-functionalized samples that was tentatively attributed to molecular aggregation. In particular, the emission peak maximum displays a significant blue-shift as excitation is selected at longer wavelengths (Figure 5.13 of the Annexes). Also, the lineshape of these spectra differs from that of the displaced dye in solution by presenting a lower relative intensity of the second vibronic. These characteristics are amenable for an excitonic interaction of H-type, as known for molecular dye aggregates in which π-stacking of conjugated macrocyclic dyes results in a colinear alignment of their transition dipoles.[28] The lowest excitonic state of H-aggregates is usually a dark state because of cancellation between the individual transition dipoles of the coupled molecules, which could explain the absence of emission enhancement in the NS-functionalized samples. However, this excitonic interaction would have to be in the weak coupling regime due to the absence of major spectral changes. Alternative explanations for the spectral wavelength dependence could invoke a solvatochromic type of shift in the local environment at the nanorod surface and the spectral selection of a sub-population of dye molecules upon changing the excitation wavelength.

The contrast between the emission properties of nano-assemblies prepared by tip- and NS-functionalization illustrates the importance of site-selective approaches for particle conjugation with functional molecular components. Site-selective approaches enable the concentration of the desired functionality at the plasmon hot-spots, thus, maximizing the intended effects in the

nano-composite systems, either for enhancing fluorescence emission by antenna effects, or for molecular sensing based on the refraction index sensitivity of the plasmon resonance.

5.5. Model simulations of a single dye on a gold nanorod

A comparison of the antenna effect on the dye's emission between the tip and side positions at the nanorod surface was examined by model simulations. The spatial heterogeneity of plasmon-molecule interactions has motivated to perform detailed model simulations of the antenna effect for different dye positions on the particle surface (Figure 5.5). The aim was to clearly show the differences of emission enhancement between the tip and side regions of the nanorod geometry. For this purpose, the excitation rate enhancement (γ_{exc}) and the radiative (K_r) and non-radiative (K_{nr}) decay rates of an emitter were estimated for selected positions on the particle surface at the tip and side regions. Along with the intrinsic radiative (k_0) and non-radiative (k_{nr}) decay rates of Atto-647N in water, it was possible to estimate a fluorescence enhancement factor (F/F^0) for each emitter position, as indicated in Figure 5.5A.

Simulations were performed within a wavelength interval covering the absorption and emission spectra of Atto-647N dye, in order to retrieve spectrally averaged enhancement factors that could afford a fair comparison with the experimental ones. The plots of Figure 5.5B-D provide detailed insight into the spectral dependence of the enhancement effect on each photophysical rate, which has been previously discussed.[29] Furthermore, it also illustrates the enhancement dependence on the dye's orientation relative to the nanorod particle. Figure 5.5E shows the complete set of emitter positions probed on the particle surface superimposed on the near-field enhancement map calculated for excitation at 620 nm. This wavelength was chosen to coincide with the data shown in Figure 5.3B and D. The enhancement factors displayed in Figure 5.5F show that these do not vary significantly in the tip region (positions 1-4) and correspond to an emission increase of about 10-fold (or slightly smaller, if orientation averaging of the emitter's dipole is considered). The emission enhancement decreases away from the tip region (position 4) when proceeding towards the rod side (position 7). Accordingly, in the middle position the dye's emission should be suppressed for an orthogonal orientation of the emitter's dipole.

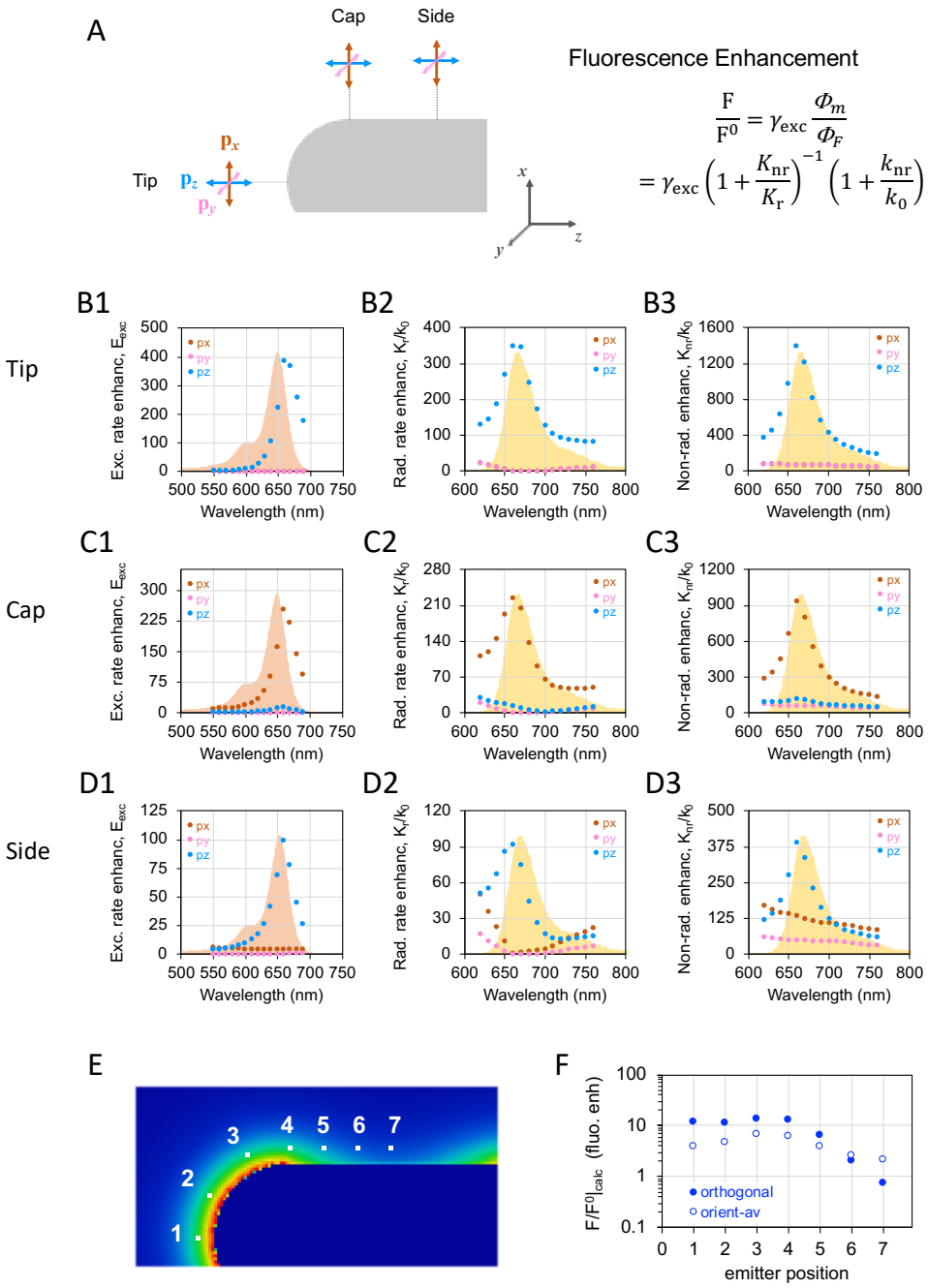

Figure 5.5 - Theoretical estimation of fluorescence enhancement using DDA simulations. (A) Scheme of the dye-particle model showing the dye emitter in three selected positions of tip, cap and side - the enhancement factor is calculated from $F/F^0 = \gamma_{exc} \times \Phi_m / \Phi_F$ using the excitation rate enhancement and the relative fluorescence quantum yield (see 5.10.6 of the Experimental Section for other details). (B-D) Enhancement factors for the excitation, radiative and non-radiative decay rates (γ_{exc}, K_r and K_{nr}, respectively) of an emitter in the tip, cap and side regions - for comparison, the normalized absorption or emission spectrum of Atto-647N dye is shown in the background (orange and yellow shaded areas, respectively), also, the decay rates were normalized by the dye's intrinsic radiative decay rate (k_0 = 1.4 × 10^8 s^{-1}). (E) Set of emitter positions considered on the particle surface displayed on the near-field enhancement map of the simulated gold nanorod for excitation at 620 nm. (F) Fluorescence enhancement factors calculated from DDA simulations for different emitter positions considering either an orthogonal orientation of the emitter's dipole (closed symbols) or an average orientation (open symbols).

The simulation results confirm that the dispersion of dye molecules over the side regions of a gold nanorod antenna should, on the overall, contribute to a lower emission enhancement effect. The difference between the tip and side regions increases steeply as the excitation wavelength comes closer to the surface plasmon resonance peak (Figure 5.14 in the Annexes), showing that the distribution of dye attachment affects more critically the overall enhancement in that condition. A direct quantitative comparison between simulations and experimental results may be impaired by sample's heterogeneity in the distribution of particle size and shape and also by variations from particle-to-particle in the number of dye molecules attached. Nevertheless, the simulations show that distributing dye molecules non-selectively over the surface will decrease the overall antenna effect as opposed to concentrating the same (or a smaller) amount of dye at the plasmon hot-spots in the tip regions.

5.6. Single-particle emission in colloidal suspension

The emission properties of the dye-particle nano-assemblies were further investigated at single-particle detection level by confocal fluorescence microscopy. The emission intensity time traces from dilute colloidal suspensions of these nano-assemblies with sub-nanomolar concentrations show intense fluorescence burst events with maximum photon detection rates in the order of hundreds of counts per ms for an excitation power of only 4.4×10^{-3} kW/cm^2 (Figure 5.6). Further information from these intensity traces was obtained from their autocorrelation function (ACF), as shown in Figure 5.6E and F. The ACF curves show two relaxation components that were attributed to the rotational and translational diffusion motions of the dye-particle nano-assemblies in colloidal suspension.[30] The relaxation times fitted for the short and long relaxation times ($\tau_\perp$ an τ_w) correspond to the values theoretically estimated using a modified version of Einstein-Smoluchowski relation for a rod-like particle geometry (Table 5.2 of the Annexes).[31]

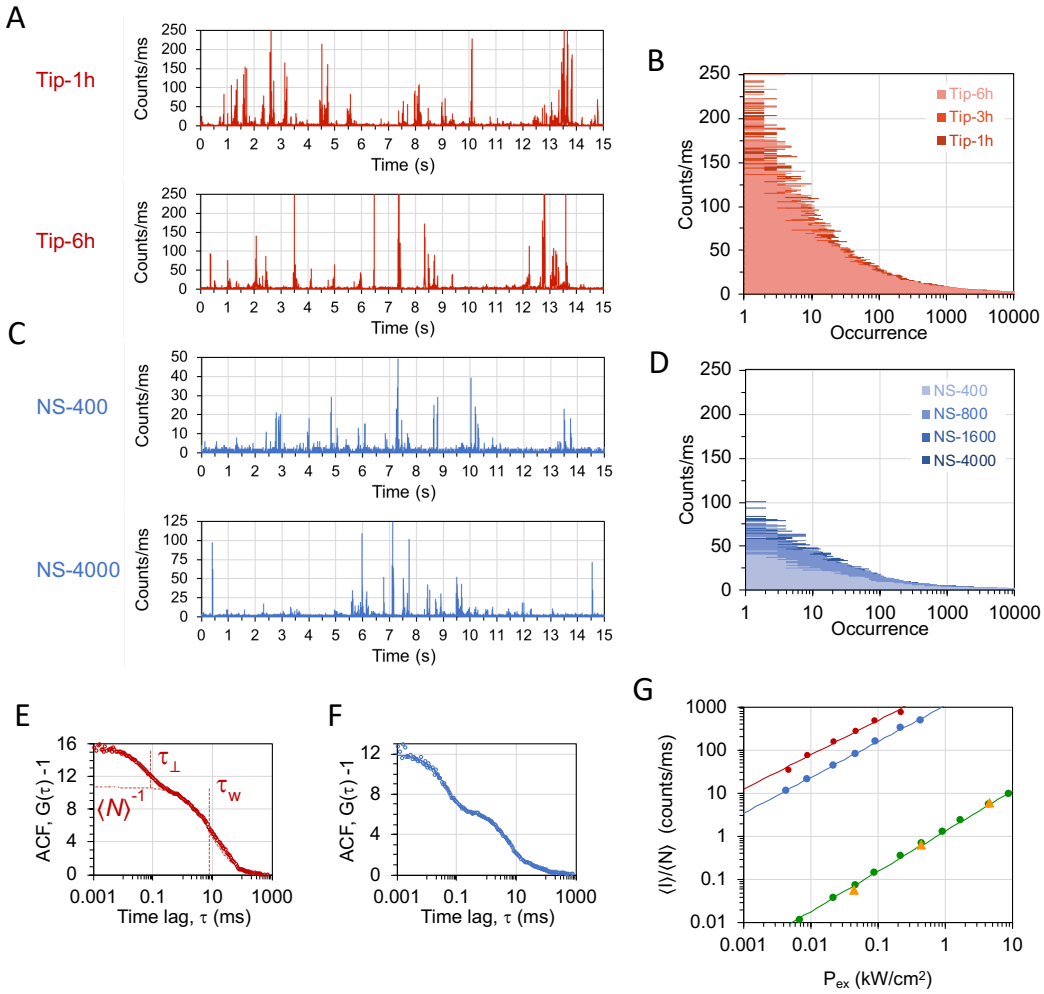

Figure 5.6 - Fluorescence emission of dye-particle nano-assemblies characterized by confocal fluorescence microscopy. (A) Intensity time traces and (B) photon counting histograms of sub-nanomolar suspensions of tip-functionalized gold nanorod samples obtained for excitation at 639 nm with a power of 4.4×10^{-3} kW/cm^2 - traces are shown for a binning interval of 1 ms. (C,D) Similar plots for NS-functionalized gold nanorod samples. (E,F) Fluorescence autocorrelation function (ACF) of dye-particle nano-assemblies obtained by tip- and NS-functionalization, respectively. (G) Values of individual brightness ⟨I⟩/⟨N⟩ obtained from intensity traces, as a function of the excitation power (P_{ex}) for tip-functionalized samples (red symbols) and for non-selectively functionalized samples (blue symbols) - for comparison, the individual brightness of a single dye-labeled DNA chain (green symbols) and that from one-photon luminescence emission of single gold nanorods (orange triangles) is shown.

The analysis of ACF curves also provided an estimate of the average occupation number ⟨N⟩ of dye-labeled particles in the confocal volume, which was combined with the mean trace intensity ⟨I⟩ to determine an individual brightness ⟨I⟩/⟨N⟩, which is a sample average for single-particle emission. The comparison between values of ⟨I⟩/⟨N⟩ show that tip-functionalized nano-assemblies are stronger emitters than the NS-functionalized ones and that, in general, dye-particle nano-assemblies have an emission that is approximately three orders of magnitude more intense than that of a single dye-labeled oligonucleotide (Figure 5.6G). The photoluminescence emission from the gold nanorods alone (without dye) that can be directly excited by one-photon absorption

is also negligible (orange triangles), when compared with the emission from dye-particle nano-assemblies. The qualitative trends observed in the individual brightness of tip- and NS-functionalized nano-assemblies are consistent with the results from ensemble emission. The fluorescence decays of dye-particle nano-assemblies show ultrafast decays that are below the setup's time resolution (Figure 5.16 of the Annexes).

5.7. Single-particle fluorescence imaging

The chemical attachment of dye molecules onto colloidal nanoparticles is a stochastic process that is prone to originate a dispersion of the number of dye molecules attached per particle.[32–34] The heterogeneity in the degree of dye-labeling will affect the individual brightness of dye-particle nano-assemblies, and thus it will have crucial implications on their performance as single-object nanoprobes. In order to characterize the variation of emission properties from particle to particle and between differently functionalized samples, were performed single-particle fluorescence measurements on surface-immobilized dye-particle assemblies. In these measurements, the excitation laser beam is not polarized on the sample's plane, which means that immobilized objects have approximately the same probability of being excited independently of their orientation on the surface. Nevertheless, it was clearly perceptible that the emission intensity from the diffraction-limited spots in the sampled images showed a certain degree of particle-to-particle variability (Figure 5.7). The maximum emission intensity was obtained from point-spread function (PSF) fitting and the single-particle photoluminescence spectrum of each nano-object was obtained in order to confirm that a single gold nanorod was being measured (Figure 5.7B,C).

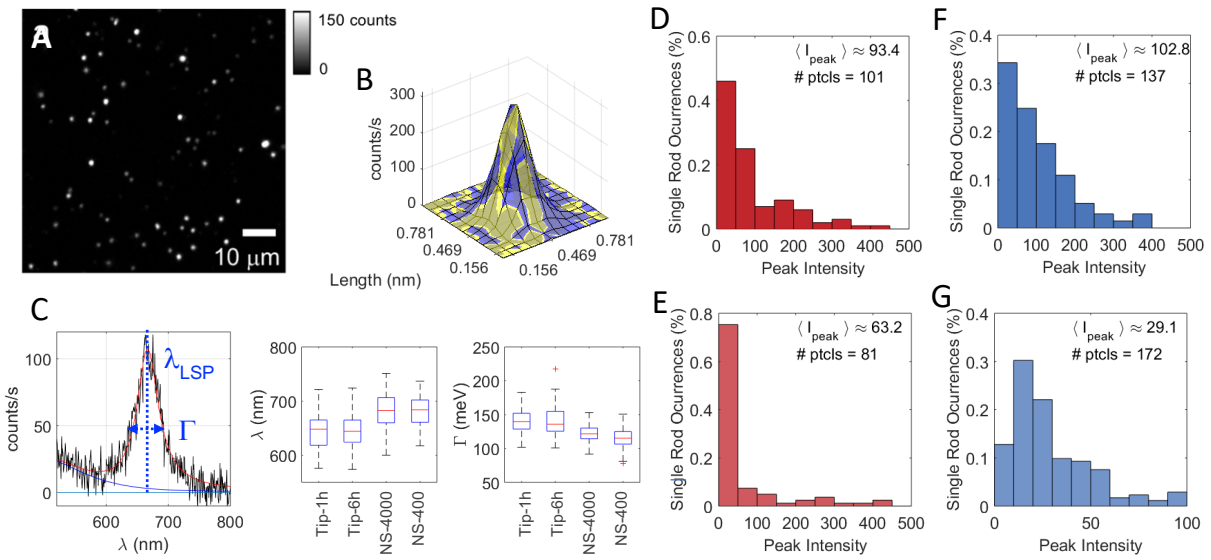

Figure 5.7 - Single-particle fluorescence measurements on surface-immobilized dye-particle assemblies. (A) Fluorescence image of a tip-functionalized sample of dye-particle nano-assemblies dispersed on a polyvinyl alcohol (PVA) polymer film - excitation at 639 nm. (B) Example of PSF fitting used to determine the emission intensity ("Peak intensity") of individual nano-assemblies (experimental - yellow surface, and fitted 2D-Gaussian - blue surface). (C) Example of the photoluminescence spectrum from a single-particle and of a Lorentzian fitting used to determine the peak wavelength (λ_{LSP}) and linewidth (Γ) - the fitted

parameters are shown as box plots in the right panels. (D,E) Histograms of emission peak intensity sampled for individual nano-assemblies of tip-functionalized samples, "Tip-1h" and "Tip-6h", respectively. (F,G) Histograms of the peak emission intensity for NS-functionalized samples, "NS-4000" (incubated overnight) and "NS-400", respectively - the insets show the sample average emission intensity, $\langle I_{peak} \rangle$, and the total number of particles sampled.

Four samples of dye-particle nano-assemblies were selected in order to compare the emission properties of tip- and NS-functionalization. Firstly, tip-functionalized particles with 1 hour incubation ("Tip-1h") are compared with non-selectively functionalized particles with a dye-per-particle loading ratio of 4000 and incubated overnight ("NS-4000"). This pair of samples affords a comparison between the dye-particle nano-assemblies of lowest and highest dye content, respectively, of 36 and 327 dye molecules per particle for "Tip-1h" and "NS4000" samples (Figure 5.3C and G). In the second comparison, the tip-functionalized particles for 6 hours ("Tip-6h") are compared with the non-selective functionalized particles incubated with a dye-per-particle ratio of 400 ("NS-400"). This pair of samples affords a comparison between the dye-particle nano-assemblies with approximately the same dye content of 93 and 102 dye molecules per particle, respectively for "Tip-6h" and "NS-400", but prepared with a different functionalization protocol.

The emission intensities of individual particles in samples "Tip-1h" and "NS-4000" are distributed in a similar way, despite their striking difference in the average number of dye molecules per particle (Figure 5.7D,F). Remarkably, the "Tip-1h" sample with an average of only 36 dye molecules per particle is composed of objects with an emission intensity comparable to those in "NS-4000" that have an average dye content ca. 10 times larger. It is plausible to assume that the emission properties of tip-functionalized samples are dominated by dye molecules attached to the tip hot-spots, which will produce the largest possible antenna effects. The non-selective functionalization with high loading ratios of dye molecules, such as sample "NS-4000", will also have a significant number of dye molecules attached at the tips. This comparison is only effective for non-selective functionalization at high dye contents, because otherwise the dispersion of dye molecules over the surface regions of weak enhancement will negatively affect the individual brightness of dye-particle assemblies. For instance, the "NS-400" sample is mostly composed of objects with less than 100 counts of peak intensity. This sample can be compared with "Tip-6h", which has a similar average number of dye molecules per particle, but displays a distribution of stronger emission intensities (Figure 5.7E and G). The differences between tip- and non-selective functionalization may also be appreciated in the spectral properties of individual nano-objects. For instance, the plasmon peak wavelength of surface-immobilized samples is strongly red-shifted in non-selectively functionalized dye-particles relatively to tip-functionalized dye-particles. This result is consistent with the formation of a thicker organic coating layer around dye-particles prepared by non-selective functionalization, because of the combination of attached PEG and DNA chains onto the gold nanorod surface.

5.8. Cell internalization assays

The conjugation of gold nanoparticles with DNA oligonucleotides opens up the possibility of developing multi-functional nano-composite systems that combine the strong optical response of plasmonic nanoparticles with the molecular recognition capability of DNA biotechnology, such as molecular beacons or aptamers. These nano-assemblies are particularly promising for *in situ* probing of biological processes in live cells, or *in vivo* conditions, using fluorescence imaging. In order to confirm the potential of the dye-particle nano-assemblies developed here for future applications in live cell studies, these were investigated in cell internalization studies by confocal fluorescence microscopy with sub-diffraction spatial resolution. The "NS-4000" sample was chosen because it is already biocompatible after preparation by ligand exchange of CTAB with a PEG coating. For internalization assays, mouse neuroblastoma N2a were used, which have been genetically modified to express a fusion construct of prion protein with yellow fluorescent protein anchored to the plasma membrane for fluorescence labeling of the cell contour.[35] Live N2a cells were incubated in the presence of a sub-nanomolar concentration of fluorescent particles from the "NS-4000" sample that corresponded to a density of 24 particles per μm^2. After one day of incubation time, it was already possible to verify the uptake of these fluorescent particles by the N2a cells (Figure 5.8). This figure shows that red-emitting fluorescent dye-particles have been internalized by the cells and, from the orthogonal projection, it is clear that these particles are present inside the cells.

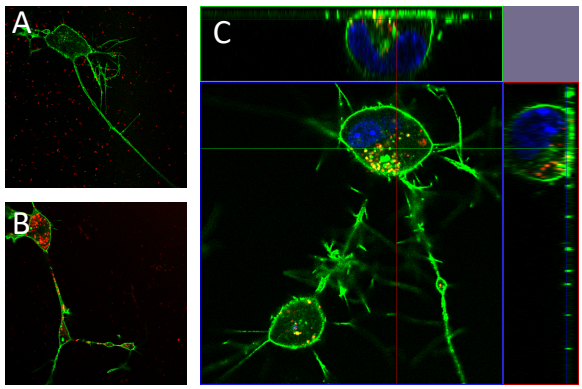

Figure 5.8 - Cell internalization of fluorescent dye-particle nano-assemblies by live neuroblastoma N2a cells expressing stably a fusion of the prion protein-yellow fluorescent protein (YFP)-glycosylphosphatidylinositol (GPI)-anchored to label the plasma membrane. (A) Confocal microscopy image of N2a cells immediately after the addition ($t = 0$) of dye-particles showing their location outside the cell. (B) After an incubation time of 24 hours showing that dye-particles have been internalized, and (C) high-resolution fluorescence image after 48 hours of incubation time showing by orthogonal projection that dye-particle assemblies are inside the cell volume.

5.9. Remarks and follow-up

The conjugation of dye-labeled DNA oligonucleotides with gold nanorods is fundamental for the development of multifunctional fluorescent nanoprobes. Here, it was shown that the functionalization route for conjugation of dye-labeled DNA oligonucleotides onto gold nanoparticles is crucial for achieving an effective plasmon-enhanced emission from these nano-assemblies. By using a procedure for thiol attachment directed to the nanorods' tips where plasmon hot-spots are located, it was possible to measure an ensemble effect of emission enhancement of about one order of magnitude in tip-functionalized nano-assemblies. On the other hand, the comparison with a non-selective coating procedure showed that attaching dye molecules indiscriminately over the surface is detrimental for observing emission enhancement. In fact, the results show that, in order to obtain dye-particle nano-assemblies displaying a comparable fluorescence emission, the non-selective approach requires a much larger number (approximately 10 times more) of dye molecules loaded per particle than the tip-functionalization approach. Simulations of discrete dipole approximation gave further insight into the surface distribution of plasmon-enhanced emission by confirming that tip regions afford an effective enhancement, while side regions exhibit a negligible effect or even emission quenching.

The use of tip-selective approaches for the assembly of fluorescent probes based on gold nanorods is not commonly explored in most literature reports, which means that those systems may suffer from poor enhancement of dye molecules positioned at the nanorods' side. The comparison between enhancement factors previously reported could serve as a benchmark for evaluating the advantages of tip- over non-selective functionalization. Such a comparison is provided in Table 5.1. However, instead of a direct comparison between enhancement factors, which may depend critically on the selected dye's intrinsic quantum yield, it is more relevant to use a figure-of-merit proposed in the literature.[36] This is mostly pertinent for the dye-particle assemblies developed in this work, because Atto-647N dye has already a high quantum-yield of ca. 65% in aqueous medium. The figure-of-merit evaluated for the several examples presented in Table 5.1 shows that tip-selective functionalization, as proposed here, stands out in terms of the achieved enhancement effect.

Table 5.1 - Comparison of literature reports on dye-particle assemblies based on gold nanorods that display fluorescence enhancement. The examples selected illustrate the diversity of surface chemistries used for dye assembly onto gold nanorods, although most approaches are not tip-selective. The enhancement factors presented on this table are the top values reported on each study.

Reference	λ_{LSP} length × width	Dye assembly onto gold NRs	Tip	Purpose or application	Enhanc. factor	FOM [a]
[14]	804 nm (46 × 11)	Human Serum Albumin with covalently linked IR800 dye	No	Fundamental study	9	0.9
[15]	647 nm (89 × 42)	Silica shell with entrapped oxazine 725 dye	No	Fundamental study	37 [b]	5.2
[37]	800 nm (35 × 9.3)	Poly(styrene-alt-maleic acid) with non-covalently attached indocyanine green	No	Photodynamic therapy, hyperthermia and near-infrared optical imaging	1.3	0.034
[38]	850 nm (50 × 12)	CTAB bilayer with electrostatically adsorved chlorin e6	No	Fluorescence detection and photodynamic therapy	3	0.54
[39]	776 nm (43 × 12) [c]	Silica shell with covalently linked IRDye	No	Fundamental study	10	0.7
[40]	843 nm (54 × 13)	Silica shell with adsorbed doxorubicin dye	No	Fundamental study	2.9	0.26
[4]	820 nm (85 × 20)	Silica shell with covalently linked porphyrin, T790	No	Two-photon imaging and photodynamic therapy	2.1	0.32
[3]	668 nm (47 × 19)	Silica shell with covalently linked phthalocyanine, AlC4Pc	No	Co-enhancement of fluorescence and singlet oxygen generation	7	2.8
[41]	654 nm (49 × 21)	Silica shell with covalently linked porphyrin, TCPP	No	Sensor for detection of pyrophosphate in aqueous solution	4.5	0.45
[42]	664 nm (50 × 25)	Oligo dsDNA spacer with 45-bp labeled with Quasar 670	Yes [d]	Array biochip for ultrasensitive DNA analysis	< 2	< 0.6
[43]	615 nm (40 × 17)	Polyelectrolytes (PSS/PDADMAC) with electrostatically adsorved CdSe/CdZnS QDs	No	Fundamental study	10.8	2.2
This work	662 nm (71 × 25)	Oligo dsDNA spacer with 10-bp labeled with Atto-647N	Yes	Fundamental study	17	11

[a] FOM= Enh. factor $\times \Phi_F$ is a figure-of-merit defined in Ref. 36 for comparison of enhancement effects between dyes of strikingly different quantum yield, Φ_F [b] In this work, the enhancement effect was evaluated from a single-particle type of measurement, while other examples in the table are from ensemble measurements [c] The nanorod size was assessed from TEM images reported in Ref. 39. [d] In this work, the dye molecules are assembled onto surface-immobilized nanorods, instead of an attachment in colloidal dispersion that is used in the remaining examples.

The results herein reported could significantly improve the performance of dye nano-assemblies for imaging or sensing applications. In fact, this tip-functionalization approach was used for attaching fluorescently-labeled DNA probes, such as molecular beacons, onto the tips of gold nanorods for nucleic acid detection, as discussed next in Chapter 6. The internalization of dye-particle nano-assemblies and their successful detection inside living cells could be further exploited for developing nano-assemblies carrying functional DNA constructs for nucleic acid sensing, which could have potential for probing gene transcription inside living cells. These studies could be focused on tip-functionalized gold nanorods, because an effective emission enhancement is observed with a low number of attached dye molecules, which leaves more surface available for loading other cargo or functional units onto these nano-assemblies.

5.10. Experimental section

5.10.1. Materials

Gold nanorods in aqueous suspension stabilized by CTAB with an average size of 25 nm × 71 nm were purchased from Nanopartz Inc. (Loveland, USA) - product no. A12-25-650-CTAB-DIH-25, lot F3216. DNA oligonucleotides purified by HPLC were purchased from STAB Vida (Monte da Caparica, Portugal) with the following sequences: a dye-labeled strand, (Atto-647N)-5'-GAGTCTGGAC-(C6-SH)-3' and a non-labeled complementary strand, 3'-CTCAGACCTG-(C6-SH)-5', where C6 stands for a hexamethylene spacer. Thiolated poly(ethylene glycol) (mPEG-SH, M_w~5,000), Tween 20, CTAB (≥ 99%) and poly(vinyl alcohol) (PVA, 99%, MW~89,000-98,000) were supplied by Sigma-Aldrich. Phosphate-buffered saline (PBS) buffer was acquired as tablets also from Sigma-Aldrich. Sodium citrate tribasic dihydrate (Sigma-Aldrich, ≥ 99.5%) and citric acid (Sigma-Aldrich, ≥ 99.5%) were used to prepare citrate buffer with pH 3. Ultrapure water (18.2 MΩ.cm) was obtained with a Milli-Q purification system (Merck-Millipore) and used in all preparations. All reagents were used as obtained.

5.10.2. Instrumentation

A PerkinElmer, model Lambda 35, UV/Vis spectrophotometer was used to measure the extinction spectra. Corrected fluorescence emission spectra were recorded with a FluoroLog-3 spectrophotometer (Horiba Jobin Yvon, Tokyo, Japan). Confocal fluorescence microscopy and single-particle spectroscopy measurements were performed on a time-resolved confocal fluorescence microscope, model MicroTime 200, from PicoQuant GmbH (Berlin, Germany). The microscope setup details were previously described in Chapter 3. The SymPhoTime software, version 5.3.2.2, from PicoQuant GmbH (Berlin, Germany) was used for data acquisition and analysis. Live cell internalization studies were conducted on a laser scanning confocal microscope, model LSM710, from Zeiss (Jena, Germany). Transmission electron microscopy (TEM) characterization was performed on a Hitachi H-8100 electron microscope operating at 200 kV.

5.10.3. Tip-selective functionalization of gold nanorods

The tip-selective approach uses the CTAB surfactant bilayer already present in the gold nanorods to direct the dye-labeled oligonucleotides to the tip hot-spots.[7–9] Firstly, the ssDNA sequences indicated above were hybridized in 0.5× PBS for at least 1 h at room temperature using a 25% molar excess of the non-labeled sequence. Then, the functionalization mixture was obtained by adding the dsDNA hybrid (0.5× PBS) to the gold nanorods at a molar ratio of 4000 oligos-per-particle to give a final particle concentration of 1 nM in a volume of 90 µL. The concentration of CTAB was constant at 10 mM during the incubation time. The mixture was allowed to react at room temperature for 1, 3 and 6 hours. At the end of each time interval, the reaction was halted by washing the unbounded oligonucleotides in eight centrifugation cycles with resuspension in 500 µL of aqueous CTAB (10 mM). All samples were stored in the suspension at 4 ºC until further use. The number of dye-labeled oligonucleotides attached per gold nanorod was determined by a ligand displacement protocol using 2-mercaptoethanol, as reported in Ref. 25. For this purpose, a working curve was previously established by measuring the fluorescence intensity from solutions of dye-labeled oligonucleotides with known concentrations in the presence of 2-mercaptoethanol (Figure 5.9).

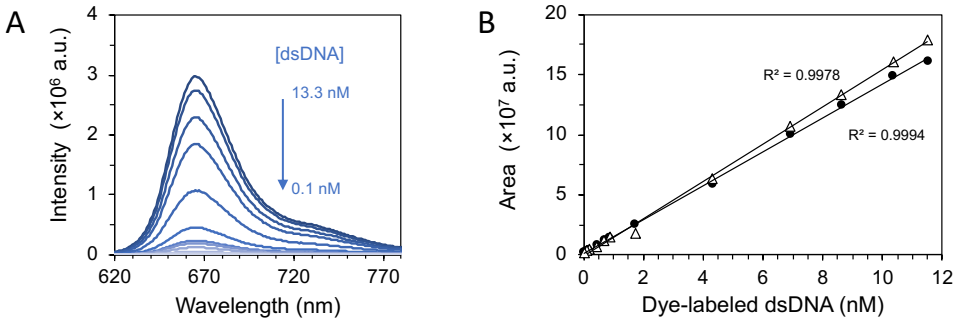

Figure 5.9 - Additional information for evaluating the number of dye-labeled oligonucleotides attached per gold nanorod. (A) Emission spectra of dye-labeled oligonucleotides with known concentrations in the presence of 2-mercaptoethanol (20 mM) obtained for an excitation wavelength of 600 nm. (B) Working curve for the determination of dye-labeled oligonucleotide concentration in the displacement assays: here represented as the integrated emission spectra (area) for solutions of known concentrations of dye-labeled oligonucleotides in PBST buffer (closed circles) and aqueous CTAB (open triangles) both in the presence of 2-mercaptoethanol (20 mM).

The emission spectra were recorded for excitation wavelengths in the range of 600 to 650 nm in steps of 10 nm. The experimental enhancement factors were calculated from the ratio between the areas of emission spectra of the dye-particle assemblies and that of the same sample after dye displacement (Figure 5.17 of the Annexes).

5.10.4. Non-selective functionalization of gold nanorods

For comparison purposes, a non-selective functionalization approach was used for the attachment of dye-labeled oligonucleotides onto gold nanorods. This approach consists of a two-step ligand exchange process in which CTAB is first replaced by thiolated mPEG-SH

molecules and then by dye-labeled dsDNA oligonucleotides following a protocol that was adapted from Ref. 20. Briefly, a volume of 2 mL of gold nanorods (0.2 nM) in aqueous CTAB (1 mM) was centrifuged (6000 rpm, 15 mins), the supernatant was discarded, and the pellet was resuspended in aqueous mPEG-SH (250 μL, 10 μM) and Tween 20 (250 μL, 0.2 wt %). The solution was centrifuged (6000 rpm, 15 mins) and the supernatant was replaced again with mPEG-SH and Tween 20. This procedure was repeated two times to wash away the CTAB detergent. The second ligand exchange begins with hybridization of the ssDNA sequences, as described in the previous section. After that, the hybrid (35 μL) was added to the PEG-stabilized gold nanorods (10 μL) to obtain the following molar ratios of dye-per-particle: 400, 800, 1600 and 4000, while keeping the particle concentration fixed at ca. 2 nM. Then, citrate buffer at pH 3 (20 μL, 0.5 M) and PBS (35 μL, 1×) were added, and functionalization was allowed to proceed for 1 h at room temperature. Finally, the unreacted oligonucleotides were washed by six centrifugation cycles with resuspensions in PBST buffer (mixture of PBS with Tween 20, 0.01 wt %).

The surface charge of tip- and NS-functionalized gold nanorod samples was assessed from measurements of zeta potential (Table 5.4 of the Annexes).

5.10.5. Single-particle fluorescence spectroscopy

Fluorescence emission from dye-particle nano-assemblies in colloidal suspension was characterized by Fluorescence Correlation Spectroscopy (FCS). These measurements were performed with picosecond diode laser excitation at 639 nm and by selecting emission with a bandpass filter centered at 695 nm and a transmission window of 55 nm. The emission intensity time traces were collected from a sub-nanomolar suspension of functionalized gold nanorods (ca. 10 μm above the coverslip surface) during a time interval of 60 or 120 s for several excitation powers in the range from 4.4×10^{-3} to 4.4 kW/cm^2. The acquisition in time-tagged time-resolved mode also provided fluorescence decays for the same samples. Single-particle emission intensity and one-photon luminescence measurements were characterized on surface-immobilized samples. For this purpose, NS- or tip-functionalized gold nanorods were diluted to a sub-nanomolar concentration in a PVA solution (1% v/v) and deposited on glass coverslips by spin-coating. Fluorescence emission was measured using excitation at 639 nm with a power of 4.4×10^{-2} kW/cm^2 to minimize photodamage effects, which were evaluated from several consecutive image acquisitions using a scanning resolution of 0.156 nm per pixel and an integration time per pixel of 0.6 ms. Then, excitation wavelength was changed to 482 nm and an excitation power of ca. 50 kW/cm^2 was used to measure the one-photon luminescence spectrum from individual gold nanorods. The spectral lineshape was fitted with a Lorentzian function using a home-made MATLAB program. The corresponding diffraction-limited spots in the fluorescence images obtained with excitation at 639 nm were fitted with a 2D-gaussian using an adapted MATLAB routine for point-spread function fitting.

5.10.6. Simulations of Discrete Dipole Approximation

The method of discrete dipole approximation was used to obtain estimates of the plasmonic enhancement effect of a gold nanorod on the fluorescence emission from Atto-647N dye. A full detailed description of the calculation procedures can be found in Refs. 11 and 44. In this work, the simulated particle was a spherically capped cylinder with a diameter of 25 nm and length of 61 nm. The volume of this particle was discretized as an array of cubic elements with a side of 0.25 nm. The values reported for the dielectric function of gold by Johnson and Christy were renormalized to the dielectric constant of water in order to describe the particle and its surrounding environment.[45] The fluorescent dye was modelled as a point-like dipole emitting at specific wavelengths each representing a spectral component within the dye's emission spectrum.[11] The magnitude of the dye's transition dipole moment was calculated from its rate of spontaneous emission,[46] by using the fluorescence quantum yield and lifetime determined for the dye-labeled oligonucleotide in water, Φ_F = 0.57 and τ = 4 ns (data not shown). The separation between the emitter and the metal surface was kept constant at a distance of about 4 nm that matches the DNA spacer length. Two conditions were considered regarding the emitter's transition dipole orientation: it was either assumed to be orthogonal to the metal surface; or it was orientationally averaged over three independent directions of space. For each probed position, the fluorescence enhancement, F/F^0, was estimated from DDA simulations from the product of the excitation rate enhancement, γ_{exc}, and the relative emission quantum yield of the dye modified by the plasmonic particle, $F/F^0 = \gamma_{exc} \times \Phi_m/\Phi_F$. The excitation rate enhancement was obtained from $\gamma_{exc} = |\mathbf{E}|^2/|\mathbf{E_0}|^2$, which is the near-field enhancement at the incident wavelength in the position assumed for the dye molecule. The relative emission quantum yield of the dye, Φ_m/Φ_F, was calculated from the radiative, K_r, and non-radiative, K_{nr}, decay rates modified by the plasmonic antenna using the theoretical formalism described by D'Agostino et al.[47]

5.10.7. Cell internalization assays

Mouse neuroblastoma N2a cells genetically modified to express stably a construct of the prion protein fused to the YFP-GPI-anchored for labeling the cell membrane were used in the internalization assays.[35] The genetically modified N2a cell line was cultured at 37 ºC under 5% CO_2 in DMEM supplemented with 10% FBS, 100 µg/mL streptomycin and 100 U/mL penicillin (Invitrogen, USA) and incubated in the presence of a sub-nanomolar concentration of NS-functionalized gold nanorods. Cellular uptake was imaged 24 hours after incubation with nanorods and again two days later (after replacement of culture medium) by fluorescence imaging in a laser scanning confocal microscope equipped with a 63× plan-apochromatic 1.4 NA oil immersion objective and sub-diffraction spatial resolution (Carl Zeiss Axio Observer Z1 mounted LSM710 confocal microscope). Three detection channels were used for excitation at 405, 514 and 633 nm, respectively, for detection of nuclei stained with Hoechst 33342 dye, cell membranes labeled with PrP-YFP-GPI-anchor fusion protein, and dye-particle nano-assemblies labeled with Atto-647N dye.

5.11. References

(1) Jang, B.; Park, J.-Y.; Tung, C.-H.; Kim, I.-H.; Choi, Y. Gold Nanorod−Photosensitizer Complex for Near-Infrared Fluorescence Imaging and Photodynamic/Photothermal Therapy *In Vivo*. *ACS Nano* **2011**, *5* (2), 1086–1094. https://doi.org/10.1021/nn102722z.
(2) Wu, Q.; Chen, L.; Huang, L.; Wang, J.; Liu, J.; Hu, C.; Han, H. Quantum Dots Decorated Gold Nanorod as Fluorescent-Plasmonic Dual-Modal Contrasts Agent for Cancer Imaging. *Biosens. Bioelectron.* **2015**, *74*, 16–23. https://doi.org/10.1016/j.bios.2015.06.010.
(3) Ke, X.; Wang, D.; Chen, C.; Yang, A.; Han, Y.; Ren, L.; Li, D.; Wang, H. Co-Enhancement of Fluorescence and Singlet Oxygen Generation by Silica-Coated Gold Nanorods Core-Shell Nanoparticle. *Nanoscale Res. Lett.* **2014**, *9* (1), 666. https://doi.org/10.1186/1556-276X-9-666.
(4) Zhao, T.; Yu, K.; Li, L.; Zhang, T.; Guan, Z.; Gao, N.; Yuan, P.; Li, S.; Yao, S. Q.; Xu, Q.-H.; Xu, G. Q. Gold Nanorod Enhanced Two-Photon Excitation Fluorescence of Photosensitizers for Two-Photon Imaging and Photodynamic Therapy. *ACS Appl. Mater. Interfaces* **2014**, *6* (4), 2700–2708. https://doi.org/10.1021/am405214w.
(5) Wang, L.; Song, Q.; Liu, Q.; He, D.; Ouyang, J. Plasmon-Enhanced Fluorescence-Based Core-Shell Gold Nanorods as a Near-IR Fluorescent Turn-On Sensor for the Highly Sensitive Detection of Pyrophosphate in Aqueous Solution. *Adv. Funct. Mater.* **2015**, *25* (45), 7017–7027. https://doi.org/10.1002/adfm.201503326.
(6) Chen, H.; Shao, L.; Li, Q.; Wang, J. Gold Nanorods and Their Plasmonic Properties. *Chem Soc Rev* **2013**, *42* (7), 2679–2724. https://doi.org/10.1039/C2CS35367A.
(7) Caswell, K. K.; Wilson, J. N.; Bunz, U. H. F.; Murphy, C. J. Preferential End-to-End Assembly of Gold Nanorods by Biotin−Streptavidin Connectors. *J. Am. Chem. Soc.* **2003**, *125* (46), 13914–13915. https://doi.org/10.1021/ja037969i.
(8) Shibu Joseph, S. T.; Ipe, B. I.; Pramod, P.; Thomas, K. G. Gold Nanorods to Nanochains: Mechanistic Investigations on Their Longitudinal Assembly Using α,ω-Alkanedithiols and Interplasmon Coupling. *J. Phys. Chem. B* **2006**, *110* (1), 150–157. https://doi.org/10.1021/jp0544179.
(9) Nie, Z.; Fava, D.; Kumacheva, E.; Zou, S.; Walker, G. C.; Rubinstein, M. Self-Assembly of Metal–Polymer Analogues of Amphiphilic Triblock Copolymers. *Nat. Mater.* **2007**, *6* (8), 609–614. https://doi.org/10.1038/nmat1954.
(10) Fu, Y.; Zhang, J.; Lakowicz, J. R. Plasmon-Enhanced Fluorescence from Single Fluorophores End-Linked to Gold Nanorods. *J. Am. Chem. Soc.* **2010**, *132* (16), 5540–5541. https://doi.org/10.1021/ja9096237.
(11) Khatua, S.; Paulo, P. M. R.; Yuan, H.; Gupta, A.; Zijlstra, P.; Orrit, M. Resonant Plasmonic Enhancement of Single-Molecule Fluorescence by Individual Gold Nanorods. *ACS Nano* **2014**, *8* (5), 4440–4449. https://doi.org/10.1021/nn406434y.
(12) Wientjes, E.; Renger, J.; Cogdell, R.; van Hulst, N. F. Pushing the Photon Limit: Nanoantennas Increase Maximal Photon Stream and Total Photon Number. *J. Phys. Chem. Lett.* **2016**, *7* (9), 1604–1609. https://doi.org/10.1021/acs.jpclett.6b00491.
(13) Zhang, W.; Caldarola, M.; Lu, X.; Pradhan, B.; Orrit, M. Single-Molecule Fluorescence Enhancement of a near-Infrared Dye by Gold Nanorods Using DNA Transient Binding. *Phys. Chem. Chem. Phys.* **2018**, *20* (31), 20468–20475. https://doi.org/10.1039/C8CP03114B.
(14) Bardhan, R.; Grady, N. K.; Cole, J. R.; Joshi, A.; Halas, N. J. Fluorescence Enhancement by Au Nanostructures: Nanoshells and Nanorods. *ACS Nano* **2009**, *3* (3), 744–752. https://doi.org/10.1021/nn900001q.
(15) Ming, T.; Zhao, L.; Yang, Z.; Chen, H.; Sun, L.; Wang, J.; Yan, C. Strong Polarization Dependence of Plasmon-Enhanced Fluorescence on Single Gold Nanorods. *Nano Lett.* **2009**, *9* (11), 3896–3903. https://doi.org/10.1021/nl902095q.
(16) Su, H.; Zhong, Y.; Ming, T.; Wang, J.; Wong, K. S. Extraordinary Surface Plasmon Coupled Emission Using Core/Shell Gold Nanorods. *J. Phys. Chem. C* **2012**, *116* (16), 9259–9264. https://doi.org/10.1021/jp211713y.

(17) Abadeer, N. S.; Brennan, M. R.; Wilson, W. L.; Murphy, C. J. Distance and Plasmon Wavelength Dependent Fluorescence of Molecules Bound to Silica-Coated Gold Nanorods. *ACS Nano* **2014**, *8* (8), 8392–8406. https://doi.org/10.1021/nn502887j.
(18) Szekrényes, D. P.; Pothorszky, S.; Zámbó, D.; Osváth, Z.; Deák, A. Investigation of Patchiness on Tip-Selectively Surface-Modified Gold Nanorods. *J. Phys. Chem. C* **2018**, *122* (3), 1706–1710. https://doi.org/10.1021/acs.jpcc.7b11211.
(19) Janicek, B. E.; Hinman, J. G.; Hinman, J. J.; Bae, S. hyun; Wu, M.; Turner, J.; Chang, H.-H.; Park, E.; Lawless, R.; Suslick, K. S.; Murphy, C. J.; Huang, P. Y. Quantitative Imaging of Organic Ligand Density on Anisotropic Inorganic Nanocrystals. *Nano Lett.* **2019**, *19* (9), 6308–6314. https://doi.org/10.1021/acs.nanolett.9b02434.
(20) Li, J.; Zhu, B.; Zhu, Z.; Zhang, Y.; Yao, X.; Tu, S.; Liu, R.; Jia, S.; Yang, C. J. Simple and Rapid Functionalization of Gold Nanorods with Oligonucleotides Using an MPEG-SH/Tween 20-Assisted Approach. *Langmuir* **2015**, *31* (28), 7869–7876. https://doi.org/10.1021/acs.langmuir.5b01680.
(21) Baumann, V.; Friedrich Röttgermann, P. J.; Haase, F.; Szendrei, K.; Dey, P.; Lyons, K.; Wyrwich, R.; Gräßel, M.; Stehr, J.; Ullerich, L.; Bürsgens, F.; Rodríguez-Fernández, J. Highly Stable and Biocompatible Gold Nanorod–DNA Conjugates as NIR Probes for Ultrafast Sequence-Selective DNA Melting. *RSC Adv.* **2016**, *6* (105), 103724–103739. https://doi.org/10.1039/C6RA17156G.
(22) Xu, L.; Kuang, H.; Xu, C.; Ma, W.; Wang, L.; Kotov, N. A. Regiospecific Plasmonic Assemblies for *in Situ* Raman Spectroscopy in Live Cells. *J. Am. Chem. Soc.* **2012**, *134* (3), 1699–1709. https://doi.org/10.1021/ja2088713.
(23) Zijlstra, P.; Paulo, P. M. R.; Orrit, M. Optical Detection of Single Non-Absorbing Molecules Using the Surface Plasmon Resonance of a Gold Nanorod. *Nat. Nanotechnol.* **2012**, *7* (6), 379–382. https://doi.org/10.1038/nnano.2012.51.
(24) Wang, G.; Akiyama, Y.; Kanayama, N.; Takarada, T.; Maeda, M. Directed Assembly of Gold Nanorods by Terminal-Base Pairing of Surface-Grafted DNA. *Small* **2017**, *13* (44), 1702137. https://doi.org/10.1002/smll.201702137.
(25) Demers, L. M.; Mirkin, C. A.; Mucic, R. C.; Reynolds, R. A.; Letsinger, R. L.; Elghanian, R.; Viswanadham, G. A Fluorescence-Based Method for Determining the Surface Coverage and Hybridization Efficiency of Thiol-Capped Oligonucleotides Bound to Gold Thin Films and Nanoparticles. *Anal. Chem.* **2000**, *72* (22), 5535–5541. https://doi.org/10.1021/ac0006627.
(26) Hill, H. D.; Millstone, J. E.; Banholzer, M. J.; Mirkin, C. A. The Role Radius of Curvature Plays in Thiolated Oligonucleotide Loading on Gold Nanoparticles. *ACS Nano* **2009**, *3* (2), 418–424. https://doi.org/10.1021/nn800726e.
(27) Wang, G.; Akiyama, Y.; Takarada, T.; Maeda, M. Rapid Non-Crosslinking Aggregation of DNA-Functionalized Gold Nanorods and Nanotriangles for Colorimetric Single-Nucleotide Discrimination. *Chem. - Eur. J.* **2016**, *22* (1), 258–263. https://doi.org/10.1002/chem.201503834.
(28) Hestand, N. J.; Spano, F. C. Expanded Theory of H- and J-Molecular Aggregates: The Effects of Vibronic Coupling and Intermolecular Charge Transfer. *Chem. Rev.* **2018**, *118* (15), 7069–7163. https://doi.org/10.1021/acs.chemrev.7b00581.
(29) Khatua, S.; Paulo, P. M. R.; Yuan, H.; Gupta, A.; Zijlstra, P.; Orrit, M. Resonant Plasmonic Enhancement of Single-Molecule Fluorescence by Individual Gold Nanorods. *ACS Nano* **2014**, *8* (5), 4440–4449. https://doi.org/10.1021/nn406434y.
(30) Busson, M. P.; Rolly, B.; Stout, B.; Bonod, N.; Wenger, J.; Bidault, S. Photonic Engineering of Hybrid Metal-Organic Chromophores. *Angew. Chem. Int. Ed.* **2012**, *51* (44), 11083–11087. https://doi.org/10.1002/anie.201205995.
(31) Ortega, A.; García de la Torre, J. Hydrodynamic Properties of Rodlike and Disklike Particles in Dilute Solution. *J. Chem. Phys.* **2003**, *119* (18), 9914–9919. https://doi.org/10.1063/1.1615967.
(32) Burrows, N. D.; Lin, W.; Hinman, J. G.; Dennison, J. M.; Vartanian, A. M.; Abadeer, N. S.; Grzincic, E. M.; Jacob, L. M.; Li, J.; Murphy, C. J. Surface Chemistry of Gold Nanorods. *Langmuir*

2016, *32* (39), 9905–9921. https://doi.org/10.1021/acs.langmuir.6b02706.
(33) Blythe, K. L.; Willets, K. A. Super-Resolution Imaging of Fluorophore-Labeled DNA Bound to Gold Nanoparticles: A Single-Molecule, Single-Particle Approach. *J. Phys. Chem. C* **2016**, *120* (2), 803–815. https://doi.org/10.1021/acs.jpcc.5b08534.
(34) Liu, T.; Liu, S.; Jiang, W.; Wang, W. Tracking Sub-Nanometer Shift in the Scattering Centroid of Single Gold Nanorods during Electrochemical Charging. *ACS Nano* **2019**, *13* (6), 6279–6286. https://doi.org/10.1021/acsnano.8b09636.
(35) Tavares, E.; Macedo, J. A.; Paulo, P. M. R.; Tavares, C.; Lopes, C.; Melo, E. P. Live-Cell FRET Imaging Reveals Clustering of the Prion Protein at the Cell Surface Induced by Infectious Prions. *Biochim. Biophys. Acta BBA - Mol. Basis Dis.* **2014**, *1842* (7), 981–991. https://doi.org/10.1016/j.bbadis.2014.02.002.
(36) Punj, D.; Regmi, R.; Devilez, A.; Plauchu, R.; Moparthi, S. B.; Stout, B.; Bonod, N.; Rigneault, H.; Wenger, J. Self-Assembled Nanoparticle Dimer Antennas for Plasmonic-Enhanced Single-Molecule Fluorescence Detection at Micromolar Concentrations. *ACS Photonics* **2015**, *2* (8), 1099–1107. https://doi.org/10.1021/acsphotonics.5b00152.
(37) Kuo, W.-S.; Chang, C.-N.; Chang, Y.-T.; Yang, M.-H.; Chien, Y.-H.; Chen, S.-J.; Yeh, C.-S. Gold Nanorods in Photodynamic Therapy, as Hyperthermia Agents, and in Near-Infrared Optical Imaging. *Angew. Chem. Int. Ed.* **2010**, *49* (15), 2711–2715. https://doi.org/10.1002/anie.200906927.
(38) Huang, X.; Tian, X.-J.; Yang, W.; Ehrenberg, B.; Chen, J.-Y. The Conjugates of Gold Nanorods and Chlorin E6 for Enhancing the Fluorescence Detection and Photodynamic Therapy of Cancers. *Phys. Chem. Chem. Phys.* **2013**, *15* (38), 15727. https://doi.org/10.1039/c3cp44227f.
(39) Abadeer, N. S.; Brennan, M. R.; Wilson, W. L.; Murphy, C. J. Distance and Plasmon Wavelength Dependent Fluorescence of Molecules Bound to Silica-Coated Gold Nanorods. *ACS Nano* **2014**, *8* (8), 8392–8406. https://doi.org/10.1021/nn502887j.
(40) Tian, X.; Guo, J.; Tian, Y.; Tang, H.; Yang, W. Modulated Fluorescence Properties in Fluorophore-Containing Gold Nanorods@mSiO2. *RSC Adv.* **2014**, *4* (18), 9343. https://doi.org/10.1039/c3ra46082g.
(41) Wang, L.; Song, Q.; Liu, Q.; He, D.; Ouyang, J. Plasmon-Enhanced Fluorescence-Based Core-Shell Gold Nanorods as a Near-IR Fluorescent Turn-On Sensor for the Highly Sensitive Detection of Pyrophosphate in Aqueous Solution. *Adv. Funct. Mater.* **2015**, *25* (45), 7017–7027. https://doi.org/10.1002/adfm.201503326.
(42) Mei, Z.; Tang, L. Surface-Plasmon-Coupled Fluorescence Enhancement Based on Ordered Gold Nanorod Array Biochip for Ultrasensitive DNA Analysis. *Anal. Chem.* **2017**, *89* (1), 633–639. https://doi.org/10.1021/acs.analchem.6b02797.
(43) Trotsiuk, L.; Muravitskaya, A.; Kulakovich, O.; Guzatov, D.; Ramanenka, A.; Kelestemur, Y.; Demir, H. V.; Gaponenko, S. Plasmon-Enhanced Fluorescence in Gold Nanorod-Quantum Dot Coupled Systems. *Nanotechnology* **2020**, *31* (10), 105201. https://doi.org/10.1088/1361-6528/ab5a0e.
(44) Teixeira, R.; Paulo, P. M. R.; Costa, S. M. B. Gold Nanoparticles in Core–Polyelectrolyte–Shell Assemblies Promote Large Enhancements of Phthalocyanine Fluorescence. *J. Phys. Chem. C* **2015**, *119* (37), 21612–21619. https://doi.org/10.1021/acs.jpcc.5b04667.
(45) Johnson, P. B.; Christy, R. W. Optical Constants of the Noble Metals. *Phys. Rev. B* **1972**, *6* (12), 4370–4379. https://doi.org/10.1103/PhysRevB.6.4370.
(46) Novotny, L.; Hecht, B. Principles of Nano-Optics. *Camb. Univ. Press Camb.* **2012**, 584.
(47) D'Agostino, S.; Della Sala, F.; Andreani, L. C. Dipole-Excited Surface Plasmons in Metallic Nanoparticles: Engineering Decay Dynamics within the Discrete-Dipole Approximation. *Phys. Rev. B* **2013**, *87* (20). https://doi.org/10.1103/PhysRevB.87.205413.

5.12. Annexes

5.12.1. Optimal distance estimation for fluorescence enhancement at the tips of gold nanorods

The estimation of the optimal distance for emission enhancement at the nanorod's tips, from model simulations using the DDA method, is shown in the next figure.

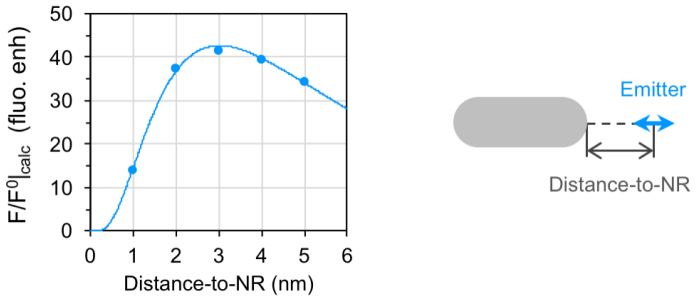

Figure 5.10 - Fluorescence enhancement factors, F/F^0, calculated from DDA simulations of an emitter with the photophysical properties of Atto-647N dye positioned at the tip of a gold nanorod with a size of 25 nm × 61 nm - see dye-particle configuration on the right-side scheme - for excitation and emission at 639 and 700 nm, respectively. The calculated enhancement factors show that the maximum enhancement effect for this particle configuration is about 40-fold emission increase at a distance of 3 to 4 nm away from the particle's surface.

5.12.2. Emission spectra from tip- and non-selective functionalized gold nanorods

In Figure 5.11 are shown the emission spectra from nano-assemblies that were used to quantify the amount of dye loaded per particle and how it affects the fluorescence enhancement.

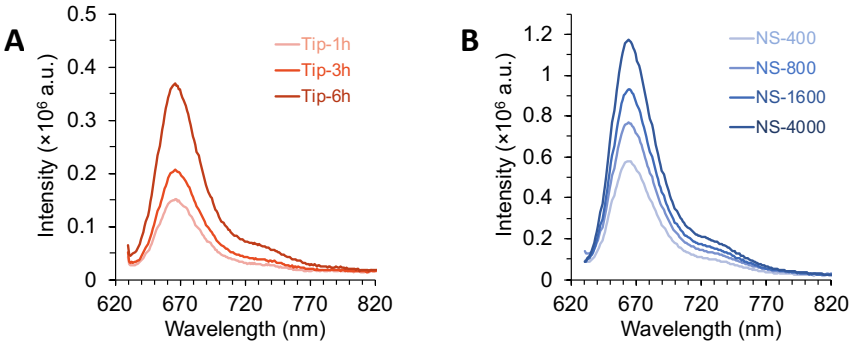

Figure 5.11 - Emission spectra of dye displaced from nano-assemblies used to quantify the amount of loaded DNA per particle. (A) Tip-selective functionalized gold nanorod samples for several incubation times. (B) non-selective functionalized gold nanorod samples for various DNA loading ratios - excitation wavelength at 620 nm.

5.12.3. Simulated spectra for the dye's enhanced emission by a gold nanorod

Comparison between the normalized emission from tip-functionalized gold nanorods and that of the displaced dye molecules and simulated spectral that suggest the apparent absence of spectral reshaping in the plasmon-coupled emission of the dye-particle assemblies (Figure 5.12).

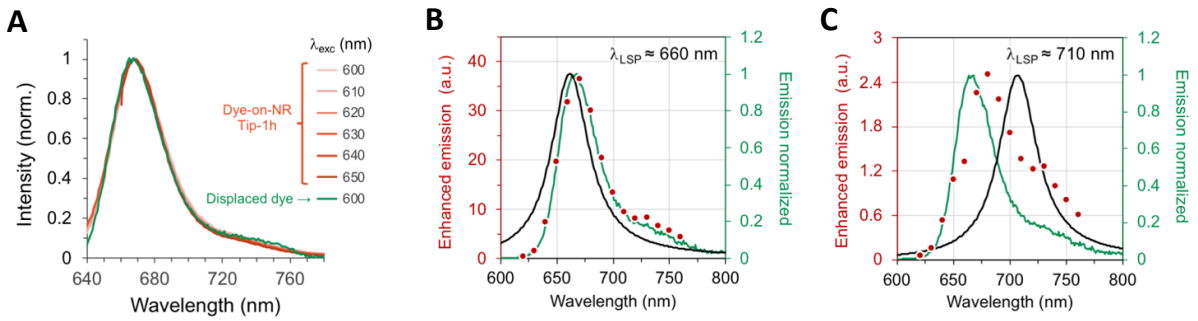

Figure 5.12 - Simulated spectra for the dye's enhanced emission by a gold nanorod. (A) Normalized emission spectra of tip-functionalized gold nanorods (sample "Tip-1h") measured for several excitation wavelengths (red curves) showing a similar lineshape and comparison to the emission spectrum of the displaced dye in aqueous solution (green curve). (B,C) simulated spectra for the dye's enhanced emission by a gold nanorod (red dots), in the case of: (B) good spectral overlap between the dye's emission (green curve) and the longitudinal surface plasmon band (black curve); or (C) large mismatch between them. These simulations suggest that a possible explanation for the apparent absence of spectral reshaping in plasmon-coupled emission of the dye-particle assemblies could be due to a good spectral overlap between the dye's emission and the longitudinal surface plasmon band.

5.12.4. Spectral dependence on the excitation wavelength

The spectral dependence of non-selectively functionalized gold nanorods on the excitation wavelength is represented in the following figure.

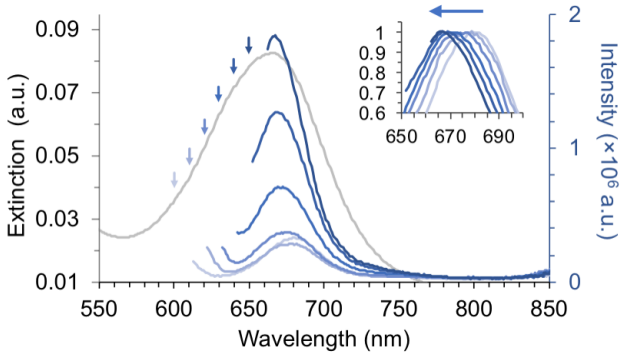

Figure 5.13 - Extinction spectrum of the non-selectively functionalized gold nanorods for "NS-4000" sample (grey curve) and emission spectra of the same sample for several excitation wavelengths (blue curves) indicated by the arrows over the extinction spectrum. The inset shows the change in the fluorescence spectrum close to its maximum, as excitation is selected at longer wavelengths (see arrow).

The spectral dependence of the calculated enhancement factor on the excitation wavelength for an average of the positions simulated in the tip and side of a nanorod is shown in Figure 5.14.

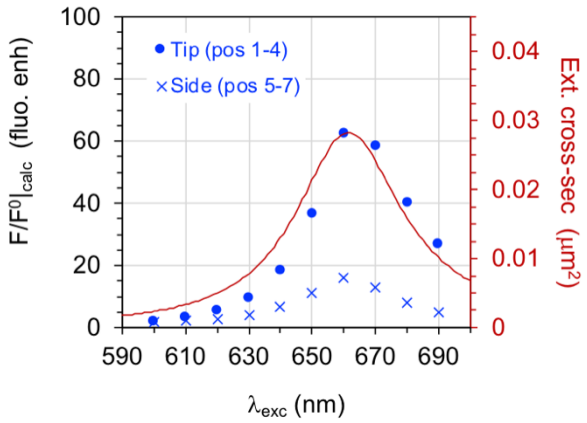

Figure 5.14 - Spectral dependence of the calculated enhancement factor (F/F^0) on the excitation wavelength for an average of the positions simulated at the tip and side regions (circles and crosses, respectively). The simulated emitter positions are shown in Figure 5.5E of the main text. These results consider an average dipole orientation of the emitter. The calculated extinction spectrum for the simulated nanorod is depicted in red - axis on the right-side.

5.12.5. Analysis of autocorrelation function curves from single-particle fluorescence emission

Further information from the intensity traces shown in Figure 5.6 of the main text was obtained from their autocorrelation function (ACF). The ACF curves show two relaxation components that were attributed to rotational and translational diffusion motions of the dye-particle nano-assemblies in colloidal suspension,[30]

$$G(\tau) - 1 = \left(1 - A_s e^{-\tau/\tau_\perp}\right) \times \frac{1}{N}\left(1 + \frac{\tau}{\tau_w}\right)^{-1}\left(1 + \frac{\tau}{\kappa^2 \cdot \tau_w}\right)^{-1/2} \quad (1)$$

The relaxation times for the short component were used to calculate the rotational diffusion coefficient of the dye-particle nano-assemblies from: $\tau_\perp = 1/6D_r^\perp$. The values of $\tau_\perp$ fitted from the ACF curves of samples "Tip-1h" and "NS-4000" (shown in Figure 5.6E,F of the main text) were 80 and 49 μs, and these correspond to $Dr^\perp$ values of 2.1 and 3.4 ms^{-1}, respectively (see Table 5.2 below). For comparison purposes, the rotational diffusion coefficient for these nano-objects was theoretically estimated using a modified version of Einstein–Smoluchowski relation for a rod-like particle geometry,[31]

$$D_r^\perp = 3\frac{kT(\ln p + C_r^\perp)}{\pi\,\eta\,L^3} \quad (2)$$

where p is the ratio between the rod's length L and diameter d, and $C_r^\perp$ is an end-effect term that depends on the aspect ratio, $C_r^\perp = -0.662 + 0.917/p - 0.050/p^2$. The dimensions of gold nanorods were 25 nm × 71 nm, but were increased by the length of the DNA which is approximately 4 nm. This yielded an estimate of 4.8 ms^{-1} for the rotational diffusion coefficient that compares well with the experimental values fitted from ACF curves. Similarly, the long relaxation times of 7.7 and

5.6 ms for samples "Tip-1h" and "NS4000" were used to calculate the respective translational diffusion constants ($\tau_w = w_{xy}^2 / 4D_t$) yielding values of 6.2 and 7.8 μm²/s for these samples. The latter values compare well to the theoretical estimate of 8.0 μm²/s obtained for a rod-like object with the size previously assumed for these nano-assemblies,[31]

$$D_t = \frac{kT(\ln p + C_t)}{3\pi \eta L} \quad (3)$$

where p is again the ratio between the rod's length L and diameter d, and C_t is an end-effect term that depends on the aspect ratio, $C_t = 0.312 + 0.565/p - 0.100/p^2$. The ACF curves of the control systems are quite different (results not shown), because these display a single relaxation component with longer decay times due to the translational diffusion of dye-labeled oligonucleotides either bound to CTAB micelles ("Control 1"), or free in solution ("Control 2"), which are both objects much smaller than gold nanorods (Figure 5.15).

Table 5.2 - Values of the short and long relaxation times ($\tau_\perp$ an τ_w) fitted from ACF curves of samples of dye-particle nano-assemblies studied, and respective rotational and translational diffusion coefficients ($D_r^\perp$ and D_t) obtained from experimental data or theoretically estimated.

		$D_r^\perp$ /ms^{-1}		D_t /μm²s^{-1}		
Sample	$\tau_\perp$/μs	exp.	calc.	τ_w/ms	exp.	calc.
Tip-1h	80	2.1	4.8	7.7	6.2	8.0
Tip-3h	57	2.9		5.7	8.2	
Tip-6h	96	1.7		6.7	6.7	
NS-400	52	3.2	4.8	5.1	8.3	8.0
NS-800	54	3.1		6.3	6.7	
NS-1600	51	3.3		5.4	8.0	
NS-4000	49	3.4		5.6	7.8	

5.12.6. Intensity time traces of control systems and decays of dye-particle nano-assemblies and the same controls

Examples of intensity time traces of two control systems that do not show intense fluorescence bursts are shown in Figure 5.15.

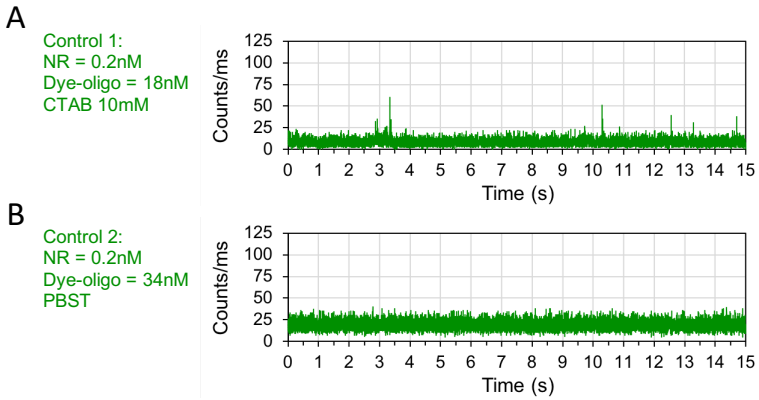

Figure 5.15 - Examples of intensity time traces of two control systems that do not show intense fluorescence bursts when the same amounts of the components present in samples "Tip-6h" and "NS-4000", respectively, are simply mixed together in (A) aqueous CTAB or (B) PBST buffer (i.e. without performing the functionalization protocols) - these intensity traces were measured for a much higher excitation power, 0.44 kW/cm², than those presented in Figure 5.6 of the main text.

The fluorescence decays of the dye-particle nano-assemblies in colloidal suspension and their control systems are graphically represented in the next figure.

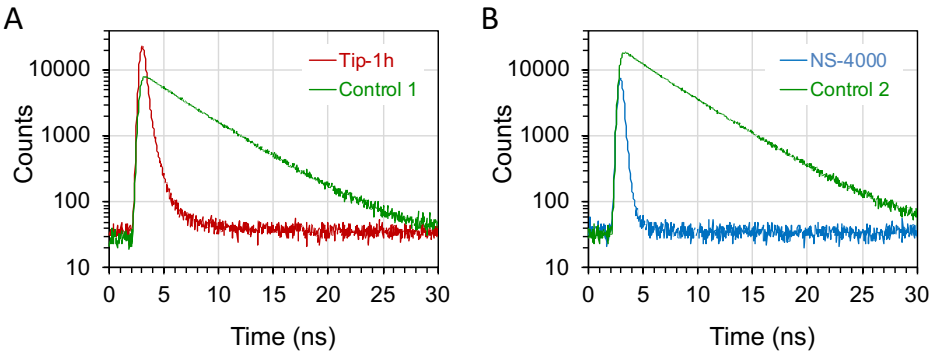

Figure 5.16 - Fluorescence decays of dye-particle nano-assemblies in colloidal suspension. (A) Tip-functionalized gold nanorods (sample "Tip-1h") and its control sample and (B) non-selectively functionalized gold nanorods (sample "NS-4000") and its control sample - control samples are described in Figure 5.15. All measurements were performed in a time-resolved fluorescence microscope with picosecond diode laser excitation at 639 nm with a power of 4.4×10^{-3} kW/cm² for dye-particle samples, or a power of 0.44 kW/cm² for control systems, and for emission selected with a bandpass filter centered at 695 nm with a transmission window of 55 nm.

5.12.7. Determination of fluorescence enhancement factors

The experimental enhancement factors in tip-functionalized gold nanorods were calculated from the spectra shown in the following figure.

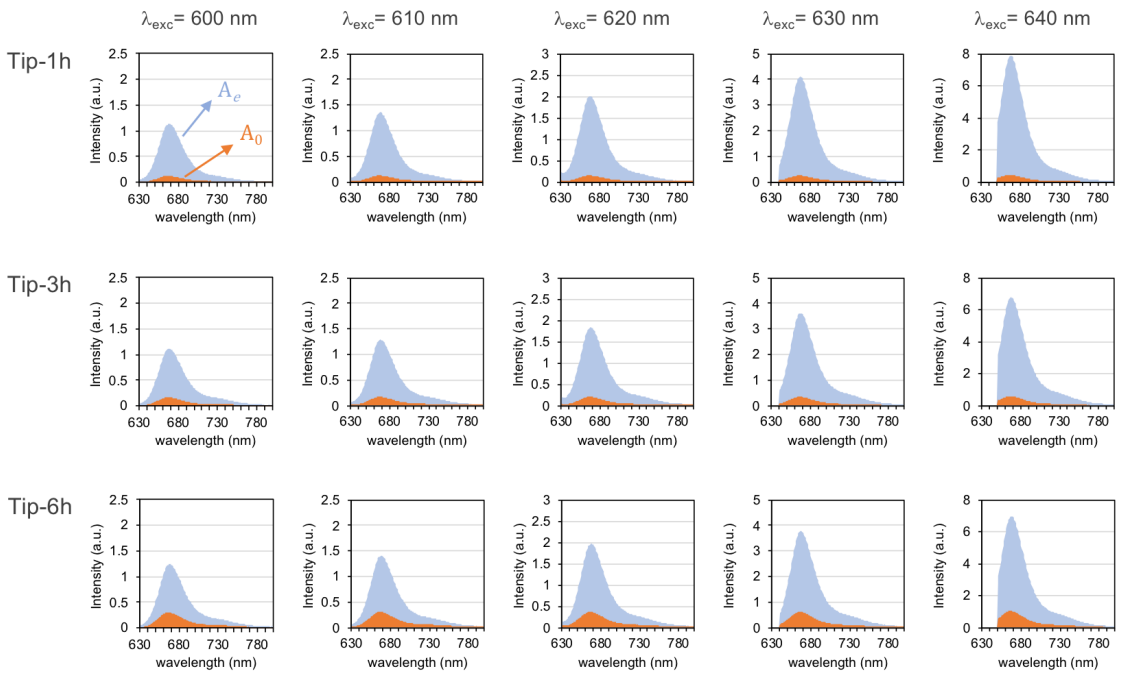

Figure 5.17 - Evaluation of fluorescence enhancement in tip-functionalized gold nanorods from comparison of the emission spectra of dye-particle nano-assemblies (light blue shaded areas) with that of the same sample after displacement of dye-labeled oligonucleotides into solution (orange shaded areas) - the enhancement factor is determined from the ratio of the respective areas, Fluo. enh = A_e/A_o. The data is displayed according to the excitation wavelength (λ_{exc}), as indicated at top of each column, and the sample incubation time used for DNA loading (1, 3 and 6 hours), as indicated at the beginning of each line.

From the calculations were obtained the values of enhancement factors shown in Table 5.3.

Table 5.3 - Fluorescence enhancement factors determined from data shown in Figure 5.17.

Enhancement factor	**λ_{exc} /nm**					
	600	610	620	630	640	650
Tip-1h	7.2	8.5	10.6	13.4	15.5	17.0
Tip-3h	5.7	6.4	7.7	9.3	10.4	11.2
Tip-6h	3.7	4.1	4.8	5.6	6.2	6.6

5.12.8. Determination of the zeta potential of dye-particle nano-assemblies

The surface charge of dye-particle nano-assemblies (Table 5.4) was assessed in a Zetasizer Nano ZS from Malvern Instruments Ltd (Malvern, UK), using the Zetasizer Software, version 7.10. The zeta potential of all samples was recorded at 25 ºC and 6 measurements were made to guarantee data reproducibility. The zeta potential values for NS-functionalized samples were measured in sub-nanomolar concentrations in water and are negative, because the CTAB bilayer in the "unmodified" nanorod sample is first replaced with thiolated PEG ("mPEG only" sample) and then dye-labeled oligonucleotides are inserted (in various loading ratios), which are negatively charged. For tip-functionalized gold nanorods, a previous dilution to sub-nanomolar concentrations was performed with aqueous CTAB (10 mM). The values of zeta potential determined for these samples probably reflect the micellar composition of the medium.

Table 5.4 - Values of zeta potential determined for gold nanorod samples.

Gold nanorod samples	ζ-potential/mV
unmodified[a]	31 ± 5
mPEG only	-15 ± 2
NS-400	-22 ± 3
NS-800	-19 ± 2
NS-1600	-26 ± 1
NS-4000	-29 ± 2
unmodified[b]	53 ± 4
Tip-1h	69 ± 6
Tip-3h	58 ± 4
Tip-6h	58 ± 3

[a] Original gold nanorods in aqueous CTAB 1 mM or [b] 10 mM.

Chapter 6

Fluorescence Signalling of DNA Probes Functionalized onto Gold Nanorods

6. Fluorescence signalling of DNA probes functionalized onto gold nanorods

The research described in this chapter aims at the development of a nano-object for nucleic acid biosensing from the conjugation of molecular beacons onto gold nanorods, hereafter generally referred to as nanohybrid biosensor. Molecular beacons are widely used to detect nucleic acids by a conformational change of the beacon that generates a fluorescence signal (signal-on), as described in Chapter 1. The sensitivity of these probes is however limited by the signal they generate. One strategy to overcome this problem relies on plasmonic nanoantennas that can enhance fluorescence emission from dye molecules in their vicinity. This approach has been generally employed for the amplification of fluorescence signalling schemes used for sensing.[1–3]

6.1. Introduction

Recent advances in the field of plasmonics that have delivered emission enhancement of several orders of magnitude have not yet been explored for fluorescence sensing. In this thesis, it was envisioned to explore such remarkable enhancements for improving sensor responses and to push the limit of detection of nucleic acids, thereby, dismissing any pre-amplification (e.g. reverse transcription-polymerase chain reaction, RT-PCR) or multi-labeling steps. Also, by using a molecular beacon type of approach, the molecular recognition and signalling can take place in a single step, much like a label-free biosensing assay. The enhanced fluorescence signalling effect was aimed at contributing toward the application of the proposed nanohybrid biosensor as a reliable, accurate, easy-to-use, portable and cost-effective diagnostic tool. In this regard, for the proof-of-concept, molecular beacon probes were designed to detect synthetic nucleic acid targets proposed in the literature as biomarkers with potential application in medical diagnostics of dengue virus and sleeping sickness (human African trypanosomiasis) infections, and cancer/cardiovascular (or other) diseases (microRNA-145).

For the diagnostic of dengue a synthetic dengue viral RNA sequence from DENV-2 serotype of New Guinea C 44 (position 1008) was chosen as the target.[4] For sleeping sickness, a 17-mer DNA probe of a specific sequence situated within the 18S ribosomal RNA gene of the *Trypanosoma brucei* parasite,[5–8] which belongs to both *T. b. gambiense* (GenBank accession number AJ009141) and *T. b. rhodesiense* (GenBank accession number AJ009142), was used.[8] Detection of a oligonucleotide sequence of miRNA-145 mimics[9–12] was also performed. These sequences are shown in Figure 6.1.

6.2. Design of nanohybrid biosensors for nucleic acids' detection

The DNA hairpin probes were designed to operate by a conformation-induced change in the efficiency of a Förster Resonance Energy Transfer (FRET) process. This change is triggered by the hybridization of a nucleic acid target sequence to the hairpin's loop region that induces conversion from a closed conformation (high FRET, low emission) to an open conformation (low FRET, high emission). The fluorogenic dual-labeled probes involved in FRET are a donor-acceptor pair, in which the donor was chosen to be Atto-647N dye and the acceptor was either Deep Dark Quencher II (hereafter, DDQ II) or QSY™ 21 (hereafter, QSY 21).

The donor and acceptor are linked to separate, partially complementary, single-stranded DNA (ssDNA) sequences that are assembled into the molecular beacon probe: one ssDNA sequence contains the dye Atto-647N (F-Seq) and another ssDNA the quencher (DDQ II or QSY 21) molecule (Q-Seq). These ssDNA spontaneously hybridize and fold to yield the hairpin configuration shown schematically in Figure 6.1A.

The assembled beacons have terminal thiol groups for the attachment onto gold surfaces. A linear segment of 10-bp double-stranded DNA (dsDNA) is used to place the Atto-647N about 4 nm away from the particle surface, in order to avoid metal quenching. Next to this linear segment there is a 4-nt long spacer (CAAG), followed by a stem-and-loop structure. The loop region has a ssDNA sequence complementary to the target sequence. The stem is a 6-bp region rich in C-G pairs to ensure a proper hairpin closure in the absence of target. The acceptor is covalently linked to the 3'-end so that in the closed hairpin conformation it is near the donor.

The molecular beacons' working principle is illustrated in Figure 6.1C, using the example of dengue viral RNA sequence detection. (For the design and closing/opening dynamics of the hairpins used for detection of DNA and miR-145 targets see Figure 6.19 of the Annexes - section 6.9). Briefly, when the hairpin loop is in a closed conformation, fluorescence emission of Atto-647N is strongly quenched by the acceptor moiety. Upon hybridization of a nucleic acid target sequence with the loop region, the hairpin opens and emission from Atto-647N is recovered, thus, signalling the detection event.

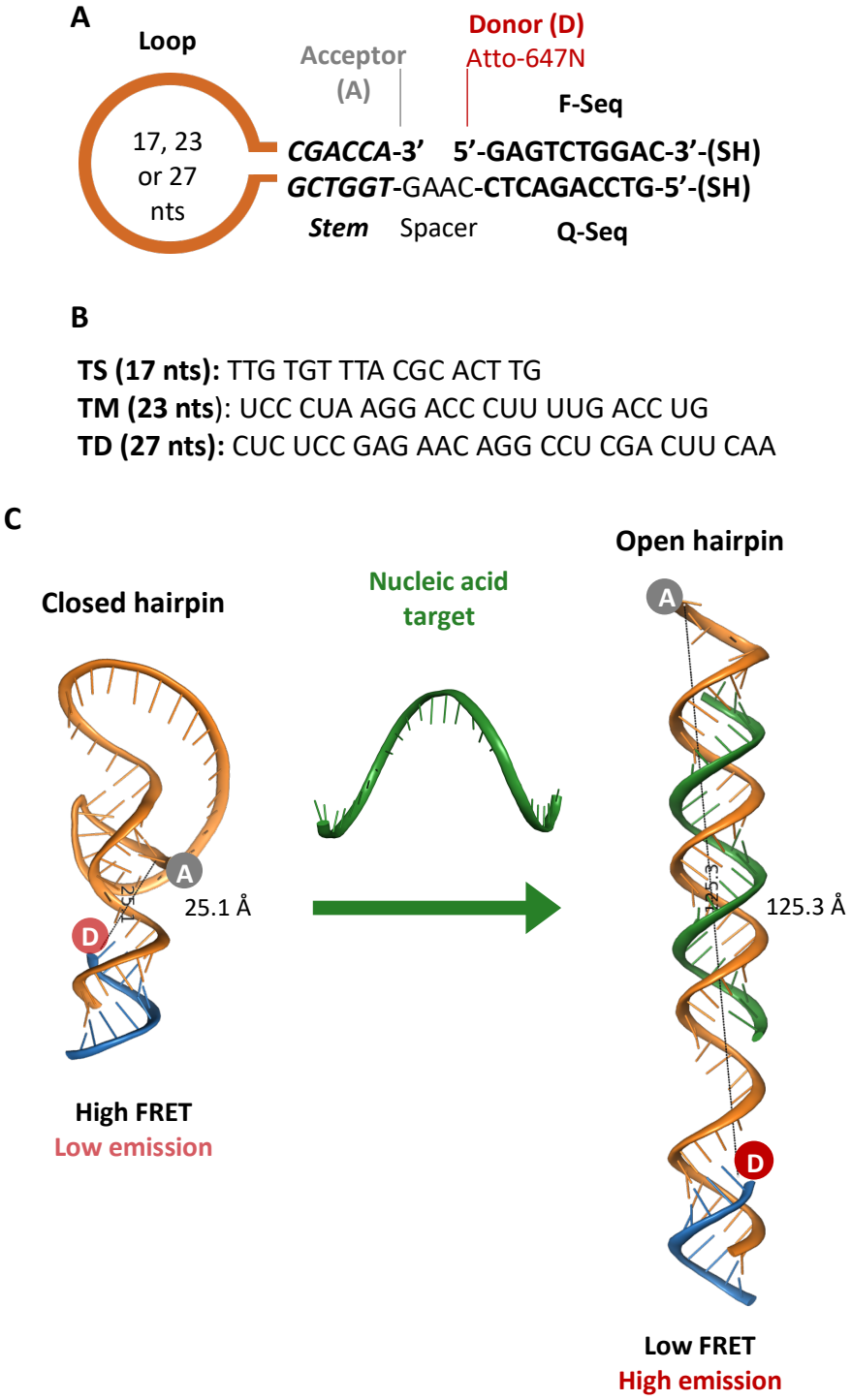

Figure 6.1 - Design of the molecular beacons used for detection of nucleic acids of interest. (A) Scheme of the molecular beacons. The beacon is formed by hybridization of an Atto-647N labeled DNA strand (F-Seq) with another strand labeled with DDQ II or QSY 21 acceptor molecules (Q-Seq). The loop region of the hairpins has 17, 23 or 27 nucleotides (nts), with complementary sequences to selected targets for (B) sleeping sickness (TS), miRNA-145 (TM) and dengue virus (TD), respectively. (B) Representation of an assembled hairpin used for detection of a dengue virus RNA sequence (in green), composed by an Atto-647N donor molecule (red dot) labeled into a ssDNA sequence (in blue, F-Seq) and another ssDNA strand (in orange, Q-Seq) labeled with an acceptor molecule (grey dot). The nucleic acid target sequence is complementary with the loop region of the hairpin. Sensing occurs when the hairpin changes from a closed conformation of high FRET efficiency (or low emission) to an open conformation upon

hybridization of the target with the loop region, resulting in low FRET efficiency and high fluorescence emission.

Atto-647N is a red-emitting dye that is commonly used for labeling DNA molecules in biophysical studies and single-molecule fluorescence experiments.[13–16] This is due to its photophysical properties (high fluorescence quantum yield, Φ_F = 0.65), high thermal and photo stability, and strong absorption.[17] The excitation and emission wavelength maxima, respectively ca. 646 and 664 nm,[17] are also advantageous because of the near-infrared biological window which minimizes interference from sample's auto-fluorescence. In order to assure a good spectral match of the dye-antenna pair, and a slight red-shift of the dye's emission relatively to the longitudinal surface plasmon (LSP) peak wavelength, a gold nanorod with a size of 25 nm × 71 nm (width × length) and a LSP wavelength at 661 nm was chosen for plasmonic antenna.[18]

The distance between the dye and the particle's surface is a crucial parameter because at short distances the gold nanoparticle quenches fluorescence, while at long distances the antenna effect decays rapidly.[19] Previous simulations using the discrete dipole approximation (DDA) method have indicated that for this dye-antenna pair the optimal distance is about 3 to 4 nm away from the gold nanorod's tip (with a colinear emission dipole orientation).[20] As discussed in Chapter 5, the maximum enhancement calculated for this situation corresponds to a 40-fold increase of emission. Thus, the beacon was designed with a 10-bp linear segment (ca. 3.4 nm) between the thiol groups and the position of the dye at the F-Seq.

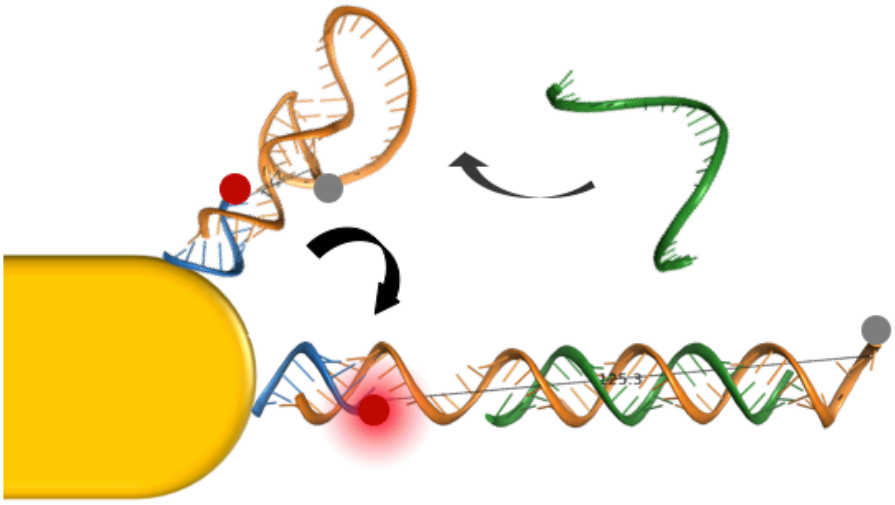

Figure 6.2 - Scheme (not to scale) of the nanohybrid biosensor proposed for the detection of nucleic acids: a gold nanorod is tip-functionalized with fluorescently-labeled hairpin probes that upon target molecular recognition provides increased sensitivity in nucleic acids' detection. This is due to amplification of fluorescence, induced by the plasmonic antenna effect of the gold nanorod over the dye's emission.

DDQ II and QSY 21 are called dark quenchers because they decay from higher electronic states by non-radiative processes (hence are dark).[21] In dark quenchers, a high rate deactivation by internal conversion contributes to a short excited state lifetime. This means that the probability

for other competing relaxation pathways, such as fluorescence, intersystem crossing, and photochemistry is reduced. Hence, when compared to conventional fluorescent acceptors, dark quenchers perform better for FRET experiments in bioassays, because they do not contribute with background fluorescence and, thus, provide greater sensitivity (low signal-to-noise ratio).[21,23-24]

DDQ II is based on 1,4-diaminoanthraquinone chromophore (Figure 6.3A), and it was developed by the group of Tom Brown.[25] It is license-free and it has been used in molecular beacons as a long-wavelength fluorescence quencher because of its absorption maximum at about 630 nm (Figure 6.3B) that provides a broad quenching range between 550-720 nm. Thus, it can efficiently suppress the fluorescence of Atto-647N dye, because of its partial spectral overlap (depicted in grey in Figure 6.3B).

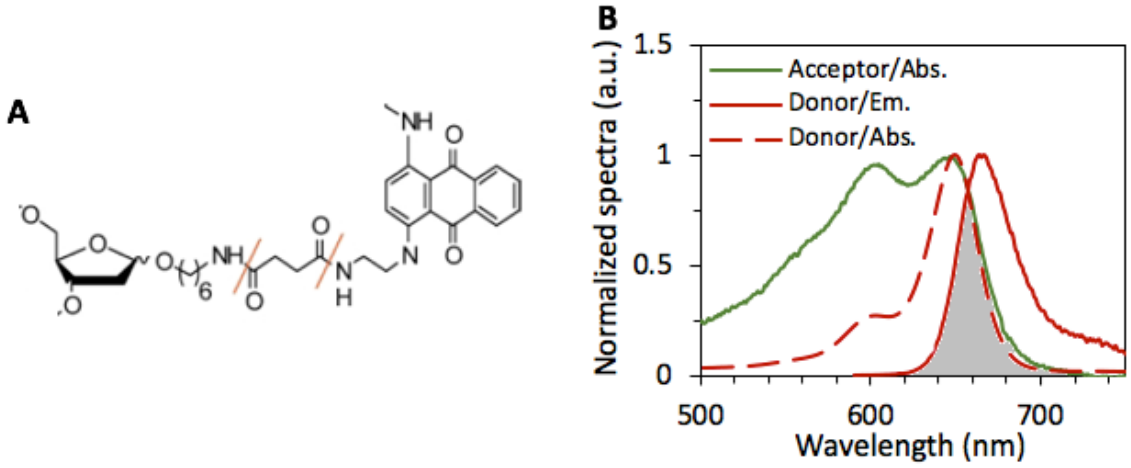

Figure 6.3 - The acceptor molecule DDQ II. (A) Chemical structure.[25] (B) Normalized absorption spectrum (green line) while labeled on a Q-Seq chain and spectral overlap (in grey) between emission of donor Atto-647N (red line) labeled onto F-Seq and absorption of DDQ II.

On the other hand, QSY 21 has a broad and intense absorption range of 540-750 nm[26] with maximum around 660 nm,[27] and therefore has a better overlap with Atto-647N's emission than DDQ II (Figure 6.4B). It consists mainly of two 2,3-dihydro-1-indolyl rings and one benzene ring attached to the central xanthene ring (Figure 6.4A). It is suggested that the intrinsic low fluorescence quantum-yield of QSY 21 (and other QSYs) involves a twisted intramolecular charge transfer state due to free molecular rotation of the bond between the N atom and the xanthene moiety.[28,29] For this reason, it makes an excellent energy acceptor in FRET applications.[30]

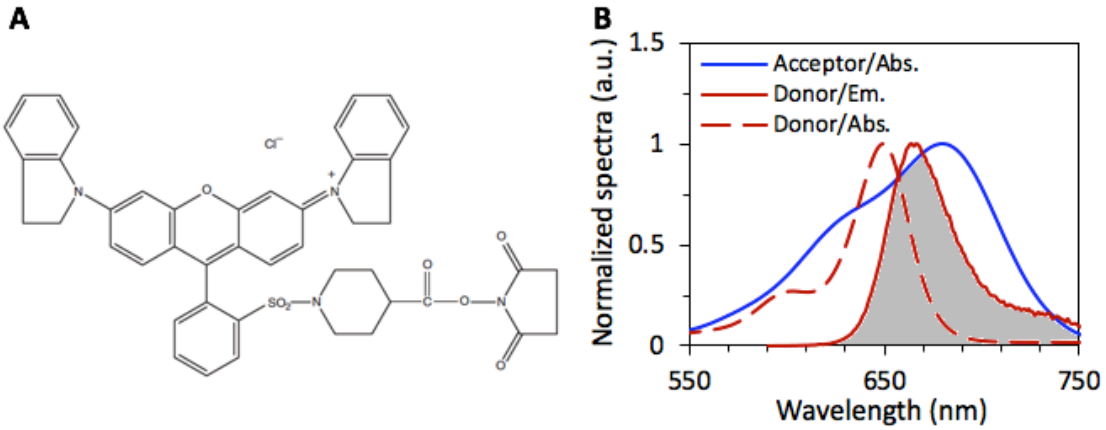

Figure 6.4 - The acceptor molecule QSY 21. (A) Chemical structure.[31] (B) Normalized absorption spectrum (blue line) while labeled on a Q-Seq strand and spectral overlap (in grey) between emission of donor Atto-647N (red line) labeled onto F-Seq and absorption of QSY 21.

Calculations of FRET efficiency (Eq. 6 of Chapter 1) were performed for the above-mentioned donor-acceptor pairs. The spectral overlap integral, a dipole orientation factor of 2/3, the refraction index of water, the normalized emission spectrum and Φ_F of Atto-647N in the absence of acceptors, and the molar absorption coefficient of the acceptors were considered. The calculation of Förster's radius (Eq. 7 of Chapter 1) yielded values of 43 and 70 Å for Atto-647N/DDQ II and Atto-647N/QSY 21, respectively. This means that DDQ II is less efficient than QSY 21 for quenching Atto-647N dye by a FRET process. Nonetheless, the estimated donor-acceptor distances in the closed hairpin configurations are well below the Förster's radius, which should ensure a quenching effect strong enough for fluorescence signalling purposes.

FRET efficiency curves for the donor-acceptor pairs Atto-647N/DDQ II and Atto-647N/QSY 21 are shown in Figure 6.5. The vertical lines depict the estimated donor-acceptor distances in the closed and open hairpin conformations for the several targets.

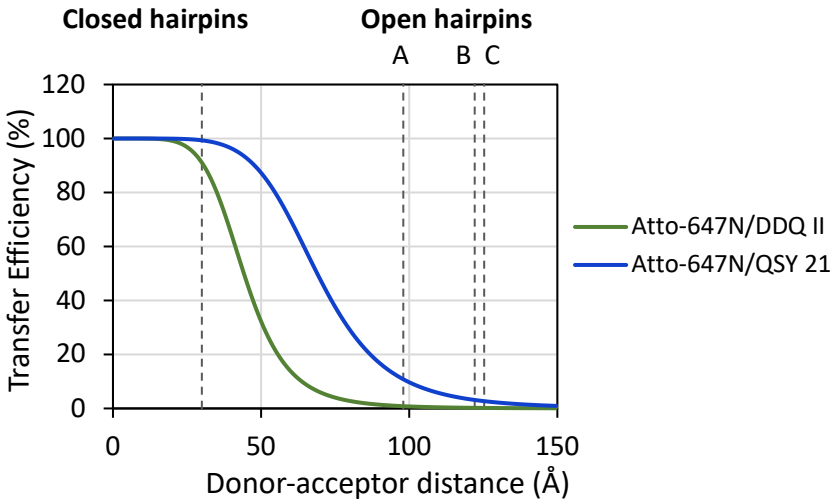

Figure 6.5 - Theoretical energy transfer efficiency curve from Atto-647N dye to acceptors DDQ II (green line) and QSY 21 (blue line). "Closed hairpins" stands for DDQ II- and QSY 21-labeled molecular

beacons in closed conformations, with A, B and C representing open hairpins hybridized with sleeping sickness, miRNA-145 and dengue virus targets, respectively.

Firstly, the estimated distances between the end nucleotides in the closed hairpin is about 30 Å (left vertical dashed line Figure 6.5). In this case, the estimated FRET efficiency is above 90% for DDQ II and almost 100% for QSY 21, which should guarantee a strong quenching effect. On the other hand, open hairpins are expected to have minimal energy transfer efficiencies as a result of dye-quencher separation distances well-above the calculated Förster's radius, thus providing robust fluorescence signalling response. Assuming the schematic structures of beacon-target assemblies represented in Figure 6.1 and in Figure 6.19 of the Annexes, those distances would be around 98, 122 and 125 Å for the beacons used for detection of sleeping sickness, miRNA-145 and dengue virus, respectively.

6.3. Fluorescence signalling of molecular beacons in solution

The functionality of the molecular beacons was first characterized in solution by time-resolved confocal fluorescence microscopy, in order to assess the hairpin closing/opening and the FRET efficiency in response to the respective targets. This technique provides measurements of fluorescence intensity and emission lifetimes with single-molecule sensitivity from a microscopic observation volume inside the sample. The correlation function of fluorescence intensity time-traces, using the technique of Fluorescence Correlation Spectroscopy (FCS), is employed to study fluorescence fluctuations in the microsecond to second timescale. These may arise from translational diffusion or conformational changes in the molecular beacons. The microscope also operates in time-correlated single-photon counting (TCSPC) that provides the sample's fluorescence decay from a single measurement (i.e. simultaneous FCS and TCSPC from a confocal detection volume).

6.3.1. Confocal fluorescence microscopy studies

Firstly, the assembly of molecular beacons through hybridization of F-Seq and Q-Seq strands was studied in phosphate-buffered saline (PBS) buffer. The expected outcome was the suppression of the dye's fluorescence due to a high FRET efficiency with the quencher in the closed hairpin configuration. Afterwards, the target sequences were added to open the beacons, which would restore fluorescence, thereby signalling the molecular detection event. Measurements were executed by placing a droplet of each sample on top of a glass coverslip and acquiring a point trace with the confocal volume centered 10 μm inside the solution.

Initially, the set of molecular beacons labeled with DDQ II were examined. For the sake of simplicity, these beacons were named BD1, BS1 and BM1 according to the respective target being either dengue virus, *T. brucei*, or miR-145. Furthermore, the suffix label no. "1" represents quencher DDQ II and makes a distinction to beacons with QSY 21 that were labeled as no. "2". The results discussed next are focused on the beacon designed for detection of the RNA target

associated with dengue virus. They serve the purpose of illustrating the biosensor strategy developed here, while the remaining examples are illustrative of the versatility of the strategy to detect other nucleic acid targets.

Figure 6.6 shows a set of experimental results (intensity time traces, autocorrelation functions and fluorescence decays) that were acquired for the three situations measured: (i) first, only sequence F-Seq (1 nM) in solution; (ii) after addition of Q-Seq (100 nM) to assemble molecular beacon BD1 and; (iii) finally, after addition of target TD (2 μM) to test the beacon's response (the complete assembly is termed as BD1TD).

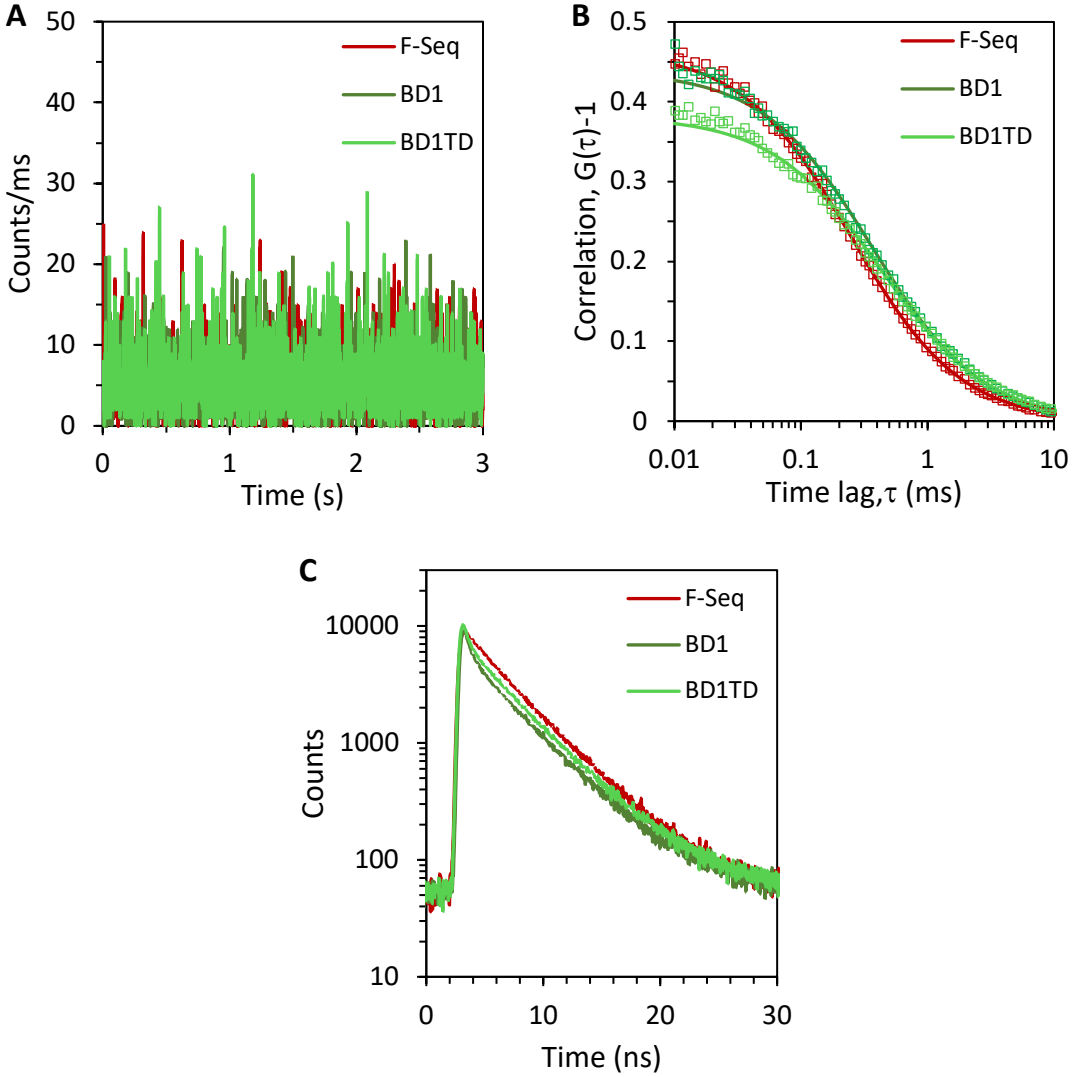

Figure 6.6 - Characterization of the functionality of molecular beacon BD1 in 1× PBS buffer by time-resolved confocal fluorescence microscopy and FCS. For F-Seq (in red, 1 nM), molecular beacon BD1 after addition of Q-Seq for BD1 (in dark green, 100 nM) and beacon response to target TD (in light green, 2 μM) were measured: (A) fluorescence intensity time traces (binning interval of 1 ms), (B) autocorrelation functions and (C) fluorescence decays. All measurements were performed using a laser light excitation of 639 nm.

From the previous set of data, three parameters were initially assessed to evaluate the performance of beacon BD1 (Figure 6.7): (i) diffusion coefficient from fitting the autocorrelation functions with a 3D-Brownian diffusion model for one species;[32] (ii) the mean fluorescence intensity of the sample; (iii) the average fluorescence lifetime from a multi-exponential fitting of the decay curves.

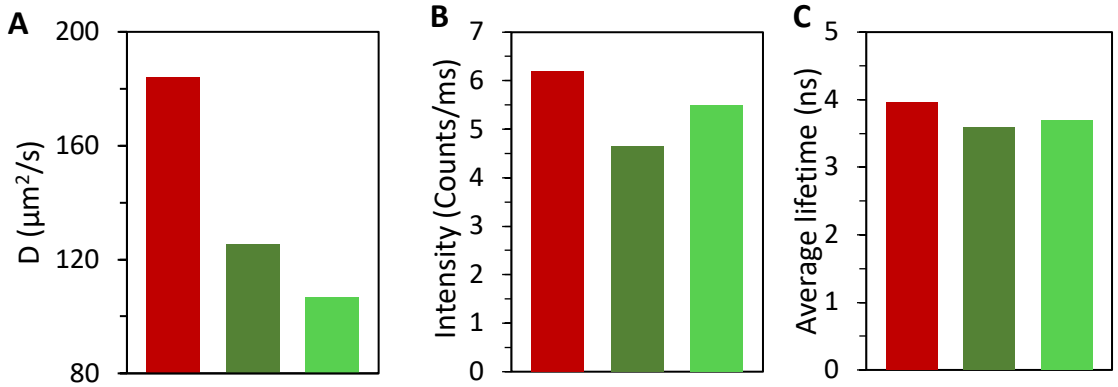

Figure 6.7 - Parameters used to evaluate the functionality of molecular beacon BD1 in aqueous solution. (A) Diffusion coefficients (abbreviated as "D"), (B) mean trace fluorescence intensities and (C) average fluorescence lifetime of F-Seq alone (red columns), then with addition of Q-Seq for BD1 (dark green columns), and later after addition of target TD (light green columns).

The diffusion coefficient decreases with the addition of each component, which is qualitatively the expected result from their sequential assembly, i.e. after the association of each component the hydrodynamic radius of the hybridized conjugates increases, and as a consequence the diffusion coefficient diminishes accordingly to the Stokes-Einstein relation.[33] The average fluorescence intensity and lifetime both decreased when Q-Seq for BD1 was added to F-Seq. This is also the expected result because of the quenching effect of DDQ II on Atto-647N's emission. After addition of target TD, both parameters increase, which qualitatively also corresponds to the expected result since the target's hybridization with the hairpins' loop region should induce its opening. However, the small amplitude of the variations observed in both parameters indicates that the beacon might not be functioning properly. In particular, the fluorescence decay of BD1 displayed a long decay component of significant weight and with a lifetime similar to that of F-Seq alone, which is not in line with the expected FRET efficiency for the closed hairpin conformation. This issue will be further discussed below. An ill-defined closure of the hairpin would not explain why the initial dyes' fluorescence was not totally recovered when the target was added. Although, here the explanation could be that in the open hairpin conformation the dye-quencher distances still allow for FRET to occur, but with a low efficiency due to the long distances (this feature will also be discussed below). The limitations found in BD1's signalling of target RNA were also found for molecular beacons BS1 and BM1 (Table 6.1).

Table 6.1 - Analysis of the functionality of DDQ II-labeled molecular beacons BS1 and BM1 in aqueous solution: diffusion coefficients, fluorescence intensities and average lifetime of F-Seq alone and then after addition of Q-Seq sequences ("BS1" and "BM1") and later following addition of targets ("w/ target").

	Diffusion coef. ($\mu m^2/s$)	Intensity (counts/ms)	Average lifetime (ns)
F-Seq	186.7	6.2	4
BS1	142.6	4.5	3
w/ target	132.8	4.8	3.1
F-Seq	189.5	6.5	4
BM1	123.9	5.3	3.6
w/ target	108.4	6.0	3.8

When analyzing the parameters, beacons BS1 and BM1 followed the same tendencies of BD1 with more or less similar values. Therefore, the earlier final assumptions made regarding the functionality of BD1 can be extrapolated for BS1 and BM1. However, the shorter loop sequence in BS1 seems to play a role in the retrieved value for the diffusion coefficient, which is larger than BD1 or BM1 that are similar in their sizes. Also, the decrease on the average fluorescence lifetime and intensity was more expressive for BS1 relatively to BM1 or BD1. This can be tentatively attributed to either a higher fraction of closed BS1 hairpins, or to shorter donor-acceptor distances in the open hairpin conformations, when compared to BM1 and BD1, thus increasing FRET efficiency.

Next, the fluorescence decays were analyzed in more detail from the values of lifetimes and amplitudes of a multi-exponential fitted curve (Table 6.2).

Table 6.2 - Fluorescence lifetimes (τ_i) and amplitudes (A_i) obtained from decay curve's fitting for DDQ II-labeled molecular beacons (BD1, BS1 and BM1) and beacon-target assemblies ("w/ target"). Concentrations of F-Seq, Q-Seq and targets were 1 nM, 100 nM and 2 μM, respectively, in 1× PBS.

	A_1	τ_1 (ns)	A_2	τ_2 (ns)	A_3	τ_3 (ns)	χ^2
BD1	0.64	4.20	0.27	1.14	0.09	0.21	1.06
w/ target	0.62	4.25	0.31	1.42	0.07	0.23	0.97
BS1	0.79	4.07	0.14	1.10	0.07	0.22	0.996
w/ target	0.79	4.16	0.14	1.34	0.07	0.23	1.01
BM1	0.65	4.25	0.28	1.51	0.07	0.23	1.07
w/ target	0.63	4.28	0.30	1.46	0.07	0.20	1.11

Two parameters were used for evaluation of the functionality of DDQ II-labeled beacons: their unquenched fraction and their quenching efficiency (also in the presence of target sequences), as indicated in Table 6.3. The first parameter was calculated assuming that the long decay component is due to Atto-647N dye that for some reason is not quenched and, thus, emits

with the intrinsic decay time of F-Seq. Initially, the hypotheses considered for this abnormal fraction of unquenched dyes was either: i) F-Seq not hybridized with Q-Seq or; ii) hybridized, but in an open hairpin conformation or; iii) hybridized, but with a non-labeled (defective) Q-Seq or; (iv) free Atto-647N due to mislabeling of F-Seq. As discussed later, it was found that hypothesis ii) explains better the full set of experimental results. The unquenched fraction was then calculated from the area of the long decay component ($I_{un} = A_1 \times \tau_1$) divided by the decay curve area of F-Seq sample without Q-Seq ($I_0 = A_0 \times \tau_0$), both registered for the same acquisition time. As for the quenching efficiency, it was calculated assuming that the short decay components in the beacon samples correspond to emission from Atto-647N dyes that are effectively quenched by FRET, here tentatively attributed to closed hairpins. The usual formula for FRET efficiency calculated from emission lifetimes ($\phi_{ET} = 1 - \tau_{av}/\tau_0$) was used, but here considering an average of the short decay components: $\tau_{av} = \Sigma_{i=2,3} A_i \tau_i / \Sigma_{i=2,3} A_i$.

Table 6.3 - Fraction of unquenched molecular beacons BD1, BS1 and BM1, and their quenching energy transfer efficiency (also in the presence of the respective targets - "w/ target").

	Fraction unquenched, I_{un}/I_0 (%)	**Quenching efficiency, ϕ_{ET} (%)**
BD1	62.6	92
w/ target	-	92
BS1	51.9	93
w/ target	-	92
BM1	70.5	91
w/ target	-	92

The fractions of unquenched beacons were significantly high, between 51.9-70.5%, meaning that the majority of Atto-647N molecules present in solution were still emissive. The most plausible interpretation for this lack of quenching of Atto-647N relies on insufficiently closed hairpins, hence limiting FRET efficiency. Other possible explanations were also scrutinized, such as contamination with free Atto-647N dye, Q-Seq strands mis-labeled and/or free F-Seq strands that did not hybridize with Q-Seq. The first hypothesis can be dismissed because if there was a significant fraction of free dye, then the FCS curves would in principle show a clear evidence of a bi-modal distribution of emitters due to the difference in diffusion times between free and labeled species. The second hypothesis can also be dismissed because absorption spectra allowed for quantification of quencher and DNA contents in the Q-Seq sequences. These corresponded to stoichiometric ratios of 1.1, 0.9 and 1.2 DDQ II molecules per DNA chain for Q-Seq for BD1, Q-Seq for BS1 and Q-Seq for BM1, respectively. These results confirm that the amount of quencher-labeling is as expected relatively to the oligonucleotide content. The third hypothesis was investigated with a titration type of assay, as described below.

The lower unquenched fraction of BS1 beacons relatively to BD1 and BM1 may be due to the hairpin's length (BS1 has a loop region with 17 nucleotides when compared to 23 in BM1 and 27 in BD1). This feature was tentatively attributed to a better loop closure provided by more stable conformations within hairpins or even by secondary structures in ill-defined loops. In this regard, possible secondary structures using the OligoAnalyzer Tool of Integrated DNA Technologies (IDT), Inc. (https://eu.idtdna.com/calc/analyzer, considering oligonucleotide and salt (Na^+) concentrations of 100 nM and 137 mM, respectively) were predicted. The tool rendered 7 structures for Q-Seq for BS hairpin sequences when compared to 10 and 17 for Q-Seq for BD and Q-Seq for BM, respectively. A greater probability for partial and aleatory complementarities within the loop is expected for longer chains. However, the relative stability of these secondary structures within the complex conformational landscape of these hairpins must also be considered.

In general, quenching efficiency was above 90% for all beacons (Table 6.3), which is considerably high. This means that FRET efficiency of the Atto-647N/DDQ II pair should be sufficient to allow for a low emission state if closed hairpins would be the dominant fraction in the absence of target. Yet, this was not confirmed experimentally and the insignificant changes in quenching efficiency after addition of target further compromised the functionality of the beacon.

6.3.1.1. Signalling response of QSY 21-labeled molecular beacons

The first strategy to increase the signalling response was to replace DDQ II for QSY 21 as dark quencher of the beacons. Although, this was later proven to be a misleading approach (due to ill-defined hairpin closure), it was expected that by replacing the quencher for QSY 21 this would afford a larger Förster's radius. Hence, it would result in an improved quenching efficiency by FRET. The results on molecular beacons labeled with QSY 21 (BD2, BS2 and BM2) are described hereafter.

Primarily, the hybridization between the two components of molecular beacon BD2 was followed by performing a titration assay. The concentration of F-Seq was kept constant at 1 nM and the concentration of Q-Seq was increased from 1 up to 200 nM.

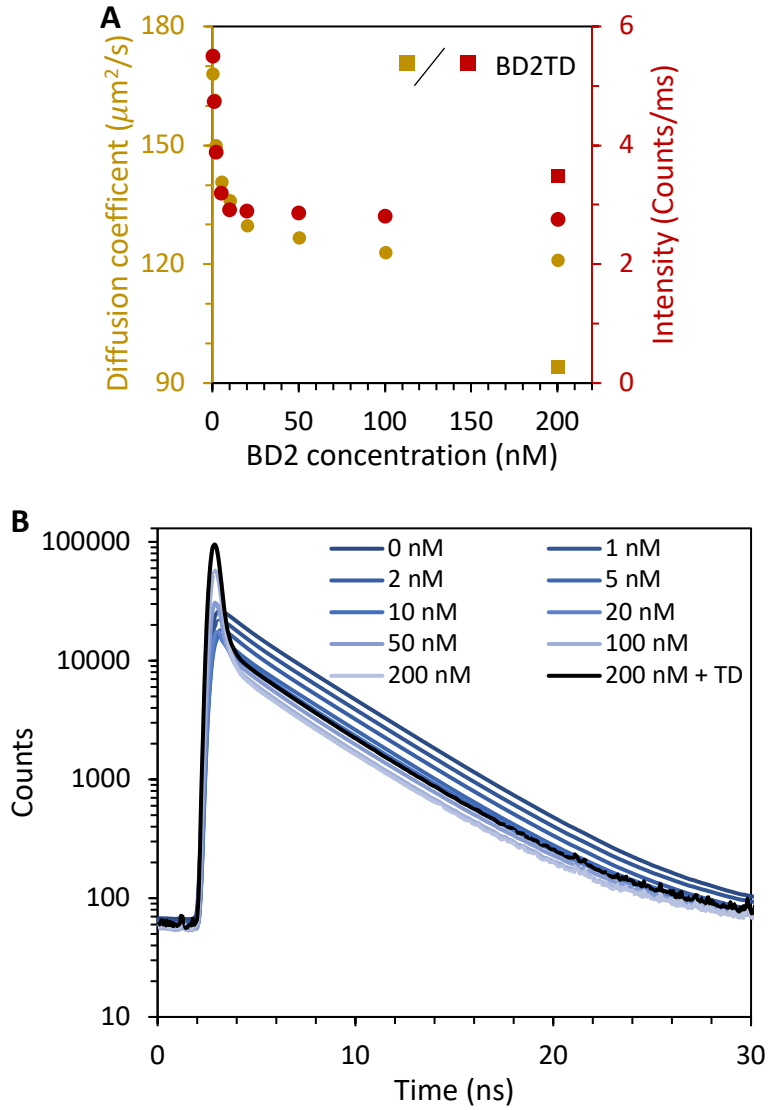

Figure 6.8 - Fluorescence titration of molecular beacon BD2 in 1× PBS buffer performed using confocal fluorescence microscopy with single-molecule sensitivity. The concentration of F-Seq was fixed at 1 nM while increasing Q-Seq for BD2 concentration from 1 to 200 nM, followed by addition of target TD. (A) Diffusion coefficients (in orange) obtained from autocorrelation functions and average fluorescence intensities (in red) from histograms. The addition of target TD (2 μM) is represented by squares ("BD2TD"). (B) Fluorescence decay fitted curves for F-Seq (dark blue), increasing concentrations of Q-Seq for BD2 (all other blue lines), and addition of TD (black line). Values correspond to the average of three consecutive measurements performed with a laser excitation at 639 nm using a power of 12 kW/cm².

The titration assay showed the association of the F-Seq and Q-Seq from the gradual decrease in the diffusion coefficient and also in the average emission intensity, which stabilizes at excess Q-Seq concentrations (Figure 6.8A). One interesting behaviour of this beacon was that the intensity's decrease for 100 nM of Q-Seq (from 5.5 to 2.8) was more expressive than that obtained in the previous BD1 beacon (from 5 to 4.7 counts/ms). As expected, FRET efficiency of the Atto-647N/QSY 21 pair was more pronounced than for the Atto-647N/DDQ II pair. However, the fluorescence decays show that even in the limit of complete hybridization of F-Seq

with Q-Seq, there is a long decay component with a reasonable weight (Figure 6.8B) that indicates a significant fraction of unquenched dye. This result suggests that also in this case there is a condition of ill-defined closure that affects the beacon performance. Furthermore, the fluorescence recovery after target addition (2 μM) was quite similar to the one verified when testing beacon BD1 (square symbols). This possibly demonstrates that, as before, there is a residual quenching effect in the open hairpin conformations.

The apparent association constant, *Ka*, for the hybridization between F-Seq and Q-Seq for BD2 sequences was determined following Ref. 34. It was assumed a 1:1 bimolecular interaction for the hybrid formation and the diffusion coefficients of free and bound species (Figure 6.8A) were used. A value of 3.0×10^8 M^{-1} was obtained for *Ka*, which is comparable to other reported values of binding constants for oligonucleotides of similar length.[35]

Figure 6.9 shows the same set of experimental results as Figure 6.6, but for molecular beacon BD2 and the response to its target RNA. For beacons BS2 and BM2 the same assays were also performed (data is not shown here).

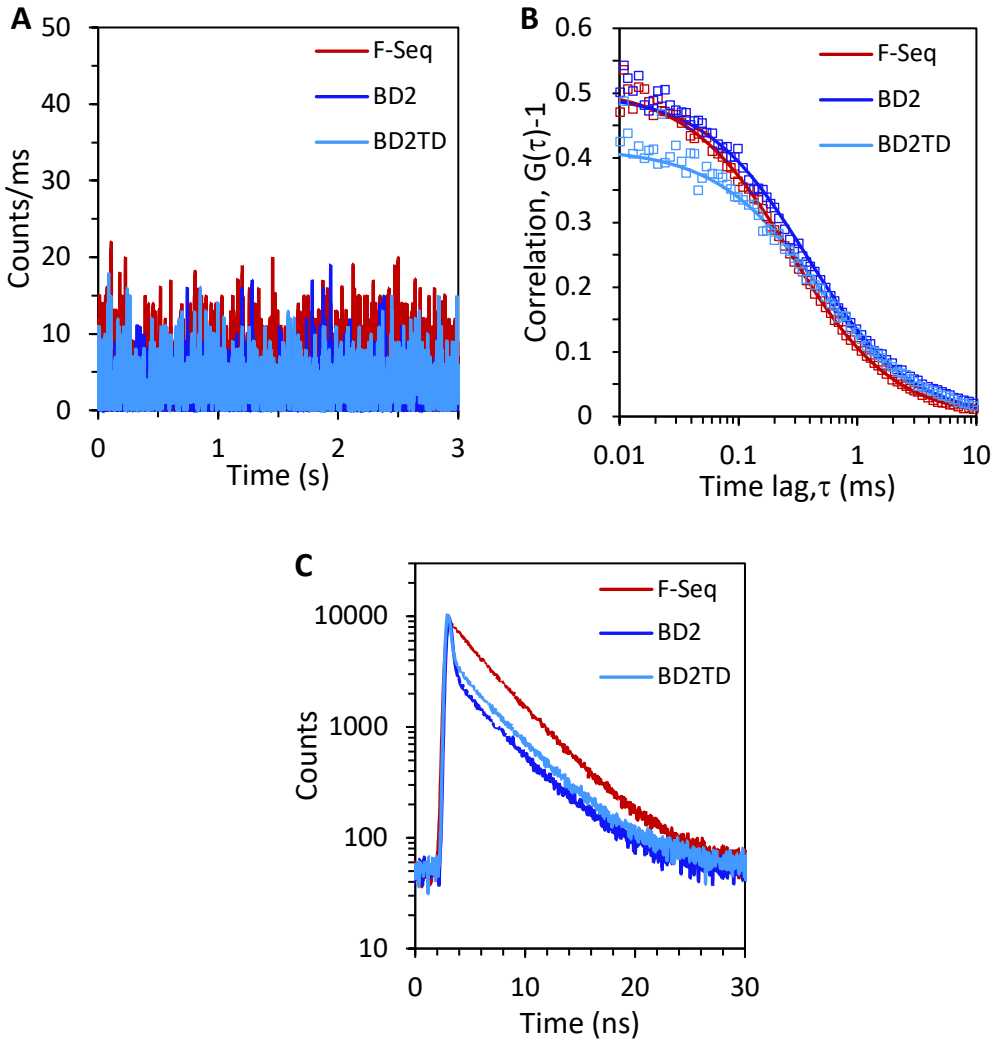

Figure 6.9 - Characterization of the functionality of molecular beacon BD2 in 1× PBS buffer by time-resolved confocal fluorescence microscopy and FCS. (A) Fluorescence intensity time traces (binning

interval of 1 ms), (B) autocorrelation functions and (C) fluorescence decays for F-Seq (in red, 1 nM), beacon BD2 after addition of the respective Q-Seq (in dark blue, 100 nM), and beacon response to target TD (in light blue, 2 μM). All measurements were performed using a laser light excitation of 639 nm.

From the preceding data, the same parameters of diffusion coefficient, average emission intensity and fluorescence lifetime were extracted to evaluate the functionality of the beacon BD2 (Figure 6.10).

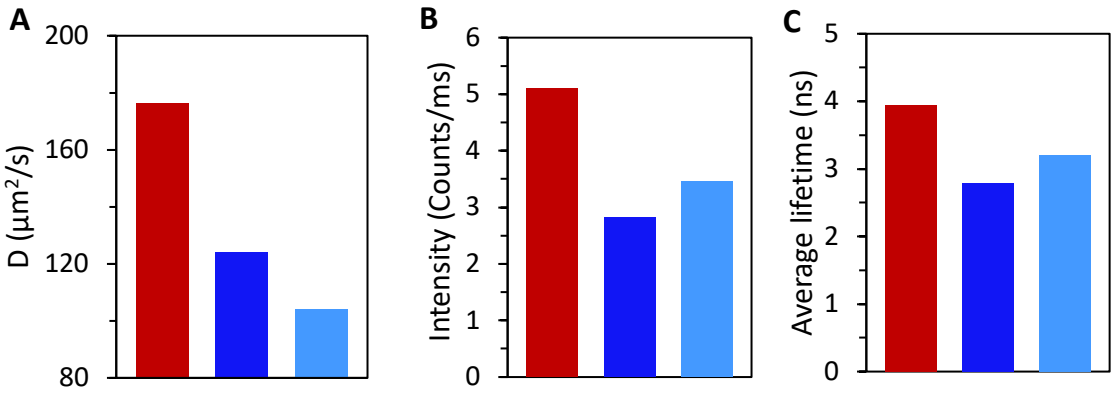

Figure 6.10 - Parameters used to evaluate the functionality of molecular beacon BD2 in aqueous solution. (A) Diffusion coefficients (abbreviated as "D"), (B) mean trace fluorescence intensities and (C) average lifetime of F-Seq *per se* (red columns), then following addition of Q-Seq for BD2 (dark blue columns), and later after addition of target TD (light blue columns).

The diffusion coefficients for the several hybrid species (BD2 alone and hybridized to target) coincide with the previous values obtained for BD1. This result is consistent because the nucleic acid sequences are exactly the same, only the quencher was changed. In turn, fluorescence lifetime and intensity displayed a qualitative behavior similar to that previously observed. However, the original dyes' fluorescence intensity was quenched down to 55% after addition of Q-Seq for BD2, a much larger effect than the previous value of 76% for BD1. As for the second step, the dyes' emission recovery after target addition is much higher than for BD1, which corresponds to a larger signalling response. Undeniably, signalling was enhanced owing to a better contrast between the low and high emission states (although far from what was originally planned). The influence of the larger Forster's radius of the donor-acceptor pair with QSY 21 played a definite role here.

Generally, these results on beacon BD2 confirm its assembly and recognition of the RNA target, with relevant improvements when compared to BD1. The same improvement was also found for beacons BS2 and BM2 (Table 6.4).

Table 6.4 - Parameters used to evaluate the functionality of QSY 21-labeled molecular beacons BS2 and BM2 in aqueous solution: diffusion coefficients, fluorescence intensities and average lifetime of F-Seq alone, following addition of Q-Seq sequences ("BS2" and "BM2") and then after addition of targets ("w/ target").

	Diffusion coef. ($\mu m^2/s$)	Intensity (counts/ms)	Average lifetime (ns)
F-Seq	174.6	5.1	4.0
BS2	163.1	2.9	2.5
w/ target	143.8	2.9	2.5
F-Seq	176.5	4.4	4.0
BM2	123.1	3.3	2.7
w/ target	110.9	3.7	3.1

The fluorescence decays were further analyzed by retrieving the values of lifetimes and amplitudes of short and long components from multi-exponential fittings (Table 6.5).

Table 6.5 - Fluorescence lifetimes (τ_i) and amplitudes (A_i) obtained from decay curve's fitting for QSY 21-labeled molecular beacons (BD2, BS2 and BM2) and beacon-target assemblies ("w/ target"). Concentrations of F-Seq, Q-Seq and targets were 1 nM, 100 nM and 2 μM, respectively, in 1× PBS.

	A_1	τ_1 (ns)	A_2	τ_2 (ns)	A_3	τ_3 (ns)	χ^2
BD2	0.95	4.14	0.04	1.48	0.01	0.09	1.12
w/ target	0.91	4.04	0.08	1.54	0.01	0.09	1.04
BS2	0.98	4.28	0.02	2.42	0.01	0.05	1.16
w/ target	0.97	4.22	0.02	2.62	0.01	0.07	1.17
BM2	0.96	4.32	0.03	2.40	0.01	0.08	1.13
w/ target	0.89	4.38	0.07	2.79	0.04	0.12	1.16

As before, the fraction of unquenched beacons and their quenching efficiency (and for beacon-target assemblies) were also evaluated (Table 6.6).

Table 6.6 - Fraction unquenched of molecular beacons BD2, BS2 and BM2, and quenching energy transfer efficiency for the same beacons (also in the presence of the respective targets - "w/ target").

	Fraction unquenched, I_{un}/I_0 (%)	Quenching efficiency, ϕ_{ET} (%)
BD2	30.5	97
w/ target	-	97
BS2	25.1	98
w/ target	-	98
BM2	39.1	97
w/ target	-	94

The fractions of unquenched beacons between 25.1-39.1% were still high, but significantly lower than when testing DDQ II as quencher. These results were again in contradiction to the initial purpose of a low emission state of the beacons, thus, supporting the hypotheses made about the incomplete closing of hairpins. Indeed, the same nucleic acid sequences are used for the series with QSY 21. Therefore, it is expectable that these beacons would suffer from the same issues of incorrect stem closure, as it seems to be the case.

The quenching efficiency, as calculated from the short decay components only (Table 6.6), was very high and close to 100% for all beacons, and increased when compared to beacons labeled with DDQ II. This result can be explained by the larger Förster's radius of Atto-647N/QSY 21 pair - 70 Å compared to 43 Å for Atto-647N/DDQ II. The results are also in agreement with the theoretical energy transfer efficiencies (Figure 6.5), that showed that in the closed hairpin conformation the FRET efficiency is above 90% for DDQ II and almost 100% for QSY 21.

Considering the estimated melting temperatures (T_m) of 43.9, 47.8 and 56.3 ºC for beacons BM, BD and BS, respectively, theoretically the hairpins should be closed at the room temperature (~25 ºC) at which the studies were performed. In the presence of the targets, T_m's of the open hairpins are 67.5, 72 and 57.3 ºC, thus, also at room temperature, the beacons should be hybridized with the targets, as planned. So, the issues found with the beacons' performance could have not been anticipated on the basis of T_m estimates. Nevertheless, the models for calculating the T_m are based on approximations that can have its limitations. Besides, the beacons were designed with terminal quenchers, dyes and thiols, thus being more complex than the sequences considered in the calculations (OligoAnalyzer Tool considering oligonucleotide and salt (Na^+) concentrations of 1 μM and 137 mM, respectively).

Molecular beacons labeled with QSY 21 showed a slightly better performance in aqueous solution than DDQ II-labeled probes. Yet, since all beacons still revealed some limitations on the closing/opening response and on fluorescence signalling of targets, a deeper complementary study was performed by conventional fluorescence spectroscopy (see section 6.9.3 of Annexes for more details). These results were part of the master thesis of Inês Silva,[36] which joined this project at the host laboratory during the last year of this doctoral thesis. Briefly, results indicated that QSY 21-labeled beacons are more efficient in quenching Atto-647N's emission than the ones with DDQ II, in agreement with the studies discussed in this section. Also, in both series "1" and "2" of the beacons, upon addition of target sequences, the increase in the quantum yield was remarkably low (between 2 to 5%). This lack of response confirms the previously mentioned limitations of all beacons in respect to their closing/opening transition in signalling target detection.

Nevertheless, the perspective that the plasmon near-field effect on the FRET efficiency could improve the contrast between the "on" and "off" states, prompted to test the beacons' conjugated onto plasmonic nanoparticles, as described next.

6.4. Functionalization of molecular beacons onto gold nanorods

This section is dedicated to the conjugation of beacon probes onto gold nanorods to create nanohybrids for plasmon-enhanced fluorescence signalling of nucleic acids. The experience gathered on tip-selective (tip) and non-selective (NS) functionalization protocols, as described in Chapter 5,[20] was employed here to load the beacons onto the nanorods. Unfortunately, the implementation of a tip-functionalization protocol for beacons led to irreversible aggregation of nanorods, as visually observed by the color change of nanorod suspensions from green to grey/transparent. The aggregation is tentatively attributed to a charge compensation between the negative hairpins and the positive CTAB bilayer that is present in the nanorods' corona, which possibly compromises the colloidal stabilization by electrostatic repulsion. To overcome this drawback, NS-functionalization was performed instead.

The experimental procedures used for NS-functionalization of beacons into nanorods were the same as those presented in Chapter 5: a two-step ligand exchange, in which CTAB was first replaced by thiolated mPEG-SH molecules, and then by the beacons.[20] The results presented here are for the conjugation of BD2 onto nanorods. The resulting nanohybrid particles, hereafter named NRs-BD2, were characterized by optical spectroscopy, as presented in Figure 6.11.

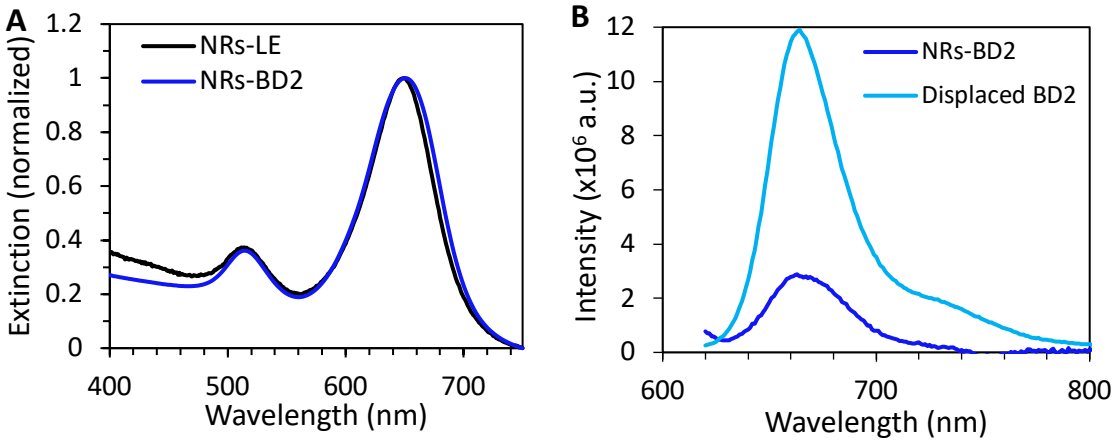

Figure 6.11 - Non-selective functionalization of BD2 onto gold nanorods. (A) Extinction spectra of nanorods after ligand exchange (black curve) and after functionalization with BD2 (dark blue curve). (B) Emission spectra of nanohybrids (dark blue curve) and BD2 displaced from the same sample (light blue curve), both measured at an excitation wavelength of 600 nm. The displacement of BD2 into solution was performed by ligand exchange with 2-mercaptoethanol (20 mM).[37]

After conjugation of BD2 to PEG-coated nanorods (NRs-LE), the LSP peaks shifted about 3 nm (Figure 6.11A). This value indicates a change in the refraction index of the nanorods' environment that was induced by the DNA coating layer and thus supports the notion that NS-functionalization was achieved.

Steady-state fluorescence measurements (Figure 6.11B) were also performed on NRs-BD2, for the evaluation of its emission properties and to assess the number of functionalized strands in each nanorod. The latter quantification was performed by using a ligand exchange procedure

with 2-mercaptoethanol, as previously described.[37] The fluorescence of the displaced beacons in solution was much higher than that of the nanohybrids, which indicates that the dye's emission is quenched in the nanohybrids. However, the fluorescence intensity of NRs-BD2 shows that there is still a significant emission. This is probably because hairpins are not entirely closed when loaded into the particles, so that the quenching mechanism by FRET is not effective.

Regarding the quantification of BD2 strands loaded into each nanorod, a value of 255 strands per rod was obtained. This number was higher than the 170 DNA hybrid chains attached per rod obtained in Chapter 5 using the same incubation time (1 h) and loading ratio (4000).[20] Since a molecular beacon in closed hairpin conformation is more voluminous than the previously studied DNA hybrid, one would anticipate that the loading on the particle's surface would be inferior because of higher steric hindrance. However, the larger loading attained in these nanohybrids may also reflect the attachment of open hairpins to the rods' surface, hence resulting in a stretched-out sequence with lesser steric hindrance.

The nanohybrids were tested in colloidal solution to evaluate their emission response to the target RNA (TD), as investigated by fluorescence correlation spectroscopy (Figure 6.12). They were first diluted in sub-nM concentrations in PBST buffer (mixture of 1× PBS with Tween 20, 0.01 wt %).

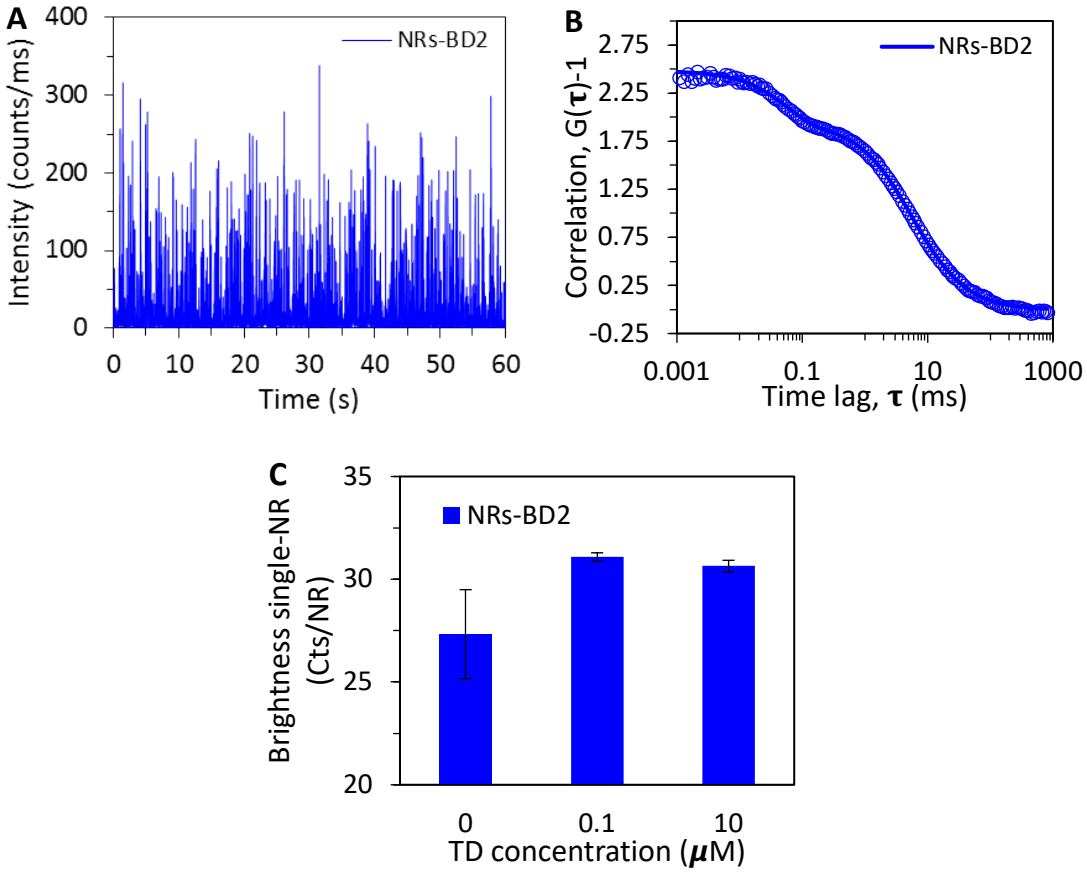

Figure 6.12 - Evaluation at the single-particle detection level of nanohybrids formed by BD2 NS-functionalized onto gold nanorods by FCS measurements. (A) Fluorescence intensity time trace

(binning interval of 1 ms) and (B) fluorescence autocorrelation function. (C) Test in aqueous solution (PBST buffer) of the fluorescence response of colloidal single nanohybrids for target TD concentrations of 0.1 and 10 μM after 30 minutes of exposure to particles. Values and error bars represent respectively the average and standard deviation of three consecutive measurements. A laser excitation of 639 nm with a power of ca. 0.04 kW/cm^2 was used in all measurements.

The emission intensity time trace of the nanohybrids shows intense and regular fluorescence burst events with maximum photon detection rates in the order of hundreds of counts per ms. The autocorrelation function obtained from this intensity trace shows two relaxation components. These are attributed to the rotational and translational diffusion motions of the nanohybrids in colloidal suspension, as also reported in the work of Chapter 5.[20] In addition, for the long relaxation, a diffusion coefficient of 7.7 μm/s^2 was obtained, which corresponds to the value theoretically estimated, 8.0 μm^2/s, using a modified version of Einstein-Smoluchowski relation for a rod-like particle with the size assumed for the nanohybrids.

In order to evaluate fluorescence signalling of the nanohybrids in response to target RNA, three consecutive measurements were performed, before and after addition of 100 nM and then 10 μM of TD. Next, the analysis of the autocorrelation curves provided an estimate of the average occupation number of nanohybrids in the confocal volume. This was combined with the mean trace intensities to determine the brightness of a single nanorod, which is considered a sample average for single-particle emission. The observed increment of 14% in the brightness of these nanohybrids when exposed to 100 nM of target is suggestive of fluorescence signalling. This response was not further improved with higher concentration of target (10 μM), which reflects the fact that the beacons at the particles' surface were probably saturated at 100 nM concentration.

The RNA target detection was also compared to previous biosensing assays based on the beacon alone (section 6.3). The response to the target in this case had an increase of about 9% on the brightness of a single dye molecule, but when BD2 was conjugated to the nanorods, the nanohybrids showed an increment of 14%. This slight increase is still far from the intended performance for the nanohybrid sensors.

Therefore, and to sum up, under the experimental conditions tested, the limited biosensor response of non-selectively functionalized gold nanorods with BD2, as well as the unsuccessful tip-functionalization results, have encouraged a change in strategy that led to the design of a new hairpin probe, as described below.

6.5. Novel hairpin probe designed for detection of dengue viral RNA

The newly designed hairpin DNA probe is also labeled with Atto-647N dye, but uses the gold nanorod as an energy acceptor instead of an organic molecule (such as a dark quencher). This 39-nucleotide probe, hereafter named HD, is composed of a 6-bp stem with a loop region of 27-nt complementary to the dengue viral RNA target (Figure 6.13). The HD beacon is modified with a thioctic acid (a heterocyclic thia fatty acid comprising pentanoic acid with a

1,2-dithiolan-3-yl group at the 5-position) at the 5' end. This could guarantee a comparable covalent attachment to the nanorod's surface relatively to the two thiol groups of the previous beacons. The Atto-647N dye is labeled at the 3' end for deliberate placement in close proximity to the nanorod's surface, thus, enabling metal quenching to provide an "off" state.[19] When the RNA target sequence hybridizes with the loop region of the hairpin, the subsequent opening of the conformation reestablishes the dye's emission, thus providing an "on" state (Figure 6.13B).

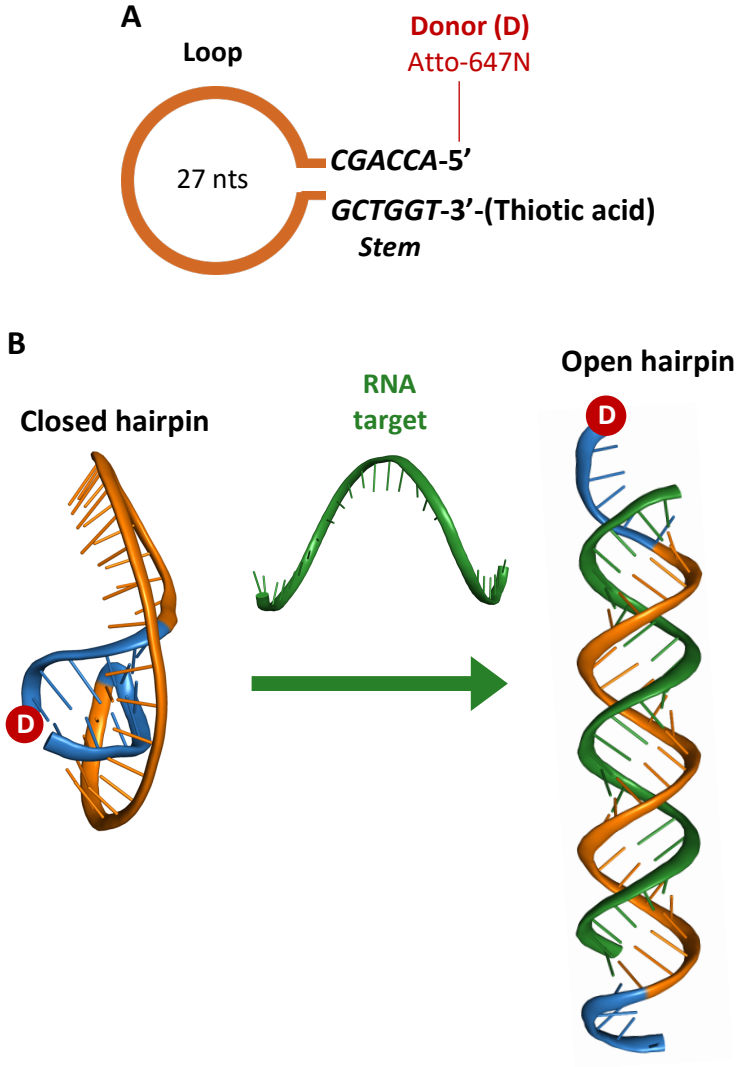

Figure 6.13 - Scheme of the design of the novel hairpin probe HD envisioned for the detection of dengue viral RNA sequences. (A) The probe is modified with an Atto-647N dye labeled on the 3' end and a thiotic acid moiety on the 5' end. The loop region of the hairpin has 27 nucleotides in order to hybridize with the RNA target. The 6 nts at both ends of the probe are complementary and fold spontaneously forming the stem that closes the hairpin. (B) Representation of the hairpin (in orange) labeled with an Atto-647N donor molecule (red dot). The blue regions are the nucleotides that form the stem closing the hairpin. The RNA target sequence (in green) is complementary with the loop region of the hairpin and when their hybridization occurs the hairpin changes from a closed conformation to an open conformation.

The conjugation of the hairpin probe with gold nanorods to form nanohybrid biosensors is schematically represented in Figure 6.14. The objective here was to achieve plasmon-enhanced fluorescence signalling of biomolecular detection events and provide high sensitivity in nucleic acid biosensing responses.

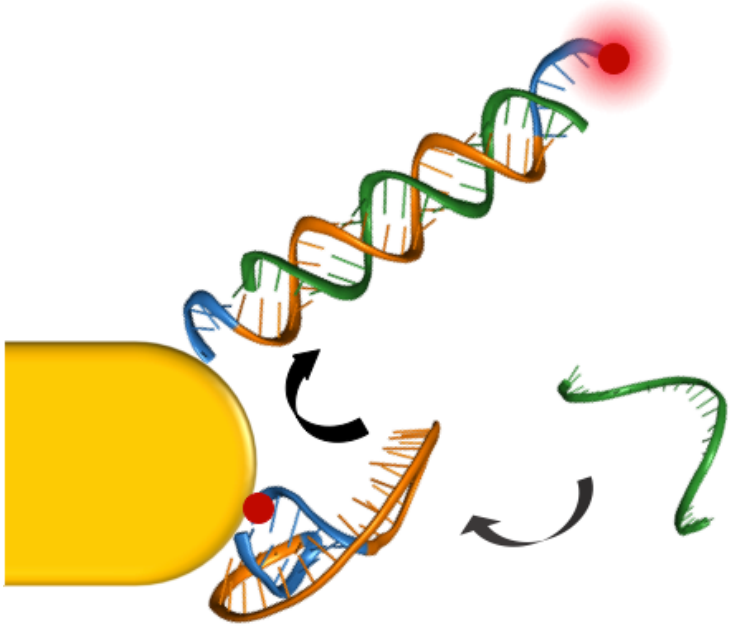

Figure 6.14 - Scheme (not-to-scale) of the newly proposed nanohybrid biosensor for the detection of dengue viral RNA: a gold nanorod is tip-functionalized with fluorescently-labeled hairpin probes that in a closed conformation allow the proximity of the dye (red dot) to the nanorod's surface for quenching of fluorescence, as the nanorod acts as an energy acceptor.

6.5.1. Functionalization of HD onto gold nanorods and sensing response in aqueous solutions

Prior to functionalization, the novel HD hairpin probe was studied by performing an optical spectroscopic characterization and by determining the fluorescence quantum yield (see Figure 6.21 and Table 6.14 of the Annexes). The possible secondary structures and the melting temperature of HD are shown in Table 6.15 of the Annexes.

Tip-selective and NS-functionalization (for comparison purposes) were used to conjugate the HD hairpin probe onto gold nanorods in colloidal suspension following the protocols described in Chapter 5.[20] Stable particles were obtained with both approaches, as characterized by the extinction spectra in Figure 6.15A and B. This constituted a major progress relatively to the previous conjugations with the molecular beacons that, in most cases, resulted in rod aggregation. It was shown in the literature that oligonucleotides with a thioctic acid moiety functionalized onto gold nanoparticles provided higher loadings and higher stability (in the presence of thiols from dithiothreitol) than particles prepared with oligonucleotides carrying a single thiol.[39]

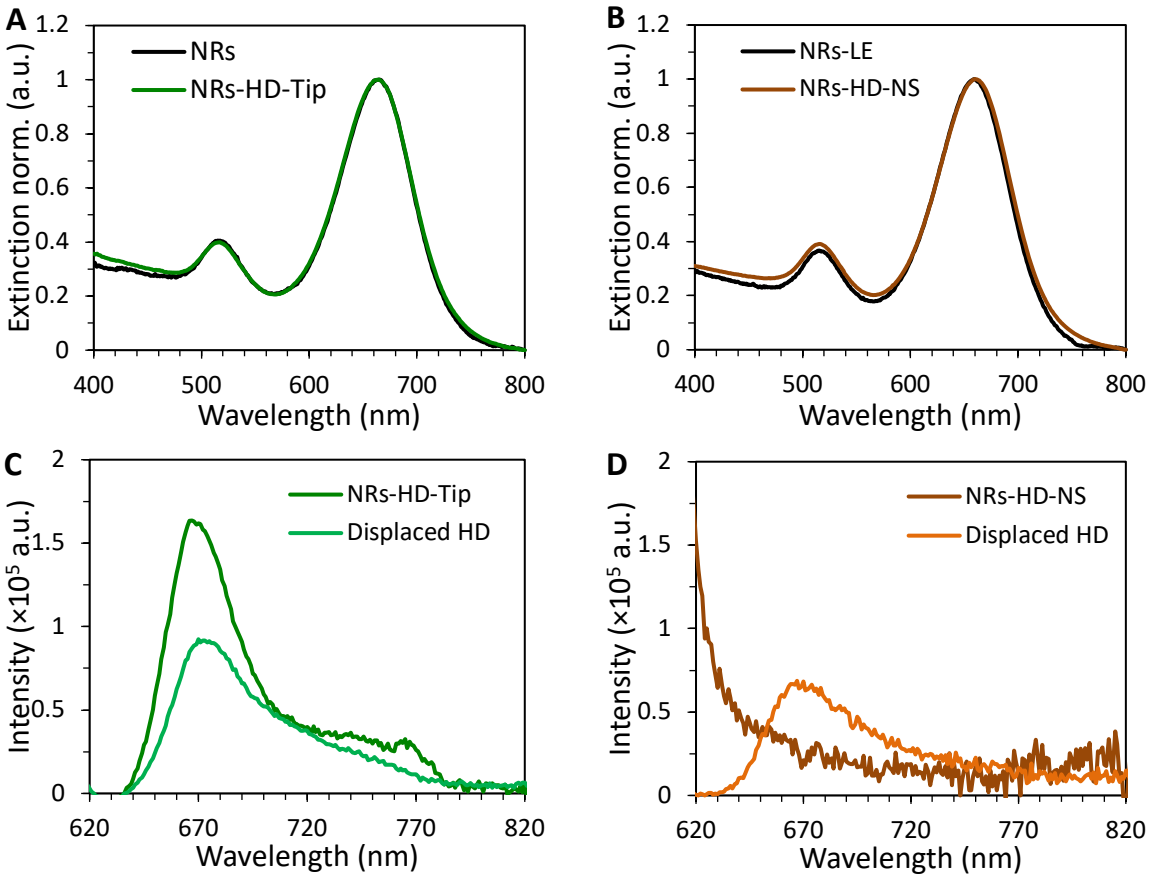

Figure 6.15 - Tip- and NS- functionalization of HD onto gold nanorods. (A) and (B) are extinction spectra for tip- and NS-functionalization, respectively. "NRs" are nanorods stabilized by CTAB. "NRs-LE" represents nanorods after ligand-exchange reactions. (C) and (D) are emission spectra of nanohybrids after tip- (dark green curve) and NS-functionalization (dark orange curve), respectively, and of HD displaced from the same samples by ligand exchange with 2-mercaptoethanol (20 mM).[37] These spectra were measured at an excitation wavelength of 600 nm.

Only minor LSP peak shifts of 1 nm were measured on both nanohybrids after the functionalization procedures. In particular, blue- and red-shifts were obtained respectively for NRs-HD-Tip and NRs-HD-NS samples, in relation to rods before loading of HD.

Steady-state fluorescence measurements (Figure 6.15C and D) were also performed. Interestingly, the nanohybrids prepared by tip-functionalization exhibited significant fluorescence, while the ones NS-functionalized displayed no fluorescence. This difference can indicate that hairpins are conjugated onto the nanorods in distinct conformations. In tip-functionalized nanorods the presence of CTAB may contribute to incomplete or even non-closing of the stem. Possibly this is due to electrostatic interactions of the DNA strand with the surfactant bilayer, so that the dye's distance to the nanorod's surface is greater than in the case of a closed hairpin leading to emission, instead of particle-induced quenching, as initially planned. In the NRs-HD-NS sample, the PBST medium may have contributed to a better closure of the hairpin's stem. Indeed, an excessive salt concentration has been reported to stabilize closed and secondary conformations.[40]

The ensemble emission measurements also allowed to assess the number of hairpins attached to each nanorod using the same displacement quantification method as before.[37] Values of 81 and 50 HD strands per nanorod were obtained for tip- and NS-functionalization, respectively. These results are in opposition to what was expected from the work discussed in Chapter 5/Ref. 20, in which tip-functionalization rendered lower loadings of DNA hybrids.

It was also possible to evaluate the fluorescence enhancement effect, but in tip-functionalized particles only, because NS-functionalized had no fluorescence. This was performed by comparing the emission spectrum from a sample of nanohybrids with that from the same sample after displacing HD into solution by ligand exchange with 2-mercaptoethanol.[37] The values obtained are presented in Table 6.7.

Table 6.7 - Fluorescence enhancement of NRs-HD-Tip nanohybrids obtained in displacement assays, with variation of the excitation wavelength (λ_{exc}).

	Fluor. enhancement			
λ_{exc} (nm)	**600**	**610**	**620**	**630**
NRs-HD-Tip	1.6	1.7	1.7	2.1

In agreement with the work discussed in Chapter 5/Ref. 20, tip-functionalization rendered nanohybrids with enhanced fluorescence emission, while the non-selective approach presented only emission suppression.

The biosensing ability of colloidal nanohybrids in aqueous solution was also tested by adding the RNA target (2 μM) for 30 minutes. The emission response was assessed by comparing the emission spectrum from a sample of nanohybrids to that of the same sample now in the presence of target. The results were similar regardless of the functionalization procedure: absence of fluorescence signalling. This means that there was no response of the nanobiosensors to the presence of the RNA target in solution. Probably this was due to the already open or incompletely open hairpins. Moreover, in tip-functionalized nanorods, the presence of a CTAB bilayer perhaps interfered with a proper target hybridization with the hairpin's loop by means of electrostatic interactions. For NS-functionalized nanorods, the limitation caused by electrostatic interactions is due to the negative charge of the hairpins and that of the target, which probably also hampers hybridization.

The misleading results on the first NRs-HD-Tip sample led us to prepare new samples of tip-functionalized nanohybrids considering some experimental variations. Apart from nanohybrids with HD in the closed hairpin conformation (i.e. without target), a new sample was also prepared of HD hybridized with the target (HDTD). This would provide open hairpins later conjugated onto nanorods. This trial would allow the assessment of the fluorescence enhancement induced in the dyes' emission that could be attained in the open hairpin conformation. In addition, it was intended to evaluate if the loading of HD chains would be increased by using a more linear and rigid dsDNA chain like HDTD.

Initially, to confirm the conformational difference between HD and HDTD the fluorescence autocorrelation curves (Figure 6.23 of the Annexes) were acquired in 0.5× PBS (as used in the functionalization). The values obtained for the diffusion coefficients were 110 and 84 $\mu m^2/s$, respectively for HD and HDTD. These values support the hybridization of HD with the target, because the hydrodynamic radius of the HDTD hybrid is supposedly larger than that of HD, and thus, supports target association as intended.

After functionalization, both types of nanohybrids were stable in CTAB solutions of 1 mM, as evaluated by the extinction spectra of Figure 6.16A. The decrease of CTAB's concentration from 10 to the critical micelle concentration of 1 mM[41] was meant to reduce interference from CTAB detergent on the hairpin probe, and later in the target sensing assays. In agreement to previous HD-nanorod conjugates, LSP peak blue shifts of 1 and 2 nm were measured for the HD- (NRs-HD) and HDTD-tip-functionalized nanorods (NRs-HDTD), in comparison to nanorods before loading of oligonucleotides.

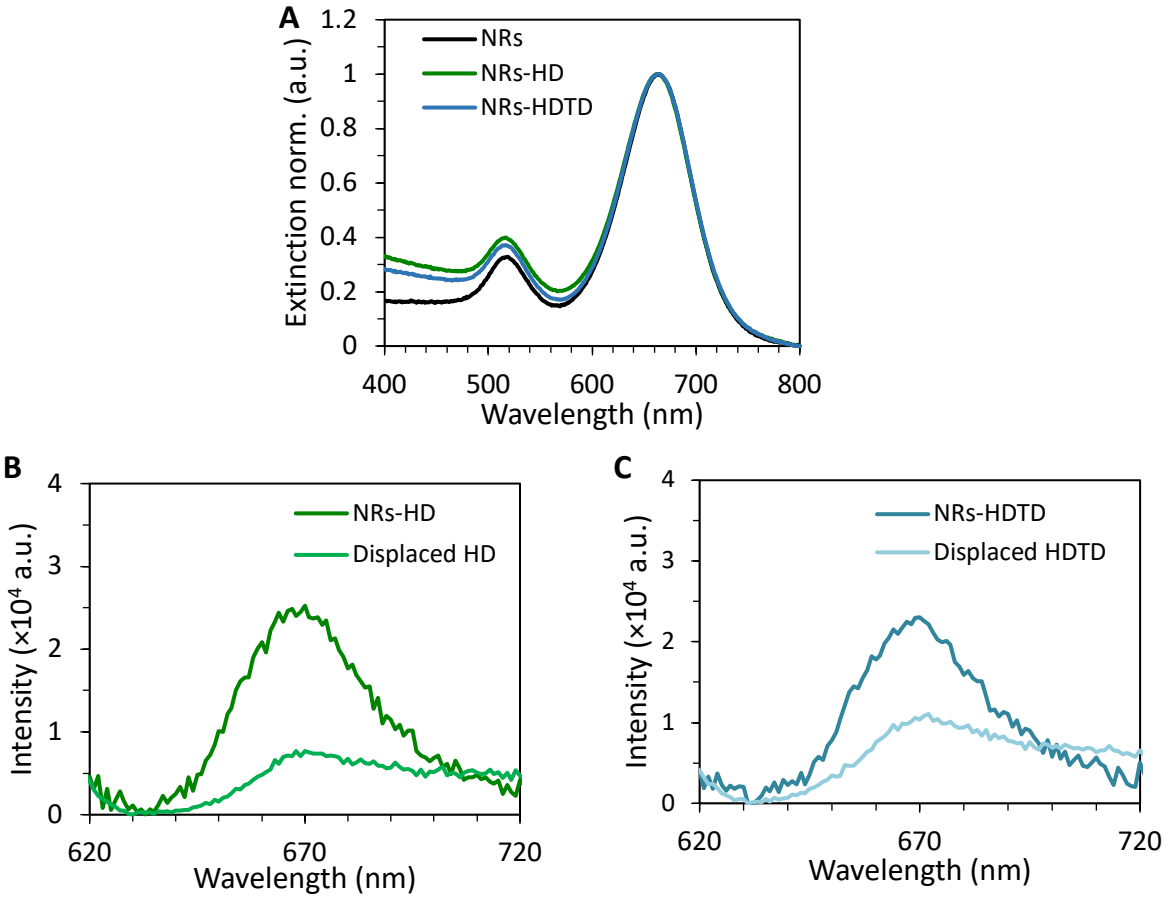

Figure 6.16 - Tip-functionalization of gold nanorods with HD (NRs-HD) and with HD hybridized with TD target (NRs-HDTD). (A) Extinction spectra of the nanohybrids - "NRs" are nanorods stabilized by CTAB (1 mM). (B) and (C) are emission spectra of NRs-HD and NRs-HDTD nanohybrids, respectively, and of HD and HDTD displaced from the same samples by ligand exchange with 2-mercaptoethanol (20 mM), measured at 600 nm.

Ensemble spectra (Figure 6.16B and C) of nanohybrids were performed to quantify the load of probes-per-nanorod. The values of 35 HD and 42 HDTD probes per rod were obtained, in agreement to the tip-functionalization protocol of Chapter 5/Ref. 20.

Table 6.8 shows the fluorescence enhancements factors at 600 and 620 nm excitation wavelengths. These were also calculated for each type of nanohybrids by comparing the emission spectrum from their sample with that from the same sample after displacing HD or HDTD into solution.

Table 6.8 - Fluorescence enhancement factor for samples NRs-HD and NRs-HDTD obtained in displacement assays while varying the excitation wavelength (λ_{exc}).

	Fluor. enhancement	
λ_{exc} (nm)	**600**	**620**
NRs-HD	2.8	3.5
NRs-HDTD	1.9	3.1

The fluorescence enhancement detected for NRs-HD nanohybrids is slightly larger than that for NRs-HDTD (for both excitation wavelengths measured). This difference may arise from the possible larger distance between dyes and the rods' tips, attained in the stretched HDTD chain, which could decrease the antenna effect.[19] In the particular case of NRs-HD, the fluorescence enhancement increased from 1.6 to 2.8 at an excitation wavelength of 600 nm, when comparing to the previous tip-functionalized particles. The difference in probes loading - 81 in the previous experiment and 35 in this one - may be one of the reasons for this increment. As less dye molecules are inserted at the nanorod side and mostly at the tips, the average fluorescence enhancement increases, thus contributing to the overall increased nanohybrid emission. Again, incomplete and/or absence of closure of the hairpins may contribute to the emission of the NRs-HD sample, instead of a particle-induced quenching effect as initially planned for closed hairpins.

The biosensing response of the previous colloidal nanohybrids (sample NRs-HD) in aqueous solution was also tested by adding the RNA target (2 μM; 30 minutes), but no fluorescence emission was obtained. The lack of response to the RNA target may again be caused by the hairpins being already opened even in the target's absence. However, one cannot exclude an eventual interference of CTAB molecules in the target hybridization.

Unfortunately, a fluorescence signalling response from these nanohybrids was not obtained as initially projected. This failure has driven the development of assays on surface-immobilized nanohybrids. With this strategy change, target hybridization assays in the absence of CTAB (or other surface agents) become possible.

6.5.2. Fluorescence signalling on surface-immobilized nanohybrids

The biosensing assays described here were carried out with the nanohybrids immobilized on glass coverslips modified to covalently bind gold particles. This organic coating was achieved using well-established surface silanization procedures. The surface immobilization of former HD-tip-functionalized gold nanorods (sample NRs-HD in Figure 6.16) enabled their study by single-particle spectroscopy on a confocal fluorescence microscopy setup (Figure 6.17A).

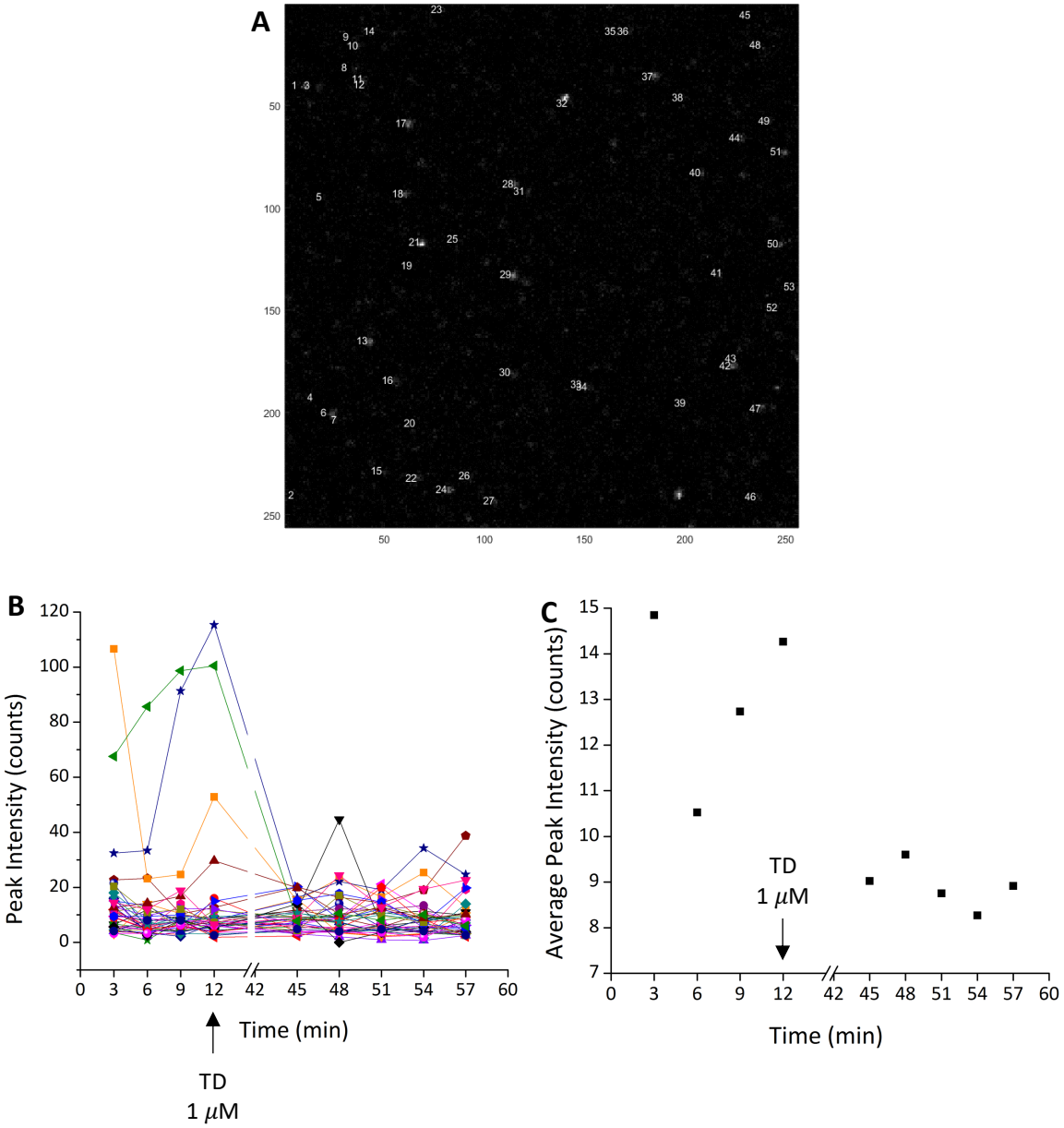

Figure 6.17 - Surface-immobilized nanohybrids formed by HD functionalized onto the tips of gold nanorods (NRs-HD). (A) Probed image of nanohybrids recognized by their photoluminescence and identified as points with numbers. The image was obtained with 40 × 40 μm, 256 pixels, at 639 nm and 0.04 kW/cm² laser irradiation. (B) Single emitter tracking and (C) average peak intensity in relation to time of the nanohybrids, prior and after addition of target RNA at t = 12 mins (TD, 1 μM in 1× PBS). A total of 38 points were analysed for each graph.

With this surface immobilization approach, and unlike in the case of ensemble measurements in colloidal suspension, CTAB can be completely removed from the nanorods' surface through washing without affecting stability of the particles. The removal of the positively charged CTAB bilayer minimizes undesired electrostatic interactions, which could interfere with target hybridization; or the spontaneous closing of hairpins. Also, eventually the evaluation of the sensing response at single-particle level (Figure 6.17B), would allow in principle to detect single-molecule hybridization events.

The response to the target RNA was tested by performing measurements of single-particle fluorescence on the nanohybrids (previous Figure 6.17B and C). These were exposed to multiple irradiations of the same area, before and after target addition. As can be seen in the previous figure, the sensing response to the target was inexistent, even after approximately 1 hour of exposure. Possibly the hybridization of the target with the loop's hairpin did not occur due to incomplete removal of CTAB molecules from the surface of the nanorods, thus limiting the increment of the particles' peak intensities that could signal the molecular detection. Unfortunately, these results have not demonstrated a nanohybrid sensor with plasmon-enhanced fluorescence signalling. Nevertheless, the experience harnessed from this work has contributed to improve the strategies toward the ultimate goal of detecting single-molecule hybridization events.

6.6. Remarks and follow-up

Functionalization of fluorescently-labeled probes onto plasmonic hot-spots at the tips of gold nanorods was performed for the development of nanohybrid biosensors. The major advantage of this approach over free probes would be to exploit enhanced fluorescence signalling, in response to target species, which would provide biosensors with more sensitivity for nucleic acid detection. However, under the conditions investigated, the designed molecular beacons presented limitations when tested alone in solution. In view of this chapter's overall results, possible improvements of the nanohybrid's components - molecular beacons and nanoparticles - are discussed next.

First of all, the stem could be increased or enriched in CG content, because the possible structures obtained using the OligoAnalyzer tool suggest that the first (AT) pair of the stem do not effectively close, and thus may contribute to mis-folded hairpin conformations. On the other hand, the length of the stem could be reduced to 5 base pairs, since beacons with shorter stems allow faster hybridization kinetics and improved sensitivities. However, since they can suffer from lower signal-to-background ratios and selectivity, a compromise needs to be found.[42,43]

Other major changes could also be implemented, such as the labeling strategy. Instead of terminal-labeled dyes connected by linker chains, that are flexible and can affect FRET distances, the dye-labeling could be done directly onto a nucleotide.[16] Since dye-DNA interactions are known to stabilize the closed conformation of hairpins, this could circumvent the limitations verified here in the beacons' closing. In addition, synthetic nucleic acids such as locked nucleic

acid (LNA) or peptide nucleic acid (PNA), which have higher sensitivity and selectivity than DNA probes, could be explored to redesign the beacons.[43]

Also, beacons alone could be characterized more extensively. The influence of ionic strength, temperature and oligonucleotide length on the kinetic and equilibrium constants of binding and dissociation could be studied.[44] In this regard, the lack of significant response to targets, which restricts their use for biosensing applications, could also be related to salt concentration, or to the lack of divalent counterion species. As reported, this effect stabilizes closed and secondary conformations instead of allowing opening of the hairpins.[40] Therefore, the influence of salt concentration on the beacons could be studied to assess minimum background fluorescence (low emission state), and on beacon-target assemblies to evaluate top signalling responses (high emission state) at room temperature.[40] Nevertheless, preliminary studies along these lines did not provided yet promising results.[36]

Regarding the unsuccessful tip-functionalization of molecular beacons, in which the issue was the particles' stability, variations to the protocol could be performed. For example, increase reaction time or fine-tuning salt concentration to shield the negative charges of the long hairpins' chains, possibly preventing the formation of complexes between CTAB micelles and molecular beacons. A biocompatibility strategy on these tip-functionalized nanorods could provide particles without CTAB, stable and adequate to interact with targets more effectively. In this regard, several alternatives were tested, i.e. using PEG or PEG/BSPP/Tween 20[45] and PAA/PAH[46] as substitution ligands, but without the intended outcome. Alternatively, the nanorods could be stabilized with a citrate coating before or after functionalization with the beacons.[47,48] In fact, gold nanospheres that already have a citrate coating were functionalized with the new hairpin probe, but due to unclear results, further studies are necessary.

In this work, the plasmonic hot-spots for signal enhancement were the tips of elongated gold nanoparticles, such as nanorods. Alternatively, gold nanoparticles assembled as dimers could be used to develop nano-gaps with molecular beacons placed in the hot-spot for highly sensitive biomolecular detection of nucleic acids. To this end, the beacon would need to be adapted to function as a linker between particles. For example, the stem of the hairpin could be extended to bare another two thiol functions located in opposite ends of a dsDNA segment designed to be 30-bp long. This length would provide a gap distance of at most 10 nm between the assembled nanoparticles. For nanospheres, and considering the work discussed in Chapter 3/Ref. 49 the particle's size of 80 nm, or more, could enable an efficient scattering of the dye's emission, thereby, resulting in better antenna efficiencies. This work already proved that such a dimer configuration can support emission enhancements of a red-emitting dye up to 3 orders of magnitude. Also, dimers of gold nanorods in head-to-head configuration using beacons could be developed to obtain even larger field enhancements in the nano-gap,[50] when compared to dimers of spherical particles. Such large enhancements could have a similar benefit in the sensitivity of

nucleic acid detection and would contribute to fully explore fluorescence emission increase by plasmonic antennas for sensing applications.

6.7. Experimental section

6.7.1. Materials

Gold nanorods coated by CTAB surfactant with an approximate size of 25 nm × 71 nm and with a LSP peak wavelength of 661 nm (product no. A12-25-650-CTAB-DIH-25, lot F3216) were acquired from Nanopartz Inc. (USA) as aqueous suspensions with an optical density of 1. DNA oligonucleotides purified by high-performance liquid chromatography were purchased from STAB Vida (Portugal), except QSY 21-labeled strands that were acquired from ThermoFisher Scientific (USA). Dye-labeled strand, F-Seq, had the following sequence: (Atto-647N)-5'-GAGTCTGGAC-(C6-SH)-3', with C6 representing a hexamethylene spacer. Q-Seq sequences, hairpin probe HD, and targets are described in the next table.

Table 6.9 - Sequences of hairpins (Q-Seq strands and HD), respective modifications/quenchers and nucleic acid target sequences.

Labels	Modifications	Hairpin sequences	Targets
Q-Seq of BD1	5' C6 Thiol 3' DDQ II	5'-**GTC CAG ACT C** CA AG***T GGT CG***T TGA AGT CGA GGC CTG TTC TCG GAG AG***C GAC CA***-3' Length: 53 nts	Dengue virus RNA, TD[4] 5'-CUC UCC GAG AAC AGG CCU CGA CUU CAA-3' Length: 27 nts
Q-Seq of BD2	5' C6 Thiol Modifier S-S 3' QSY 21		
Q-Seq of BS1	5' C6 Thiol 3' DDQ II	5'-**GTC CAG ACT C** CA AG***T GGT CG***C AAG TGC GTA AAC ACA A***CG ACC A***-3' Length: 43 nts	Sleeping sickness DNA, TS[5–8] 5'-TTG TGT TTA CGC ACT TG-3' Length: 17 nts
Q-Seq of BS2	5' C6 Thiol Modifier S-S 3' QSY 21		
Q-Seq of BM1	5' C6 Thiol 3' DDQ II	5'-**GTC CAG ACT C** CA AG***T GGT CG***C AGG TCA AAA GGG TCC TTA GGG A***CG ACC A***-3' Length: 49 nts	microRNA-145, TM[9–12] 5'-UCC CUA AGG ACC CUU UUG ACC UG-3' Length: 23 nts
Q-Seq of BM2	5' C6 Thiol Modifier S-S 3' QSY 21		
HD	5' Thioctic Acid 3' Atto-647N	5'-***TGG TCG*** TTG AAG TCG AGG CCT GTT CTC GGA GAG ***CGA CCA***-3' Length: 39 nts	Dengue virus RNA, TD[4] 5'-CUC UCC GAG AAC AGG CCU CGA CUU CAA-3' Length: 27 nts

CTAB (≥ 99%), thiolated poly(ethylene glycol) (mPEG-SH, MW~5,000) and Tween 20 were supplied by Sigma-Aldrich (USA). Sodium citrate tribasic dihydrate (Sigma-Aldrich, ≥ 99.5%) and

citric acid (Sigma-Aldrich, ≥ 99.5%) were used to prepare citrate buffer with pH 3. Atto-647N in the form of NHS-ester derivative was purchased from ATTO-TEC GmbH. Phosphate-buffered saline buffer as tablets from Sigma was dissolved in ultrapure water. (3-mercaptopropyl)-trimethoxysilane (MPTMS) was from Aldrich with 95% purity. Ultrapure water (18.2 MΩ·cm) was obtained with a Milli-Q purification system (Merck-Millipore, USA) and used in all preparations. All reagents were used as obtained. Microscope coverslips of ∅ 22 mm were produced by Menzel-Gläser (Gerhard Menzel GmbH, Germany).

6.7.2. Instrumentation

A PerkinElmer, model Lambda 35, UV/Vis spectrophotometer was used to acquire absorption or extinction spectra. Corrected fluorescence emission spectra were recorded with a FluoroLog-3 spectrophotometer (Horiba Jobin Yvon, Japan). Confocal fluorescence microscopy with single-molecule sensitivity measurements were performed on a time-resolved confocal fluorescence microscope, model MicroTime 200, from PicoQuant GmbH (Germany). The microscope setup details were previously described in Chapter 3. Single-particle spectra were collected with a QE Pro (Ocean Optics, Germany) spectrometer, that was fiber coupled to the confocal microscope. The SymPhoTime software, version 5.3.2.2, from PicoQuant GmbH was used for data acquisition and analysis. Glass surfaces were cleaned using an UV/ozone chamber model PSD-UV3 from Novascan.

6.7.3. Confocal fluorescence microscopy studies

Prior to performing measurements on molecular beacons, glass coverslips had to be prepared. Briefly, round glass coverslips were extensively cleaned by sonication (20 min) in RBS 50 detergent (5% v/v) and absolute ethanol. Coverslips were rinsed with ultrapure water between steps and at the end. After drying with N_2, coverslips were exposed to UV/ozone for 2 hours and a small liquid tank was mounted.

Separate aqueous solutions in 1× PBS for each oligonucleotide concentration were freshly prepared from working stock solutions at room temperature. To study the functionality of each beacon in solution, three consecutive steps were performed. Initially, 100 μL of F-Seq with 1 nM was placed on the tank cell in the glass coverslip. After an incubation step of 30 minutes, 11.1 μL of each Q-Seq sequences' solution with 1 μM (final concentration of 100 nM) were added and allowed to hybridize with the F-Seq for another 30 min for beacon assembly. Finally, 2.3 μL of each respective target sequence (100 μM; final concentration of 2 μM) were inserted and hybridization of beacon-target assembly was left for 30 min. For the titration assay of BD2 in 1× PBS, the concentration of F-Seq was kept fixed at 1 nM and the solution incubated for 20 min. After, the concentration of Q-Seq from BD2 was increased from 1 until 200 nM, followed by addition of RNA target (TD, 2 μM). Between each addition of Q-Seq and later of TD, 20 min were given to allow for hybridization of oligonucleotides.

Measurements were performed in the time-resolved confocal fluorescence microscope. Laser excitation at 639 nm with a pulse repetition rate of 20 MHz was focused by a 60× water immersion objective ca. 10 μm above the coverslip surface. All measurements were made at room temperature (ca. 25 ºC) with acquisition times of 180 seconds. For emission intensity-lifetime measurements, a laser excitation power of ca. 1.6 kW/cm^2 was used to acquire point fluorescence intensity time traces, while fluorescence autocorrelation curves were obtained at ca. 4 kW/cm^2. In the titration assay, three consecutive measurements were performed in each addition step, using a power of 12 kW/cm^2. The focal area and detection volume were calibrated, in every new coverslip, by using Atto655-COOH and considering as reference value a diffusion coefficient of 425 mm^2 s^{-1} in water at 25 ºC.

Time traces of fluorescence intensity were cross-correlated to avoid after-pulsing artifacts. Also, by applying reconvolution fitting, it was possible to obtain amplitudes and lifetimes of short and long components in a multi-exponential fitting. The use of an IRF insured a more accurate fitting than what could be obtained with a tail fitting and allowed a better estimation of the relative amplitude of each lifetime component. The IRF was obtained using the scattering signal from a dispersion of gold nanorods, resulting in a Full Width at Half Maximum (FWHM) of ca. 0.5 ns.

6.7.4. Molecular beacons' fluorescence quantum yield and lifetime determination

The fluorescence quantum yield and lifetime were assessed for Atto-647N dye, F-Seq (1 μM), Q-Seq strands (1 μM), DDQ II-/QSY 21-labeled molecular beacons (F-Seq and Q-Seq with 0.5 and 1 μM, respectively, except for BS1 that was 0.25 and 0.5 μM) and beacon-target assemblies (with 2 μM of each target). All solutions were prepared in 1× PBS.

The relative determination method was implemented to obtain the quantum yields.[51,52] This method is based on the comparison of the integral emission spectra of a standard dye versus that of the sample (dye) being studied, under identical conditions. The standard dye must have a known quantum yield and similar optical properties as the sample, thus cresyl violet was selected, with a known quantum yield of 56% in ethanol at 24 ºC.[52] The method involves acquiring absorption and emission spectra. For this, 10 mm quartz cuvettes were used in both respective instruments to minimize on the calculation the effect of scattering losses at the interface. Internal filter effects were avoided by ensuring maximum extinction values below 0.2 absorbance and concentration of standard dye was adjusted rather than that of samples. Emission spectra of standard and sample were obtained with excitation at 580 nm.

Lifetime determination was performed in the time-resolved confocal fluorescence microscope (front-face geometry) by TCSPC technique. A droplet of each sample used for quantum yield's assessment was placed in separates areas of clean glass coverslips. A point fluorescence intensity time trace was acquired with the laser beam with excitation at 639 nm focused ca. 10 μm above the coverslip surface. Q-Seq sequences were excited at 0.8 kW/cm^2 and all other samples at 0.08 kW/cm^2 for 2 minutes. Again, reconvolution fitting was applied to obtain relative

amplitudes of each lifetime component in a multi-exponential fitting, assuming a fixed value for the same IRF (FWHM).

6.7.5. Functionalization of gold nanorods with molecular beacons

Two approaches were used for the attachment of molecular beacons onto gold nanorods, a tip-selective and a non-selective functionalization, following the protocols described previously in Chapter 5/Ref. 20. First, for assembly of beacons, F-Seq and Q-Seq sequences were hybridized in 0.5× PBS for at least 1 h at room temperature using a 25% molar excess of Q-Seq strands. Afterwards, to prepare the functionalization mixture for a tip-selective procedure, beacons (0.5× PBS) were added to nanorods in aqueous CTAB (10 mM) at a dye-per-particle molar ratio of 4000 to give a final rods' concentration of 1 nM in a volume of 90 μL. The mixtures were allowed to react at room temperature for 1 hour (experiment with BD2) or 24 hours (experiments with BD2, BS2 and BM2). At the end, the reaction was halted by washing unbounded oligonucleotides by eight centrifugation cycles with resuspension in aqueous CTAB (10 mM, 500 μL). All samples were stored in the colloidal suspension at 4 ºC until further use.

The non-selective functionalization is briefly described next. First, a volume of 2 mL of gold nanorods (0.2 nM) in aqueous CTAB (1 mM) was centrifuged (6000 rpm, 15 mins), the supernatant was discarded, and the pellet was resuspended in aqueous mPEG-SH (250 μL, 10 μM) and Tween 20 (250 μL, 0.2 wt%). The solution was centrifuged (6000 rpm, 15 mins) and the supernatant was replaced again with mPEG-SH and Tween 20. This procedure was repeated one more time to wash away CTAB. The second ligand exchange started with hybridization of F-Seq and Q-Seq sequences (from BD2), as described for the tip-functionalization. After, beacons (35 μL in 0.5× PBS) were added to the PEG-stabilized nanorods (10 μL) to give a molar ratio of dye-per-particle of 4000, while keeping the particle concentration fixed at ca. 2 nM. Next, citrate buffer at pH 3 (20 μL, 0.5 M) and PBS (35 μL, 1×) were added, and functionalization proceed for 1 h at room temperature. Lastly, unreacted oligonucleotides were washed by six centrifugation cycles with resuspensions in PBST buffer (mixture of PBS with Tween 20, 0.01 wt %). Samples were also stored in the colloidal suspension at 4 ºC until further use.

The number of molecular beacon BD2 attached per gold nanorod was determined by a reported ligand displacement protocol using 2-mercaptoethanol.[53] Nanohybrids were previously diluted to sub-nM concentration using PBST buffer. A working curve was previously established by measuring the fluorescence intensity from solutions of beacon BD2 in PBST with known concentrations in the presence of 20 mM of 2-mercaptoethanol, as shown in the next figure. The emission spectra were recorded with excitation wavelengths at 600 nm.

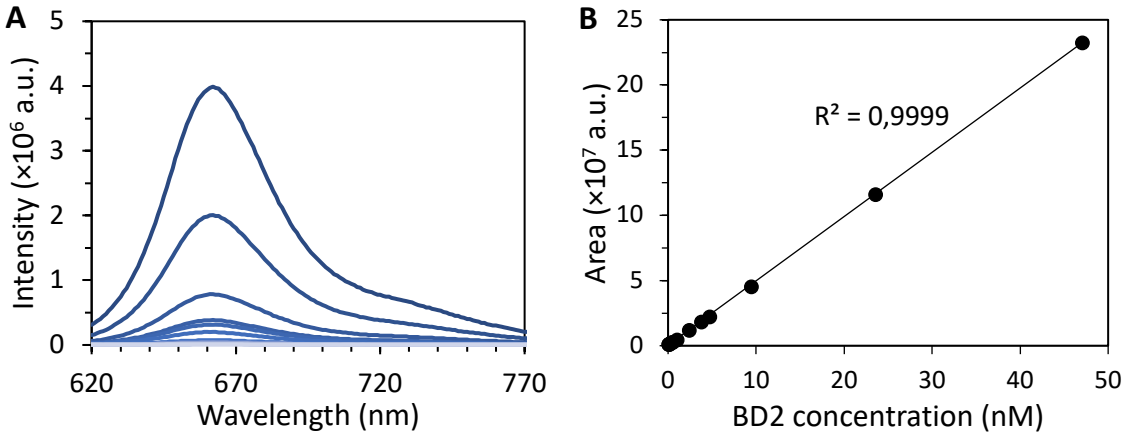

Figure 6.18 - Quantification of the number of beacon BD2 chains attached per gold nanorod. (A) Emission spectra of BD2 solutions with known concentrations (between 0 and 47 nM from down to top) in PBST buffer and in the presence of 2-mercaptoethanol (20 mM), obtained for an excitation wavelength of 600 nm. (B) Working curve for the determination of BD2's concentration in the displacement assays - represented as the integrated emission spectra (area) of the solutions measured in (A).

Characterization of the fluorescence emission of colloidal nanohybrids formed by beacon BD2, was performed by FCS measurements at room temperature. For the evaluation of the sensing response of colloidal single nanohybrids NRs-BD2 to dengue virus RNA target, fluorescence intensity time traces were also acquired. First, nanohybrids were diluted to a sub-nM concentration in PBST. In the sensing assay three consecutive measurements were performed: to the nanohybrids alone and in the presence of target after 30 min exposure, first at a concentration of 0.1 μM and later of 10 μM. All measurements were performed at a laser excitation of 639 nm with a power of ca. 0.04 kW/cm^2 and with the beam focused ca. 10 μm above the coverslip surface, during a time interval of 180 s.

6.7.6. Novel hairpin probe designed for the detection of dengue viral RNA

The fluorescence quantum yield of the hairpin probe, HD, designed for detection of the RNA target, was also performed considering the abovementioned relative determination method.[51,52] HD was prepared with 1 μM in 1× PBS, PBST and CTAB (10 mM) and the quantum yield was also measured after addition of target (2 μM) to each solution.

For the attachment of hairpin probes onto gold nanorods, again tip-selective and non-selective functionalization approaches were implemented, following the protocols as described previously in Chapter 5/Ref. 20 and in the above section. Hybridization of HD with the target sequence (2-fold excess) was carried out in 0.5× PBS for at least 1 hour, prior to tip-functionalization of nanorods with the resulting HDTD hybrid. The hybridization was afterwards confirmed by FCS measurements using a laser excitation at 639 nm.

Concerning the determination of the number of probes (HD and HDTD) attached per gold nanorod, a displacement method using 2-mercaptoethanol was also performed (see Figure 6.22 of the Annexes). The emission spectra were acquired with an excitation wavelength of 600 nm.

The dye displacement by ligand exchange with 2-mercaptoethanol was also used in the determination of the fluorescence enhancement of the nanohybrids. Emission spectra were recorded for excitation wavelengths between 600 to 630 nm in steps of 10 or 20 nm depending on samples.

Biosensing assays to evaluate the response in colloidal suspension of the nanohybrids to artificial RNA target from dengue virus (2 μM, 30 minutes exposure) were performed by assessing their fluorescence though acquisition of the emission spectra of each sample before and after insertion of the target (incubation time of 30 minutes).

Biosensing assays were also carried out with the nanohybrids immobilized on silanized glass surfaces. First, round glass coverslips were extensively cleaned prior to use by sonication (20 min) in RBS 50 detergent (5% v/v) and methanol. The coverslips were rinsed with ultrapure water between steps and at the end. After drying with N_2, they were exposed to a UV/ozone treatment for 2 hours. For silanization, clean slides were immersed in a 5% (v/v) solution of MPTMS in methanol for 30 min, rinsed thoroughly with methanol to remove unbound silane from the glass surface, sonicated for 10 min in methanol and blow dried with N_2. Then, HD-tip-functionalized nanorods were immobilized by drop-casting, at a sub-nM concentration in 1 mM of CTAB, during 30 min on the silanized coverslips. After, these were rinsed with ultrapure water, placed in PBS for 30 min to remove unbound particles, rinsed again with ultrapure water and blow dried with N_2. The surface immobilization enabled the characterization of the nanohybrids by confocal fluorescence microscopy coupled with single-particle spectroscopy. Probed images of the nanohybrids were obtained with 40 × 40 μm, 256 pixels, at 639 nm and 0.04 kW/cm^2 laser irradiation to minimize photodamage effects. Single particles (a total of 38) were identified by their photoluminescence and tracking of their peaks' intensity in relation to time was performed prior and 30 min after the addition of the RNA target sequence (1 μM in 1× PBS).

6.8. References

(1) Bauch, M.; Toma, K.; Toma, M.; Zhang, Q.; Dostalek, J. Plasmon-Enhanced Fluorescence Biosensors: A Review. *Plasmonics* **2014**, *9* (4), 781–799. https://doi.org/10.1007/s11468-013-9660-5.

(2) Fothergill, S. M.; Joyce, C.; Xie, F. Metal Enhanced Fluorescence Biosensing: From Ultra-Violet towards Second near-Infrared Window. *Nanoscale* **2018**, *10* (45), 20914–20929. https://doi.org/10.1039/C8NR06156D.

(3) Jeong, Y.; Kook, Y.-M.; Lee, K.; Koh, W.-G. Metal Enhanced Fluorescence (MEF) for Biosensors: General Approaches and a Review of Recent Developments. *Biosens. Bioelectron.* **2018**, *111*, 102–116. https://doi.org/10.1016/j.bios.2018.04.007.

(4) Johnson, B. W.; Russell, B. J.; Lanciotti, R. S. Serotype-Specific Detection of Dengue Viruses in a Fourplex Real-Time Reverse Transcriptase PCR Assay. *J. Clin. Microbiol.* **2005**, *43* (10), 4977–4983. https://doi.org/10.1128/JCM.43.10.4977-4983.2005.

(5) Deborggraeve, S.; Büscher, P. Recent Progress in Molecular Diagnosis of Sleeping Sickness. *Expert Rev. Mol. Diagn.* **2012**, *12* (7), 719–730. https://doi.org/10.1586/erm.12.72.

(6) Deborggraeve, S.; Lejon, V.; Ekangu, R. A.; Mumba Ngoyi, D.; Pati Pyana, P.; Ilunga, M.; Mulunda, J. P.; Büscher, P. Diagnostic Accuracy of PCR in Gambiense Sleeping Sickness

Diagnosis, Staging and Post-Treatment Follow-Up: A 2-Year Longitudinal Study. *PLoS Negl. Trop. Dis.* **2011**, *5* (2), e972. https://doi.org/10.1371/journal.pntd.0000972.
(7) Mugasa, C. M.; Schoone, G. J.; Ekangu, R. A.; Lubega, G. W.; Kager, P. A.; Schallig, H. D. F. H. Detection of Trypanosoma Brucei Parasites in Blood Samples Using Real-Time Nucleic Acid Sequence-Based Amplification. *Diagn. Microbiol. Infect. Dis.* **2008**, *61* (4), 440–445. https://doi.org/10.1016/j.diagmicrobio.2008.03.019.
(8) Deborggraeve, S.; Claes, F.; Laurent, T.; Mertens, P.; Leclipteux, T.; Dujardin, J. C.; Herdewijn, P.; Buscher, P. Molecular Dipstick Test for Diagnosis of Sleeping Sickness. *J. Clin. Microbiol.* **2006**, *44* (8), 2884–2889. https://doi.org/10.1128/JCM.02594-05.
(9) Das, A. V.; Pillai, R. M. Implications of MiR Cluster 143/145 as Universal Anti-OncomiRs and Their Dysregulation during Tumorigenesis. *Cancer Cell Int.* **2015**, *15* (1). https://doi.org/10.1186/s12935-015-0247-4.
(10) Tang, L.; Wei, D.; Yan, F. MicroRNA-145 Functions as a Tumor Suppressor by Targeting Matrix Metalloproteinase 11 and Rab GTPase Family 27a in Triple-Negative Breast Cancer. *Cancer Gene Ther.* **2016**, *23* (8), 258–265. https://doi.org/10.1038/cgt.2016.27.
(11) Yang, J.; Liu, Q.; Cao, S.; Xu, T.; Li, X.; Zhou, D.; Pan, L.; Li, C.; Huang, C.; Meng, X.; Zhang, L.; Wang, X. MicroRNA-145 Increases the Apoptosis of Activated Hepatic Stellate Cells Induced by TRAIL through NF-KB Signaling Pathway. *Front. Pharmacol.* **2018**, *8*. https://doi.org/10.3389/fphar.2017.00980.
(12) Ding, J.; Sun, D.; Xie, P. Elevated MicroRNA-145 Inhibits the Development of Oral Squamous Cell Carcinoma through Inactivating ERK/MAPK Signaling Pathway by down-Regulating HOXA1. *Biosci. Rep.* **2019**, *39* (6). https://doi.org/10.1042/BSR20182214.
(13) Vietz, C.; Lalkens, B.; Acuna, G. P.; Tinnefeld, P. Synergistic Combination of Unquenching and Plasmonic Fluorescence Enhancement in Fluorogenic Nucleic Acid Hybridization Probes. *Nano Lett.* **2017**, *17* (10), 6496–6500. https://doi.org/10.1021/acs.nanolett.7b03844.
(14) Wang, D.; Vietz, C.; Schröder, T.; Acuna, G.; Lalkens, B.; Tinnefeld, P. A DNA Walker as a Fluorescence Signal Amplifier. *Nano Lett.* **2017**, *17* (9), 5368–5374. https://doi.org/10.1021/acs.nanolett.7b01829.
(15) Kasper, R.; Harke, B.; Forthmann, C.; Tinnefeld, P.; Hell, S. W.; Sauer, M. Single-Molecule STED Microscopy with Photostable Organic Fluorophores. *Small* **2010**, *6* (13), 1379–1384. https://doi.org/10.1002/smll.201000203.
(16) Hartmann, A.; Krainer, G.; Schlierf, M. Different Fluorophore Labeling Strategies and Designs Affect Millisecond Kinetics of DNA Hairpins. *Molecules* **2014**, *19* (9), 13735–13754. https://doi.org/10.3390/molecules190913735.
(17) Atto-647N manufacturer. https://www.atto-tec.com/fileadmin/user_upload/Katalog_Flyer_Support/Catalogue_2009_2010.pdf (Accessed: 02 August 2020).
(18) Khatua, S.; Paulo, P. M. R.; Yuan, H.; Gupta, A.; Zijlstra, P.; Orrit, M. Resonant Plasmonic Enhancement of Single-Molecule Fluorescence by Individual Gold Nanorods. *ACS Nano* **2014**, *8* (5), 4440–4449. https://doi.org/10.1021/nn406434y.
(19) Willets, K. A.; Wilson, A. J.; Sundaresan, V.; Joshi, P. B. Super-Resolution Imaging and Plasmonics. *Chem. Rev.* **2017**, *117* (11), 7538–7582. https://doi.org/10.1021/acs.chemrev.6b00547.
(20) Botequim, D.; Silva, I. I. R.; Serra, S. G.; Melo, E. P.; Prazeres, D. M. F.; Costa, S. M. B.; Paulo, P. M. R. Fluorescent Dye Nano-Assemblies by Thiol Attachment Directed to the Tips of Gold Nanorods for Effective Emission Enhancement. *Nanoscale* **2020**, *12* (11), 6334–6345. https://doi.org/10.1039/D0NR00267D.
(21) Le Reste, L.; Hohlbein, J.; Gryte, K.; Kapanidis, A. N. Characterization of Dark Quencher Chromophores as Nonfluorescent Acceptors for Single-Molecule FRET. *Biophys. J.* **2012**, *102* (11), 2658–2668. https://doi.org/10.1016/j.bpj.2012.04.028.
(22) Holzmeister, P.; Wünsch, B.; Gietl, A.; Tinnefeld, P. Single-Molecule Photophysics of Dark

Quenchers as Non-Fluorescent FRET Acceptors. *Photochem Photobiol Sci* **2014**, *13* (6), 853–858. https://doi.org/10.1039/C3PP50274K.
(23) Xia, W.; Whitten, D.; McBranch, D. WO2005030979 - Dark Quenchers For Fluorescence Resonance Energy Transfer (FRET) In Bioassays, 2005.
(24) Wang, T.-H.; Peng, Y.; Zhang, C.; Wong, P. K.; Ho, C.-M. Single-Molecule Tracing on a Fluidic Microchip for Quantitative Detection of Low-Abundance Nucleic Acids. *J. Am. Chem. Soc.* **2005**, *127* (15), 5354–5359. https://doi.org/10.1021/ja042642i.
(25) May, J. P.; Brown, L. J.; Rudloff, I.; Brown, T. A New Dark Quencher for Use in Genetic Analysis. *Chem. Commun.* **2003**, No. 8, 970–971. https://doi.org/10.1039/b300934c.
(26) Kabeláč, M.; Zimandl, F.; Fessl, T.; Chval, Z.; Lankaš, F. A Comparative Study of the Binding of QSY 21 and Rhodamine 6G Fluorescence Probes to DNA: Structure and Dynamics. *Phys. Chem. Chem. Phys.* **2010**, *12* (33), 9677. https://doi.org/10.1039/c004020g.
(27) Katherine Johansson, M. Choosing Reporter-Quencher Pairs for Efficient Quenching Through Formation of Intramolecular Dimers. In *Fluorescent Energy Transfer Nucleic Acid Probes*; Humana Press: New Jersey, 2006; Vol. 335, pp 17–30. https://doi.org/10.1385/1-59745-069-3:17.
(28) Jones, G.; Jackson, W. R.; Choi, C. Y.; Bergmark, W. R. Solvent Effects on Emission Yield and Lifetime for Coumarin Laser Dyes. Requirements for a Rotatory Decay Mechanism. *J. Phys. Chem.* **1985**, *89* (2), 294–300. https://doi.org/10.1021/j100248a024.
(29) Vogel, M.; Rettig, W.; Sens, R.; Drexhage, K. H. Structural Relaxation Of Rhodamine Dyes With Different N-Substitution Palterns: A Study Of Fluorescence Decay Times And Quantum Yields. *Chem. Phys. Lett.* **1988**, *147* (5), 9.
(30) Schwartz, D. E.; Gong, P.; Shepard, K. L. Time-Resolved Förster-Resonance-Energy-Transfer DNA Assay on an Active CMOS Microarray. *Biosens. Bioelectron.* **2008**, *24* (3), 383–390. https://doi.org/10.1016/j.bios.2008.04.015.
(31) Sabnis, R. W. *Handbook of Fluorescent Dyes and Probes*; 2015.
(32) Rigler, R.; Elson, E. S. *Fluorescence Correlation Spectroscopy: Theory and Applications*; Schäfer, F. P., Toennies, J. P., Zinth, W., Series Eds.; Springer Series in Chemical Physics; Springer Berlin Heidelberg: Berlin, Heidelberg, 2001; Vol. 65. https://doi.org/10.1007/978-3-642-59542-4.
(33) Edward, J. T. Molecular Volumes and the Stokes-Einstein Equation. *J. Chem. Educ.* **1970**, *47* (4), 261. https://doi.org/10.1021/ed047p261.
(34) Rosa, A. M. M.; Prazeres, D. M. F.; Paulo, P. M. R. Fluorescence Correlation Spectroscopy Study of the Complexation of DNA Hybrids, IgG Antibody, and a Chimeric Protein of IgG-Binding ZZ Domains Fused with a Carbohydrate Binding Module. *Phys. Chem. Chem. Phys.* **2017**, *19* (25), 16606–16614. https://doi.org/10.1039/C7CP00662D.
(35) Yu, F. Oligonucleotide Hybridization Studied by a Surface Plasmon Diffraction Sensor (SPDS). *Nucleic Acids Res.* **2004**, *32* (9), e75–e75. https://doi.org/10.1093/nar/gnh067.
(36) Silva, I. I. R. Plasmon Coupled Fluorescence in Gold Nanorods for Enhanced Optical Detection of Oligonucleotides, Master Thesis, 2019.
(37) Demers, L. M.; Mirkin, C. A.; Mucic, R. C.; Reynolds, R. A.; Letsinger, R. L.; Elghanian, R.; Viswanadham, G. A Fluorescence-Based Method for Determining the Surface Coverage and Hybridization Efficiency of Thiol-Capped Oligonucleotides Bound to Gold Thin Films and Nanoparticles. *Anal. Chem.* **2000**, *72* (22), 5535–5541. https://doi.org/10.1021/ac0006627.
(38) Ortega, A.; García de la Torre, J. Hydrodynamic Properties of Rodlike and Disklike Particles in Dilute Solution. *J. Chem. Phys.* **2003**, *119* (18), 9914–9919. https://doi.org/10.1063/1.1615967.
(39) Pérez-Rentero, S.; Grijalvo, S.; Peñuelas, G.; Fàbrega, C.; Eritja, R. Thioctic Acid Derivatives as Building Blocks to Incorporate DNA Oligonucleotides onto Gold Nanoparticles. *Molecules* **2014**, *19* (7), 10495–10523. https://doi.org/10.3390/molecules190710495.
(40) Tsukanov, R.; Tomov, T. E.; Masoud, R.; Drory, H.; Plavner, N.; Liber, M.; Nir, E. Detailed Study of DNA Hairpin Dynamics Using Single-Molecule Fluorescence Assisted by DNA

Origami. *J. Phys. Chem. B* **2013**, *117* (40), 11932–11942. https://doi.org/10.1021/jp4059214.
(41) Patel, V.; Dharaiya, N.; Ray, D.; Aswal, V. K.; Bahadur, P. PH Controlled Size/Shape in CTAB Micelles with Solubilized Polar Additives: A Viscometry, Scattering and Spectral Evaluation. *Colloids Surf. Physicochem. Eng. Asp.* **2014**, *455*, 67–75. https://doi.org/10.1016/j.colsurfa.2014.04.025.
(42) Tsourkas, A. Hybridization Kinetics and Thermodynamics of Molecular Beacons. *Nucleic Acids Res.* **2003**, *31* (4), 1319–1330. https://doi.org/10.1093/nar/gkg212.
(43) Yang, C. J. *Molecular Beacons*; Springer: New York, 2013.
(44) Bielec, K.; Sozanski, K.; Seynen, M.; Dziekan, Z.; ten Wolde, P. R.; Holyst, R. Kinetics and Equilibrium Constants of Oligonucleotides at Low Concentrations. Hybridization and Melting Study. *Phys. Chem. Chem. Phys.* **2019**, *21* (20), 10798–10807. https://doi.org/10.1039/C9CP01295H.
(45) Li, J.; Zhu, B.; Zhu, Z.; Zhang, Y.; Yao, X.; Tu, S.; Liu, R.; Jia, S.; Yang, C. J. Simple and Rapid Functionalization of Gold Nanorods with Oligonucleotides Using an MPEG-SH/Tween 20-Assisted Approach. *Langmuir* **2015**, *31* (28), 7869–7876. https://doi.org/10.1021/acs.langmuir.5b01680.
(46) Huang, J.; Jackson, K. S.; Murphy, C. J. Polyelectrolyte Wrapping Layers Control Rates of Photothermal Molecular Release from Gold Nanorods. *Nano Lett.* **2012**, *12* (6), 2982–2987. https://doi.org/10.1021/nl3007402.
(47) Mehtala, J. G.; Zemlyanov, D. Y.; Max, J. P.; Kadasala, N.; Zhao, S.; Wei, A. Citrate-Stabilized Gold Nanorods. *Langmuir* **2014**, *30* (46), 13727–13730. https://doi.org/10.1021/la5029542.
(48) Lio, D. C. S.; Liu, C.; Wiraja, C.; Qiu, B.; Fhu, C. W.; Wang, X.; Xu, C. Molecular Beacon Gold Nanosensors for Leucine-Rich Alpha-2-Glycoprotein-1 Detection in Pathological Angiogenesis. *ACS Sens.* **2018**, *3* (9), 1647–1655. https://doi.org/10.1021/acssensors.8b00321.
(49) Paulo, P. M. R.; Botequim, D.; Jóskowiak, A.; Martins, S.; Prazeres, D. M. F.; Zijlstra, P.; Costa, S. M. B. Enhanced Fluorescence of a Dye on DNA-Assembled Gold Nanodimers Discriminated by Lifetime Correlation Spectroscopy. *J. Phys. Chem. C* **2018**, *122* (20), 10971–10980. https://doi.org/10.1021/acs.jpcc.7b12622.
(50) Kar, A.; Thambi, V.; Paital, D.; Khatua, S. *In Situ* Modulation of Gold Nanorod's Surface Charge Drives the Growth of End-to-End Assemblies from Dimers to Large Networks That Enhance Single-Molecule Fluorescence by 10 000-Fold. *Nanoscale Adv.* **2020**, *2* (7), 2688–2692. https://doi.org/10.1039/D0NA00303D.
(51) Würth, C.; Grabolle, M.; Pauli, J.; Spieles, M.; Resch-Genger, U. Relative and Absolute Determination of Fluorescence Quantum Yields of Transparent Samples. *Nat. Protoc.* **2013**, *8* (8), 1535–1550. https://doi.org/10.1038/nprot.2013.087.
(52) Brouwer, A. M. Standards for Photoluminescence Quantum Yield Measurements in Solution (IUPAC Technical Report). *Pure Appl. Chem.* **2011**, *83* (12), 2213–2228. https://doi.org/10.1351/pac-rep-10-09-31.
(53) Demers, L. M.; Mirkin, C. A.; Mucic, R. C.; Reynolds, R. A.; Letsinger, R. L.; Elghanian, R.; Viswanadham, G. A Fluorescence-Based Method for Determining the Surface Coverage and Hybridization Efficiency of Thiol-Capped Oligonucleotides Bound to Gold Thin Films and Nanoparticles. *Anal. Chem.* **2000**, *72* (22), 5535–5541. https://doi.org/10.1021/ac0006627.
(54) Doose, S.; Neuweiler, H.; Sauer, M. A Close Look at Fluorescence Quenching of Organic Dyes by Tryptophan. *ChemPhysChem* **2005**, *6* (11), 2277–2285. https://doi.org/10.1002/cphc.200500191.
(55) Zanetti-Domingues, L. C.; Tynan, C. J.; Rolfe, D. J.; Clarke, D. T.; Martin-Fernandez, M. Hydrophobic Fluorescent Probes Introduce Artifacts into Single Molecule Tracking Experiments Due to Non-Specific Binding. *PLoS ONE* **2013**, *8* (9), e74200. https://doi.org/10.1371/journal.pone.0074200.
(56) Nazarenko, I. Effect of Primary and Secondary Structure of Oligodeoxyribonucleotides on

the Fluorescent Properties of Conjugated Dyes. *Nucleic Acids Res.* **2002**, *30* (9), 2089–2195. https://doi.org/10.1093/nar/30.9.2089.

6.9. Annexes

6.9.1. Structures of the molecular beacons designed for DNA and miRNA-145 detection

The structures of the molecular beacons designed for the detection of a DNA sequence associated with sleeping sickness and miRNA-145 are represented in the next figure, both in closed and open hairpin conformations.

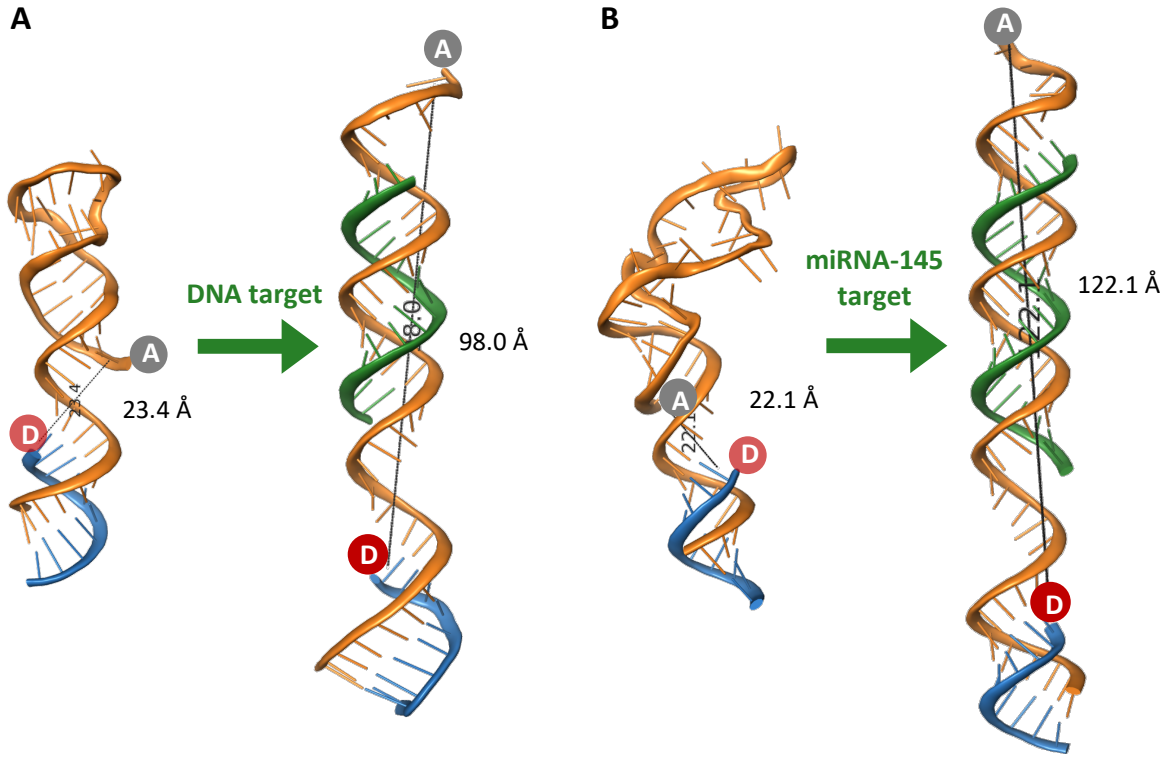

Figure 6.19 - Molecular beacons designed for the detection of nucleic acid targets: DNA sequence associated with sleeping sickness (A) and miRNA-145 (B). Beacons are formed by an Atto-647N donor molecule (red dot) labeled into a ssDNA sequence (in blue, F-Seq) and another DNA sequence (in orange, Q-Seq) labeled with an acceptor molecule (grey dot). Both are in closed and open hairpins' conformation (upon hybridization of targets (in green) with the loop region of the hairpin) as represented in the structures of the left and right side, respectively, of each (A) and (B).

The theoretical thermodynamic analysis (using the OligoAnalyzer Tool and considering oligonucleotide and salt (Na^+) concentrations of 100 nM and 137 mM, respectively) of the closing/opening dynamics of the hairpins correspond to the pretended effect. The change in the Gibbs free energy, $\Delta G°$, of the hairpins' stem has a value of -11.55 kcal.mole^{-1}. Those of Q-Seq for BS, Q-Seq for BM and Q-Seq for BD loop regions hybridized with the respective targets have values of -30.27, -44.86 and -52.61 kcal.mole^{-1}, respectively. Since the $\Delta G°$ of the closed beacons is smaller than that of the beacons hybridized with the targets, this validates, at least

theoretically, the opening and the design of the beacons. The increment (negative) in ΔG° values is due to the increase in the number of nucleotides on the hairpins' loop from 17 in Q-Seq for BS, to 23 in Q-Seq for BM and 27 in Q-Seq for BD.

6.9.2. Absorption spectra of the nucleic acid targets

The absorption spectra of the target sequences used for RNA, DNA and miRNA-145 detection are represented in Figure 6.20, where the characteristic absorption bands of nucleic acids at around 260 nm are visible.

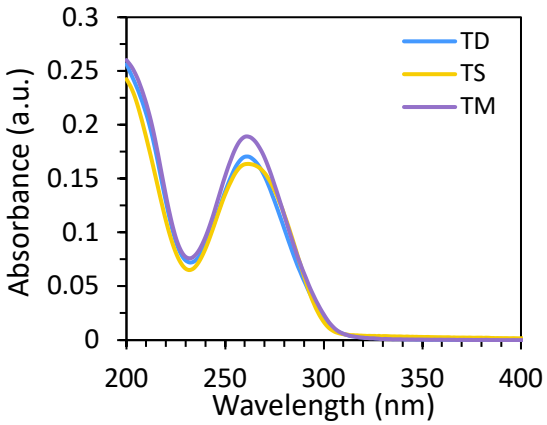

Figure 6.20 - Absorption spectra of synthetic target sequences (1 μM): dengue viral RNA (TD), sleeping sickness-associated DNA (TS) and miRNA-145 (TM).

6.9.3. Fluorescence quantum yield and decay analysis in solution

Table 6.10 presents the values of fluorescence quantum yield and lifetime (see section 6.9.4 of Annexes) of dark quenchers DDQ II and QSY 21 labeled onto Q-Seq sequences.

Table 6.10 - Fluorescence quantum yield (Φ_F) and lifetime (τ_i) assessment for DDQ II- and QSY 21-labeled sequences (1 μM).

	Φ_F (%)	A_1	τ_1 (ns)	A_2	τ_2 (ns)	χ^2
Q-Seq for D1	1	0.77	0.187	0.23	0.533	1.235
Q-Seq for S1	0.5	n.a.	n.a.	n.a.	n.a.	n.a.
Q-Seq for M1	0.6	0.69	0.175	0.31	0.462	1.067
Q-Seq for D2	0.2	0.96	0.011	0.04	1.312	1.088
Q-Seq for S2	0.2	1	0.014	n.a.	n.a.	1.069
Q-Seq for M2	0.2	0.99	0.025	0.01	1.373	1.052

The fluorescence quantum yields of Atto-647N dye and F-Seq are presented in the next table. The decay times and amplitudes from a multi-exponential curve analysis of fluorescence decays is also shown here.

Table 6.11 - Fluorescence quantum yield (Φ_F) and lifetime (τ_i) assessment of Atto-647N dye and F-Seq (1 μM).

	Φ_F (%)	A_1	τ_1 (ns)	A_2	τ_2 (ns)	χ^2
Atto-647N	62	1.00	3.47	-	-	1.86
		0.98	3.52	0.02	0.26	1.12
F-Seq	56	0.95	4.05	0.05	1.05	1.13

The quantum yield's value of Atto-647N, 62%, matches well the reported value for the dye in aqueous solution, 65%,[17] while for F-Seq the value of obtained was 56%. The difference can be possibly justified by Atto-647N dye unexpectedly interacting with the nucleotides of F-Seq. However, there are currently no works published about the interaction of Atto-647N with nucleotides that resulted in quenching of the dye's emission. In other dyes for example, such as Atto-655 (used in the work of Chapter 3), electron donor-acceptor interactions with DNA bases may cause fluorescence quenching, by means of guanosine's low oxidation potential.[54] Still, it was reported that Atto-647N triggered high levels of non-specific interactions in protein conjugates.[55] So, it is hypothesized that the hydrophobicity of Atto-647N in F-Seq creates non-specific interactions between its positively charged N^+ atom, that is delocalized by resonance along the molecule's ring, and the negative DNA chain backbone with subsequent charge transfer from the electron rich nucleotides to the dye, resulting in a slight quenching effect.[56] Also, unexpectedly, for Atto-647N's decay fitting with reasonable χ^2 were required two exponential components.

The next table shows that molecular beacons BD1 and BM1 exhibited quantum yields of around 45%, while for BS1 the measured quantum yield was significantly lower, 15%.

Table 6.12 - Fluorescence quantum yield (Φ_F) and lifetime (τ_i) evaluation for DDQ II-labeled molecular beacons (BD1, BS1 and BM1) and beacon-target assemblies ("w/ target"). Concentrations of F-Seq, Q-Seq and targets were 0.5, 1 and 2 μM, respectively, except for BS1 that was 0.25, 0.5 and 1 μM, correspondingly. All solutions were prepared in 1× PBS.

	Φ_F (%)	A_1	τ_1 (ns)	A_2	τ_2 (ns)	A_3	τ_3 (ns)	χ^2
BD1	46	0.87	4.54	0.11	2.00	0.02	0.21	1.03
w/ target	50	0.86	4.56	0.12	2.24	0.02	0.22	1.04
BS1	15	0.74	4.18	0.17	1.32	0.10	0.24	1.13
w/ target	19	0.74	4.27	0.17	1.68	0.09	0.25	1.04
BM1	44	0.85	4.53	0.13	2.09	0.02	0.27	0.97
w/ target	49	0.89	4.49	0.09	1.79	0.02	0.23	1.00

Regarding QSY 21-labeled beacons (Table 6.13) these are more efficient in quenching Atto-647N's emission than the previous with DDQ II, as can be seen by the significant and consistent reduction of the fluorescence quantum yields, especially for BD2 and BM2.

Table 6.13 - Fluorescence quantum yield (Φ_F) and lifetime (τ_i) assessment for QSY 21-labeled molecular beacons (BD2, BS2 and BM2) and beacon-target assemblies ("w/target"). Concentrations of F-Seq, Q-Seq and targets were 0.5, 1 and 2 μM, respectively, in 1× PBS.

	Φ_F (%)	A_1	τ_1 (ns)	A_2	τ_2 (ns)	A_3	τ_3 (ns)	χ^2
BD2	15	0.86	4.50	0.11	2.05	0.03	0.01	1.15
w/ target	17	0.84	4.48	0.14	2.26	0.03	0.01	1.08
BS2	10	0.91	4.34	0.07	1.41	0.01	0.01	1.04
w/ target	12	0.86	4.13	0.12	1.76	0.01	0.01	1.02
BM2	12	0.83	4.34	0.10	1.30	0.07	0.01	1.12
w/ target	17	0.79	4.23	0.10	1.65	0.03	0.01	1.09

Concerning the fluorescence decays of the beacons, before and after target hybridization, it was required a multi-exponential decay function with three components to properly fit the decay curves with a χ^2 close to one. The main component has a lifetime similar to that of F-Seq (4.05 ns), so it can be attributed to a fraction of unquenched emission from the Atto-647N labels. This component is attributed mostly to open, or to ill-defined closed, hairpin configurations, in which the donor-acceptor distance precludes an efficient FRET process. One cannot completely exclude the possibility of a minor fraction of unlabeled Q-Seq strands, or of free F-Seq, but previous control experiments suggest that these alternative explanations are not the main contribution for the unquenched component. The intermediate decay time with values between 1-2.3 ns and a relative weight of 7-17%, is attributed to Atto-647N emission quenched by FRET in the assembled beacons. These are insufficiently closed but with donor-acceptor distances close enough for a mild FRET efficiency. The short decay time component is attributed to a minor fraction of correctly closed beacons, in which the donor-acceptor distance is well below the Förster radius and an efficient FRET process occurs. The latter component might also have a minor contribution from ill-closed hairpins that within a larger conformational landscape allow for some configurations with short donor-acceptor distances.

6.9.4. Novel hairpin probe HD

The optical spectroscopic characterization of HD was performed by acquiring its absorption, excitation and emission spectra, represented in the next figure.

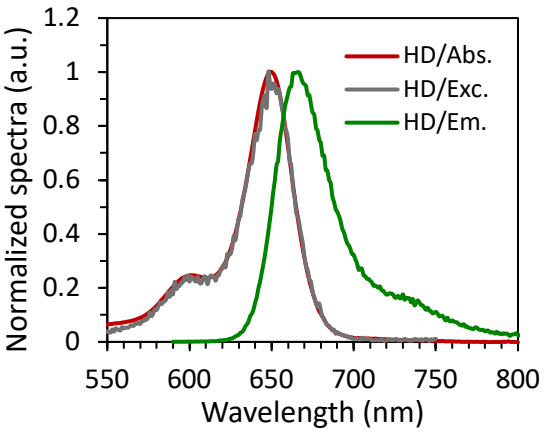

Figure 6.21 - Optical spectroscopic characterization of the new hairpin probe HD (1 μM): absorption (red curve), excitation with emission at 760 nm (grey curve) and emission with excitation at 580 nm (green curve) measured in 1× PBS buffer.

The spectra lineshape of HD and its maximum wavelengths of absorption and emission agree well with an equivalent Atto-647N dye-labeled sequence. The fluorescence quantum yield was also determined, including in the presence of the target TD, by performing the early-mentioned relative determination method. The values obtained are shown in the following Table 6.14 and allowed an elementary evaluation of the probe's functionality.

Table 6.14 - Fluorescence quantum yield (Φ_F) determination for HD and hairpin probe-target assemblies ("w/ target") in 1× PBS, PBST and 10 mM of CTAB. Concentration of HD and target TD were 1 and 2 μM, respectively.

	Φ_F (%)
HD in PBS	39
w/ target	51
HD in PBST	44
w/ target	52
HD in CTAB	34
w/ target	31

The possible secondary structures of HD hairpin probe are shown in the next table.

Table 6.15 - Possible secondary structures of hairpin probe HD obtained in the OligoAnalyzer Tool (oligonucleotide and salt (Na^+) concentrations of 1 μM and 137 mM, respectively). ΔG^o, T_m, ΔH^o and ΔS^o are respectively the change in the Gibbs free energy, the melting temperature, and the change in enthalpy and in entropy.

Structure	ΔG^o (kcal.mole^{-1})	T_m (ºC)	ΔH^o (kcal.mole^{-1})	ΔS^o (cal.K^{-1}mole^{-1})
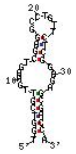	-6.2	47.8	-87.3	-272.02
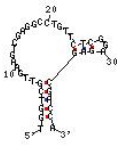	-4.22	46	-64	-200.5
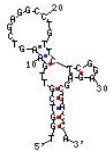	-3.37	37.2	-85.8	-276.46
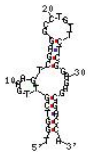	-3.16	35.9	-90	-291.26
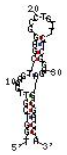	-3.15	38.3	-74.1	-237.96
	-3.15	38.3	-74.1	-237.96
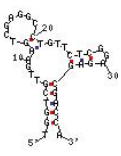	-3.13	36.9	-81.9	-264.18

For the quantification of the number of HD and HDTD probes attached per gold nanorod a ligand displacement protocol with 2-mercaptoethanol was used. Previously, a working curve was established by measuring the fluorescence intensity from solutions of HD with known concentrations in the presence of 20 mM of 2-mercaptoethanol and of PBST buffer

(non-selective functionalization) or 10 mM of CTAB (tip-selective functionalization), as shown in Figure 6.22.

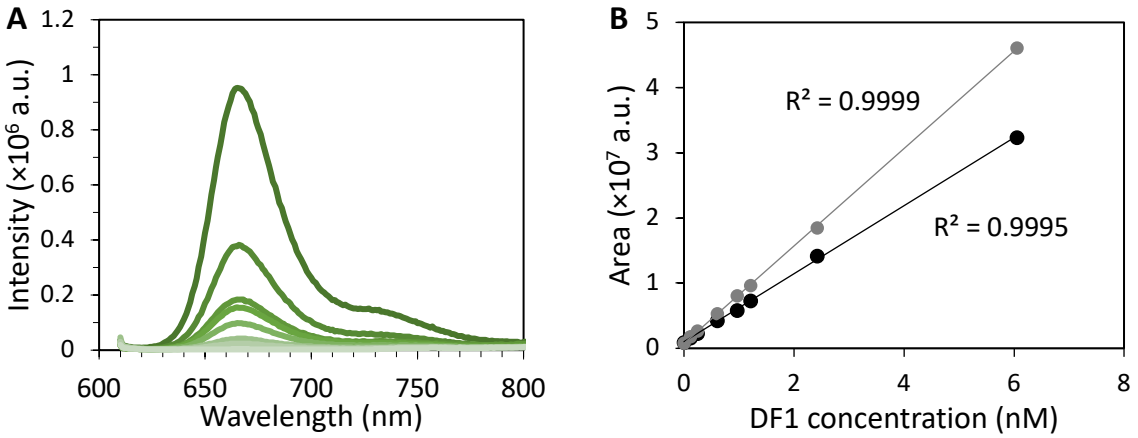

Figure 6.22 - Assessment of the number of HD strands attached per gold nanorod. (A) Emission spectra of hairpin probes with known concentrations (between 0 and 5 nM from down to top) in the presence of CTAB (10 mM) and of 2-mercaptoethanol (20 mM), obtained for an excitation wavelength of 600 nm. (B) Calibration curve for the determination of the concentration of HD in the displacement assays: represented as the integrated emission spectra (area) for solutions of known concentrations of HD in PBST (black circles) and in aqueous CTAB (10 mM, grey circles), both in the presence of 2-mercaptoethanol (20 mM).

Hybridization of HD with the RNA target sequence (HDTD) was confirmed by acquiring fluorescence autocorrelation functions of HD and HDTD solutions by FCS measurements (Figure 6.23).

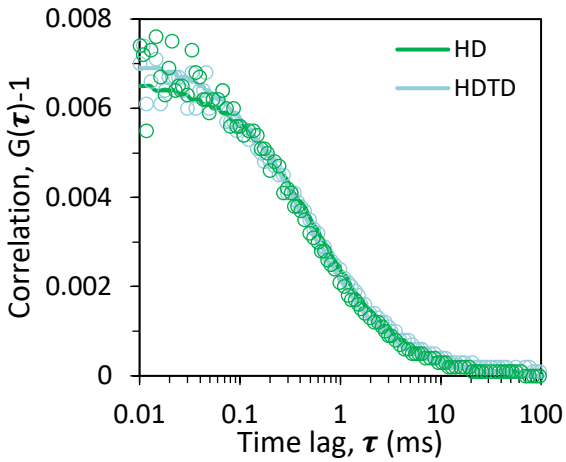

Figure 6.23 - Fluorescence autocorrelation functions of HD and also HD but hybridized with target TD (HDTD), both performed by FCS measurements with an excitation wavelength of 639 nm.

Chapter 7

Concluding Remarks and Future Perspectives

7. Concluding remarks and future perspectives

Nanotechnology has a pivotal role in our contemporary society, in which technologies operating at the nanoscale have recently evolved in an unprecedented way. Its application in the fields of biotechnology and medicine has led to the emergence of nanomedicine, which has now evolved to a point that it is envisioned that in a near future it will provide outstanding advances in healthcare solutions for the general population, not only in clinical environment but also in transitional or home scenarios. One particular example is that of nanobiosensors for medical diagnostics. In this scientific and technological picture, the present doctoral thesis was developed by aiming at an impactful contribution to the field of nanobiosensors with research studies on fluorescently-labeled DNA probes conjugated onto gold nanoparticles. These nanohybrid sensors are foreseen as a possible route towards highly-sensitive detection of nucleic acids proposed as disease biomarkers.

The work developed was mostly concerned with the evaluation of emission enhancement on dye-labeled probes by gold nanoparticle antennas, in view of its application for signal amplification of fluorescence-based sensors. In particular, artificial DNA hairpin probes or molecular beacons were designed for the detection of nucleic acids and, their conjugation onto gold nanorods was explored toward novel biosensor tools with more sensitivity for nucleic acids' detection. This approach promises huge advances and, despite how challenging, it is one worth pursuing.

In the initial part of this research (Chapter 3), the characterization of fluorescence enhancement of red-emitting dyes by a single gold nanorod or, alternatively, by a dimer of gold nanospheres, was performed. Both particle geometries turned out to be powerful and useful nanoantennas. Afterwards, the ability of binding molecular components selectively at plasmon hot-spots was explored through a plasmon-induced photochemical reaction (Chapter 4). In the proof-of-concept, the photochemical functionalization was tested by attaching biotin receptors onto surface-immobilized nanorods. Preliminary results suggested that the photochemical reaction was successful, as planned, but the lack of improvement over chemical functionalization has driven a change in strategy.

A major development of this thesis was the validation of a tip-specific functionalization of dye-labeled DNAs onto gold nanorods to effectively achieve fluorescence enhancement (Chapter 5). It was found that tip-specific functionalization afforded fluorescence enhancements of about one order of magnitude, while indiscriminate surface coating led to undesired emission quenching in nanohybrids. These studies highlighted the importance of site-selective approaches for hot-spot functionalization in the pursue of maximizing plasmon-enhanced fluorescence effects. This result was explored next for the development of a fluorescence-based sensor (Chapter 6). Preliminary tests on the molecular beacons alone resulted in limited sensor responses, which led to a new hairpin probe that was designed to make use of the gold nanorod as an energy acceptor, instead of organic molecules used in the previous design. The tip-functionalization of nanorods with this novel hairpin probe was performed with success, but exploratory assays with the nanohybrids resulted up to now in marginal fluorescence signalling upon target recognition.

Potential improvements to these systems have already been analyzed in Chapter 6. Yet, taking into consideration the overall objective of this thesis' research plan, some further considerations are added below on promising lines of research that can be pursued in the future.

One interesting possibility consists of employing the gold nanodimers of Chapter 3 for developing fluorescence-based sensors. This system actually presented the larger fluorescence enhancements, even though, later, gold nanorods were preferred due to their simplicity and ease of surface functionalization. Still, alternative procedures for particle dimerization could be implemented, which would enable the conjugation of molecular beacon probes onto nanodimers. For instance, the author has previously shown the separate functionalization of two samples of gold nanoparticles with complementary single-stranded DNA sequences to assemble through hybridization both particle samples into a dimer.[1]

As discussed in Chapter 6, by positioning molecular beacons in the gap region of nanorod dimers it would be possible to increase sensor responses. Hence, by combining the expertise on tip-specific functionalization and particle purification by gel electrophoresis, it may be possible to produce dimers of gold nanorods in end-to-end configuration, as reported in the literature using DNA and also other ligands.[2–7] The DNA spacers formed by molecular beacons would allow controlling the interparticle gaps, which will be a crucial asset to obtain even larger field enhancements. Dimer particles based on a tip-to-tip assembly of other sharp particle shapes, like nanotriangles could also be contemplated.[6] The previous experience of the author on the synthesis and functionalization of colloidal silver nanotriangles would be valuable for this purpose.[8]

As soon as the proof-of-concept of the nanohybrid sensor could be achieved, the next challenge would be biosensing assays with target nucleic acids performed in model buffered samples or in real samples, for example, by accessing biological samples (e.g. blood, plasma, serum) containing genetic material of the disease-causing agents. A rigorous elucidation of the interactions between nanohybrids and biomolecules in biological fluids would be of utmost importance.

A marginal improvement suggested here concerns the gold-sulfur bond. Despite being the most widely used in the preparation of metal nanoparticle-based sensors, it is labile, so it may not guarantee enough stability. So, for a more reliable attachment of molecular beacons on the surface of gold nanoparticles, this issue could be circumvented by replacing thiol- with selenol-derivatized oligos due to the higher stability of the gold-selenol bond.[9,10]

The nanohybrid sensors should be further characterized in colloidal solution or while immobilized, in terms of their limit of detection, dynamic range and selectivity. In this regard, one possible route to further extend the dynamic range of the biosensor could be the simultaneous probing of hundreds of multiple individual nanohybrids using widefield single-particle microscopy. It was shown that the simultaneous detection of hundreds of nanoparticles, each performing as a single plasmonic biosensor, would allow us to perform target detection over an extended dynamic range of 7 decades in concentration.[11] Most likely, a similar strategy could provide amplification- or label-free detection of nucleic acids in the sub-picomolar or even femtomolar

range. The ability to reach such low detection limits would contribute significantly toward the application of these nanosensors as a tool for diagnostics. For instance, it could also be a useful strategy to develop rapid tests that detect the viral RNA of SARS-CoV-2, since several sequences were readily suggested as possible biomarkers of the COVID-19 disease.[12,13] This would contribute to contain the spread of the disease, alleviate social and medical infrastructures and systems, and aid in plan prevention and mitigation activities.

In a long-term perspective, if highly emissive and biocompatible nanohybrids are developed by tip-specific functionalization procedures, the molecular beacon-based sensor can eventually be used for cell imaging studies, and as a carrier with functional DNA features for nucleic acid sensing with additional potential for probing gene transcription inside living cells. The ultimate goal of detection of single-molecule nucleic acid hybridization, that could be opened up by plasmon-enhanced fluorescence, would enable the development of improved biosensors. Moreover, the nanohybrids can be implemented in a microfluidic device with integrated optics for fluorescence signal readout and lab-on-a-chip application.[14–17] In fact, fluorescence detection is the most used technique in microfluidics due to its high sensitivity, selectivity, and remarkable efficiency.[14] This approach will allow the evaluation of improved sensing response due to plasmon-enhanced fluorescence signalling in a model device. For instance, the incorporation of the nanohybrids in smartphone-based platforms, already integrated with microfluidics, could be developed, as these can be used straightforward by end-users and possibly patients at the point-of-care (e.g. at home).[18–20] Smartphone fluorescence microscopy,[21] including plasmon-enhanced,[22] can be a valuable tool to this end. Since the accurate detection of disease biomarkers is of growing interest for a broad scientific and medical community, these approaches and the suggested research paths can contribute to the creation of more portable and cost-effective diagnostic and (why not?) therapeutic tools.

7.1. References

(1) Francisco, A. P.; Botequim, D.; Prazeres, D. M. F.; Serra, V. V.; Costa, S. M. B.; Laia, C. A. T.; Paulo, P. M. R. Extreme Enhancement of Single-Molecule Fluorescence from Porphyrins Induced by Gold Nanodimer Antennas. *J. Phys. Chem. Lett.* **2019**, *10* (7), 1542–1549. https://doi.org/10.1021/acs.jpclett.9b00373.
(2) Jones, S. T.; Zayed, J. M.; Scherman, O. A. Supramolecular Alignment of Gold Nanorods via Cucurbit[8]Uril Ternary Complex Formation. *Nanoscale* **2013**, *5* (12), 5299. https://doi.org/10.1039/c3nr01454a.
(3) Tan, S. F.; Anand, U.; Mirsaidov, U. Interactions and Attachment Pathways between Functionalized Gold Nanorods. *ACS Nano* **2017**, *11* (2), 1633–1640. https://doi.org/10.1021/acsnano.6b07398.
(4) Haidar, I.; Aubard, J.; Lévi, G.; Lau-Truong, S.; Mouton, L.; Neuville, D. R.; Félidj, N.; Boubekeur-Lecaque, L. Design of Stable Plasmonic Dimers in Solution: Importance of Nanorods Aging and Acidic Medium. *J. Phys. Chem. C* **2015**, *119* (40), 23149–23158. https://doi.org/10.1021/acs.jpcc.5b07135.
(5) Wang, G.; Akiyama, Y.; Kanayama, N.; Takarada, T.; Maeda, M. Directed Assembly of Gold Nanorods by Terminal-Base Pairing of Surface-Grafted DNA. *Small* **2017**, *13* (44), 1702137. https://doi.org/10.1002/smll.201702137.

(6) Chen, G.; Gibson, K. J.; Liu, D.; Rees, H. C.; Lee, J.-H.; Xia, W.; Lin, R.; Xin, H. L.; Gang, O.; Weizmann, Y. Regioselective Surface Encoding of Nanoparticles for Programmable Self-Assembly. *Nat. Mater.* **2019**, *18* (2), 169–174. https://doi.org/10.1038/s41563-018-0231-1.
(7) Peng, M.; Sun, F.; Na, N.; Ouyang, J. Target-Triggered Assembly of Nanogap Antennas to Enhance the Fluorescence of Single Molecules and Their Application in MicroRNA Detection. *Small* **2020**, *16* (19), 2000460. https://doi.org/10.1002/smll.202000460.
(8) Oliveira-Silva, R.; Sousa-Jerónimo, M.; Botequim, D.; Silva, N. J. O.; Prazeres, D. M. F.; Paulo, P. M. R. Density Gradient Selection of Colloidal Silver Nanotriangles for Assembling Dye-Particle Plasmophores. *Nanomaterials* **2019**, *9* (6), 893. https://doi.org/10.3390/nano9060893.
(9) Hu, B.; Cheng, R.; Liu, X.; Pan, X.; Kong, F.; Gao, W.; Xu, K.; Tang, B. A Nanosensor for in Vivo Selenol Imaging Based on the Formation of AuSe Bonds. *Biomaterials* **2016**, *92*, 81–89. https://doi.org/10.1016/j.biomaterials.2016.03.030.
(10) Hu, B.; Kong, F.; Gao, X.; Jiang, L.; Li, X.; Gao, W.; Xu, K.; Tang, B. Avoiding Thiol Compound Interference: A Nanoplatform Based on High-Fidelity Au-Se Bonds for Biological Applications. *Angew. Chem.* **2018**, *130* (19), 5404–5407. https://doi.org/10.1002/ange.201712921.
(11) Beuwer, M. A.; Prins, M. W. J.; Zijlstra, P. Stochastic Protein Interactions Monitored by Hundreds of Single-Molecule Plasmonic Biosensors. *Nano Lett.* **2015**, *15* (5), 3507–3511. https://doi.org/10.1021/acs.nanolett.5b00872.
(12) Chu, D. K. W.; Pan, Y.; Cheng, S. M. S.; Hui, K. P. Y.; Krishnan, P.; Liu, Y.; Ng, D. Y. M.; Wan, C. K. C.; Yang, P.; Wang, Q.; Peiris, M.; Poon, L. L. M. Molecular Diagnosis of a Novel Coronavirus (2019-NCoV) Causing an Outbreak of Pneumonia. *Clin. Chem.* **2020**, *66* (4), 549–555. https://doi.org/10.1093/clinchem/hvaa029.
(13) Udugama, B.; Kadhiresan, P.; Kozlowski, H. N.; Malekjahani, A.; Osborne, M.; Li, V. Y. C.; Chen, H.; Mubareka, S.; Gubbay, J. B.; Chan, W. C. W. Diagnosing COVID-19: The Disease and Tools for Detection. *ACS Nano* **2020**, *14* (4), 3822–3835. https://doi.org/10.1021/acsnano.0c02624.
(14) Ismail Basha; Eric Ho; Caffiyar Yousuff; Nor Hamid. Towards Multiplex Molecular Diagnosis—A Review of Microfluidic Genomics Technologies. *Micromachines* **2017**, *8* (9), 266. https://doi.org/10.3390/mi8090266.
(15) Rana, A.; Zhang, Y.; Esfandiari, L. Advancements in Microfluidic Technologies for Isolation and Early Detection of Circulating Cancer-Related Biomarkers. *The Analyst* **2018**, *143* (13), 2971–2991. https://doi.org/10.1039/C7AN01965C.
(16) Shi, H.; Nie, K.; Dong, B.; Long, M.; Xu, H.; Liu, Z. Recent Progress of Microfluidic Reactors for Biomedical Applications. *Chem. Eng. J.* **2019**, *361*, 635–650. https://doi.org/10.1016/j.cej.2018.12.104.
(17) Caneira, C. R. F.; Soares, R. R. G.; Pinto, I. F.; Mueller-Landau, H. S.; Azevedo, A. M.; Chu, V.; Conde, J. P. Development of a Rapid Bead-Based Microfluidic Platform for DNA Hybridization Using Single- and Multi-Mode Interactions for Probe Immobilization. *Sens. Actuators B Chem.* **2019**, *286*, 328–336. https://doi.org/10.1016/j.snb.2019.01.133.
(18) Geng, Z.; Zhang, X.; Fan, Z.; Lv, X.; Su, Y.; Chen, H. Recent Progress in Optical Biosensors Based on Smartphone Platforms. *Sensors* **2017**, *17* (11), 2449. https://doi.org/10.3390/s17112449.
(19) Huang, X.; Xu, D.; Chen, J.; Liu, J.; Li, Y.; Song, J.; Ma, X.; Guo, J. Smartphone-Based Analytical Biosensors. *The Analyst* **2018**, *143* (22), 5339–5351. https://doi.org/10.1039/C8AN01269E.
(20) Kim, D. W.; Jeong, K. Y.; Yoon, H. C. Smartphone-Based Medical Diagnostics with Microfluidic Devices. In *Smartphone Based Medical Diagnostics*; Elsevier, 2020; pp 103–128. https://doi.org/10.1016/B978-0-12-817044-1.00007-7.
(21) Vietz, C.; Schütte, M. L.; Wei, Q.; Richter, L.; Lalkens, B.; Ozcan, A.; Tinnefeld, P.; Acuna, G. P. Benchmarking Smartphone Fluorescence-Based Microscopy with DNA Origami Nanobeads: Reducing the Gap toward Single-Molecule Sensitivity. *ACS Omega* **2019**, *4* (1), 637–642. https://doi.org/10.1021/acsomega.8b03136.

(22) Wei, Q.; Acuna, G.; Kim, S.; Vietz, C.; Tseng, D.; Chae, J.; Shir, D.; Luo, W.; Tinnefeld, P.; Ozcan, A. Plasmonics Enhanced Smartphone Fluorescence Microscopy. *Sci. Rep.* **2017**, *7* (1). https://doi.org/10.1038/s41598-017-02395-8.